Cooperativity, Fluctuations and Inhomogeneities in Soft Matter

Cooperativity, fluctuations and inhomogeneities in soft matter

A dissertation presented
by

Jayson Joseph Paulose

to
The School of Engineering and Applied Sciences
in partial fulfillment of the requirements
for the degree of
Doctor of Philosophy
in the subject of

Applied Physics

Harvard University
Cambridge, Massachusetts
May 2013

Thesis advisor

Professor David R. Nelson

Author

Jayson Joseph Paulose

Cooperativity, fluctuations and inhomogeneities in soft matter

Abstract

This thesis presents four investigations into mechanical aspects of soft thin structures, focusing on the effects of stochastic and thermal fluctuations and of material inhomogeneities.

First, we study the self-organization of arrays of high-aspect ratio elastic micropillars into highly regular patterns *via* capillary forces. We develop a model of capillary-mediated clustering of the micropillars, characterize the model using computer simulations, and quantitatively compare it to experimental realizations of the self-organized patterns. The extent of spatial regularity of the patterns depends on the interplay between cooperative enhancement and history-dependent stochastic disruption of order during the clustering process.

Next, we investigate the influence of thermal fluctuations on the mechanics of homogeneous, elastic spherical shells. We show that thermal fluctuations give rise to temperature- and size-dependent corrections to shell theory predictions for the mechanical response of spherical shells. These corrections diverge as the ratio of shell radius to shell thickness becomes large, pointing to a drastic breakdown of classical shell theory due to thermal fluctuations for extremely thin shells.

Finally, we present two studies of the mechanical properties of thin spherical shells with structural inhomogeneities in their walls. The first study investigates the effect of a localized reduction in shell thickness—a soft spot—whereas the second studies shells with a smoothly varying thickness. In both cases, the inhomogeneity significantly alters

the response of the shell to a uniform external pressure, revealing new ways to control the strength and shape of initially spherical elastic capsules.

Contents

Title Page i
Abstract iii
Table of Contents v
Citations to Previously Published Work viii
Acknowledgments ix
Dedication xii

1 Introduction **1**
1.1 Cooperativity and stochasticity in elastocapillary self-organization 2
1.2 Statistical physics of thin elastic shells 10
1.2.1 Elastic energy of plates and shells 10
1.2.2 Statistical mechanics of solid membranes 14
1.2.3 Experimental realizations of fluctuating shells 17
1.3 Buckling of inhomogeneous shells 19
1.3.1 Buckling of uniform spherical shells 21
1.3.2 Controlling buckling using inhomogeneities 26
1.3.3 Experimental motivation 28

2 A two-parameter sequential adsorption model applied to microfiber clustering **31**
2.1 Microfiber clustering and order formation 37
2.1.1 Ordering mechanism and formulation of the CSA model 38
2.1.2 Choice of CSA model rates 41
2.2 Simulation results 43
2.2.1 Mean coverage at saturation 43
2.2.2 Domain sizes, chord lengths and domain wall densities 45
2.2.3 Pair correlations 52
2.2.4 Diffracted intensity 57
2.3 Experimental results 61
2.4 Conclusion 66

3 Statistical physics of pressurized spherical shells **70**
3.1 Elastic energy of a thin shell 73
3.2 Anharmonic corrections to elastic moduli 75

3.3 Simulations of thermally fluctuating shells . . . 76
3.4 Conclusion and outlook . . . 82

4 Buckling pathways in spherical shells with soft spots 84
4.1 Elastic theory of thin spherical shells . . . 85
4.1.1 Elastic energy of thin shells . . . 88
4.1.2 Shells with soft spots . . . 88
4.2 Numerical results . . . 89
4.3 Governing equations of shell theory . . . 94
4.3.1 Equations in polar coordinates . . . 95
4.4 Buckling of uniform spherical shells under pressure . . . 96
4.5 Snap-through of soft caps . . . 100
4.5.1 Mechanism for snap-through buckling . . . 101
4.5.2 Non-dimensionalizing the equations . . . 103
4.5.3 Analysis of linearized equations . . . 107
4.5.4 Nonaxisymmetric buckling . . . 109
4.5.5 Axisymmetric buckling . . . 114
4.6 Collapse of the remainder . . . 120
4.6.1 Energetics of a nearly isometric inversion in a shell with a soft cap . 121
4.6.2 Dependence of collapse pressure on cap size and thickness . . . 126
4.7 Hysteresis . . . 127
4.8 Conclusion . . . 129

5 Buckling of shells with a smoothly varying thickness profile 132
5.1 Experimental motivation . . . 133
5.1.1 Measurement of buckling properties . . . 134
5.2 Buckling pressure of a shell with a smoothly varying thickness . . . 135
5.2.1 Comparison to experimental measurements . . . 140
5.3 Volume change prior to buckling . . . 141
5.3.1 Time delay before buckling for experimental capsules . . . 142
5.4 Postbuckling shapes . . . 144
5.4.1 Experimental observations . . . 144
5.4.2 Numerical simulations . . . 146
5.5 Hysteresis properties . . . 147
5.6 Conclusion . . . 150

A Elastic energy of nearly isometric inversions in spherical shells 151

B Capillary clustering of microfibers: methods 156
B.1 Details of numerical simulation . . . 156
B.2 Experimental methods . . . 157

C Thermally fluctuating spherical shells: analytical calculations **158**
C.1 Fields and strains in shallow shell theory 158
C.2 Elimination of in-plane phonon modes and uniform spherical contraction by Gaussian integration 162
C.3 One-loop contributions to the self-energy 164
C.4 Calculation of fluctuation spectrum with spherical harmonics 168
C.5 Linear response of the shell to point forces 170

D Simulations of thermally fluctuating shells **173**
D.1 Monte Carlo Simulations of randomly triangulated shells 173
D.2 The fluctuation spectrum from computer simulations 175
D.3 Simulations of shells indented by point-like forces 175
D.4 Measuring the effective spring constant from fluctuations 176

E Numerical simulations of zero-temperature shells **179**

F Derivation of the nonlinear equations of shallow shell theory **184**

G Fluid flow through an inhomogeneous spherical capsule **187**
G.1 Flow rate out of an inhomogeneous capsule 187
G.2 Estimate of capsule permeability 188

Bibliography **190**

Citations to Previously Published Work

Chapter 2 appears in its entirety as

> **Two-parameter sequential adsorption model applied to microfiber clustering**
> J. Paulose, D. R. Nelson, and J. Aizenberg, *Soft Matter* **6**, (2010).

Chapter 3 appears in its entirety as

> **Fluctuating shells under pressure**
> J. Paulose, G. A. Vliegenthart, G. Gompper, and D. R. Nelson, *Proceedings of the National Academy of Sciences of the USA* **109**, 19551–19556 (2012).

Chapter 5 is based on the manuscript

> **Delayed buckling and guided folding of inhomogeneous capsules**
> S. S. Datta, S.-H. Kim, J. Paulose, A. Abbaspourrad, D. R. Nelson, and D. A. Weitz, *Physical Review Letters* **109**, 134302 (2012).

A manuscript based on Chapter 4 has been submitted for peer review.

Acknowledgments

I have been fortunate to have Prof. David R. Nelson as my advisor. David introduced me to many beautiful and elegant physical problems, and gave me able guidance and ample independence as I pursued their answers. His ability to draw insightful connections between the problem at hand and other areas of physics has come to my rescue more than once, and continues to amaze me. I thank him for his guidance and mentorship over the past six years.

I am also grateful to the members of my thesis committee. Prof. Joanna Aizenberg has been an invaluable mentor and guide who gave me my first research projects in graduate school, including the opportunity to perform experiments myself. I have learned a lot about formulating and attacking a scientific problem from Prof. Michael Brenner, and his enthusiasm for figuring things out is something I aspire to achieve in my own career. Prof. Subir Sachdev always spared his time and expertise for me, whether to explain the subtleties of statistical mechanics or to help me get in touch with his colleagues at other institutions. I thank my committee for their supervision and guidance of this thesis.

My collaborators in experiment and simulation have kept me honest as a theorist, and taught me a lot. I thank the members of the Aizenberg lab, particularly Sung Hoon Kang, Francis Gibaud, Boaz Pokroy and Ben Hatton; Gerrit Vliegenthart and Prof. Gerhard Gompper at the Forschungszentrum Jülich; Anderson Shum and Sujit Datta from the Weitz lab; Guangnan Meng from the Manoharan lab; and James Weaver at the Wyss Institute. I also thank my colleagues in soft matter at Harvard, particularly Zorana Zeravcic, Wolfram Möbius, Ariel Amir, Eleni Katifori, Madhav Mani, Kirill Korolev, Melanie Müller, Andrej Kosmrlj, Max Lavrentovich, and Thip Chotibut, for discussions on a wide range of topics over the years. Special thanks are due to Prof. Vinny Manoharan for his guidance on scientific and career-related matters, and to Prof. John Hutchinson, a guru of shell theory who has been a wonderful source of wisdom and inspiration.

I am grateful to my fellow graduate students Ben Feldman, Chin Lin Wong, David Benjamin, Eddie Schlafly, Eleanor Millman, Giovanni Zevi Della Porta, Jack DiSciacca, Julia Rasmussen, Laura Jeanty, Michael Gullans, Nick Hutzler, Raji Shankar, Renee Sher, Sofia Magkiriadou, Tess Williams, Tina Lin, and Yiwen Chu for the late-night problem set sessions, trips to Rustica, hiking expeditions, dinners, jam sessions, squash games, concerts, Super Bowl parties, puppet show practices, dim sum brunches and movie nights that made graduate school so much fun.

I thank the administrators at Harvard SEAS, Harvard Physics, the NSF MRSEC and the Harvard International Office who took care of things that needed taking care of.

I thank the Neils Bohr Institute and Neils Bohr International Academy, Prof. Gerhard Gompper's group at the Forschungszentrum Jülich, and the Harvard ATLAS group at CERN for hosting me during periods in which a significant part of the work reported in this thesis was carried out. I am grateful to the Physics graduate students for welcoming me into the G1 area when I lacked an office.

I also thank my family, and my friends from all walks of life, for their love and support during my time in graduate school. Special thanks to my former housemates Greg Snyder, Steph Jacobs and Charlie Bergen; my Free Parking bandmates; my Orange-Sox friends; and the Harvard Dudley Dragon Boat team for all the good times we've had together. I also thank Dinky Aunty and Manikat Achen for being my guardians and my closest family in the United States, and Tracy and Roger Jeanty for always making me feel at home in Sherborn or at Squam.

I am indebted to my family, who instilled in me the values of hard work, discipline and curiosity that made all of my accomplishments, including this thesis, possible. My sister was my first role model, setting a high bar in academic, career and life accomplishments. I thank her for her constant love and inspiration. Without my parents' com-

plete dedication to their children's upbringing and education, their emphasis on learning and reading, their patient answers to my incessant questions about the world, their encouragement of my sometimes quirky hobbies, and their unending love and care, I would not have become the scientist I am today. They gave me the support and the freedom I needed to follow my dreams, from India to Singapore to the United States, and were there for me every step of the way, through many twists and turns. This thesis is the culmination of my long academic journey, and I dedicate it to my parents.

For my happiness and well-being during the many years of work that went into this dissertation, I owe the most to Laura Jeanty—my companion, partner, and fellow adventurer through practically all of graduate school. Through her own example, she has challenged and inspired me to become a better scientist and a better person, reinforcing my passion for physics and restoring my faith in my own abilities whenever my motivation ran low, while also ensuring that I never lost sight of the things that are truly important. Between the lines of this thesis lies the unwritten story of our journey together, one that I am excited to continue on beyond these pages. Thank you, Laura, for everything.

To Mummy and Daddy

Chapter 1

Introduction

Soft matter is the stuff of our everyday lives. From polymers to colloidal assemblies to living cells, a wide range of systems derive their mechanical strength from weakly interacting polyatomic building blocks rather than a rigid lattice of atoms, making them easy to deform. Mechanical softness may also arise because of geometry: aluminum foil, graphene, and optical fibers are all flexible because of their small extent in one or more material dimensions. Soft structures display a host of interesting mechanical phenomena over a wide range of materials and length scales — witness the complex wrinkling of a dried raisin, or the wild thermal undulations of a red blood cell membrane. As a result of their mechanical softness, they exhibit instabilities in which small changes in external forces induce large, potentially discontinuous changes in shape. A variety of driving forces, such as capillary and osmotic forces and notably thermal fluctuations, may be important for these deformations, and the effects of structural nonuniformities, stochasticity and entropy can be paramount. Understanding the mechanics of soft structures contributes to our fundamental understanding of natural structures that arise in biological matter, and also has important applications in nanotechnology, enabling the design of new functional materials and structures.

This thesis investigates three different phenomena that involve the mechanics of thin soft structures: the competition between cooperative and history-dependent stochastic effects in the self-organization of flexible micropillars into ordered clusters (Chapter 2), the influence of thermal fluctuations on the mechanical properties of spherical shells (Chapter 3), and the effect of inhomogeneities in the thickness of spherical shells on their response to an external pressure (Chapters 4 and 5). Although the phenomena cover a range of physical concepts that call for various theoretical and computational approaches, they are nevertheless linked by common themes. Chapters 2 and 3 both focus on the application of statistical physics ideas to soft matter systems, whereas chapters 4 and 5 highlight the importance of geometry in determining the mechanical response of curved membranes when thermal fluctuations are unimportant. Connecting all the phenomena is the underlying physics of slender elastic structures, whether rods or shells. In the following sections of this introductory chapter, we introduce the phenomena that will be discussed in detail in the subsequent chapters, focusing on essential physical principles, experimental motivations, and relevant past work.

1.1 Cooperativity and stochasticity in elastocapillary self-organization

Self-assembly and self-organization refer to the spontaneous formation of global ordered structures due to local interactions between components or uniformly applied driving forces, without directed manipulation of individual components during the ordering process. Typically, self-assembly refers to processes in which the desired structure is the equilibrium configuration of the components, whereas self-organization may involve driving the system out of equilibrium to obtain the final structure. Both are important paradigms

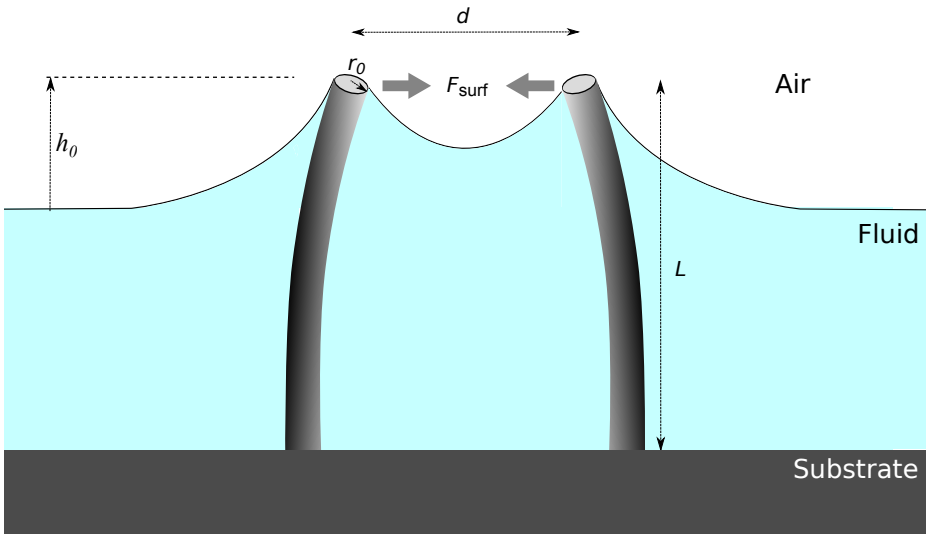

Figure 1.1: The phenomenon of elastocapillary coalescence. Two elastic rods that perturb a fluid surface experience a capillary force F_{surf} that draws their tips to each other, causing them to deform.

for assembling functional structures out of building blocks ranging from individual molecules to macroscopic objects [1]. Technology has yet to enable large numbers of microscale components to be manipulated individually and reliably, but many physical and chemical techniques have been developed to tune the interactions among different components, or between components and their surroundings, to induce them to self-organize into desired structures. Biological systems also rely on self-assembly and self-organization to construct functional structures from their building blocks, e.g. the folding of polypeptides into the desired protein structure, or the assembly of viral capsids from their constituent proteins. Understanding self-assembly and self-organization is of fundamental as well as technological importance.

A commonly exploited driving force in self-assembly and self-organization of soft structures is the capillary force between objects that perturb a fluid interface. Capillary forces are sufficient to cause slender objects to bundle together, overcoming their resistance

to deformation. This everyday phenomenon, familiar to us from the clumping of wet hair and of paintbrush bristles, is known as *elastocapillary coalescence* [2]. Fig. 1.1 illustrates the mechanism, for a pair of elastic pillars attached to a substrate being wet by an evaporating liquid. When the liquid level falls below the tips of the pillars, the interface is pinned to the tips, distorting the interface from the planar shape that minimizes its surface area. The net interfacial energy associated with the surface perturbation is reduced when two pillar tips move closer to each other, giving rise to an attractive capillary force between tips. For small interfacial perturbations, and when the distance between the pillar tips is small compared to the capillary length $\sqrt{\gamma/\rho g}$ of the liquid (γ is the surface tension, ρ the liquid density and g the gravitational acceleration), the capillary force resembles a Coulomb attraction [3]:

$$F_{\text{surf}}(d) \approx -2\pi\gamma Q^2/d, \tag{1.1}$$

where d is the distance between pillar tips, and Q is a "capillary charge" associated with each pillar (identical in this case) which is set by the nature of the pinning at the tip. For instance, if we restrict the angle of the meniscus to be pinned to some value ψ at $r = r_0$, where r_0 is the radius of the cylindrical pillar, then $Q \approx r_0 \tan\psi$. Alternatively, if we require the interface to be pinned to some height h_0 above the unperturbed surface far away from the pillars, then $Q \propto h_0$. (If we had objects with different wetting properties perturbing the interface, we would assign different charges Q_1 and Q_2 to the objects; they could even have opposite sign corresponding to a repulsive capillary interaction.) The capillary length associated with water is around 2 mm, which makes Eq. (1.1) valid for separations up to fractions of a millimeter; *i.e.* relevant for microscale systems. For separations larger than the capillary length of the liquid, the interaction is screened by gravity and dies out exponentially [4].

For the capillary force to be sufficient to bring two pillar tips into coalescence,

we must compare it to the force needed to bend the pillars to bring their tips together. For small deflections, the force needed to move the pillar tips is linear in the deflection x: $F_{\text{bend}} \sim (Er_0^4/L^3)x$ up to prefactors of order 1, where E is the Young's modulus and L the pillar length [5]. Comparing the scale of the capillary forces, $\gamma Q^2/d \sim \gamma r_0^2/d$, to the scale of elastic deflection forces $Er_0^4 d/L^3$ needed to bring the tips together over the separation d, gives a critical pillar length $L_c \sim (Er_0^2 d^2/\gamma)^{1/3}$ above which pillar tips can coalesce due to capillary forces. For pillars of diameter $r_0 = 100$ nm, with a typical value of Young's modulus $E = 1$ GPa and a liquid with surface tension of 0.07 N/m (similar to water), L_c is a few microns for separations of $d = 1$ µm; *i.e.* capillary forces are sufficient to bring together micropillars a tenth of a micron in diameter, spaced about a micron apart and a few microns in height. This makes elastocapillary coalescence a viable mechanism for self-organization of elastic structures at length scales that are important for biological, photonic and colloidal applications. Following the coalescence, van der Waals or chemical adhesion of the pillar tips can stabilize the clusters formed, allowing them to persist even after the wetting liquid has evaporated completely.

Clustering *arrays* of microscale pillars with one end attached to a substrate gives rise to interesting collective phenomena in elastocapillary self-organization. Fig. 1.2 gives two examples. Fig. 1.2(a) shows the pattern formed due to elastocapillary coalescence of vertical micropillars distributed randomly on a substrate to which one end of each micropillar is attached (reported in Ref. [6]). Clumps of micropillars are observed with a characteristic clustering size that is set by the relation between elasticity, capillarity and interpillar distance. The final structure differs significantly in its surface properties from the initial array. Fig. 1.2(b) shows the result of capillary clustering in a *regular* array of micropillars initially arranged in a square lattice (from Ref. [7]). The relation between pillar stiffness, surface tension and interpillar distance is such that the system preferentially

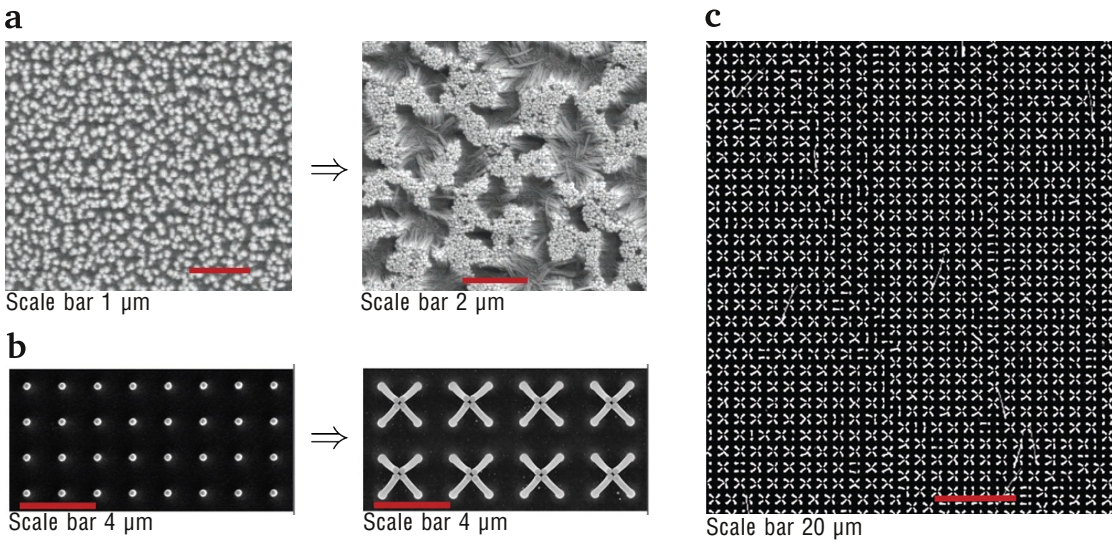

Figure 1.2: Capillary clustering of arrays of vertical micropillars with one end attached to a substrate and the other end free. Scanning electron microscopy (SEM) images are shown looking vertically down on the substrate. (a) Silicon micropillars randomly distributed on a flat substrate shown before (left) and after (right) capillary clustering. In the unclustered state, the tips of the individual pillars are visible as light dots. The pillars are roughly 0.02–0.1 μm in diameter, 0.9 μm in height and separated by 0.1 μm on average. (b) Epoxy micropillars arranged in a highly regular square array, before (left) and after (right) capillary clustering. The pillars are 0.3 μm in diameter, 5 μm in height and nearest neighbors are separated by 2 μm in the square array. The system forms 2×2 clusters of four individual pillars joined at the tip, which appear as a characteristic $\times$ shape in the top-down SEM image. (c) Larger region of experiment shown in (b), depicting long-range ordering of 2×2 clusters into domains. Image credits: (a) from J.-G. Fan et al, *Nano Letters* **4**, 2133 (2004); (b), (c) from B. Pokroy et al, *Science* **323**, 237 (2009).

forms 2×2 clusters of four adjacent pillars joined at the tip. Strikingly, these clusters form ordered domains that extend over many lattice lengths [Fig. 1.2(c)]. Such self-organized ordered patterns may find application in fabricating dynamic substrates with tunable surface properties (the periodicity of surface features is an important determinant of the adhesion and wetting properties of a substrate), or in trapping colloidal particles suspended in the wetting liquid into ordered arrays for functional purposes. In Chapter 2, we investigate the ordering mechanism in elastocapillary clustering of micropillars arranged in square arrays. We develop, characterize and test a model of pattern formation through irreversible clustering events on a square lattice that explains many statistical features of the final clustering patterns, including the spatial extent of the ordered regions and the density of boundaries separating four translationally equivalent domains.

The formation of ordered patterns during the clustering process is a result of a meniscus-mediated cooperativity in clustering, as explained in Ref. [7]. Briefly, the formation of a lone cluster on the lattice of initially upright pillars happens due to random imperfections in the substrate or nonuiformities in the local evaporation rate which affect the capillary interactions between pillars. Once a cluster forms, however, it distorts the meniscus nearby and consequently the capillary attraction with neighboring pillars [which depends on the distance between pillar tips, following Eq. (1.1)] in a way that induces the formation of 2×2 clusters at nearby positions. This leads to a cascade of clustering events propagating outward from the initial cluster, leaving behind an ordered square superlattice of 2×2 clusters with twice the spacing of the pillars themselves. (See Chapter 2 for further details of the cooperative clustering mechanism.)

However, the ordered arrangement of clusters does not persist across the entire sample. In the experiment, isolated clustering events occur in different regions of the sample through a stochastic process, nucleating different clustering cascades that grow

simultaneously. When the advancing edge of one such cascade meets another, the two ordered regions may be incompatible, and a boundary is formed between distinct ordered regions, out of registry by half a unit cell separation. Fig. 1.2(c) shows many of these ordered regions, separated by domain boundaries that largely follow the lattice directions. The characteristic size of each ordered region is set by the competition between the rates of cooperative and stochastic clustering: a high rate of stochastic nucleation creates many competing cascades, bringing down the average size of ordered regions. Another important determinant of the final cluster patterns is that the clustering is *irreversible* as the liquid evaporates. Once a 2×2 cluster is formed, it does not unbind during the course of the experiment. This means that there is no analogue of a coarsening mechanism that would allow clusters to rearrange themselves to improve the overall order of the patterns. The precise history of the clustering process is crucial in determining the statistics of the final patterns.

The model we develop in Chapter 2 incorporates these basic ingredients of stochasticity, cooperativity and irreversibility. The emphasis is not on the mechanical aspects of an individual clustering event, but rather on the statistical properties of the patterns that arise as a result of multiple events on the same substrate. The model treats the formation of 2×2 clusters as sequential events, starting with a square lattice of initially upright pillars. Isolated clusters have a uniform probability of forming anywhere on the lattice where upright pillars are available, *via* stochastic events. However, once a cluster has been formed, the rate of cluster formation is enhanced by cooperative capillary forces in nearby positions on the square lattice. Clusters, once formed, do not unbind, and the process continues until no more 2×2 groups of free pillars are left. This sequential process is amenable to investigation *via* numerical simulations, which we use to characterize various statistical properties of the resulting patterns as the relative importance of cooperativity to stochas-

ticity is varied. We compare these statistical properties (such as average domain size and density of domain boundaries) to those measured in experimental realizations similar to those depicted in Fig. 1.2(c).

The procedure of sequential cluster formation we have just described does not directly include the elastodynamics of the clustering pillars; the dynamical details are subsumed into the stochastic and cooperative clustering rates, which are inferred from the experimental patterns. Therefore, our model could equally well be used to describe the adsorption of atoms or molecules onto a surface (such as the crystalline arrangement of a metal surface, providing a lattice of adsorption sites). Beginning with an empty square lattice, we cover the lattice by depositing individual atoms randomly on the surface (the adsorption of an atom at a lattice site corresponds to the formation of a cluster at that position). Atoms, once deposited, cannot unbind or move, and the deposition of an atom prevents further deposition on the same lattice site. However, it may increase the affinity of nearby lattice sites —- a mechanism of cooperativity in the irreversible adsorption process, that can lead to growing clusters of adsorbed atoms, much like the cascades of cluster formation discussed above. Models of such nonequilibrium adsorption of particles on a surface are known as *sequential adsorption* models [8]. Originally developed to describe the deposition of gas atoms on metallic surfaces, they have been been applied to pattern formation in processes as varied as car parking and protein adsorption onto substrates [9]. The particular lattice geometry and the capillary-mediated interactions in our problem inspired a sequential adsorption model with a new form of cooperativity that was not considered previously. One of the main results of the analysis in Chapter 2 is that this new cooperativity disrupts, rather than enhances, the order in the cluster patterns. We find evidence for such disruption of order in our experimental system; similar mechanisms may be relevant in other sequential adsorption processes.

The work described in Chapter 2 was performed in collaboration with the research group of Prof. Joanna Aizenberg, whose previous work inspired the analysis, and in whose laboratory the experiments were performed.

1.2 Statistical physics of thin elastic shells

Soda cans, ping-pong balls, and architectural domes are all examples of *shells*, thin-walled structures with an underlying curvature in their undeformed state. The elastic response of such structures to external forces is fundamentally determined by their geometry in several ways: first, their small extent in one dimension compared to the other two makes them much easier to bend than to stretch; second, the relationship between deformations and strains is inherently nonlinear, even if the material itself obeys linear (Hookean) elasticity; finally, the background curvature in their shape provides a geometric stiffness to such structures that tends to stabilize them compared to flat elastic sheets (or *plates*) made of the same material. These properties become apparent upon studying the elastic energy associated with deformations in thin plates and shells.

1.2.1 Elastic energy of plates and shells

An enormous simplification in the elastic description of thin plates and shells (when the thickness h is small compared both to the extent of the system and the radii of curvature that describe deviations from planarity) comes from reducing the three-dimensional problem of determining stresses throughout the material to a two-dimensional one. Thin shell theory is concerned only with deformations of the *mid-surface*, which is the set of points equidistant from the two free surfaces bounding the material. The departure of this surface from its initial, stress-free configuration is captured in a two-dimensional strain tensor u_{ij}

which quantifies changes in the local metric of the surface at each point, and a bending tensor $k_{ij} = K_{ij} - K^0_{ij}$ that quantifies the difference in the curvature K_{ij} of the deformed surface from the initial curvature K^0_{ij} (the indices i, j of these second-rank tensors run over the two coordinate directions tangent to the surface at each point). For instance, $K^0_{ij} = \delta_{ij}/R$ for a shell whose undeformed shape is a sphere of radius R (where δ_{ij} is the Kronecker delta function). For a shell made up of an isotropic, Hookean material with (three-dimensional) Young's modulus E, thickness h and Poisson ratio ν, the elastic energy density $F_{\rm el}$ at any point in the mid-surface is quadratic in the strain and bending tensors [10]:

$$\begin{aligned} F_{\rm el} = \frac{Y}{2(1-\nu^2)} \left[(u_{11}+u_{22})^2 - 2(1-\nu)(u_{11}u_{22} - u_{12}^2) \right] \\ + \frac{\kappa}{2} \left[(k_{11}+k_{22})^2 - 2(1-\nu)(k_{11}k_{22} - k_{12}^2) \right], \end{aligned} \tag{1.2}$$

where

$$Y \equiv Eh \tag{1.3}$$

is the two-dimensional Young's modulus and

$$\kappa \equiv \frac{Eh^3}{12(1-\nu^2)} \tag{1.4}$$

is the bending rigidity, both set by the material properties E, h and ν of the bulk material making up the shell. The total elastic energy of the shell is obtained by integrating the elastic energy density over the entire mid-surface. The dependencies of the two-dimensional (2D) elastic constants on the three-dimensional (3D) material properties show that the relative energy contribution of stretching far overwhelms the contribution due to bending as the shell thickness h becomes small. Thus, extremely thin plates and shells are much easier to bend than to stretch, as exemplified by a sheet of paper.

The dimensional reduction from 3D to 2D elasticity introduces errors of order $|h/R|$ and $(h/L)^2$, where R and L are the characteristic radius of curvature and size of the undeformed shell; *i.e.* Eq. (1.2) becomes exact in the limit of infinitely thin shells. When

the initial curvature of the undeformed surface is set to zero, Eq. (1.2) also describes the elastic energy of flat plates, as well as solid *tethered membranes*, *i.e.* monomers (atoms or molecules) linked to form a flat elastic network that can support shear [11]. Unlike plates or shells, membranes can approximate ideal two-dimensional shapes, with their Young's modulus and bending rigidity treated as intrinsic properties of the surface, rather than originating from a bulk material with a thickness in the third dimension.

The elastic energy density, Eq. (1.2), is constructed from invariants (the trace and the determinant) of the strain and bending tensors, and is therefore independent of the choice of coordinate system. These tensors can be expressed in terms of the displacements (two tangential to the initial surface and one normal to it) of the mid-surface in three-dimensional space, for which a coordinate system is required, and further approximations may be needed. Appendix C.1 presents one such set of relations for Cartesian coordinates tangential to a section of the shell with dimensions small compared to its radius of curvature, known as *shallow-shell theory*. Rather than focusing on a particular choice of coordinates, we present here key scaling properties of strains and bending moments with the normal displacement w; these results play a major role in the mechanics and statistical physics of thin shells.

For small displacements of the mid-surface (compared to the size and radius of curvature of the shell), the components of the bending tensor can be represented solely in terms of spatial derivatives of the normal displacement: $k_{ij} \sim \partial_i \partial_j w$, where w is the normal displacement and ∂_i refers to a spatial derivative in the ith tangential direction ($i \in \{1, 2\}$). Contributions of the tangential displacements to the bending tensor are insignificant for thin shells, as long as the characteristic length of deformations is small compared to the largest radius of curvature of the shell [10]. The strain tensor, on the other hand, has linear contributions from gradients of the tangential displacements, but the contribution of the

normal displacement is again unique in that it couples to the underlying curvature of the shell in its undeformed state: $u_{ij} \sim k^0_{ij} w$, where k^0_{ij} is the curvature tensor of the undeformed surface. (For instance, a spherical shell of radius R has $u_{ij} \sim w/R$.) This coupling makes curved shells fundamentally different from flat plates, for which the lowest order contribution of w to the strain tensor is quadratic ($u_{ij} \sim \partial_i w \partial_j w$), rather than linear. A flat plate can accommodate transverse deformations to its mid-surface by paying only a bending energy cost, but a curved shell also pays a stretching energy cost at linear order in the deformation. Since stretching is energetically costlier than bending for thin shells, curved shells are inherently stiffer purely due to their geometry. A roof sinusoidally corrugated in one direction is stiffened against bending in an orthogonal direction for this reason.

This geometric stiffness gives rise to an important elastic length scale for deformations in curved shells with characteristic radius of curvature R. For a normal deflection that varies over a characteristic length l, the bending and stretching energy contributions are comparable when

$$\kappa k_{ij}^2 \sim Y u_{ij}^2 \Rightarrow \kappa \left(\frac{w}{l^2}\right)^2 \sim Y \left(\frac{w}{R}\right)^2 \Rightarrow l \sim \left(\frac{\kappa R^2}{Y}\right)^{1/4} = \frac{\sqrt{hR}}{[12(1-\nu^2)]^{1/4}} \equiv \ell. \tag{1.5}$$

The elastic length scale ℓ sets the typical spatial extent for deformations of curved shells. For instance, if an inward force is applied at some point on the shell, the resulting normal deflection extends over a length of order ℓ. In the mechanical failure of spherical shells under large external loads, ℓ sets the wavelength of the unstable deflection mode that leads to loss of stability, as well as the sharpness of large deformations that appear above the failure load (described in more detail in Section 1.3).

So far, we have only considered linear contributions of the displacements to the strain tensor. For small strains (*i.e.* displacements small compared to the size of the shell), the higher order contributions of the tangential deformation fields are small compared to

the linear contributions, and can be ignored. However, the next-order contribution of the normal deformation to the strain tensor, which scales as $\partial_i w \partial_j w$, need not be insignificant even for small strains. A comparison of its magnitude to the linear contribution when the deformation varies on a length scale l shows that the nonlinear contribution becomes significant for deflections that scale as

$$\left(\frac{w}{l}\right)^2 \sim \frac{w}{R} \Rightarrow w \sim \frac{l^2}{R} \text{ or larger,} \tag{1.6}$$

which can be very small for normal deflections that vary over short length scales compared to the radius of curvature. For a deformation that varies over the elastic length scale $\ell \sim \sqrt{hR}$ which is the characteristic deformation scale in curved shells, the nonlinear contribution is significant when $w \sim h$, *i.e.* for deflections of order the shell thickness or larger. The strains are still very small for such deflections ($u_{ij} \sim h/R$), but the nonlinearity cannot be ignored. The same nonlinearity is also relevant for small deflections in flat plates [5].

The nonlinear contribution of the normal deformations to the strain tensor is essential for many interesting aspects of the mechanics of thin plates and shells, such as buckling under external loads [12, 10] (see also Section 1.3 and Chapters 4 and 5) and the focusing of stresses into narrow regions when thin materials are crumpled [13]. It also has a remarkable effect on the *statistical* mechanics of thin plates and shells, which we briefly describe in the following section.

1.2.2 Statistical mechanics of solid membranes

The statistical physics of polymer chains determines many aspects of their behavior independently of the detailed chemistry of the constituent monomers [14]. Thin elastic sheets and solid membranes can be regarded as the two-dimensional equivalent of polymers, and studying their statistical mechanics has proven similarly fruitful [11, 15]. Just as

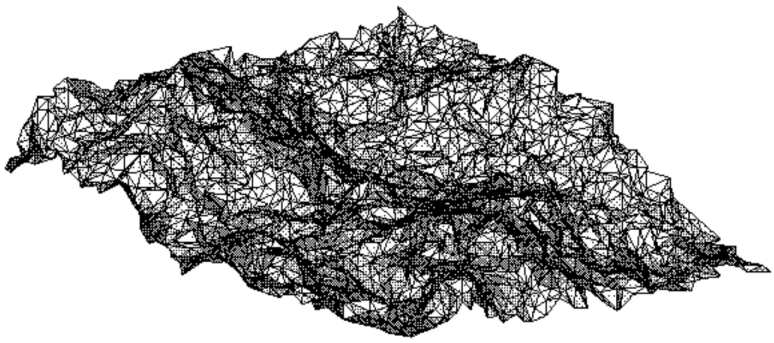

Figure 1.3: Numerical simulation of a tethered membrane with a bending rigidity and Young's modulus, flat in its ground state, exhibiting thermal fluctuations at finite temperature (from Bowick *et al*, arXiv:cond-mat/9603157).

floppy polymer chains exhibit wild thermal undulations that largely determine their long-wavelength mechanical behavior, membranes may experience thermal shape fluctuations that influence their mechanical response. The statistical mechanics of these shape fluctuations is even richer than in polymers, because the combination of bending and stretching deformations of these two-dimensional objects creates more complex shapes than can be realized with linear polymers.

Fig. 1.3 shows a numerical simulation of an initially flat elastic membrane at a finite temperature T. Entropy favors thermal shape fluctuations within the membrane with deformation energies of order $k_B T$. One might expect the elastic response of such a wildly fluctuating sheet to be very different from a zero temperature sheet, which would be perfectly smooth. The effect of the fluctuations was quantitatively established in studies of the statistical mechanics of flat solid membranes with the elastic energy of deformations described by Eq. (1.2) [16, 17], revealing the crucial role of the nonlinear contribution of normal displacements to the strain tensor ($u_{ij} \sim \partial_i w \partial_j w$) identified in Section 1.2.1. In the absence of this nonlinearity, the normal displacements contribute quadratically to the elastic energy *via* the bending energy term. The normal deformation field can be broken down into a linear superposition of independent oscillatory components at differ-

ent wavelengths l, each with energy density that scales as $\kappa(w/l^2)^2$, that do not interact with each other. However, including the nonlinear term introduces a quartic contribution $\sim Y(w/l)^4$ to the stretching energy that couples deformation modes at different length scales, with the strength of the coupling set by the Young's modulus Y. The coupling of long-wavelength normal deformations to the thermally generated shape fluctuations at smaller wavelengths drastically increases the energy of these deformations compared to a quiescent membrane [16]. Counter-intuitively, the thermal fluctuations at small scales have the effect of *stabilizing* the membrane against fluctuations at longer length scales by increasing the effective bending rigidity through the nonlinear interactions, giving rise to a stable flat phase with long-range alignment of the surface normals over the entire membrane at low yet finite temperatures. The nonlinear interactions completely dominate the elastic behavior of this flat phase, giving rise to strongly renormalized effective elastic moduli κ_R and Y_R that are no longer material constants but depend on the length scale l of the deformation in a nontrivial manner [17, 18]:

$$\kappa_R \sim l^{0.82}, \qquad Y_R \sim l^{-0.36}. \tag{1.7}$$

The effective bending rigidity associated with long wavelength deformations diverges with increasing wavelength, and the effective Young's modulus vanishes! These remarkable departures from the conventional behavior of zero-temperature solid membranes amount to a breakdown of classical elasticity theory due to thermal fluctuations for flat solid membranes.

The anomalous elastic properties described above for monolayer "tethered surfaces" [11] are also expected to apply to extremely thin *plates* that have some thickness in the third dimension, as long as the thickness is low enough so that the bending rigidity [Eq. (1.4)] is comparable to the thermal energy $k_B T$. However, the statistical mechanics

of fluctuating *shells* could be different because of the underlying curvature of the shell in its undeformed state. As discussed in Section 1.2.1, curvature couples normal displacements of the surface to in-plane strains, giving rise to a linear contribution ($u_{ij} \sim w/R$, where w is the normal displacement and R is the characteristic radius of curvature in the undeformed state) in addition to the quadratic contribution ($u_{ij} \sim \partial_i w \partial_j w$). As a result, the elastic energy of thin shells has stretching energy terms that are quadratic and cubic in w and its derivatives, in addition to the quartic term responsible for interactions between different deformation modes in flat membranes. The cubic term $\sim Y(w/R)(\partial_i w\, \partial_j w)$ is an important new interaction for curved shells; it is forbidden by symmetry for flat plates, and its strength depends on the underlying curvature in addition to the Young's modulus. A closed shell may also support a pressure difference between its interior and exterior. In Chapter 3 of this thesis, we study the mechanics of thermally fluctuating spherical shells, taking into account the effects of curvature and a uniform external pressure. We use the technique of perturbation theory in temperature to take into account the nonlinearities that give rise to nontrivial effects, and compare the results with numerical simulations of fluctuating shells. The work was performed in collaboration with Gerrit Vliegenthart and Gerhard Gompper (Institute for Advanced Simulation, Forschungszentrum Jülich, Germany).

1.2.3 Experimental realizations of fluctuating shells

Shell theory continues to be a valuable tool to understand macroscopic structural elements in civil, mechanical and aerospace engineering. However, advances in experimental techniques have enabled the fabrication and characterization of shell-like elastic structures at increasingly smaller scales, with thicknesses approaching tens of nanometers or even smaller. These range from artificially created spherical microcapsules made from poly-

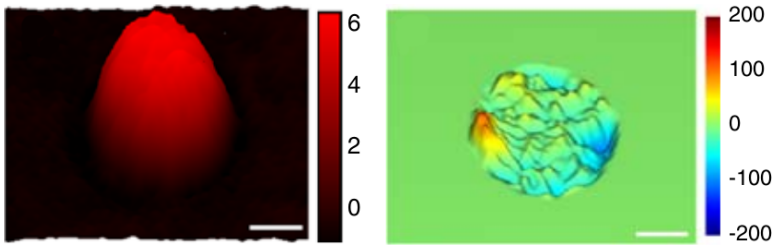

Figure 1.4: Instantaneous height field (left) and instantaneous displacements (right) for the top surface of a spherocyte red blood cell under physiological conditions, obtained using diffraction phase microscopy. Scale bar, 1.5 μm. The image on the left is colored by height of the surface above the substrate (color bar in microns). The image on the right is colored by displacement from the undeformed surface (color bar in nanometers). Figure reproduced from Y. Park *et al*, *Proc. Natl. Acad. Sci. USA* **107**, 6731 (2010).

meric [19] or protein-based [20] building blocks, to natural structures such as the mammalian red blood cell membrane [21]. At such small scales, the shell may be floppy enough for thermal shape fluctuations to arise, and the effects of these fluctuations on the mechanical response need to be considered.

Red blood cell (RBC) membranes are examples of curved shell-like elastic structures for which thermal shape fluctuations have been observed (the phenomenon is known as "flickering"). The RBC membrane is actually a composite membrane, with a fluid component (a lipid bilayer) that dominates the bending rigidity and a solid (tethered) component that provides a shear modulus. The energy of the composite membrane has a bending and a stretching component, and is therefore well approximated by a thin shell [21]. Under physiological conditions, the RBC has a characteristic biconcave flattened shape with a spatially varying curvature (discocyte phase), but abnormal RBCs under certain pathological conditions are nearly spherical (spherocyte phase). Fig. 1.4 shows the thermally induced shape fluctuations in a spherocyte RBC, measured using a technique known as diffraction phase microscopy. The deformations seen are reminiscent of the wild fluctuations responsible for the anomalous elasticity of flat membranes (Fig. 1.3). The study in

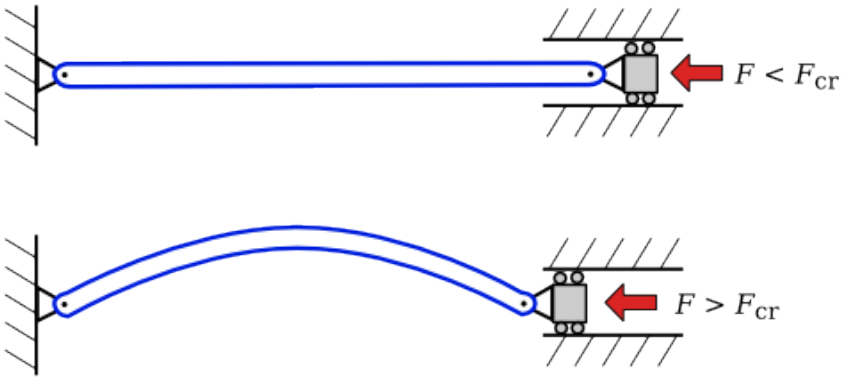

Figure 1.5: Buckling of an elastic rod under compressive forces. For forces below a threshold value F_{cr}, the rod remains straight (top). When a threshold value is crossed, however, the rod buckles into a curved shape (bottom). The buckling threshold F_{cr} can depend on the boundary conditions, which are hinged in this case.

Chapter 3 is relevant to understanding the mechanical properties of such a curved, fluctuating elastic structure.

1.3 Buckling of inhomogeneous shells

Buckling is a ubiquitous phenomenon in the mechanical response of thin rods, plates and shells. It refers to a sudden change in shape of a structure when external stresses cross a certain point, often associated with a loss of ability of the structure to support the external stress. The classic example of an elastic buckling instability is the buckling of a rod subjected to compressive stress along its long axis (Fig. 1.5): the rod initially compresses while remaining straight, but past a certain threshold force, it deforms into a curved shape and the distance between the two ends of the rod falls drastically with little additional force. Similar failure modes arise in rods, plates and shells under a variety of loading conditions [12].

Buckling of thin structures typically involves large displacements from the initial

shape, which have nonlinear strain-displacement relations and are governed by nonlinear partial differential equations. However, the onset of buckling can often be predicted by a eigenvalue analysis of the *linear* equilibrium equations in the limit of small displacements. As an example, we consider a linear buckling analysis of the rod under compressive force, with its ends hinged (originally attributed to the 18th century mathematician Leonhard Euler).

The linear equation governing the transverse deflection $y(x)$ (where x is the position coordinate along the long axis) of a rod under compressive force F, valid for small deflections, is [5]

$$EI\frac{d^2y}{dx^2} + Fy = 0, \tag{1.8}$$

where E is the 3D Young's modulus of the material making up the rod, and I is the second area moment of the rod cross-section (e.g. $I = \pi r_0^4/4$ for a cylindrical beam with circular cross section of radius r_0). Apart from the trivial solution $y(x) = 0$, the equation admits nontrivial solutions of the form $y(x) = A\sin(\sqrt{F/EI}x)$, which satisfy the boundary conditions $[y(0) = y(L) = 0; y''(0) = y''(L) = 0]$ provided

$$F = \frac{n^2\pi^2 EI}{L^2}, \tag{1.9}$$

where n is an integer. Eq. (1.9) is an eigenvalue condition that determines values of the load for which a nontrivial solution exists. The lowest nonzero eigenvalue $n = 1$ corresponds to the buckling load: $F_{\text{cr}} = \pi EI/L^2$ and the corresponding eigenmode for the deflection is $y(x) = A\sin\pi x/L$. Note that the analysis leaves the amplitude A unspecified; the mode is unstable to further growth when it appears, and the deflection quickly becomes larger than the range of validity of the linear analysis. Thus, the eigenmode prescribes the nature of the deflection immediately after loss of stability, but the final shape of the rod can only be understood by a nonlinear analysis, commonly called a *postbuckling* analysis

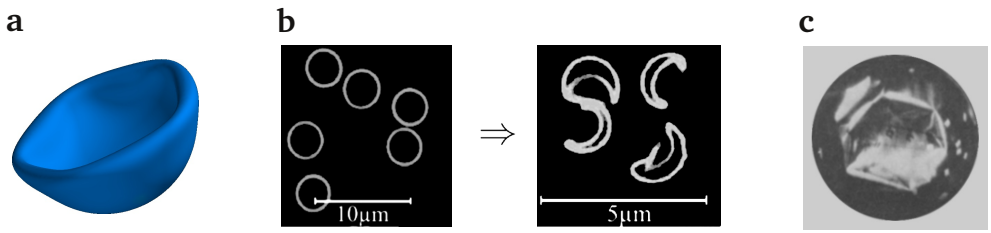

Figure 1.6: (a) Characteristic outcome of a buckling simulation on an initially spherical shell with $h/R \approx 0.05$. The shape changes abruptly from spherical to indented at the buckling pressure. Details of the simulation are provided in Appendix E. (b) Optical fluorescence micrographs of spherical polyelectrolyte capsules (radius 2 μm, thickness 4 nm), before (left) and after (right) buckling under external osmotic pressure [from Fery et al, *New J. Phys.* **6**, 18 (2004)]. (c) Metallic spherical shell with radius $R = 4.25$ in and thickness $h = 0.002$ in, buckled under constant pressure [from Berke and Carlson, *Experimental Mechanics* **8**, 548 (1968)].

of the instability.

1.3.1 Buckling of uniform spherical shells

Thin spherical shells, with an elastic energy dictated by Eq. (1.2), exhibit a buckling instability when subjected to a uniform external pressure. When an increasing hydrostatic pressure is applied, a spherical shell initially responds by contracting uniformly, but past a critical buckling pressure, its shape abruptly changes and it acquires one or more large indentations that significantly reduce the enclosed volume. Significant hysteresis is associated with this transition. In this sense, the buckling of shells in three dimensions resembles a first order phase transition, and the critical buckling pressure represents a limit of metastability. The situation is quite different for pressurized *rings* in two dimensions (or pressurized cylinders), where the behavior at buckling resembles a continuous phase transition (see, e.g. Ref. [22]). This buckling is an important failure mechanism for spherical shells and domes, and has been quantitatively studied in thin-walled spheres at scales ranging from microscopic polymer capsules [23] to metallic shells a few inches in diam-

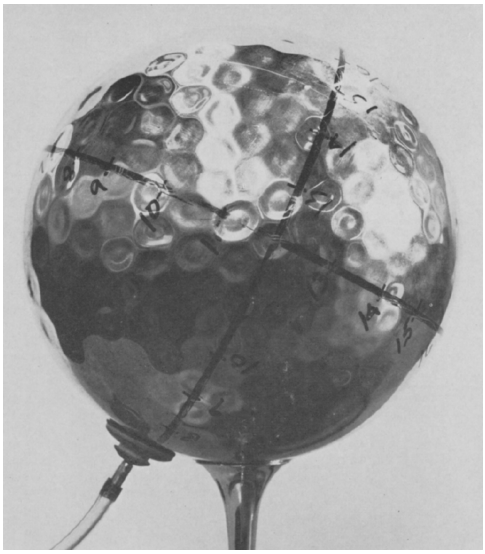

Figure 1.7: Shape of a metallic spherical shell with radius $R = 4.25$ in and thickness $h = 2.2 \times 10^{-3}$ in, induced to buckle under net external pressure but stabilized by an enclosed wax ball of slightly smaller radius. The two-dimensional periodic nature of the buckling mode is visible. Image reproduced from Carlson, Sendelbeck and Hoff, *Experimental Mechanics* **7**, 281 (1967).

eter [24, 25]. Fig. 1.6 displays the large deformations of elastic spherical shells that have buckled under pressure in numerical simulations and in experimental systems.

The buckling of uniform spherical shells under pressure is a classic problem in shell theory, with the first analytical solution for the critical buckling pressure attributed to R. Zoelly in 1915 [26]. As with the buckling of a rod, the buckling pressure p_{cr} can be derived using a linear eigenvalue analysis of the equilibrium equations derived from the elastic energy (performed in Chapter 4). The uniform contraction of the sphere is the only equilibrium solution to the governing equations of the shell at low pressures, but a nontrivial mode appears when the pressure reaches the critical value (see Chapter 4 for a derivation) given by

$$p_{\text{cr}} = \frac{2E}{\sqrt{3(1-\nu^2)}} \left(\frac{h}{R}\right)^2, \tag{1.10}$$

where E is the elastic modulus, ν the Poisson ratio, h the shell thickness and R its radius.

The corresponding deformation eigenmode has a two-dimensional periodic structure with the characteristic wavelength in both directions set by the elastic length scale introduced in the previous section [Eq. (1.5)],

$$\lambda \approx 2\pi\ell = 2\pi \frac{\sqrt{hR}}{[12(1-\nu^2)]^{1/4}} \ll R. \tag{1.11}$$

In fact, there is an infinite set of degenerate modes (associated with the rotational symmetry of the sphere) that has the required periodic structure at the critical pressure, each of which is unstable. Ultimately, the particular eigenmode that drives the buckling is selected by random imperfections or nonuniformities in the shell or the pressure field. This buckling mode is unstable, and is not ordinarily observed in experiments. However, its periodic structure can be revealed in experiments that arrest its growth. This was done in buckling experiments on metallic shells, where the buckling mode was arrested by incorporating a concentric solid ball within the shell with a slightly smaller radius [24]. The experiment (reproduced in Fig. 1.7) revealed the buckling mode to be a pattern of hexagonal dimples, whose wavelength was consistent with the elastic length scale .

The linearized stability analysis does not account for the postbuckling shape of the shell, which consists typically of a large volume-reducing indentation (see Fig. 1.6). This shape is governed by highly nonlinear equations for the deflections, and a full description of the postbuckling behavior of spherical shells typically calls for numerical methods [27, 28, 29, 30]. However, an approximate description of the postbuckling shape, due to A. V. Pogorelov [31], successfully captures the energetics and shape of the localized inversions for very thin spherical shells. It is energetically favorable for extremely thin shells to bend rather than stretch, but a closed spherical shell cannot be bent without also being stretched [27]. Therefore, large deformations in the shell would tend to localize stretching into small regions. One way to deform a spherical shell in this manner is to

invert some section of the shell by reflecting it in a plane that intersects the shell. Except for the rim of the inversion, the shape transformation is isometric with the original shape of the shell, avoiding a stretching energy penalty. At the rim, however, some stretching (together with bending) is unavoidable to avoid a singular profile with infinite bending energy density; the rim of the inversion thus has a finite width over which the singularity is smoothed out, and the deformation is not isometric. A scaling analysis of the elastic energy of the deformations confined to the narrow region (reproduced in Appendix A) reveals that the elastic energy of the inversion scales as $E_{\mathrm{el}} \sim Eh^{5/2}R^{1/2}(d/R)^{3/2}$, where d is the depth of the inversion [5]. If the shell is under external pressure p, the net energy including the work done by the pressure is $E = E_{\mathrm{el}} + p\Delta V$, where $\Delta V \sim -Rd^2$ is the volume change due to the inversion. The total energy as a function of inversion depth then has a maximum at $h_{\mathrm{max}} \sim E^2h^5/R^4p^2$. Inversions of depth $h < h_{\mathrm{max}}$ are thus expected to shrink and ultimately disappear, while inversions of depth $h > h_{\mathrm{max}}$ grow in an uncontrolled manner. At the buckling pressure $p$cr arising from the linear stability analysis, h_{max} is of the order of the shell thickness h, which means that a very small dimple is susceptible to growing uncontrollably. Therefore, as soon as the unstable mode appears, one of the dimples caused by the unstable periodically varying mode grows to form a large inversion which abruptly reduces the internal volume of the shell by a large amount. This scenario explains the postbuckling shape associated with spherical shells. The resulting inversion is stabilized by self-contact of the shell with itself, by a restriction on the internal volume of the shell due to, say, an enclosed fluid that must be expelled for the inversion to grow, or by plastic pinning of the highly deformed rim at large inversion depths. Depending on the dynamics of the process and on random imperfections in the shell, it is also possible for two or more inversions to grow until self-contact, but these shapes have a higher elastic energy compared to the shape with just one inversion and are thus metastable [28].

For extremely thin shells, inversions past a certain depth deviate from the nearly isometric form considered in the scaling analysis, instead forming rims that have a polygonal structure [as seen for metallic shells in Fig. 1.6(c)]. The transition from a circular to a polygonal inversion has aspects of a continuous transition as a function of inversion depth [30], and the associated elastic energy as a function of inversion depth does not deviate significantly from the scaling form derived above [32]. As a result, the arguments of stability of the postbuckling shape in spherical shells are largely unaffected by the transition to a polygonal rim.

Finally, shells can also be made to buckle by controlling the *volume* of the shell, rather than the external pressure. Rather than ramping up the external pressure, we can consider a shell filled with an incompressible fluid which is slowly removed to reduce the internal volume of the shell. The initial response of the shell is again to contract uniformly, until a critical volume reduction $\Delta V_{\rm cr}$ whose value is determined by a linear stability analysis (see Chapter 5):

$$\frac{\Delta V_{\rm cr}}{V_0} = \sqrt{\frac{3(1-\nu)}{1+\nu}}\frac{h}{R}, \tag{1.12}$$

where $V_0 = 4\pi R^3/3$ is the initial volume of the spherical shell. At the critical volume change, the shape of the shell changes abruptly from being spherical to having a localized indentation which is of the nearly isometric type, similar to the case of buckling under pressure. However, the indentation does not grow uncontrollably in this case, but is stabilized by the volume constraint. The inversion that appears when the shell buckles is precisely the size needed to accommodate the critical volume change. Further reductions in the internal volume are accommodated by increasing the indentation depth accordingly.

1.3.2 Controlling buckling using inhomogeneities

Shell buckling, though often considered a mode of structural failure that is to be avoided, can also be used to drive shape transitions that fulfill a particular purpose. Buckling and re-inflating spherical shells through global driving forces (such as a uniform change in pressure) allows dynamic control of the shape and occupied volume for many objects at once. Such control is particularly useful for changing the shape of shells at microscopic scales, where direct manipulation of the shape through localized forces may be challenging, but changing an external osmotic pressure or reducing the internal volume can be readily achieved through chemical methods and can be done for many shells at once. Recent experimental efforts in materials science have exploited the buckling of microscale spherical shells for the controlled release of encapsulated substances [33, 34, 35], the mass-production of anisotropic colloidal particles with a characteristic bowl-like shape similar to Fig. 1.6(a) [36], and the formation of so-called "lock" colloids, each with a well-defined indentation that can accommodate a single smaller "key" colloid for directed self-assembly into chain-like structures [37].

Even more applications for buckling-induced shape transitions could be opened up by the capability to control the conditions that trigger the buckling transition and the final shapes that arise as a result. However, the buckling behavior of uniform spherical shells is controlled primarily by one geometric parameter—the radius-to-thickness ratio of the shell—limiting the range of achievable buckling properties. For a particular material, the radius-to-thickness ratio determines the buckling pressure as well as the sharpness and polygonal nature of the inversion rim, making it difficult to control the shell strength and the postbuckling shapes independently. Furthermore, the control over the final buckled shape is limited: practically all shells buckle with the same characteristic single inversion, whose depth is set either by self-avoidance or by plastic deformations in the sharp rim that

cannot be precisely controlled. The transition is also hysteretic, *i.e.* the pressure must be reduced far below the buckling threshold to reinflate a buckled sphere, making it difficult to reverse the shape change reliably. The potential of buckling-induced shape transitions as a dynamic sculpting technique for soft structures could be augmented if the buckling and postbuckling behavior could be modified in a controlled manner, and the hysteresis could be reduced to make the shell more responsive to cyclical changes in the external pressure.

One way to modify the buckling behavior of a shell is by spatially varying the parameters determining the stiffness of the shell (the elastic modulus E, the Poisson ratio ν and/or the thickness h). For instance, if the shell is softer in some parts than in others, the softer regions will deform at lower pressures compared to a uniform shell of the same average thickness, and could induce the shell to buckle earlier as a result. However, some inhomogeneities can *qualitatively* alter the buckling and the postbuckling behavior, in addition to changing the buckling pressure. Pollen grains of certain plant species provide a striking example of such an effect [38]. These pollen grains are microscopic ellipsoidal (nearly spherical) structures with a thin outer layer that behaves like an elastic shell, enclosing a wet inner medium. The inner medium significantly reduces its volume by drying out when the pollen grain leaves the flower. If the outer shell were completely uniform, volume reduction past a certain value would induce an abrupt transition to a buckled shape with a localized indentation (the eccentricity of the ellipsoidal shape is not sufficient to significantly change the buckling behavior relative to a perfect sphere). However, some plant species have evolved large soft regions in the outer shell that modify their mechanical response in such a way that abrupt buckling events during the volume reduction are eliminated completely. Instead, the soft regions induce the pollen grains to smoothly and continuously change their shape as they dry out, and can even guide the deformation

to seal off the soft regions (which also are the regions through which the inner moisture escapes during volume reduction) so that water loss past a certain point can be prevented.

Such exquisite control over the material properties of the shell can also be achieved in artificial shells through recent advances in experimental techniques, opening up new possibilities for controlling the buckling and postbuckling behavior of elastic shells. In Chapters 4 and 5, we study how the buckling and postbuckling behavior of spherical shells is modified by specific inhomogeneities in the shell material, motivated by experimental systems in which such inhomogeneities can be realized for spherical shells. Previous theoretical and numerical studies on the buckling behavior of inhomogeneous shells focused on the effect of imperfections in the shell, which tend to significantly reduce the buckling pressure compared to the perfect spherical shell [39, 12, 40]. The forms of imperfections considered were either highly localized variations in shape and thickness [41, 42] or variations that extend over the entire sphere in a random or periodic manner [42, 43]. These were typically chosen to represent damage or imperfections in the shell that arise during its fabrication. The spatial structures of the inhomogeneities studied in Chapters 4 and 5 of this thesis differ from these earlier studies, as does the emphasis—rather than understanding accidental imperfections, we aim to study how specifically designed inhomogeneities can modify the buckling, postbuckling and hysteresis properties in potentially desirable ways.

1.3.3 Experimental motivation

In Chapter 4, we study the effect of a single "soft spot"—a region, with a circular boundary, that is uniformly thinner than the rest of the shell—on the buckling behavior of an otherwise homogeneous shell. We vary the size of the soft region as well as the ratio of thicknesses in the soft region and the remainder of the shell. This may be considered to be an

isotropic generalization of the soft sectors observed in pollen grains, whose boundaries often approximate lines of longitude [38]. Microscopic spherical shells with similar soft spots could be fabricated by confining two immiscible polymer components to the same droplet interface; the minority component could be induced to phase-separate into a domain with a circular boundary that has different material properties when solidified. (Such domains are commonly observed in two-component lipid vesicles [44, 45].) At macroscopic scales of a few centimeters to a few meters, rapid prototyping (popularly known as "3D printing") can be used to fabricate thin shells with precise inhomogeneities of practically any form, including the shells with soft spots that are the focus of our study. Rapid prototyping techniques have been used to create thin shells with precise variations in curvature [46] and thickness [47], that have a strong effect on their response to external forces and pressures. Through such techniques, practically any form of inhomogeneity can be realized in shell structures, opening up many avenues for further studies on the effects of nonuniformities on shell buckling.

The work presented in Chapter 5, performed in collaboration with the research group of Prof. David Weitz, was motivated by buckling experiments conducted on droplet-templated elastic microcapsules. The capsules were fabricated using water-oil-water double emulsion droplets prepared by microfluidics. A capillary injection system prepared drops consisting of an oil phase separating an inner water droplet from the bulk phase, also water. Due to surface tension, the two oil-water interfaces (one completely enclosed by the other) are nearly perfect spheres. The quantity of oil injected into the middle phase determines its average thickness. However, the inner water droplet is also lighter than the oil phase, and rises due to its own buoyancy. Therefore, the oil phase gradually thins out in the top of the droplet and thickens in the bottom, eventually acquiring a smoothly varying thickness that is symmetric around the axis through the top and bottom poles. The oil

phase polymerizes upon exposure to ultraviolet (UV) light, forming a thin spherical shell that freezes in the thickness variation in the oil phase at the instant of polymerization. By varying the time between droplet preparation and UV polymerization, the extent of inhomogeneity (quantified by the difference between the thickness at the top and bottom poles) can be controlled. To understand the buckling experiments on these shells with smoothly varying thicknesses, we use theoretical and numerical approaches to study the effect of the inhomogeneity on the buckling and postbuckling behavior of the capsules as a function of the average thickness and the degree of inhomogeneity.

Chapter 2

A two-parameter sequential adsorption model applied to microfiber clustering

The study of the self-assembly and self-organization of solid macro-, micro- and nanoscale structures using capillary forces mediated by a wetting liquid has made an impact in fields ranging from photonics [48] to the theory of computation [49]. In recent years, the phenomenon of elastocapillary coalescence [50] has been observed in aggregation of fibers ranging in size from the macroscopic scale [2, 51] down to micro- and nanoscales [52, 6, 53, 54, 55, 56, 7, 57]. In all these investigations, capillary forces in a wetting liquid bring together the free ends of high-aspect-ratio structures attached to a substrate to form clusters. For highly symmetrical arrangement of fibers in the individual clusters, a long-range ordering in the positions of the clusters has been reported [55, 56, 7, 57]. In particular, when the fibers are initially arranged in a square lattice and primarily form 2x2 clusters of four individual fibers connected at the tip, these 2x2 clusters themselves are ordered locally in a square superlattice with a lattice spacing twice that of the individual fibers [figure 2.1(a)]. This ordering mechanism has potential application not only as a means of creating complex three-dimensional structures with spatial regularity but also as a basis for generating

dynamic "smart" surfaces capable of ordered particle trapping and release, color changes and adaptive wetting behavior [7, 58].

A number of previous theoretical treatments of capillary-assisted clustering [51, 52, 53, 55, 54, 59] have analyzed the elastic, capillary and surface tension energies associated with fiber clustering to determine the critical stiffness of the fibers that allows clustering to occur, and the typical size/size distribution of clusters. However, less has been said about the higher-level arrangement, size and ordering of the clustered domains. A qualitative picture of long-range ordering of clusters due to the distance dependence of the capillary interactions between submerged fibers is presented in Ref. [7], and a similar description based on the stability of upright fibers is reported in Ref. [57], but to our knowledge no quantitative comparison of these descriptions with experimentally observed patterns has been made. The current work develops this aspect of capillary-mediated clustering of fibers. We propose, characterize and test a nonequilibrium dynamical model for the irreversible formation of clusters showing long-range order in a square array of fibers.

Our approach falls into a broad class of systems known as *sequential adsorption models* [8]. Sequential adsorption (SA) models describe deposition of particles on a surface through the following algorithm: a trial deposition of a particle is made on the surface (typically empty initially, though a 'seeded' surface with predeposited particles may also be studied); if the particle does not overlap with any other, the deposition is successful and the particle is permanently fixed in the chosen spot; if on the other hand the particle overlaps with an already attached particle then the trial is rejected. *Random* sequential adsorption (RSA) models refer to those in which the position of the trial deposition is chosen purely at random, while *cooperative* sequential adsorption (CSA) processes are those in which the probability of a trial deposition at any point on the surface is influenced (typically enhanced) by the presence of deposited particles nearby. Both RSA and CSA,

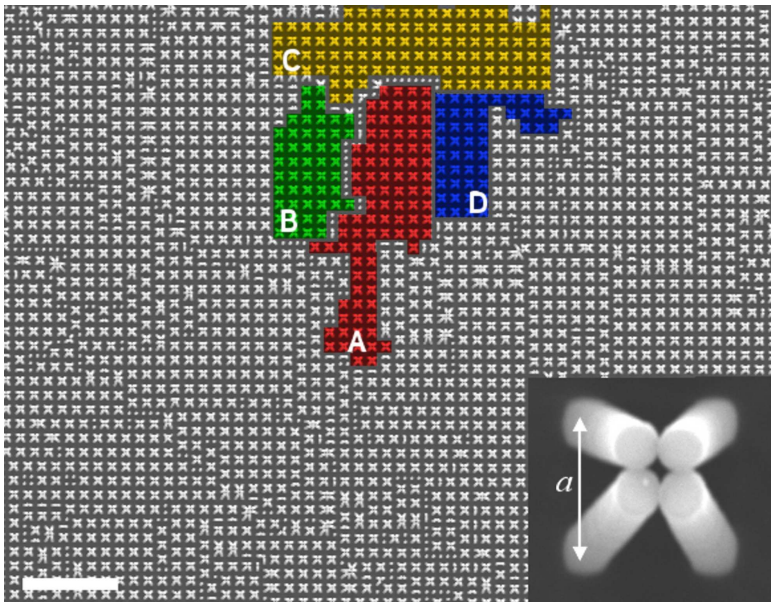

(a)

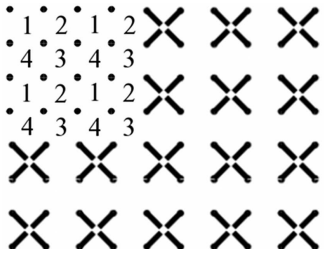

(b)

Figure 2.1: (a) Top-down scanning electron microscope (SEM) image of a region of an epoxy microfiber sample in which clusters have been induced *via* ethanol evaporation and persist due to van der Waals interactions between the touching fiber tips. Scale bar 50μm. The region predominantly shows tetramers, *i.e.* clusters of four fibers whose tips meet at a height of a few microns above the substrate, centered above the squares of the underlying lattice of fibers. The inset (bottom right) is a close-up view of a tetramer, showing the lattice spacing a of the fibers. Four distinct domains (as defined in the text) are highlighted and labeled A—D. (b) Schematic of the lattice of fibers with some formed tetramers all belonging to a single domain. (In this and following diagrams, each dot represents the base of an upright fiber while each 'x' represents the top-down view of a tetramer comprising of four fibers whose bases remain on the square lattice but tips come together at the center.) The numbers show the division of the *dual* lattice into four sublattices 1–4 corresponding to the four distinct domains shown in (a); the remainder of the lattice is occupied by a domain whose members occupy sublattice 1. In the SEM image, we may assign the tetramers of domain A to sublattice 1; domains B, C and D then belong to sublattices 2, 3 and 4 respectively.

on continuum surfaces as well as lattices, have been used to study a variety of physical, chemical and biological processes (for a comprehensive review see Ref. [8]). The questions of interest in studying such models range from predicting the final coverage of the surface when the system has evolved until no further deposition takes place (*i.e.* there is no further room for particle deposition and the system reaches a 'jammed' or 'saturated' state) to understanding the time evolution up to jamming as well as the spatial distributions and correlations of the particles at any stage.

Since the deposition events are irreversible, sequential adsorption models are typically not amenable to study *via* tools of equilibrium statistical mechanics [8]. Theoretical modeling begins with the formulation of rate equations describing the filling of empty areas of the surface with particles. The result is a hierarchical set of rate equations linking each empty configuration to the set of empty configurations that could result from the adsorption of a particle anywhere within it. These equations describe a nonequilibrium generalization of the famous dimer problem of statistical physics [60], with dimers being replaced by hard spheres in our case. One-dimensional RSA models as well as CSA models with short-range cooperative effects are exactly solvable. However, in dimensions two and higher, the hierarchy of rate equations becomes very large and is not exactly solvable even for the simplest short-range cooperative effects (such as nearest-neighbor exclusion on a lattice). A variety of approximation methods such as series expansions for small coverages (*i.e.* early times) and systematic truncation of the hierarchical rate equations has been adopted to study higher dimensional RSA/CSA models. The algorithmic nature of the SA process also makes it a good candidate for direct numerical simulation on finite-sized lattices or surfaces, which is the approach taken in this work.

With experimental patterns like the one depicted in figure 2.1(a) in mind, we develop here a model of irreversible CSA of particles on an initially empty square lattice,

under the conditions that adsorption of a particle at any site prevents further adsorption not only at the filled site but at nearest neighbor (NN) and next-nearest neighbor (2NN) positions, but increases the rate of adsorption at the third (3NN) and fourth (4NN) nearest neighbor positions. (As explained in detail in section 2.1.1, these lattice positions correspond to the positions of *plaquettes* of the microfiber array for the particular case of fiber clustering; representative NN through 4NN positions relative to a 2x2 cluster are indicated in figure 2.2(b).) Local cooperativity in the adsorption process is typically introduced by defining adsorption rates that depend on the local environment of each site [8]. For our model, we assign a rate $k(i,j) = k_0\alpha^i\beta^j$ to each site that depends on the numbers i and j of particles previously adsorbed at 3NN and 4NN positions respectively relative to the site. Enhancement of adsorption near previously adsorbed particles corresponds to $k(i,j) > k(0,0)$ for allowed values of (i,j) other than $(0,0)$. Here $k(0,0) \equiv k_0$ is the rate of adsorption of particles for a site that has no filled 3NN or 4NN sites. We shall take α and β greater than 1, so that they describe in a simple way enhanced "adsorption" (tetramer clustering in our case) at 3NN and 4NN positions respectively. While the lone particle adsorption rate k_0 determines the overall speed at which the surface is covered with particles, the nature of the adsorbed pattern at any fractional coverage and particularly at saturation depends only on α and β which are the two adjustable parameters in the model.

Our model is similar to previously studied CSA models on a square lattice with close-neighbor cooperative effects [8, 61, 62, 63, 64]. Previous studies, however, have focused on a single level of cooperativity with rates $k_i = \alpha^i k_0, \alpha > 1$ defined at each site when i is the number of occupied closest neighbor sites. (This rate choice is called a *multiplicative* or *Arrhenius* rate, in contrast to the *Eden* rate choice, $k_i = \alpha k_0, \alpha > 1$ for $i \geq 1$.) Some of these analyses are also useful in explaining the properties of our model. For example, in the regime of strong cooperativity when adsorption near occupied sites is strongly favored,

adsorbed particles tend to form growing domains or islands [62, 63] around a randomly deposited nucleation site. Here we define a domain as a group of tetramers whose centers may be connected to each other by a network of bonds each of length $2a$, where a is the lattice spacing of the square array of fibers. As shown in figure 2.1, the domains lie on one of four sublattices and domains belonging to different sublattices meet in boundaries that largely follow the principal axes of the lattice of fibers. Then k_0 may be considered the rate of nucleation of domains while the other rates describe the growth of domains. As adsorption continues, growing domains on the same sublattice coalesce upon meeting one another, while domains belonging to different sublattices meet at a frozen domain boundary. As long as all $k(i,j) > 0$, the system ultimately reaches a 'saturated' or 'jammed' state at which point no further adsorption can take place and the state of the entire lattice may be described by domain boundaries separating domains of various shapes and sizes. This saturated state is the one that is compared to the experimental domain patterns. In the fiber clustering experiments discussed above, rare anomalous clusters of 2, 3, 5, 6,... fibers constitute additional point-like defects which we disregard here.

In Section 2.1, we summarize the experiments leading to the self-organization of microfibers and motivate the CSA model with NN/2NN exclusion and 3NN/4NN cooperative effects to describe ordering and domain formation in this system. In Section 2.2, we characterize the patterns of tetramers generated by the model for a range of parameter values using computer simulations. We emphasize the effects of the newly considered 4NN cooperativity ($\beta > 1$) to contrast the current model with previously studied single-parameter models, and highlight the similarity of the tetramer-tetramer correlation functions for different values of α and β upon appropriate rescaling. In Section 2.3, we evaluate the ability of the model to reproduce patterns from an actual experiment, using a single measured quantity to fit the two parameters α and β, and compare the model's

performance to that of a similar single-parameter model. We show that a single-parameter model deviates significantly from the experimental observations, while our new double-parameter model provides an excellent description of the experimentally observed patterns. In Section 2.4, we conclude by using the insights provided by the model to improve ordering in the clustering experiment, and consider the potential relevance of the new model to various sequential adsorption processes and self-assembly. Details of the numerical simulation and the experimental procedure are reported in Appendix B.

2.1 Microfiber clustering and order formation

The formation of large ordered regions during self-organization of nanostructures *via* capillary forces has been reported by the Aizenberg group in Ref. [7]. In this section we summarize the experiment and observations that motivate our theory. Highly uniform square arrays of high-aspect-ratio nano- and microscale polymeric fibers, prepared using soft lithography as described in Ref. [65], were wet with a solvent which was allowed to evaporate under ambient conditions. As the solvent-air interface is forced below the tips of the upright fibers due to evaporation, the tips are drawn together by capillary interactions and adhere to each other upon contact *via* short-range van der Waals forces, forming clusters that persist after all the liquid has evaporated and may be observed by optical and scanning electron microscopy. Under certain conditions of fiber geometry and stiffness, the clusters formed could be primarily tetramers composed of four fibers meeting at the tips. The tetramers were arranged in highly regular arrays, with large domains (spanning several lattice lengths) composed of groups of tetramers ordered in a square superlattice of lattice constant twice the distance between fibers. A representative SEM image of such a system after clustering is shown in figure 2.1(a).

2.1.1 Ordering mechanism and formulation of the CSA model

A qualitative one-dimensional mechanism for the formation of ordered domains has been proposed [7] that propagates a breaking of the lattice symmetry into one sublattice due to the nature of the attractive capillary forces between fiber tips. For small displacements of the meniscus from the horizontal plane, the capillary forces are proportional to $\gamma r^2/d$, where γ is the surface tension of the ethanol-air interface, r the radius of the fibers and d the distance between fiber tips at the meniscus [66]. The cooperativity in cluster formation arises as a result of the inverse relationship between interfiber distance d and capillary force between fiber tips. Figure 2.2(a) illustrates this mechanism. If a dimer nucleates due to an imperfection or instability (such as a nonuniformity in the rate of evaporation of the ethanol, or slight variations in the spacing of the fiber tips when they encounter the ethanol-air interface), that event induces a fiber to buckle or bend, and the fiber to the right of the dimer then experiences a net force towards its own neighbor on its right which is closer to it than the fiber participating in the dimer on its left. Thus, the initial dimerization induces the fiber to form a new dimer with the fiber on its right. This cascade then continues, propagating a chain of dimers with periodicity $2a$. To extend this picture to two dimensions, note that the formation of a tetramer has the biggest effect on four pairs of neighboring fibers in the four cardinal directions. For instance, consider the highlighted pair of fibers in figure 2.2(b). Due to the force imbalance induced by the initial tetramer, the pair moves toward the fibers to its north, increasing the probability of forming a tetramer in position 'A' which is a third-nearest-neighbor, or 3NN, position relative to the formed tetramer. However, each destabilized fiber also has an enhanced probability of forming a tetramers at the two positions marked 'B', the 4NN positions relative to the formed tetramer. Hence the effect of the formed tetramer on the fibers closest to it is fully captured if we include both 3NN and 4NN enhancement in tetramer formation. We would

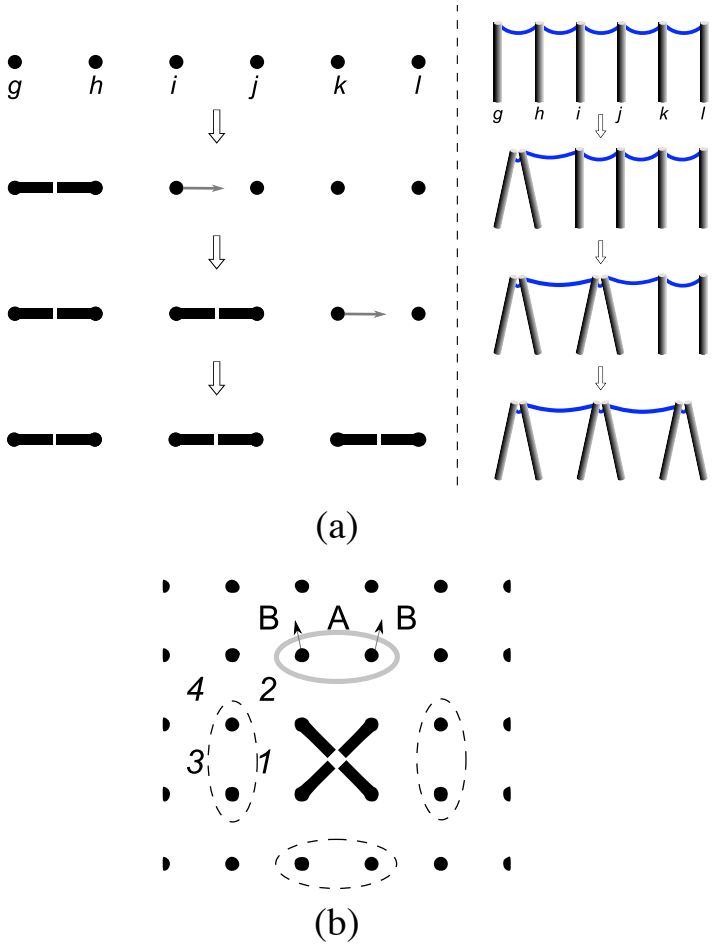

Figure 2.2: Capillary-mediated cooperative clustering. (a) illustrates the mechanism in a one-dimensional row of fibers whose tips are drawn together to form dimers (top view, left; side view, right). The large dots in the top view indicate the bases of upright fibers. When the liquid-air interface first reaches the upright fiber tips, all interfiber forces are equal. Now suppose the random formation of a cluster brings fibers g and h together. The tips of i and h are now further apart than the tips of i and j; hence i experiences an imbalance of forces (grey arrow) that induces it to cluster with its neighbor j. Now fiber k experiences a force imbalance, and the effect of the initial clustering of g and h thus cascades down the lattice. (b) extends the picture to tetramer formation in two dimensions (top view). Representative first through fourth neighbor squares or "plaquettes" relative to the nucleating tetramer are indicated by numbers 1–4. Due to the formation of a tetramer, the four highlighted pairs of fibers experience a force imbalance. As shown for the top pair, there is a resultant force on each fiber due to capillary attraction with the nearby fibers and tetramer (whose fibers perturb the ethanol-air interface further away compared to the unclustered fibers). This increases the probability of tetramer formation at the 'A' position (third-nearest neighbor), and to a smaller extent at the 'B' positions (fourth-nearest neighbors).

expect the effect to be weaker for 4NN tetramers, but to increase when the number of 3NN or 4NN neighbors is increased as more fibers are perturbed by force imbalances. (Note that tetramers cannot form at NN or 2NN positions due to a lack of a complete set of four upright fibers. Also, the absence in the experimental patterns of adjacent pairs of dimers suggests that any dimer formed near an initial tetramer immediately forms a more stable tetramer configuration with the next pair of fibers if it is available, giving rise to a 3NN or 4NN cluster. Hence we do not include the possibility of dimer formation induced by a tetramer in neighboring fibers.)

Thus the formation of ordered domains occurs in the following way: random instabilities nucleate lone tetramers in the lattice of initially upright fibers at some background rate. Once a tetramer is formed, the nature of capillary interactions enhances the rate at which tetramers are formed at 3NN and 4NN positions near it. The 3NN enhancement tends to be stronger, giving rise to the formation of ordered domains of tetramers that grow from different nucleating sites. Nucleation of a 4NN tetramer at the edge of a growing domain disrupts its growth, instead starting a domain belonging to a different sublattice. Once tetramers are formed, they do not unbind.

Note that formation of tetramers on the square lattice of fibers is equivalent to the deposition of *single particles* on sites of the *dual* square lattice (which is the lattice formed from the centers of the plaquettes formed by the fiber lattice, or equivalently the fiber lattice displaced by $a/2$ in both the x and y directions). Hence the irreversible process of tetramer formation as described above is equivalent to a *cooperative sequential adsorption* process of particles that occupy sites on a square lattice with NN/2NN exclusion and 3NN/4NN enhancement of deposition. The initial state of upright fibers (no tetramers) is equivalent to an empty initial lattice for particle deposition. The rate of deposition at each site at any instant in time is determined by the previously deposited particles (if any) at 3NN

and 4NN positions, or is equal to the rate of random or bare nucleation if there are no such deposited neighbors. The final state after all the ethanol has evaporated, when all fibers are clustered except those that do not have enough neighbors to form tetramers, corresponds to a state of jamming or saturation for adsorption on the dual lattice.

2.1.2 Choice of CSA model rates

To complete our model, we must specify the local-environment-dependent rate of adsorption of tetramers at empty sites. The transformation of a group of four upright fibers to a tetramer happens in less than a hundredth of a second [67], practically instantaneous over the time scale of the clustering of the entire sample (roughly a minute). We assume that the formation of a tetramer at a particular site on the (dual) lattice is a stochastic process with a waiting time that is exponentially distributed with a mean time τ, which depends on the geometry of the fibers, the surface and bulk properties of the fiber material, the surface tension of the evaporating liquid and the level of the ethanol-air interface, as well as the configuration of fibers and/or tetramers at nearby positions. The rate of formation (adsorption) at the particular site is then $1/\tau$. We do not attempt to calculate these rates microscopically for different local environments but treat them as parameters that we extract from a particular experimental realization by fitting to simulation results.

Even if we restrict ourselves to 3NN/4NN effects of previously formed tetramers, there are several different rates of adsorption to an empty site based on different possible configurations of previously adsorbed tetramers around it. For instance, there are five different configurations involving one, two, three or four tetramers adsorbed at 3NN sites that are not superimposable *via* rotations, and several more independent configurations when considering all possible combinations of adsorbed 3NN/4NN tetramers allowed under the exclusion rule. To reduce the number of independent parameters in the model,

we make the simplifying assumption that the adsorption rate $k(i,j)$ at any site is a function only of the *number* of tetramers adsorbed at 3NN and 4NN positions (i and j respectively) and not their spatial arrangement around the site.

The functional dependence of the rate on i and j (which, of course, take only non-negative integer values) is motivated by the observation of long unbroken domain walls along both lattice directions, which suggests that individual domains growing from different nucleation sites are largely rectangular in shape when they encounter one another. Let us focus initially on the stronger 3NN cooperativity, ignoring any dependence of the rates on j so that $k(i,j) \equiv k_i$. Then k_0, k_1 and k_2 represent respectively the rates of nucleation of a new domain, beginning of a new row at the edge of a growing domain, and growth of an incomplete row at the edge of a domain by formation of a tetramer at either end of the row. The ratio k_1/k_0 determines the average size to which domains grow before they encounter other domains and stop, while k_2/k_1 determines the size until which a growing domain remains rectangular.[1] Evans and Nord [64] have shown that multiplicative rates that satisfy $k_0 : k_1 : k_2 = 1 : \alpha : \alpha^2$ with $\alpha > 1$ give rise to domains that maintain their rectangular shape until saturation is reached in the adsorption process. In contrast, a weaker arithmetic increase in cooperativity with i such as $k_0 : k_1 : k_2 = 1 : \alpha : 2\alpha$ would lead to patterns with irregular domain walls as domains do not maintain their rectangular shape. Motivated by these observations and the experiments themselves, we choose multiplicative rates that independently grow with i and j: $k(i,j) = k_0\alpha^i\beta^j$, where α and β are the cooperativity parameters associated with 3NN and 4NN tetramers respectively. This simplified form has several advantages: it reduces the number of parameters to two while retaining

[1] The time taken to complete an edge on a rectangular domain with edge length m is $t_c \sim m/k_2$; in that time, the rectangular shape would be spoiled if a new edge is begun before the whole string of m tetramers is added to complete the growing edge. This happens $\sim mk_1t_c \approx m^2k_1/k_2$ times; hence the rectangular shape of the domain can be maintained only for $m^2k_1/k_2 \lesssim 1$ *i.e.* $m \lesssim \sqrt{k_2/k_1}$. Discussed in Ref. [64].

the desired properties of two cooperativity levels, cooperativity that increases with number of adsorbed neighbors, and support for rectangular domains; the levels of 3NN and 4NN cooperativity may be independently varied; and the similarity with (one-parameter) multiplicative rates allows a comparison with models that have been previously studied. We do not propose that the actual microscopic rates in experiment follow this choice of rates, but rather that this simplified choice reflects the local environment dependence of the actual rates sufficiently well to recreate key features of the patterns seen in experiment — particularly the relative influence of 3NN and 4NN cooperativity. As we shall see, a large number of experimental features can be understood upon adjusting just these two parameters.

2.2 Simulation results

We study the proposed CSA model using Monte Carlo simulations, described in brief in Appendix B. The simulations were carried out on 400x400 lattices, with results averaged across 100 runs for each (α, β) combination.

2.2.1 Mean coverage at saturation

The coverage θ at any point during the adsorption process is the fraction of filled sites. The saturation coverage θ^* is the coverage when no further particles can adsorb. The maximum possible coverage is achieved when the entire lattice consists of one single domain, in which case $\theta^* = 1/4$ (the NN and 2NN exclusion allows at most a fourth of the dual lattice to be covered in tetramers, all on one sublattice).

The saturation coverage is expected to increase with the cooperativity, because deviations from the maximum possible value occur only when domains with different

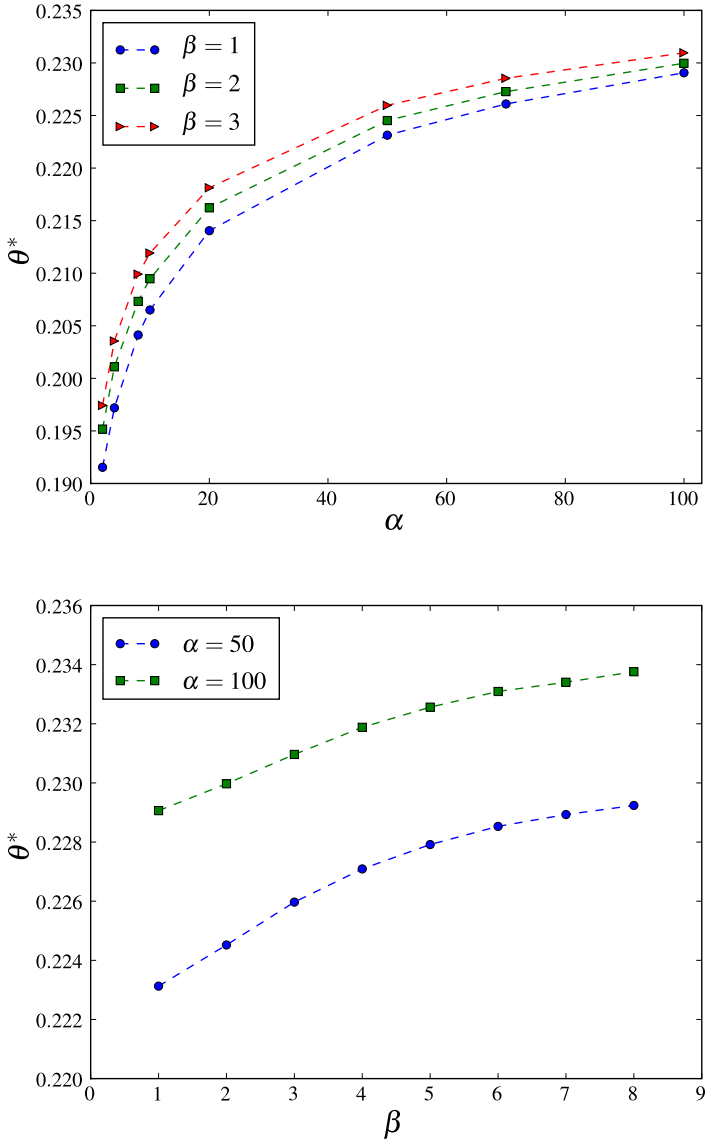

Figure 2.3: Dependence of saturation coverage, θ^*, on cooperativity parameters α and β in the CSA model (simulation). The top figure highlights the α-dependence when β is kept constant and vice-versa on the bottom. The lines are guides to the eye.

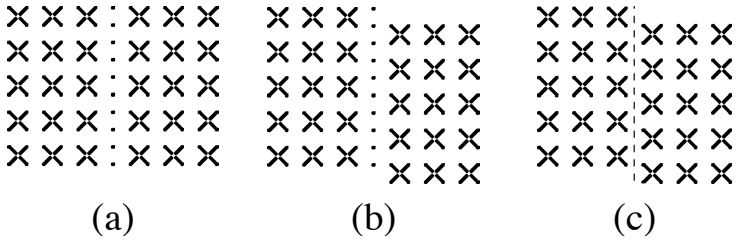

Figure 2.4: Domain walls between tetramer domains. (a) and (b) depict Type I domain walls that leave behind upright fibers (depicted by dots) which are not part of any cluster. On the dual lattice, two empty vertical rows separate the domains. The domain on the left in (a) belongs to sublattice 1 [if numbering begins from the top left as in figure 2.1(b)] while the domain on the right belongs to sublattice 2. In (b), the domain boundary is between domains on sublattice 1 and sublattice 3. (c) depicts a vertical Type II domain wall (dashed line) that does not leave behind any unclustered fibers. The domains are separated by only one row of empty sites on the dual lattice. The boundary is between a domain on sublattice 1 and one on sublattice 4. There are, of course, horizontal analogs of all three types of wall.

nucleating sites coalesce. A higher rate of tetramer formation near previously formed tetramers (compared to nucleation of lone tetramers) ensures that the dual lattice is filled with fewer domain walls; *i.e.* higher values of α and β give rise to higher values of saturation coverage, as seen in figure 2.3.

2.2.2 Domain sizes, chord lengths and domain wall densities

We have already defined domains as groups of particles (*i.e.* tetramers) connected to each other by a network of 3NN bonds. Domains belonging to different sublattices meet in domain walls that also run along the principal lattice directions. As figure 2.4(a–c) shows, there are two types of boundaries between domains that occur at saturation: boundaries involving free-standing single fibers that do not have enough neighbors to form tetramers (Type I) and boundaries that do not have such freely standing fibers (Type II). As a result of the CSA process, patterns with several domains meeting in boundaries of either type that primarily follow the principal directions of the lattice are generated (figure 2.5). "Zig-zag" domain walls that follow diagonal directions in the lattice are rare because of the

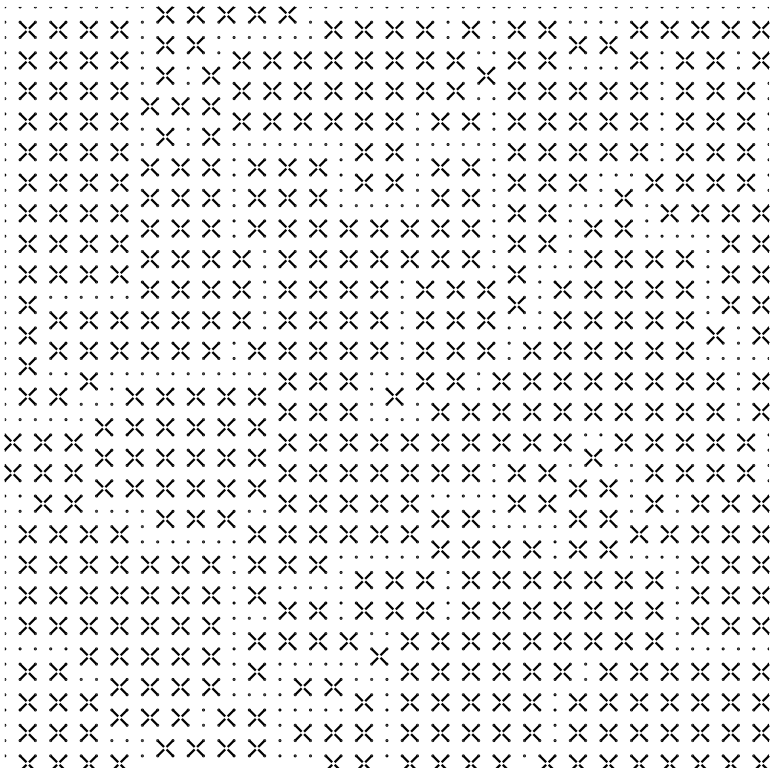

Figure 2.5: A typical result of the CSA process run to saturation has a mixture of Type I and Type II domains in both the horizontal and vertical directions. "Zig-zag" walls are occasionally seen which may be considered a combination of horizontal and vertical sections.

Arrhenius choice of rates.[2]

Once the different domains in the simulation result and the domain boundaries between them have been identified, ensemble-averaged measures of the domain size and the domain boundary lengths may be obtained. For a given simulation run, if n_s is the number of domains with s particles in them, we define the average domain size $s_{\text{av}} = \sum s n_s / \sum n_s$. We also consider the statistics of adsorbed particles on a row-by-row or column-by-column basis. Defining a chord as a contiguous string of particles connected by 3NN bonds in the vertical or horizontal direction of the lattice, we may also measure the average chord length $m_{\text{av}} = \sum m n_m / \sum n_m$ where n_m is the number of chords of length m. These are all measures of domain size that have been used in previous studies [8, 63].

We also define the domain wall densities ρ_1 and ρ_2 of type I and type II domain boundaries respectively as the total length (in lattice units) of each domain wall type at saturation divided by the number of fibers in the lattice. Zig-zag domain walls are broken up into vertical and horizontal sections which contribute to the domain wall densities as well.

Figures 2.6, 2.7, 2.8 and 2.9 summarize the dependence of these measured quantities on α and β. The effects of the two levels of cooperativity considered are different on the measures of domain size. Consider an already adsorbed particle M at the edge of a growing domain. The 3NN cooperativity enhances the adsorption of particles that belong to the same domain as M. Hence increased 3NN cooperativity, quantified by a larger value of α, corresponds to larger domains. In contrast, the effect of 4NN cooperativity is to enhance

[2]The asymptotic size of a single growing domain in an otherwise empty lattice is circular for Arrhenius-type rates. However, at its initial stages of growth the domain is rectangular since rows fill up quickly for Arrhenius rates. If we ignore 4NN cooperativity for the moment, Evans and Nord [64] have shown that growing domains retain their rectangular size up to a linear size of order $\alpha^{1/2}$ which also turns out to be the typical size a domain grows before it encounters another domain that nucleated independently. Thus domains do not attain their asymptotic shape but remain largely rectangular in the saturated state. As we shall see, the 4NN cooperativity tends to make domains even smaller and thus preserves their primarily rectangular shapes. See also footnote on page 42.

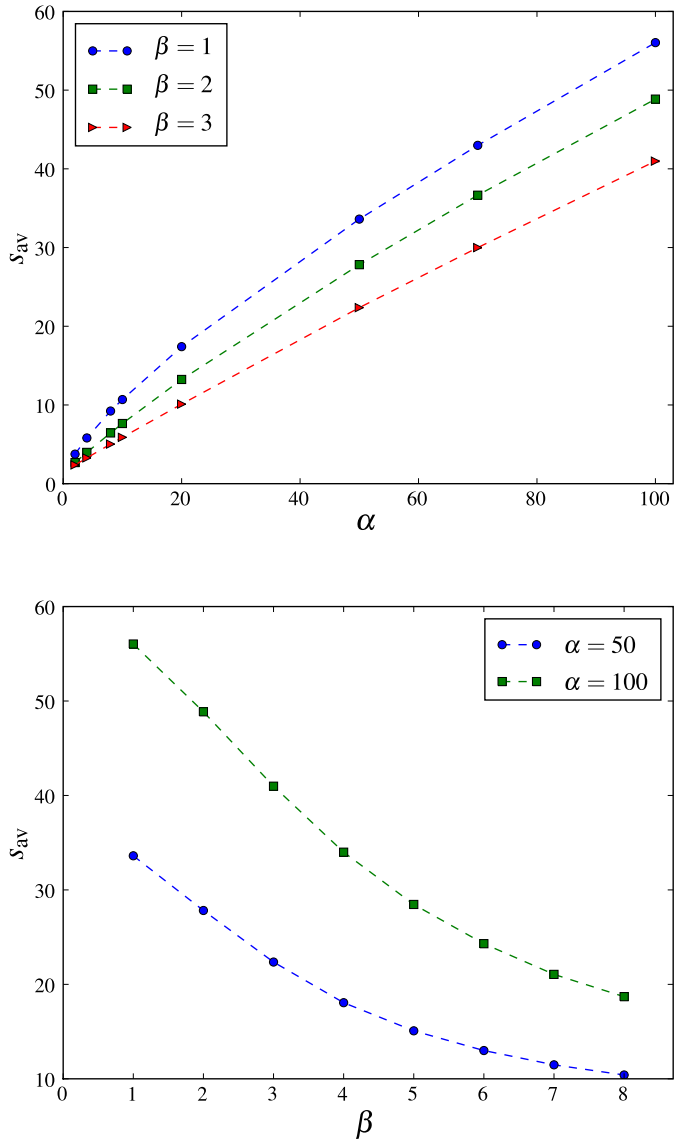

Figure 2.6: Dependence of average domain size s_{av} on cooperativity parameters α and β in the CSA model (simulation).

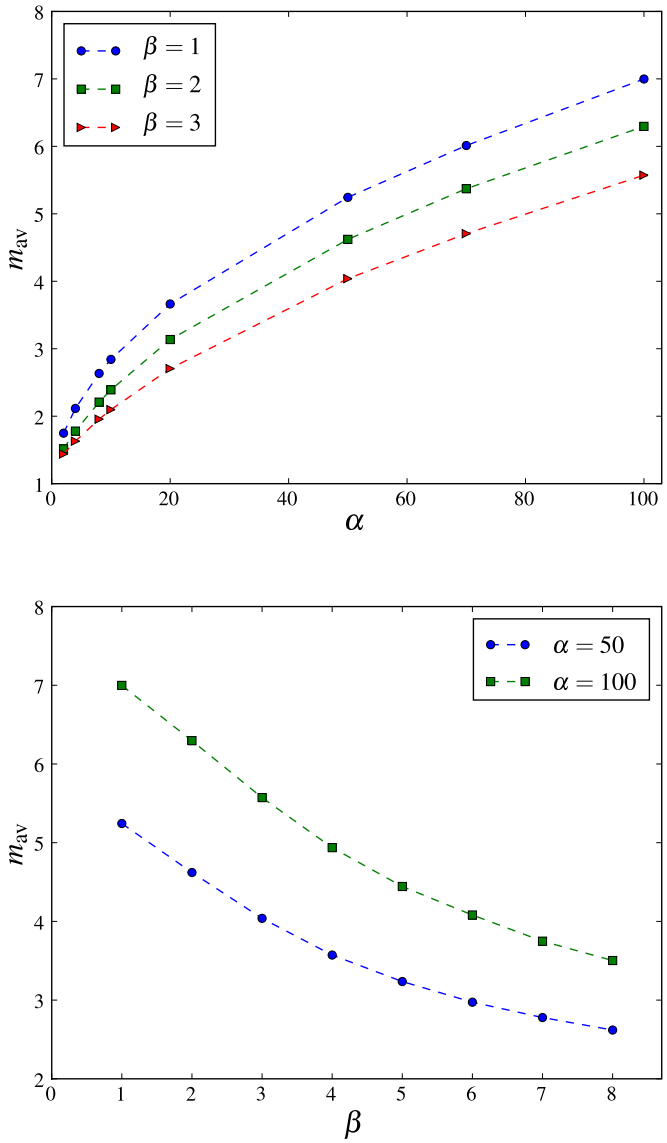

Figure 2.7: Dependence of average chord length m_{av} on cooperativity parameters α and β in the CSA model (simulation). Note the qualitatively different trends.

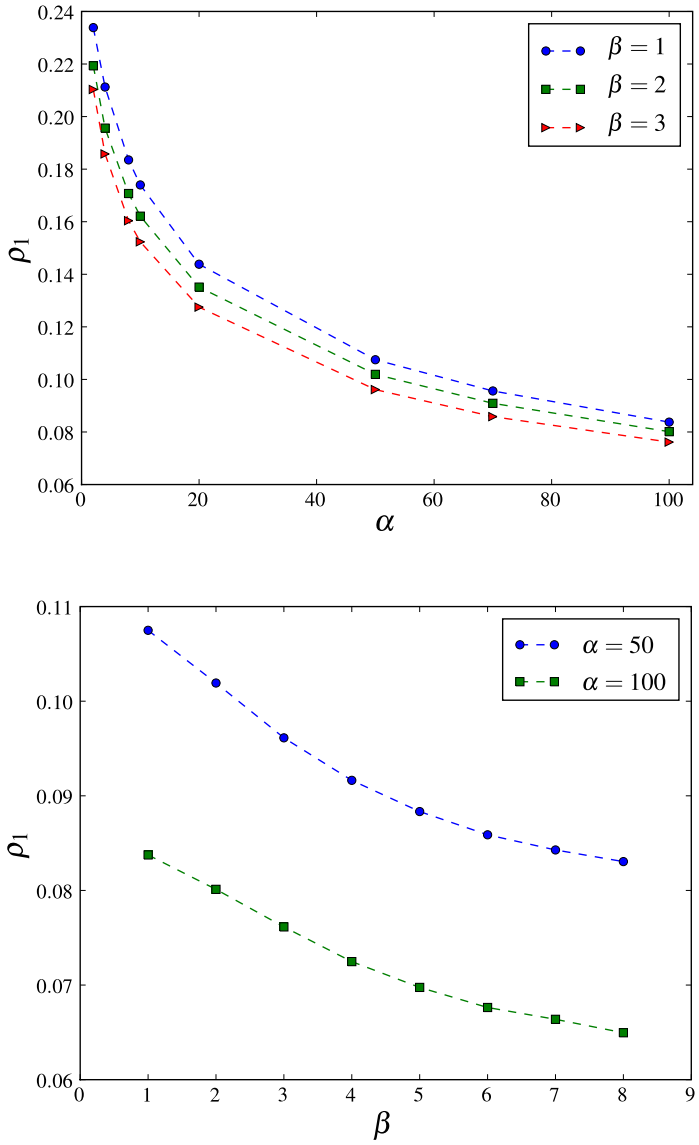

Figure 2.8: Dependence of type I domain wall density ρ_1 on cooperativity parameters α and β in the CSA model (simulation).

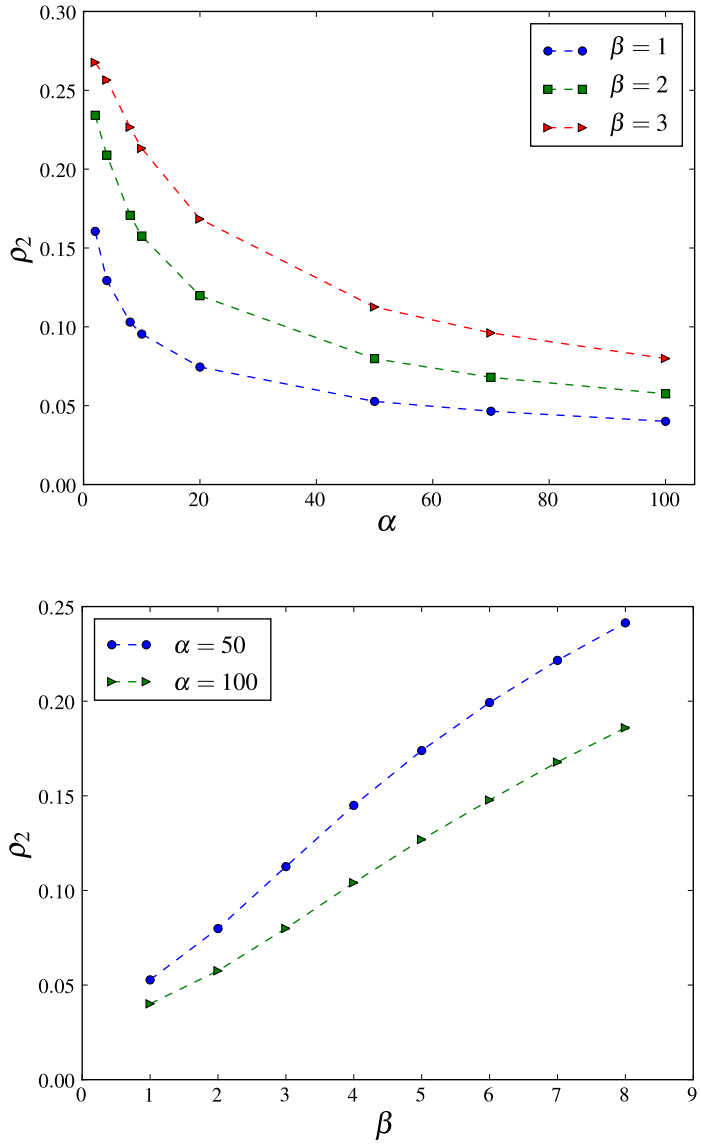

Figure 2.9: Dependence of type II domain wall density ρ_2 on cooperativity parameters α and β in the CSA model (simulation).

the rate of formation of particles that belong to a different sublattice than that occupied by M. This disrupts the growth of the domain by effectively nucleating a new domain on a *different* sublattice, giving rise to a Type II domain boundary shown in figure 2.4(c). Hence increasing the level of 4NN cooperativity, β, gives rise to smaller domains. This is seen in the measures of average domain size and average chord length from simulation, figures 2.6 and 2.7. From this argument, increasing β should also increase the density of type II domain walls, as confirmed in figure 2.9. The density of type I domain walls is essentially the density of unclustered fibers and thus closely related to the saturation coverage (increased θ^* should correspond to a fall in ρ_1 as fewer unclustered fibers are left at saturation). Hence increasing α and β both have the effect of reducing ρ_1 (figure 2.8).

A useful consequence of the competing influence of 3NN and 4NN cooperativity on domain size is that the parameters may be varied in tandem to increase the coverage at saturation without simultaneously increasing the average domain size. In previously studied models of cooperative sequential adsorption that include only one level of cooperativity (typically NN enhancement or NN exclusion and 2NN enhancement [62, 63]), increasing the rate of cooperative adsorption increases both the saturation coverage and the size of domains. In contrast, if the system exhibits cooperativity that induces adsorption of particles on a different sublattice as in the current model, then increasing this rate (β in the current model) increases the saturation coverage θ^* while decreasing the measures of domain size, s_{av} and m_{av}.

2.2.3 Pair correlations

We define spatial pair correlations at saturation as $C(x,y) = P(x,y) - \theta^{*2}$, where $P(x,y)$ is the probability that a pair of sites separated by the vector (x,y) in lattice units is occupied. Here we analyze correlations purely in the x direction, $C(x,0)$, averaged over several

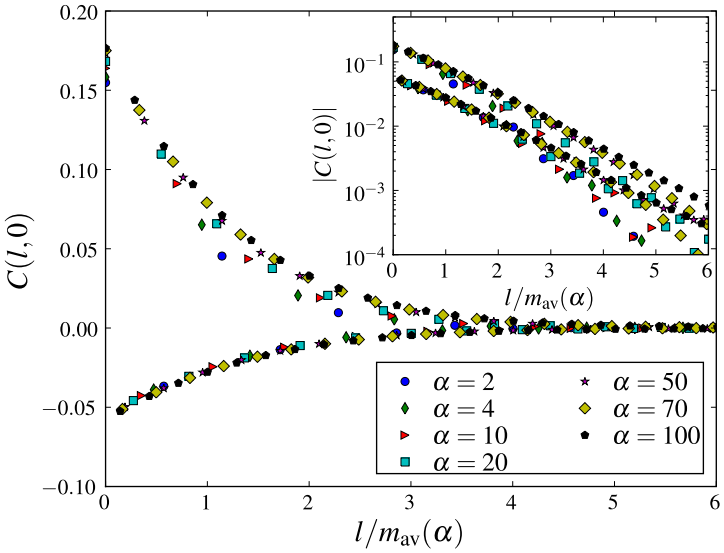

Figure 2.10: Pair correlation $C(l,0)$ for different values of α plotted against the rescaled separation $l/m_{\mathrm{av}}(\alpha)$. In all cases, $\beta = 1$. $m_{\mathrm{av}}(\alpha)$ is taken from data similar to that reported in figure 2.7 with $\beta = 1$.For $\alpha > 20$ the scaled correlations follow a universal form. The inset, which plots the absolute value of the pair correlation on a log-linear scale, shows the loss of scaling at large separations.

simulation runs. The average x and y direction correlations are equal by symmetry. The correlation $C(x,0)$ is positive for even values of the lattice separation x and negative for odd values as a consequence of nearest-neighbor exclusion in the tetramer model. For instance, $C(1,0) = -\theta^{*2}$ since $P(1,0) = 0$.

Dependence on 3NN cooperativity

At first we set β to 1 (no 4NN cooperativity) and vary α. The system is then very similar to the C(2x2) adsorption model with NN exclusion and 2NN cooperativity with Arrhenius rates studied by Evans and co-workers [63, 64] for which scaling arguments were developed by the authors using semi-deterministic domain growth models. For large α, the adsorption process resembles a deterministic nucleation and growth process in which new domains are nucleated with a rate k_0 per empty site, following which rectangular do-

mains grow at a size-dependent rate $\alpha k_0 m$ where m is the number of adsorbed particles on a growing edge of the domain. (When $\alpha \gg 1$, the time taken for a complete row to be added to the edge of a growing domain, $\sim m/(\alpha^2 k_0)$, is much smaller than the time taken for the new row to be initiated at that edge which is roughly $1/(m\alpha k_0)$. The latter is thus the rate-determining step for domain growth.) If fluctuations and edge roughening are ignored, the only relevant quantity is the ratio of the rates of domain nucleation to domain growth. Hence patterns generated by different values of α should be self-similar if they are rescaled by a characteristic length ξ that gives rise to the same nucleation to growth rate ratio for all of them. For Arrhenius rates in the limit of large α in two dimensions, this length has been shown to scale as $\xi \sim O(\alpha^{1/2})$ (Ref. [64]). At high values of α, the average linear dimension of the domains and the chord length m_{av} are expected to scale in the same fashion.

A consequence of the length scale set by the strong cooperativity is that the spatial correlations should display universal scaling on length scales $O(\xi)$ for large values of α. On length scales larger than the characteristic length, a crossover to the superexponential decay characteristic of random sequential adsorption processes is expected [63, 68]. Such behavior is indeed seen in figure 2.10.

Dependence on 4NN cooperativity

The effect of varying β while keeping the value of α constant is shown in figure 2.11. As β is increased, the positive-valued part of the correlation function [$C(l = 2n, 0)$ where n is an integer] falls. This is a result of the increased propensity for type II domain walls to form, which break up contiguous strings of adsorbed particles on the same sublattice in the x direction [see figure 2.4(c)]. On the other hand, the negative-valued part [$C(x = 2n + 1, 0)$] becomes more negative, because a particle in the domain on the left of figure 2.4(c)

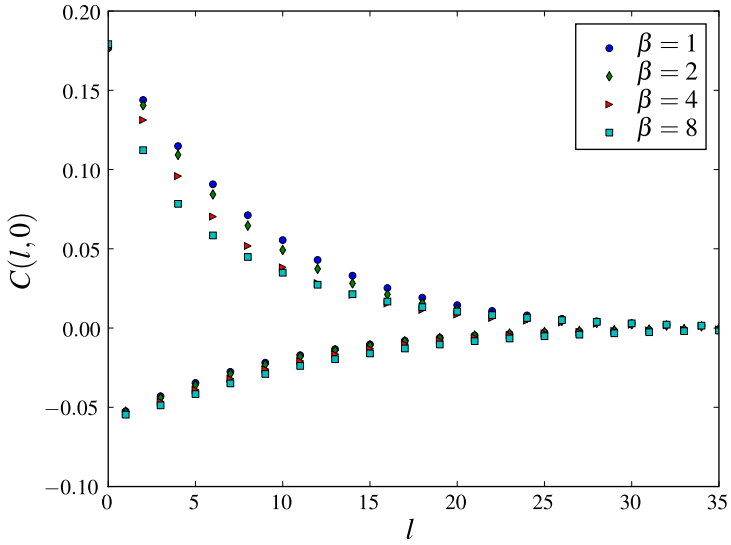

Figure 2.11: Pair correlation $C(l,0)$ for $\alpha = 100$ and different values of β against separation l in lattice units.

continues to have vacancies at positions that are odd numbers of lattice displacements along the same row into the new domain on the right.

The pair correlations in figure 2.11 *cannot* be made to overlap by rescaling the horizontal axis. (For instance, if we rescaled the l axis to make the positive-valued parts of $C(l,0)$ overlap for $\beta = 1$ and $\beta = 8$, we can see from the figure that the negative-valued parts of the curves would be pushed even further away compared to the unscaled functions.) The simple scaling of correlations seen when β was set to 1 has been lost. In the former case, scaling was justified by considering a deterministic domain nucleation and growth process where the ratio of the rates of domain nucleation to growth set the the characteristic length scale. When 4NN cooperativity is also included, the deterministic process is modified as follows: nucleation still happens at a rate k_0 per empty lattice site, and rows continue to be added to the straight edge of a growing domain at a rate $m\alpha k_0$ where m is the number of particles at the edge. However, domain growth (where a row is added to the same sublattice as the domain) now competes with the formation of a new

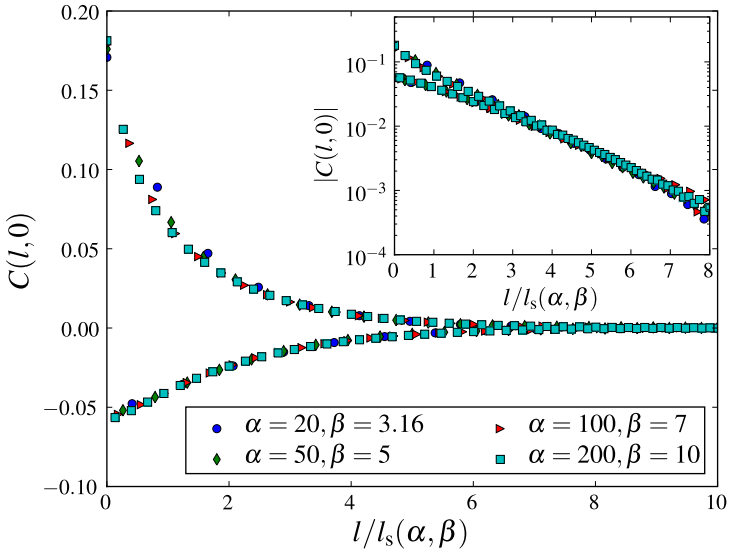

Figure 2.12: Pair correlation $C(l,0)$ for different values of (α,β) chosen such that $\alpha/\beta^2 = 2$ in all cases. The scaling length $l_s(\alpha,\beta)$ was chosen for each value of (α,β) to obtain the best data collapse. *Inset:* $|C(l,0)|$ against l/l_s on a log-linear scale.

domain on the sublattice displaced by one lattice step in either direction perpendicular to the growing edge, which happens at a rate $\sim m\beta^2 k_0$. The deterministic process thus depends on two rate ratios: the ratio of domain nucleation to growth, which is domain size dependent but controlled by α, and the ratio of domain growth to formation of a new domain at the growing edge, which equals α/β^2 for all sizes of domains.

The pair correlations do not scale as before because it is not possible to find a single characteristic length for rescaling that sets both rate ratios to be equal for patterns with different values of α and β. However, we expect that patterns with the same value of the ratio α/β^2 may be made self-similar by the appropriate rescaling that sets the nucleation-growth ratio to be uniform. This is confirmed in figure 2.12 where pair correlations for different values of (α,β) but the same value of α/β^2 have the same form upon appropriate rescaling of the horizontal axis. Note that for each of the values of α, a different value of β would not give a pair correlation that could be collapsed onto the same curves. As

before, the conclusions drawn from the deterministic model are appropriate only for large values of α where the domain nucleation and growth picture is not completely obscured by fluctuations due to the stochastic nature of the sequential adsorption model.

From the above discussion, we also see that the ratio α/β^2 quantifies of the relative influence of the 3NN and 4NN cooperativity on domain sizes. If $\alpha/\beta^2 \ll 1$, the 4NN cooperativity dominates, disrupting domain growth completely even for large α because it would be much more likely for a new row of tetramers to form on a shifted sublattice than on the same sublattice as a previously formed row. In that situation one would not observe large ordered domains at all, but rather see regions of staggered parallel rows of tetramers on alternating sublattices. The case of $\alpha/\beta^2 \ll 1$ is not relevant to the microfiber clustering system (for which domains extending over a few lattice lengths in either direction are always observed, indicating that 3NN cooperativity is dominant) and is not considered here.

2.2.4 Diffracted intensity

Although one does not typically diffract matter or light waves from the tetramer patterns studied here, Fourier analysis nevertheless provides a powerful tool for uncovering subtle patterns underlying tetramer formation. We define the diffracted intensity of the dual lattice of tetramers at a wavevector $\mathbf{q}$ as

$$I(\mathbf{q}) = \left| \sum_{x,y} e^{-i(q_x x + q_y y)} n(x,y) \right|^2 \tag{2.1}$$

where $q_x, q_y \in (-\pi, \pi)$, $n(x,y)$ is the occupation number (0 or 1) of the lattice position (x,y) and the sum runs over all lattice positions. This quantity is closely related to the diffracted intensity for scattering from the actual pattern of tetramers; it is the pattern that would be obtained if every tetramer in the pattern were replaced by a delta function scat-

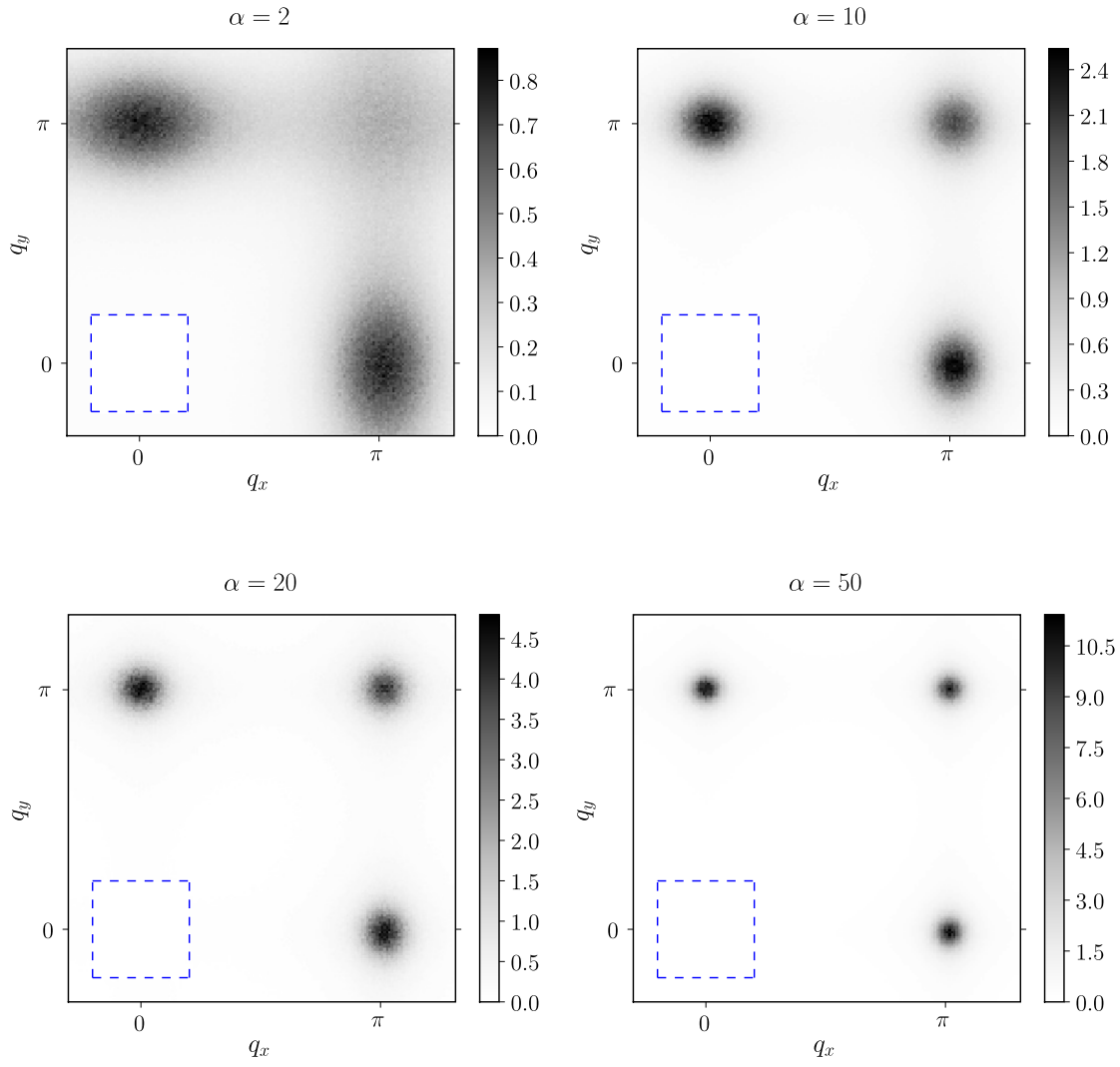

Figure 2.13: Intensity plots of diffraction patterns from simulations for different values of α. Since the pattern is fourfold symmetric, only one quadrant is shown but the x and y axes have been offset to reveal the shapes of the diffraction spots. The square region $-\pi/5 < q_x, q_y < \pi/5$ (dotted line) has been set to zero to emphasize the features near the edges. There is no 4NN cooperativity; *i.e.* $\beta = 1$ in all cases.

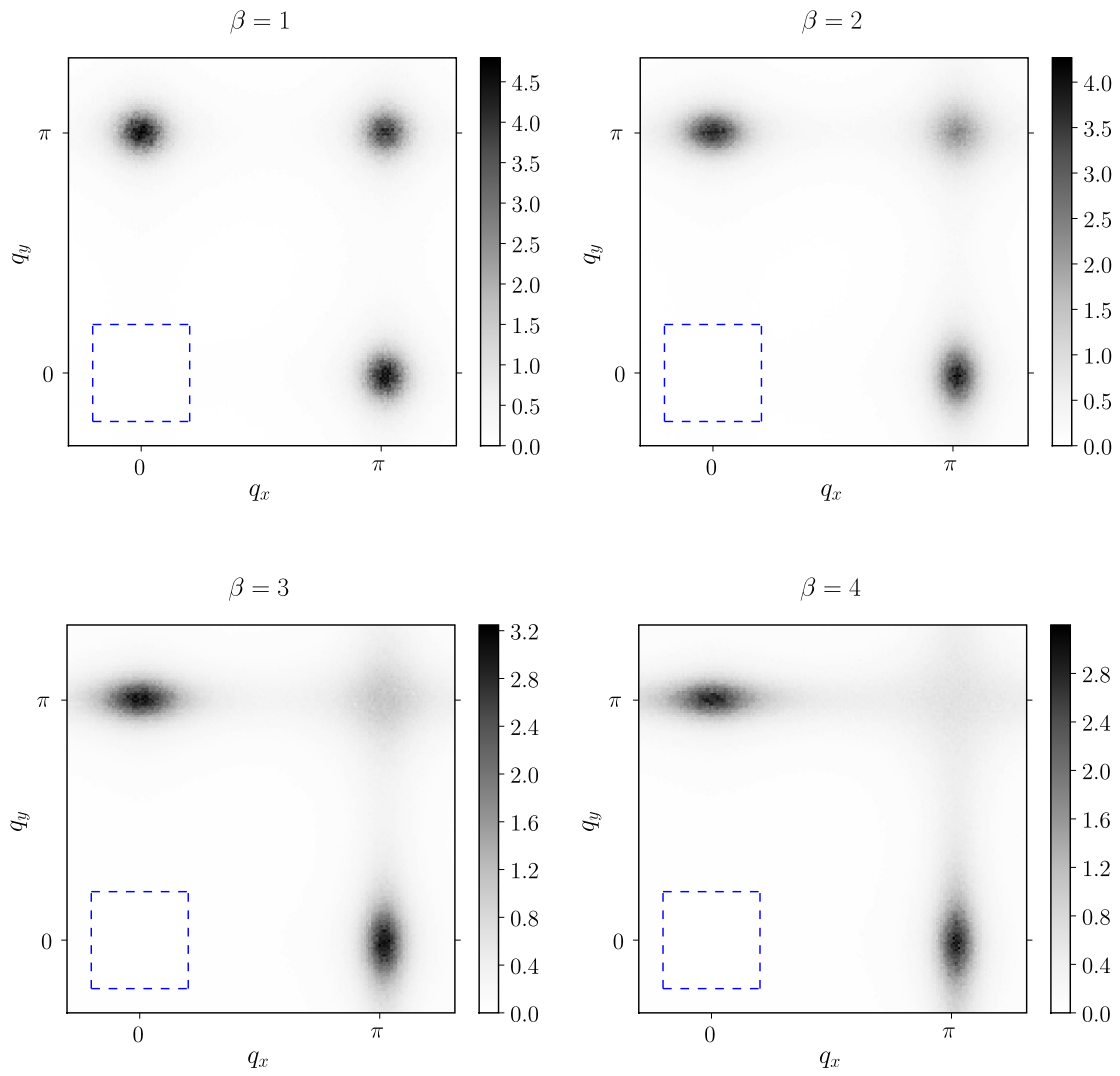

Figure 2.14: Intensity plots, similar to figure 2.13, of diffraction patterns from simulations for different values of β. In all cases, $\alpha = 20$.

terer at its center (similar to the structure factor for scattering from a collection of identical atoms). It provides information about the degree of order in the system and the types of domains and domain boundaries that are present.

In practice, the results of simulations and the experimental measurements are discrete arrays of size NxN. In this case we calculate the diffracted intensity *via* a discrete Fourier transform of the array $n(x, y)$ of occupation numbers. The resulting array provides an estimate of $I(q_x, q_y)$ for q_x, q_y taking on discrete values $2\pi n/N$ where n takes on integer values between $-N/2$ and $N/2$. Averaging the calculated patterns from several realizations of a finite-sized simulation of tetramer deposition at a particular (α, β) provides a diffraction pattern representative of that set of parameters.

A single domain is a square array of particles with a superlattice spacing of twice the underlying lattice. The diffraction pattern of an infinite domain consists of delta function peaks at $\mathbf{q} = \pm(\pi, 0), \pm(0, \pi), \pm(\pi, \pi), \pm(\pi, -\pi)$, etc., *i.e.* the reciprocal lattice of the square superlattice of particles, in addition to the origin. At finite cooperativity, finite-sized domains on different sublattices interfere to broaden these peaks in specific ways. To understand this, suppose we start with an infinite domain and create a Type II domain wall running along the y direction by shifting all the particles to the right of the origin up by one lattice position. The x coordinates of all occupied sites remain the same in the sum in equation (2.1); hence the peaks at $\mathbf{q} = (\pm\pi, 0)$ are unaffected but the peaks at nonzero values of q_y broaden in the q_x direction.[3] Analogously, Type II domain walls in the x direction broaden the peaks with $q_x \neq 0$ in the q_y direction. Type I domain walls have an effect of either diminishing the strength of peaks or broadening them perpendicular to

[3]The width of a diffraction peak in either direction is inversely proportional to the correlation length of the pair correlation in that direction. The domain wall reduces pair correlations in the x direction (by dephasing rows of adsorbed particles that extended across the entire lattice) but not in the y direction, hence affecting the peak width along q_x but not q_y.

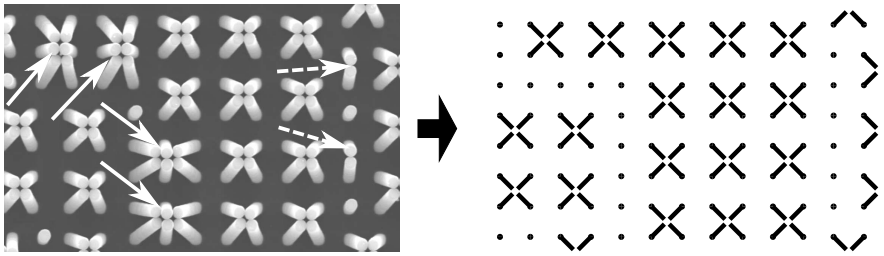

Figure 2.15: A section of an experimental image (left) compared to its interpretation in terms of tetramers on a lattice (right) within the framework of our model. Notice especially that the hexamer (3x2) clusters, indicated by solid arrows, have been interpreted as being parts of a continuous type I domain boundary. Similarly, dimers that form along another type I boundary, indicated by dashed arrows, are interpreted as a row of lone fibers.

their non-zero momentum direction.

Increasing α while setting $\beta = 1$ constant (figure 2.13) sharpens the principal reciprocal lattice peaks by reducing domain wall densities, allowing large domains to dominate the diffraction pattern. At a constant value of α, increasing the value of β (figure 2.14) increases Type II domain wall densities exclusively, thus broadening the peaks at $(0, \pm\pi)$ and $(\pm\pi, 0)$ perpendicular to the non-zero momentum and diminishing the peaks at $(\pm\pi, \pm\pi)$.

2.3 Experimental results

To test our theoretical ideas, we conducted clustering experiments on a sample of size 2 cm x 1 cm, with fibers of height 10¯m and diameter 1.8¯m arranged in a square array with lattice constant 3.5¯m (Sample I). Experimental details are in Appendix B. Optical microscope images were taken of a 182 x 182 fiber area at a time, and a pattern recognition program written in MATLAB® (MathWorks, Inc.) was used to identify the positions of the formed tetramers on the dual lattice. Thus a 182 x 182 lattice of empty and filled sites

was obtained from each image, the filled sites being the ones at which a tetramer was observed. From these lattices, relevant measures such as the coverage, domain sizes and chord lengths could be measured which correspond exactly to the quantities measured from the CSA model simulations. We imaged 43 non-overlapping regions, and calculated pattern statistics for each lattice. Here we report quantities averaged across the 43 regions, and the corresponding standard error of this average is used as the error estimate.[4]

In the experiment, we also see clusters that do not strictly consist of four fibers, such as hexamers (3x2 clusters). These are primarily seen at the boundaries between ordered domains belonging to different sublattices. We interpret these clusters in the context of the tetramer adsorption model as follows: the ethanol-air interface is pinned to the tips of the fibers even as the level of the ethanol-air interface recedes below the height of the fibers. The capillary forces between fiber tips are a result of this pinning which perturbs the interface, and they increase as the height difference between fiber tips and interface increases [66]. These capillary forces compete with the elastic forces involved with bending the fibers so that their tips touch to form clusters. When the level of the ethanol-air interface is such that capillary forces are strong enough to induce tetramer clustering, tetramer formation begins and proceeds until saturation; larger cluster formation does not happen because fiber tips need to be displaced by larger distances, and higher capillary forces are needed to overcome the corresponding elastic forces. If the evaporation were stopped at this stage a pattern consisting only of tetramers and upright (unclustered) fibers would be observed. However, in the actual experiments, ethanol evaporation continues until the

[4]The standard error, $s = \sigma/\sqrt{n}$ where σ is the estimate of the standard deviation of the measured quantity and n is the number of measurements taken, is a valid estimate of the error associated with measuring a mean quantity, as long as the individual measurements are made from the same statistical distribution with a uniform value of σ. In practice, slight nonuniformities in the sample, as well as spatial irregularities in the evaporation rate of ethanol, are likely to make the cooperativity levels in each of the 43 regions slightly different from one another; *i.e.* the measurements made in each region belong to slightly different statistical distributions. This variation is not reflected in the standard error which is thus likely to underestimate the true errors in the measured quantities.

Table 2.1: Comparison of experiment to model

Quantity	Experiment	Two-parameter CSA $\alpha = 48, \beta = 2.7$	One-parameter CSA $\alpha = 41$
θ^*	0.2258 ± 0.0004	0.2253	0.2213
s_{av}	20.6 ± 0.5	23.2	29.1
m_{av}	4.0 ± 0.1	4.12	4.84
ρ_1	0.099 ± 0.002	0.099	0.115
ρ_2	0.111 ± 0.002	0.105	0.057

Comparison of measured quantities from Sample I with averaged statistics of the two-parameter and the one-parameter CSA models with parameters picked by least-squares fitting of the diffraction pattern with experiment. The simulation results are averaged over 100 instances of a 400 x 400 lattice and the standard error associated with this average is smaller than the most significant digit reported.

capillary forces become strong enough to draw some of the remaining lone fibers toward their neighbors to form dimers (clusters of two adjacent pillars), hexamers and larger sized clusters. Thus we interpret these clusters as a combination of tetramers and lone fibers when we convert the experimental images into lattice occupancy data. To be consistent with this interpretation, we translate a row of hexamers in the experiment as a row of tetramers next to a row of unclustered fibers (rather than randomly assigning a tetramer to one of the two positions it could occupy in each hexamer) because such a row is most likely to have arisen at the site of a continuous Type I domain wall which we recreate in the lattice data. Figure 2.15 shows an example of translating an experimental pattern into lattice data.

The method of fitting the experimental results to the simulations is as follows: the two-dimensional diffracted intensity defined in equation (2.1) condenses ensemble-wide properties of the generated patterns into a two-dimensional array of numbers. We thus compare the averaged diffracted intensity from the experiment to that from the simulations, choosing α and β that best fit the experimental diffraction pattern. The parameters are chosen that minimize the root mean square deviation of the diffracted intensity,

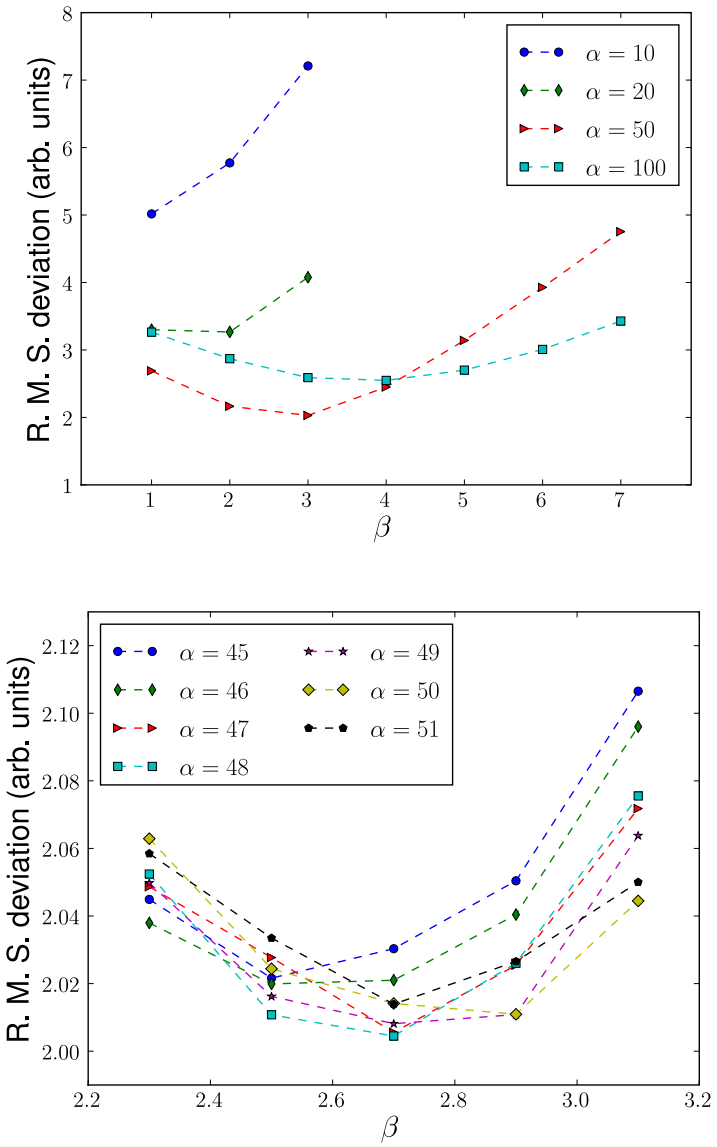

Figure 2.16: Least-squares fitting of the experimental result to simulations. Each line shows the RMS value of the difference in observed and simulated diffraction intensity (averaged across the two-dimensional array) for a particular value of α while varying β. On the top, the smallest value of of the RMS deviation decreases and then increases upon varying α over a large range, suggesting that a unique minimum can be found in the vicinity of $\alpha = 50, \beta = 3$. On the bottom, more refined parameters $\alpha = 48, \beta = 2.7$ are seen to provide the best fit with a precision of ± 1 in α and ± 0.1 in β.

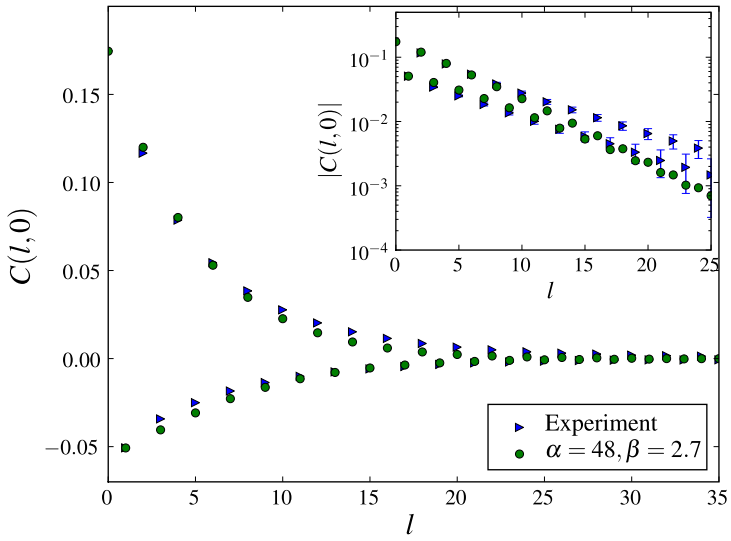

Figure 2.17: Comparison between the measured pair correlation of Sample I to the pair correlation function of the CSA model with $\alpha = 48, \beta = 2.7$. *Inset:* Absolute value of the pair correlations on a log-linear scale.

weighted by the inverse of the experimental error estimate at each (q_x, q_y). As figure 2.16 shows, such a minimum value may be extracted from the data to a reasonable precision. For our experimental measurements, we obtain $\alpha = 48 \pm 1, \beta = 2.7 \pm 0.1$.

Table 2.1 shows a comparison between experiment (second column) and the CSA model simulation for the optimized α and β values described above (third column). The measured average values of the different pattern statistics introduced previously appear to be in reasonable agreement. Figure 2.17 compares the calculated pair correlation function from the experiment to that of the CSA model with the chosen fit parameters, again showing reasonable agreement.

We can also compare the performance of the extended CSA model to a one-parameter model with only 3NN cooperativity and Arrhenius rates $k_i = k_0 \alpha^i$ for an empty site with i occupied sites at third nearest neighbor positions (this is equivalent to the two-parameter model with β set to 1). Statistics for the best fit obtained for α in the one-

parameter model have also been reported in table 2.1 (fourth column), showing that the two parameter model performs significantly better. In particular, the absence of 4NN cooperativity leads the one-parameter model to greatly underestimate ρ_2, the density of type II domain boundaries which are induced by the 4NN cooperativity mechanism. The high value of ρ_2 in the experiment confirms that the 4NN cooperativity mechanism is important in tetramer formation.

2.4 Conclusion

We have proposed a lattice sequential adsorption model of ordered tetramer clusters of microfibers driven by capillary forces. The newly introduced further-neighbor cooperativity allows independent variation of lattice coverage and average domain size: unlike previously studied cooperative sequential adsorption models, the present model allows the saturation lattice coverage to be increased without correspondingly raising the average domain size. This independence arises because the model admits additional domain boundaries that do not include unoccupied sites.

With a plausible model for ordered cluster formation as judged by the comparison of the theory to experiment, we may ask how to improve ordering in the capillary-assisted self-organization process. Clearly, increasing the rate of cooperative domain expansion relative to random domain nucleation gives rise to larger ordered domains. A low level of the ethanol-air interface relative to the height of the fiber tips increases the downward as well as inter-fiber-tip capillary forces, which would induce more random nucleation events. If we control the evaporation of the ethanol (for instance, by controlling the ambient vapor pressure of ethanol) in such a way that the interface spends a longer time at a height that induces few tetramers to form on their own, then clustering is more

likely to be triggered among fibers destabilized by the formation of clusters nearby than by the effect of the capillary forces on upright fibers. Thus the rate of bare nucleation of domains is reduced relative to their growth rate, and larger ordered domains could be produced.

The 4NN cooperativity is also a factor that leads to smaller domains. Indeed, even if domain growth arises from a single nucleation site and further isolated single-site nucleation is suppressed, there is always a chance that a domain belonging to a different sublattice begins somewhere along the growing edges of the domain as long as the 4NN cooperativity is significant. A second alternative to create uniform domains is to create artificial domain nucleation sites (say, by weakening or bending individual fibers as has been demonstrated in Ref. [65]) in a regular square array with each nucleation site created on the same sublattice and the spacing between nucleation sites smaller than the typical domain size observed in an uncontrolled clustering experiment. This strategy would enhance domains on the same sublattice and allow commensurate coalescence before random single-site nucleation or 4NN cooperativity-induced nucleation could initialize a domain belonging to a different sublattice.

A similar effect can be recreated along one dimension by imposing clustering dynamics at a front that sweeps across the sample in one direction rather than allowing random nucleation and bidirectional domain growth everywhere in the sample, as has been previously recognized in Ref. [57]. This bias can be achieved, for instance, by performing the clustering on a tilted sample. Due to the effect of gravity, the wetting layer retreats in one direction as the ethanol evaporates, and at any moment clustering happens only in a few horizontal rows near the retreating edge where the wetting layer is at its thinnest. Domain growth along the horizontal strip happens very quickly under 3NN cooperativity, following which the domain edge acts as a template for clustering in the next unclustered

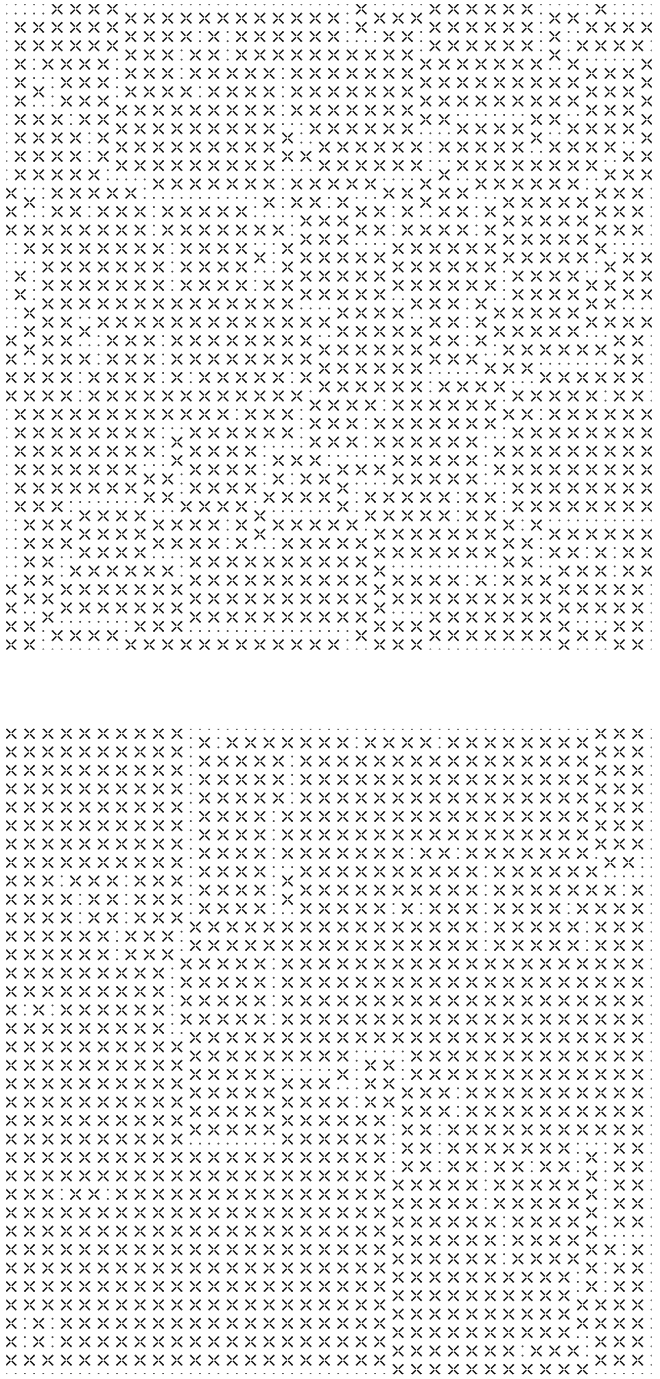

Figure 2.18: Single simulation result for CSA with $\alpha = 40, \beta = 2$ (top) compared with (bottom) a simulation with the same parameters in which clustering happens only in a strip three rows wide that is swept across the lattice from top to bottom to mimic the effect of an evaporation front (see text). There are far fewer domain boundaries in the row-by-row simulation on the right, and they tend to lie along the vertical axis.

row. This leads to extended domains in the direction of propagation of the clustering front (top to bottom), while in the perpendicular (horizontal) direction domains are broken up by 4NN cooperativity and random nucleation. A pattern resulting from a simulation of such a mechanism is shown in figure 2.18.

Finally we remark that this work could be relevant to future studies of various self-organization processes as well as sequential adsorption. For example, this model could be used to describe nonequilibrium adsorption of a molecule/complex/DNA tile that has a square/cross symmetry with the neighboring corners/ligands/arms possessing either opposite charge, or A,B,A,B recognition sites. Then the attachment of the next particle is mostly enhanced at the NN position where a bidentate junction is formed, but it will be also enhanced (but to a lesser degree) at the 2NN position where a monodentate junction is formed. Again, we arrive at double-level cooperativity in adsorption. The difference is that there will be no NN/2NN exclusion, but instead NN/2NN enhancement; otherwise, the model is largely the same. Abstraction of complex processes to lattice-type models that do not focus on microscopic details has been used with success to describe self-assembly of nanoparticles [69] and vesicle formation [70] among other processes; here we use an out-of-equilibrium lattice process to study a microscale self-organization process. The two-parameter sequential adsorption model we have developed could be relevant to more 'traditional' sequential adsorption processes of gas molecules on metal surfaces where further neighbor interactions are significant, and also to other irreversible processes that are not adsorption processes in the strict sense but nevertheless may be illuminated using such models.

Chapter 3

Statistical physics of pressurized spherical shells

The elastic theory of thin plates and shells [5], a subject over a century old, has recently found new applications in understanding the mechanical properties of a wide range of natural and artificial structures at microscopic length scales. The mechanical properties of viral capsids [71, 72, 73], red blood cells [21], and hollow polymer and polyelectrolyte capsules [74, 33, 75, 19, 76] have been measured and interpreted in terms of elastic constants of the materials making up these thin-walled structures. Theoretically, models that quantify the deformation energy of a two-dimensional membrane have been used to investigate the shapes of viral capsids [77, 78, 79] and their expected response to point forces and pressures [80, 81, 82, 83], as well as shape transitions of pollen grains [38].

Like its counterparts in other areas of science, such as fluid dynamics and the theory of electrical conduction in metals, thin shell theory aims to describe the physics of slowly varying disturbances in terms of a few macroscopic parameters, such as the shear viscosity of incompressible fluids and the electrical conductivity of metals. Despite such venerable underpinnings as the Navier-Stokes equations and Ohm's law, these hydrodynamic theories can break down, sometimes in spectacular ways. For example, it is

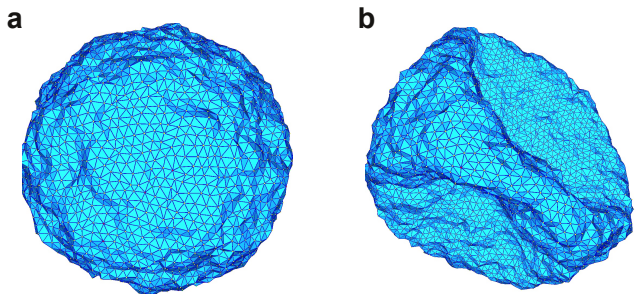

Figure 3.1: **Simulated thermally fluctuating shells. (a)** Triangulated shell with 5530 points separated by average nearest-neighbor distance r_0 with Young's modulus $Y = 577\epsilon/r_0^2$ and bending rigidity $\kappa = 50\epsilon$ at temperature $k_B T = 20\epsilon$, where ϵ is the energy scale of the Lennard-Jones potential used to generate the disordered mesh. **(b)** Same as in (a) with external pressure $p = 0.5 p_c$, where p_c is the classical buckling pressure. The thermally excited shell has already buckled under pressure to a shape with a much smaller enclosed volume than in (a).

know from mode coupling theory [84] and from renormalization group calculations [85] that thermal fluctuations cause the shear viscosity of incompressible fluids to diverge logarithmically with system size in a two-dimensional incompressible fluid. In the theory of electrical conduction, quenched disorder due to impurities coupled with interactions between electrons lead to a dramatic breakdown of Ohm's law in thin films and one-dimensional wires at low temperatures, with a conductance that depends on the sample dimensions [86].

Even more dramatic breakdowns of linear response theory can arise in thin plates and shells. Unlike the macroscopic shell structures of interest to civil engineers, thermal fluctuations can strongly influence structures with size of order microns, since the elastic deformation energies of extremely thin membranes (with nanoscale thicknesses) can be of the order of the thermal energy $k_B T$ (where k_B is the Boltzmann constant and T the temperature) for typical deformations. The statistical mechanics of *flat* solid plates and membranes (*i.e.* membranes with no curvature in the unstrained state) has been studied

previously (see [87, 15] and references therein). Thermal fluctuations lead to *scale-dependent* elastic moduli for flat membranes, causing the in-plane elastic moduli to vanish at large length scales while the bending rigidity diverges [16, 88]. These anomalies arise from the the nonlinear couplings between out-of-plane deformations (transverse to the plane of the undeformed membrane) and the resultant in-plane strains, which are second order in the out-of-plane displacements.

Much less is known about spherical shells subject to thermal fluctuations, such as the one shown in Fig. 3.1(a). In fact, the coupling between in-plane and out-of-plane modes is significantly different. Geometry dictates that a closed spherical shell cannot be deformed without stretching; as a result, out-of-plane deformations provide a *first* order contribution to the in-plane strain tensor [5]. This introduces new nonlinear couplings between in-plane and out-of-plane deformations, which are forbidden by symmetry in flat membranes. We can also consider the buckling of spherical shells under uniform external pressure, which has no simple analogue for plates [Fig. 3.1(b)]. An early exploration with computer simulations combined an analysis of the elastic energy due to the linear strain contributions of a spherical membrane with the nonlinear corrections from flat membranes to suggest new scaling behavior for thermally fluctuating spherical membranes [89]. However, an important nonlinear coupling triggered by the curved background metric was not considered, nor was the effect of an external pressure investigated. Here, we study the mechanics of fluctuating spherical shells using perturbation theory and numerical simulations, taking into account the nonlinear couplings introduced by curvature as well as the effects of a uniform external pressure.

3.1 Elastic energy of a thin shell

The elastic energy of a deformed spherical shell of radius R is calculated using *shallow-shell theory* [12]. This approach considers a shallow section of the shell, small enough so that slopes measured relative to the section base are small. The in-plane displacements of the shallow section are parametrized by a two-component phonon field $u_i(\mathbf{x})$, $i = 1, 2$; the out-of-plane displacements are described by a field $f(\mathbf{x})$ in a coordinate system $\mathbf{x} = (x_1, x_2)$ tangent to the shell at the origin.[1] We focus on *amorphous* shells, with uniform elastic properties, and can thus neglect the effect of the 12 inevitable disclinations associated with crystalline order on the surface of a sphere [77]. In the presence of an external pressure p acting inward, the elastic energy for small displacements in terms of the bending rigidity κ and Lamé coefficients μ and λ reads (see Appendix C.1 for details):

$$G = \int d^2x \left[\frac{\kappa}{2} (\nabla^2 f)^2 + \mu u_{ij}^2 + \frac{\lambda}{2} u_{kk}^2 - pf \right], \tag{3.1}$$

where the nonlinear strain tensor is

$$u_{ij}(\mathbf{x}) = \frac{1}{2} \left(\partial_i u_j + \partial_j u_i + \partial_i f \partial_j f \right) - \delta_{ij} \frac{f}{R}. \tag{3.2}$$

Here, $d^2x \equiv \sqrt{g} dx_1 dx_2$, where g is the determinant of the metric tensor associated with the spherical background metric. Within shallow shell theory, $g \approx 1$ as shown in Appendix C.1.

If we represent the normal displacements in the form $f(\mathbf{x}) = f_0 + f'(\mathbf{x})$, where f_0 represents the uniform contraction of the sphere in response to the external pressure, and f' is the deformation with reference to this contracted state so that $\int d^2x f' = 0$, then the energy is quadratic in fields u_1, u_2 and f_0. These variables can be eliminated in a functional integral of $\exp(-G[f', f_0, u_1, u_2]/k_B T)$ by Gaussian integration; details of the calculation

[1] In this Chapter and the associated Appendices, the out-of-plane displacement field is called f, rather than w, to maintain consistency with existing literature on the statistical physics of *flat* membranes [11].

are presented in Appendix C.2. The effective free energy G_{eff} which results is the sum of a harmonic part G_0 and an anharmonic part G_1 in the remaining variable $f'(\mathbf{x})$:

$$\begin{aligned} G_0 &= \frac{1}{2}\int d^2x \left[\kappa(\nabla^2 f')^2 - \frac{pR}{2}|\nabla f'|^2 + \frac{Y}{R^2}f'^2\right], \\ G_1 &= \frac{Y}{2}\int d^2x \left[\left(\frac{1}{2}P^{\mathrm{T}}_{ij}\partial_i f'\partial_j f'\right)^2 - \frac{f'}{R}P^{\mathrm{T}}_{ij}\partial_i f'\partial_j f'\right]. \end{aligned} \tag{3.3}$$

where $Y = 4\mu(\mu+\lambda)/(2\mu+\lambda)$ is the two-dimensional Young modulus and $P^{\mathrm{T}}_{ij} = \delta_{ij} - \partial_i\partial_j/\nabla^2$ is the transverse projection operator. The "mass" term $Y(f'/R)^2$ in the harmonic energy functional reflects the coupling between out-of-plane deformation and in-plane stretching due to curvature, absent in the harmonic theory of flat membranes (plates). The cubic interaction term with a coupling constant $-Y/2R$ is also unique to curved membranes and is prohibited by symmetry for flat membranes. These terms are unusual because they have system-size-dependent coupling constants. Note that an inward pressure ($p > 0$) acts like a negative R-dependent surface tension in the harmonic term. As required, the effective elastic energy of fluctuating flat membranes is retrieved for $R \to \infty$ and $p = 0$. In the following, we exclusively use the field $f'(\mathbf{x})$ and thus drop the prime without ambiguity.

When only the harmonic contributions are considered, the equipartition result for the thermally generated Fourier components $f_{\mathbf{q}} = \int d^2x\, f(\mathbf{x})\exp(i\mathbf{q}\cdot\mathbf{x})$ with two-dimensional wavevector $\mathbf{q}$ are

$$\langle f_{\mathbf{q}} f_{\mathbf{q}'}\rangle_0 = \frac{A k_{\mathrm{B}}T\delta_{\mathbf{q},-\mathbf{q}'}}{\kappa q^4 - \frac{pR}{2}q^2 + \frac{Y}{R^2}}. \tag{3.4}$$

where A is the area of integration in the (x_1, x_2) plane. Long-wavelength modes are restricted by the finite size of the sphere, *i.e.* $q \gtrsim 1/R$. In contrast to flat membranes for which the amplitude of long-wavelength ($q \to 0$) modes diverges as $k_{\mathrm{B}}T/(\kappa q^4)$, the coupling between in-plane and out-of-plane deformations of curved membranes cuts off fluctuations

with wavevectors smaller than a characteristic inverse length scale [89]:

$$q^* = (\ell^*)^{-1} = \left(\frac{Y}{\kappa R^2}\right)^{1/4} \equiv \frac{\gamma^{1/4}}{R},$$

where we have introduced the dimensionless *Föppl-von Kármán number* $\gamma = YR^2/\kappa$ [77]. We focus here on the case $\gamma \gg 1$, so $\ell^* \ll R$. As p approaches $p_c \equiv 4\sqrt{\kappa Y}/R^2$, the modes with $q = q^*$ become unstable and their amplitude diverges. This corresponds to the well-known buckling transition of spherical shells under external pressure [12]. When $p > p_c$, the shape of the deformed shell is no longer described by small deformations from a sphere, and the shallow shell approximation breaks down.

3.2 Anharmonic corrections to elastic moduli

The anharmonic part of the elastic energy, neglected in the analysis described above, modifies the fluctuation spectrum by coupling Fourier modes at different wavevectors. Upon rescaling all lengths by ℓ^*, it can be shown that the size of anharmonic contributions to $\langle|f_{\mathbf{q}}|^2\rangle$ is set by the dimensionless quantities $k_B T\sqrt{\gamma}/\kappa$ and p/p_c. The correlation function including the anharmonic terms in Eq. (3.3) is given by the Dyson equation,

$$\langle|f_{\mathbf{q}}|^2\rangle = \frac{1}{\langle|f_{\mathbf{q}}|^2\rangle_0^{-1} - \Sigma(\mathbf{q})} \tag{3.5}$$

where $\Sigma(\mathbf{q})$ is the self-energy, which we evaluate to one-loop order using perturbation theory in Appendix C.3. While $\langle|f_{\mathbf{q}}|^2\rangle$ can be numerically evaluated at any $\mathbf{q}$, an approximate but concise description of the fluctuation spectrum is obtained by expanding the self-energy up to order q^4 and defining renormalized values Y_R, κ_R and p_R of the Young's modulus, bending rigidity and pressure, from the coefficients of the expansion:

$$Ak_B T\langle|f_{\mathbf{q}\to\mathbf{0}}|^2\rangle^{-1} \equiv \kappa_R q^4 - \frac{p_R R}{2}q^2 + \frac{Y_R}{R^2} + O(q^6). \tag{3.6}$$

To lowest order in $k_B T/\kappa$ and p/p_c we obtain the approximate expressions

$$Y_R \approx Y\left[1 - \frac{3}{256}\frac{k_B T}{\kappa}\sqrt{\gamma}\left(1 + \frac{4}{\pi}\frac{p}{p_c}\right)\right], \tag{3.7}$$

$$p_R \approx p + \frac{1}{24\pi}\frac{k_B T}{\kappa}p_c\sqrt{\gamma}\left(1 + \frac{63\pi}{128}\frac{p}{p_c}\right), \tag{3.8}$$

and

$$\kappa_R \approx \kappa\left[1 + \frac{61}{4096}\frac{k_B T}{\kappa}\sqrt{\gamma}\left(1 - \frac{1568}{915\pi}\frac{p}{p_c}\right)\right]. \tag{3.9}$$

(See Appendix C.3 for details of the calculation and the complete dependence on p/p_c.) Thus the long-wavelength deformations of a thermally fluctuating shell are governed by a smaller effective Young's modulus, a larger effective bending rigidity, and a nonzero negative surface tension even when the external pressure is zero. At larger p/p_c, however, both the Young's modulus and the bending modulus fall compared to their zero temperature values, and the negative effective surface tension determined by p_R gets very large. The complete expressions for the effective elastic parameters, including the full p/p_c-dependence, show that all corrections diverge as $p/p_c \to 1$. Furthermore, the effective elastic constants are not only temperature-dependent, but also system size-dependent, since $\sqrt{\gamma} \propto R$. Although the corrections are formally small for $k_B T \ll \kappa$, they nevertheless diverge as $R \to \infty$! The thermally generated surface tension, strong dependence on external pressure, and size dependence of elastic constants are unique to spherical membranes, with no analogue in planar membranes.

3.3 Simulations of thermally fluctuating shells

We complement our theoretical calculations with Monte Carlo simulations of randomly triangulated spherical shells with discretized bending and stretching energies that translate directly into a macroscopic 2D shear modulus Y and a bending rigidity κ [90, 28].

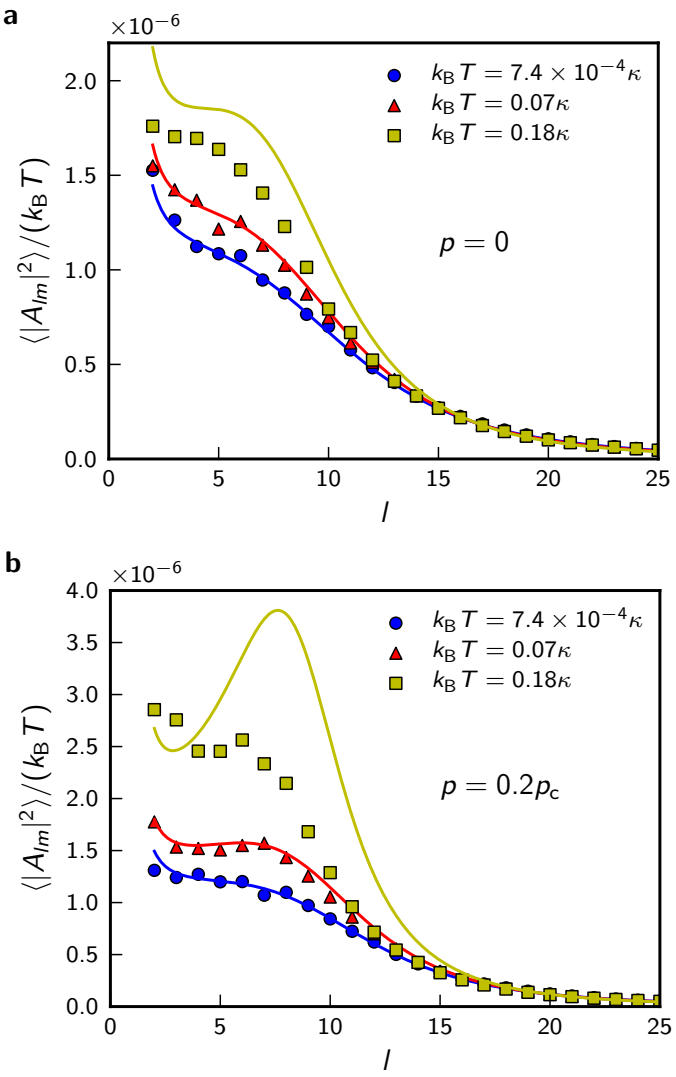

Figure 3.2: **Fluctuation spectrum in spherical harmonics.** Spherical harmonic amplitude of the shape fluctuations of elastic shells plotted against the dimensionless spherical wavenumber l for a shell with $R = 40r_0, Y = 577\epsilon/r_0^2$ and $\kappa = 50\epsilon$ at temperatures $k_BT/\kappa = 7.4 \times 10^{-4}$ (blue), 0.07 (red) and 0.18 (yellow). The fluctuation amplitudes are scaled by k_BT so that the spectra at different temperatures would coincide in the harmonic approximation. Each subfigure corresponds to a different value of the external pressure: $p = 0$ (**a**) and $p = 0.2p_c$ (**b**). The symbols are from Monte Carlo simulations, and the solid lines are the theoretical prediction, Eq. (3.11), using the renormalized elastic constants from perturbation theory [Eqs. (3.7)–(3.9)], except for the lowest temperature, where the bare elastic constants are used since the anharmonic effects are negligible.

Details of the simulation procedure are provided in Appendix D. We study shells with $600 < \gamma < 35000$ and $2 \times 10^{-6} < k_B T/\kappa < 0.5$. The anharmonic effects are negligible at the low end of this temperature range.

The fluctuation spectra of the simulated spherical shells are evaluated using an expansion of the radial displacement field in spherical harmonics [91]. The radial position of a node i at angles (ϕ, θ) can be written as $r_i(\phi,\theta) = \widetilde{R_0} + f(\phi,\theta)$ with $\widetilde{R_0}$ the average radius of the fluctuating vesicle. The function $f(\phi,\theta)$ can be expanded in (real) spherical harmonics

$$f(\phi,\theta) = R \sum_{l=0}^{l_M} \sum_{m=-l}^{m=l} A_{lm} Y_{lm}(\phi,\theta) \tag{3.10}$$

where l_M is the large wavenumber cutoff determined by the number of nodes in the lattice $(l_M+1)^2 = N$ [91]. The theoretical prediction for the fluctuation spectrum including anharmonic effects is derived in Appendix C.4; the result is

$$\begin{aligned} k_B T \langle |A_{lm}|^2 \rangle^{-1} \approx & \kappa_R (l+2)^2 (l-1)^2 - p_R R^3 \left[1 + \frac{l(l+1)}{2}\right] \\ & + Y_R R^2 \left[\frac{3(l^2+l-2)}{3(l^2+l)-2}\right]. \end{aligned} \tag{3.11}$$

Fig. 3.2 displays our theoretical and simulation results for the fluctuation spectrum. At the lowest temperature (corresponding to $k_B T\sqrt{\gamma}/\kappa \approx 0.1 \ll 1$), the spectrum is well-described by the bare elastic parameters Y, κ and p. At the intermediate temperature ($k_B T\sqrt{\gamma}/\kappa \approx 10$) anharmonic corrections become significant, enhancing the fluctuation amplitude for some values of l by about 20%–40% compared to the purely harmonic contribution. At this temperature, one-loop perturbation theory successfully describes the fluctuation spectrum. However, at the highest temperature simulated ($k_B T\sqrt{\gamma}/\kappa \approx 24$), the anharmonic corrections observed in simulations approach 50% of the harmonic contribution at zero pressure and over 100% for the pressurized shell. With such large corrections, we expect that higher-order terms in the perturbation expansion contribute significantly to

the fluctuation spectrum and the one-loop result overestimates the fluctuation amplitudes.

Similarly, thermal fluctuations modify the mechanical response when a shell is deformed by a deliberate point-like indentation. In experiments, such a deformation is accomplished using an atomic force microscope [71, 19]. In our simulations, two harmonic springs are attached to the north and south pole of the shell. By changing the position of the springs the depth of the indentation can be varied [Fig. 3.3(a), inset]. The thermally averaged pole-to-pole distance $\langle z \rangle$ is measured and compared to its average value in the absence of a force, $\langle z_0 \rangle$. For small deformations, the relationship between the force applied at each pole and the corresponding change in pole–pole distance is spring-like with a spring constant k_s: $\langle F \rangle \equiv k_s(\langle z_0 \rangle - \langle z \rangle)$. The spring constant is related to the amplitude of thermal fluctuations in the normal displacement field in the *absence* of forces by (see Appendix C.5 for the detailed derivation)

$$k_s = \frac{k_B T}{2\langle [f(\mathbf{x})]^2 \rangle} \approx \frac{k_B T}{\langle z_0^2 \rangle - \langle z_0 \rangle^2}. \tag{3.12}$$

This fluctuation-response relation is used to measure the temperature dependence of k_s from simulations on fluctuating shells with no indenters. At finite temperature, anharmonic effects computed above make this spring constant both size- and temperature-dependent:

$$k_s \approx \frac{4\sqrt{\kappa Y}}{R}\left[1 - 0.0069\frac{k_B T}{\kappa}\sqrt{\gamma}\right]. \tag{3.13}$$

Fig. 3.3(a) shows the force-compression relation for a shell with $R = 20r_0$ and dimensionless temperatures $k_B T\sqrt{\gamma}/\kappa = 1.36 \times 10^{-4}$ and $k_B T\sqrt{\gamma}/\kappa = 34$. The linear response near the origin [Fig. 3.3(b)] is very well described by k_s measured indirectly from the fluctuations in z_0 at each temperature, Eq. (3.12). The thermal fluctuations lead to an appreciable 20% reduction of the spring constant for this case. Measuring spring constants over a range of temperatures [Fig. 3.3(c)] confirms that the shell response softens as

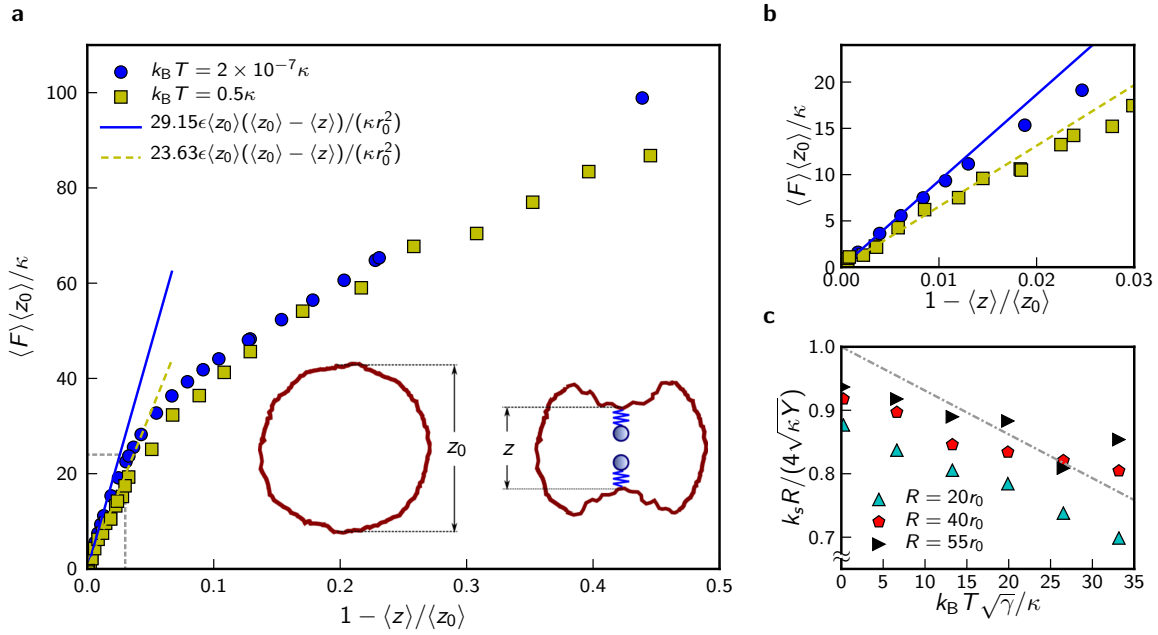

Figure 3.3: **Temperature dependence of response to point forces.** (**a**) Force-compression curves for simulations of indented shells (symbols) with $R = 20r_0$, $Y = 577\epsilon/r_0^2$ and $\kappa = 50\epsilon$ at low ($k_BT/\kappa = 2 \times 10^{-7}$) and high ($k_BT/\kappa = 0.5$) temperature. The lines show the expected linear response at small deformations with the spring constant k_s measured independently from fluctuations in z_0 ($k_s = 29.15\epsilon/r_0^2$ for $k_BT/\kappa = 2 \times 10^{-7}$, $k_s = 23.63\epsilon/r_0^2$ for $k_BT/\kappa = 0.5$). For indentation depths larger than $1 - \langle z\rangle/\langle z_0\rangle \approx 0.05$, the regions around the poles become inverted and the response becomes nonlinear. Inset: schematic showing the definition of z_0 (the pole-to-pole distance in the absence of indentations) and z (pole-to-pole distance following an indentation imposed by harmonic springs whose free ends are brought close together) for a snapshot of the fluctuating shell. (**b**) Blow-up of the boxed region near the origin in (**a**), highlighting the linear response regime. (**c**) Spring constants extracted from fluctuations for shells with three different radii as a function of temperature, rescaled by the classical result for linear response of thin shells at zero temperature. The dashed line shows the perturbation theory prediction, Eq. (3.13). The low-temperature spring constant deviates from the classical result due to a finite mesh size effect which falls with increasing R (increasing mesh size).

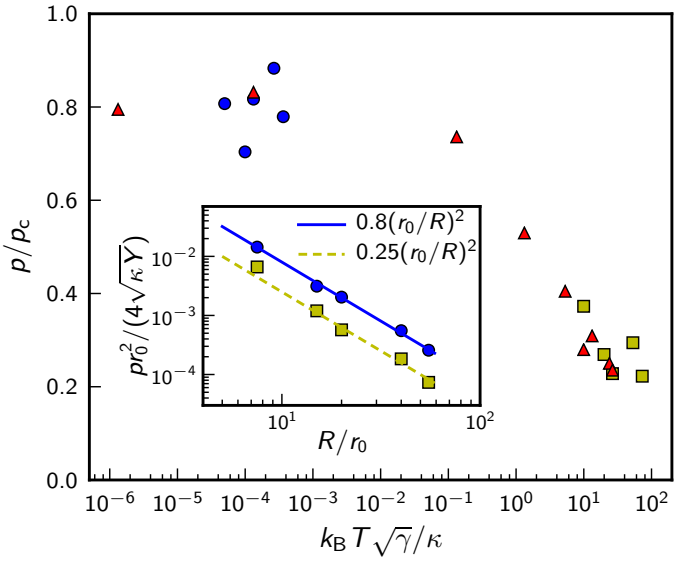

Figure 3.4: **Temperature dependence of the buckling pressure.** Buckling pressure for simulated shells at various radii and temperatures, normalized by the *classical* (*i.e.* zero temperature) critical buckling pressure p_c for perfectly uniform, zero temperature shells with the same parameters. For all shells, $Yr_0^2/\kappa = 11.54$. In separate sets of symbols, we either vary the shell radius over the range $7.5 \leq R/r_0 \leq 55$ while keeping the temperature constant ($k_BT = 2 \times 10^{-6}\kappa$, blue circles; $k_BT = 0.4\kappa$, yellow squares) or vary the temperature over the range $2 \times 10^{-8} \leq k_BT/\kappa \leq 0.4$ while keeping the radius constant at $R = 20r_0$ (red triangles). The parameter $k_BT\sqrt{\gamma}/\kappa$ sets the strength of anharmonic corrections for thermally fluctuating shells. The inset shows the $1/R^2$ dependence of the buckling pressure as the radius is varied, for shells at low and high temperature.

the temperature is increased, in agreement with the perturbation theory prediction. We note, however, a small but systematic shift due to the finite mesh size of the shells, an approximately 5% effect for the largest systems simulated here. At the higher temperatures ($k_BT\sqrt{\gamma}/\kappa > 20$), the measured spring constants deviate from the perturbation theory prediction, once again we believe due to the effect of higher-order terms.

We also simulate the buckling of thermally excited shells under external pressure. When the external pressure increases beyond a certain value (which we identify as the renormalized buckling pressure), the shell collapses from a primarily spherical shape

[Fig. 3.1(a)] to a shape with one or more large volume-reducing inversions [Fig. 3.1(b)]. For zero temperature shells, this buckling is associated with the appearance of an unstable deformation mode in the fluctuation spectrum. At finite temperature, the appearance of a mode with energy of order $k_{\mathrm{B}}T$ is sufficient to drive buckling. Anharmonic contributions, strongly enhanced by an external pressure, also reduce the effective energy associated with modes in the vicinity of q^* primarily due to the enhanced negative effective surface tension $p_{\mathrm{R}}R/2$ [see Eq. (3.8)]. As a result, unstable modes arise at lower pressures and we expect thermally fluctuating shells to collapse at pressures below the classical buckling pressure p_{c}. This is confirmed by simulations of pressurized shells (Fig. 3.4). When anharmonic contributions are negligible ($k_{\mathrm{B}}T\sqrt{\gamma}/\kappa \ll 1$), the buckling pressure observed in simulations is only $\sim$ 80% of the theoretical value because the buckling transition is highly sensitive to the disorder introduced by the random mesh. Relative to this low temperature value, the buckling pressure is reduced significantly when $k_{\mathrm{B}}T\sqrt{\gamma}/\kappa$ becomes large.

3.4 Conclusion and outlook

In summary, we have demonstrated that thermal corrections to the elastic response become significant when $k_{\mathrm{B}}T\sqrt{\gamma}/\kappa \gg 1$ and that first-order corrections in $k_{\mathrm{B}}T/\kappa$ already become inaccurate when $k_{\mathrm{B}}T\sqrt{\gamma}/\kappa \gtrsim 20$. Human red blood cell (RBC) membranes are known examples of curved solid structures that are soft enough to exhibit thermal fluctuations. Typical measured values of the shear and bulk moduli of RBC membranes correspond to $Y \approx 25\ \mu$N/m [21, 92], while reported values of the bending rigidity κ vary widely from 6 $k_{\mathrm{B}}T$ to 40 $k_{\mathrm{B}}T$ [21, 93]. Using an effective radius of curvature $R \approx 7\ \mu$m [21] gives $k_{\mathrm{B}}T\sqrt{\gamma}/\kappa$ in the range 2–35. Thus, RBCs could be good candidates to observe our predicted thermal effects, provided their bending rigidity is in the lower range of the reported values.

For continuum shells fabricated from an elastic material with a 3D Young's modulus E, thickness h and typical Poisson ratio ≈ 0.3, $k_B T\sqrt{\gamma}/\kappa \approx 100 R k_B T/(Eh^4)$. Hence very thin shells with a sufficiently high radius-to-thickness ratio (R/h) *must* display significant thermal effects. Polyelectrolyte [19] and protein-based [20] shells with $R/h \approx 10^3$ have been fabricated, but typical solid shells have a bending rigidity κ several orders of magnitude higher than $k_B T$ unless $h \lesssim 5$ nm. Microcapsules of 6 nm thickness fabricated from reconstituted spider silk [20] with $R \approx 30$ μm and $E \approx 1$ GPa have $k_B T\sqrt{\gamma}/\kappa \approx 3$, and could exhibit measurable anharmonic effects.

Thermal effects are particularly pronounced under finite external pressure—an indentation experiment carried out at $p = p_c/2$ on the aforementioned spider silk capsules would show corrections of 10% from the classical zero-temperature theory. For similar capsules with half the thickness, perturbative corrections at $p = p_c/2$ are larger than 100%, reflecting a drastic breakdown of shell theory because of thermal fluctuations. The breakdown of classical shell theory explored here points to the need for a renormalization analysis, similar to that carried out already for flat plates [11].

Chapter 4

Buckling pathways in spherical shells with soft spots

Thin spherical shells exhibit a buckling instability when subjected to a uniform external pressure. Under an increasing external pressure, idealized shells without imperfections remain spherical until a threshold pressure is reached at which the shell buckles: at this point, a very small increment in pressure triggers a large deformation in the form of one or more indentations that significantly reduce the enclosed volume. Understanding the effect of inhomogeneity in the shell material on this buckling transition, besides being a challenging problem due to the highly nonlinear nature of large deflections in shells, has the potential to uncover new ways of using buckling to provide form and function. In this chapter, we study the effect of a previously unexplored inhomogeneity that is simple, yet general: a soft spot with a circular boundary in an otherwise uniform spherical shell. We use numerical simulations and theoretical arguments to understand the buckling and postbuckling behavior as the spot size and stiffness are varied. The response of the shell may be broken down into the response of the soft region and the response of the remainder of the shell; the interplay of these responses plays a significant role in explaining the observed behavior.

Our numerical model, described in detail in Appendix E, is similar to ones used in other studies of the buckling of both uniform [28] and nonuniform [38, 94] shells under pressure. Our theoretical analysis builds on previous work both on uniform and slightly imperfect spherical shells [39, 29], and on the buckling of spherical *caps i.e.* shallow sections of spheres, with various boundary conditions [95, 96].

The rest of this chapter is structured as follows: we describe in more detail the elastic energy of deformations in thin spherical shells, and identify the dimensionless quantities that are relevant for our description. We then present our numerical results from simulations of buckling shells under external pressure, and describe different buckling pathways that arise as the parameters are changed. To explain our numerical observations, we analyze the underlying continuum shell theory equations for a soft spot embedded in the rest of the shell. To provide context, we recap the buckling behavior of uniform shells, which provides much insight on the buckling of shells with soft spots. We then consider separately the deformations of the cap, and of the remainder of the shell, using scaling arguments and approximations to understand the underlying nonlinear differential equations that describe stresses and deformations in the shell. Finally we describe the hysteresis properties of the inhomogeneous shells when the pressure is cyclically varied, which is strongly influenced by the soft region. We conclude with potential applications and possible avenues for further research.

4.1 Elastic theory of thin spherical shells

Typically, the elastic energy of deforming a three-dimensional (3D) object made up of a uniform elastically isotropic material depends on the detailed elastic strains at each point within the object and the 3D elastic Young's modulus E that relates strains to stresses.

However, a simplification can be made for elastic *plates* and *shells*, structures which have a very small extent in one of the three spatial dimensions [5, 12]. Then, it is sufficient to consider the deformation of the middle surface, a two-dimensional manifold. The elastic energy can be described using in-surface strains, which carry an energy penalty set by a two-dimensional (2D) Young's modulus Y, and changes in curvature of the middle surface, penalized by a bending rigidity κ. In terms of the 3D elastic modulus E and Poisson ratio ν of the material making up the shell, the 2D moduli are

$$Y = Eh, \tag{4.1}$$

$$\kappa = \frac{Eh^3}{12(1-\nu^2)}, \tag{4.2}$$

where h is the shell thickness. As a result, the thickness of the shell strongly affects its elastic response. In particular, for extremely thin plates and shells, the h^3-dependence of κ shows that bending is highly favored over stretching, as demonstrated by the ease of bending a piece of paper compared to stretching it.

Whereas thin, flat elastic plates can exhibit pure bending deformations with no associated in-plane stretching and consequently a very low energy cost (the aforementioned sheet of paper being an example), the same is not always true of *shells* which are curved in their undeformed state. In flat plates, the contribution of normal (out-of-plane) deformations of the mid-surface to the in-plane strain is quadratic in the deformation, whereas the contribution to the bending tensor is linear. As a result, the bending energy dominates the elastic penalty of normal deformations of flat plates. In contrast, the underlying curvature of a shell mediates a *linear* coupling between out-of-plane displacements and in-plane strains: any transverse deformation ζ introduces a strain of order ζ/R, where R is the radius of curvature of the shell in its ground state [5]. Thus, bending and stretching are intimately coupled in curved shells, unlike elastic plates and membranes which are flat in

the ground state.

An important consequence of this coupling is that normal deformations tend to be localized to narrow widths in spherical shells. A scaling analysis of the energy density reveals a length scale that sets the extent of characteristic deformations, which is small compared to the shell radius. Consider a deformation of maximum depth ζ localized over a length l in the spherical shell, which has a corresponding curvature change of approximately ζ/l^2 and strain ζ/R. The bending energy per unit area of the deformation is $\kappa\zeta^2/l^4$ while the stretching energy per unit area is $Y\zeta^2/R^2$. Minimizing the sum of the bending and stretching energies with respect to l gives rise to a typical elastic length scale of localization of deformations for which the total elastic energy is minimized,

$$l = \ell \equiv \left(\frac{\kappa R^2}{Y}\right)^{1/4} \equiv \frac{R}{\gamma^{1/4}}, \tag{4.3}$$

where we have introduced the dimensionless *Föppl-von Kármán* number,

$$\gamma \equiv \frac{YR^2}{\kappa} \approx 10\left(\frac{R}{h}\right)^2. \tag{4.4}$$

The Föppl-von Kármán number quantifies the relative importance of stretching to bending for spherical shells. It is large for thin elastic shells. Typically, a shell is considered thin, *i.e.* the abstraction to a two-dimensional surface is valid and shell theory can be used, when $h \lesssim 0.1R$; *i.e.*, $\gamma \gtrsim 1000$. Very large Föppl-von Kármáns are common in both natural and artificial systems. For instance, the radius of a ping-pong ball is about 100 times its wall thickness, leading to $\gamma \approx 10^5$. Typical values for the elastic moduli and radius of curvature of a red blood cell [21] lead to estimates for γ in the range 10^4–10^5. Therefore, typical deformations vary over a length scale ℓ that is much smaller than the radius of the shell. This separation of scales simplifies the theoretical analysis of deformations of spherical shells.

4.1.1 Elastic energy of thin shells

We use the standard Kirchhoff-Love description of thin elastic shells, in which the elastic energy density of the surface is quadratic in two-dimensional strain and curvature tensors [10]. The elastic energy is the sum of a stretching and a bending component,

$$E = \int dS \left[\frac{Y}{2(1-\nu^2)} \cdot \left((u_{11}+u_{22})^2 - 2(1-\nu)(u_{11}u_{22} - u_{12}^2) \right) + \frac{\kappa}{2} \cdot \left((k_{11}+k_{22})^2 - 2(1-\nu)(k_{11}k_{22} - k_{12}^2) \right) \right] \tag{4.5}$$

where the indices i, j label the local coordinate directions tangent to the shell mid-surface, u_{ij} is the 2×2 strain tensor and $k_{ij} = K_{ij} - K_{ij}^0$ the change in the curvature tensor K_{ij} from its initial value K_{ij}^0. The integration is carried out over the mid-surface of the shell. The stress and curvature tensors are defined to vanish when the external pressure vanishes—the equilibrium shape is a sphere of radius R. The initial curvature tensor K_{ij}^0 of the shell mid-surface is that of a sphere with radius R: $K_{ij}^0 = \delta_{ij}/R$ at every point for an orthonormal basis set up in the tangent plane to the sphere at that point.

This expression forms the basis of a discretized model of a thin shell appropriate for numerical simulation (see Appendix E). Upon picking a suitable coordinate system, rewriting the elastic energy expressions in terms of displacement fields and stress functions, and performing a functional minimization with respect to these fields, we obtain the equations of shell theory, which are nonlinear but amenable to analysis using numerical and approximate analytical methods. We use both numerical simulations and a theoretical analysis of the shell theory equations to understand the behavior of inhomogeneous shells.

4.1.2 Shells with soft spots

In our study, we restrict ourselves to a specific inhomogeneity: a thin region with a circular boundary in an otherwise uniform spherical shell. By considering a small region that is

softer than the rest of the shell, we open up the possibility of triggering an instability in the soft region before the shell as a whole collapses. (A stiffer region in the shell would affect the pressure at which the shell collapses, but would not show any additional instabilities before this collapse; we do not consider stiffer regions here.) The thin region, or *cap*, is assumed to be made of the same material as the rest of the shell (the *remainder*), but with a thickness $\tilde{h} < h$ where h is the uniform thickness of the remainder. The elastic moduli in the cap and the remainder are obtained using Eqs. (4.1) and (4.2) with the appropriate thicknesses; the cap is thus easier to bend and stretch than the shell. We treat the cap and the remainder as materially coupled to each other; *i.e.* the displacements, stresses and bending moments are continuous across the boundary between the cap and the shell.

In what follows, we will use $\tilde{Y}, \tilde{\kappa}, ...$ to refer to the properties of the cap and $Y, \kappa, ...$ for the remainder. Without loss of generality, we choose the soft cap to be centered at the north pole, and its size is then defined by the azimuthal angle α (in radians) subtended by its rim. We consider caps small compared to the rest of the shell ($\alpha \lesssim \pi/4$). The dimensionless parameters characterizing the shell are the Föppl-von Kármán number γ (computed using the elastic properties of the *remainder*), the cap-remainder thickness ratio $\tau \equiv \tilde{h}/h < 1$, and the dimensionless size $\lambda \equiv R\alpha/\ell = \alpha\gamma^{1/4}$ (which expresses the radial size of the cap in units of the elastic length scale ℓ of the remainder). Alternatively, one could use the Föppl-von Kármán number and elastic length scale of the cap, which are simply related to the remainder quantities *via* $\tilde{\gamma} = \gamma/\tau^2 > \gamma$, $\tilde{\ell} = \ell\sqrt{\tau} < \ell$.

4.2 Numerical results

We numerically simulate the buckling of shells with soft spots under hydrostatic pressure. (Details of the simulation method are provided in Appendix E.) We restrict ourselves to

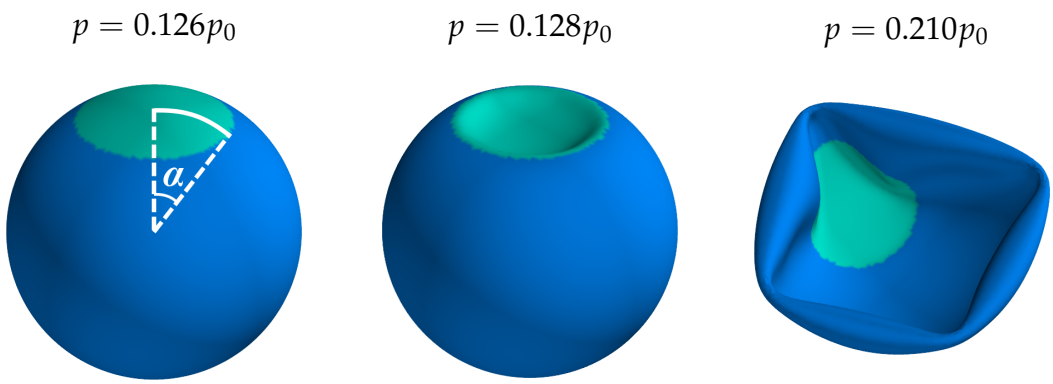

Figure 4.1: Results of a buckling simulation on a shell with $\gamma = 10^4$, $\tau = 0.4$ and cap size $\alpha = 0.52$ (where α is the azimuthal angle subtended by the spot at the center of the undeformed spherical shape), corresponding to $\lambda = R\alpha/\ell = 5.2$. Equilibrium configurations at different pressures, measured in units of the classical buckling pressure of a uniform shell without the soft spot, are shown. The mesh points in the soft region are colored differently from the remainder. The shape of the shell is spherical up to the first buckling pressure $p_{c_1} = 0.128p_0$, when the soft cap snaps through to an inverted shape. This shape is largely unchanged up to the second, more catastrophic buckling event at $p_{c_2} = 0.21p_0$.

a single inhomogeneity in the form of a region with a circular boundary that is thinner than the rest of the shell. In buckling simulations, the pressure is measured in units of the classical buckling pressure $p_0 = 4\sqrt{\kappa Y}/R^2$ of a *uniform* shell [12] with the same thickness as the remainder (see Section 4.4 for more details on the buckling transition for uniform spherical shells).

In a typical simulation, a uniform pressure p is exerted on the shell by adding a volume integral $p \int dV$ to Eq. (4.5), and the local equilibrium configuration of the shell is computed. More generally, p would be the pressure difference between the inside and the outside of the shell; if the shell contains a fluid such as air or water, we assume that it is permeable to the enveloped fluid, thus allowing reductions in volume in response to the pressure. The pressure is initially set to zero, and incremented by a small amount between successive minimization operations. Fig. 4.1 shows the outcome of a simulation on a shell with Föppl-von Kármán number $\gamma = 10^4$, thickness ratio $\tau = 0.4$, and dimensionless spot size $\lambda = 5.2$. At early stages (low pressures) the shell responds *via* a near-uniform con-

traction while maintaining a roughly spherical shape. At a critical value of the pressure, which we call p_{c_1}, the cap experiences a snap-through transition to an inverted shape, although the rest of the shell remains spherical. This shape persists until a higher critical pressure p_{c_2} is reached, at which point the rest of the shell experiences a catastrophic collapse. In real shells, this collapse would be terminated by self-contact of the shell; in our simulations, we introduce a minimum volume restriction of roughly 10% of the original volume to stabilize the collapsed shape, as it is computationally simpler to implement than self-avoidance. For this particular set of parameters, $p_{c_1} = 0.128p_0$ and $p_{c_2} = 0.21p_0$.

This buckling pathway, with two distinct buckling events observed as the pressure is ramped up, is observed over a wide range of values of τ and λ. For future reference, we will call this pathway I. However, for other parameter ranges, different behavior is observed. For modestly thinned caps such that $\tau \gtrsim 0.6$, practically all shells only display *one* buckling transition, a catastrophic collapse from a spherical shape to a fully deflated shape similar to the final shape in Fig. 4.1 without any intermediate range of pressures where only the cap has snapped through. We refer to this as pathway II. There is also a narrow range of parameters, for small values of τ and λ, in which a deformation is observed in the cap before the rest of the shell buckles, but the deformation is a smooth and continuous inversion of the shell as the pressure rises, rather than a sudden snap-through at a particular pressure. For these shells, the collapse of the rest of the shell still happens when a particular pressure is reached. This is termed pathway III in what follows. For both pathway II and pathway III, p_{c_1} refers to the critical pressure at which the lone buckling event occurs, and p_{c_2} is undefined.

Fig. 4.2 summarizes the various buckling pathways for shells with different thickness ratios τ as a function of the dimensionless size $\lambda = \alpha\gamma^{1/4}$ of the soft spot. These results are independent of γ for small spots, as will be shown in the theoretical analysis below. We

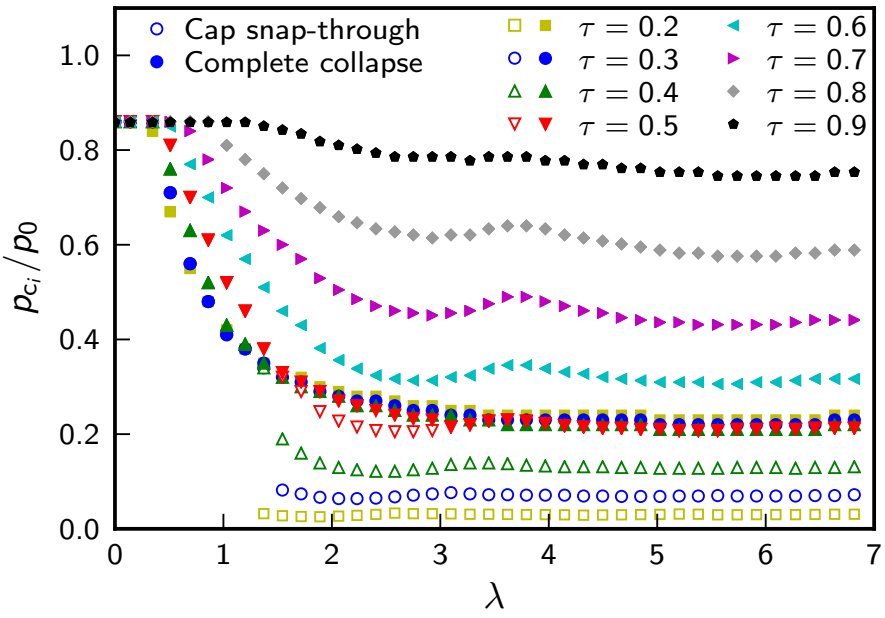

Figure 4.2: Buckling pressures p_{c_1} and p_{c_2} of the first and second buckling events as the pressure is ramped up in numerical simulations, as a function of rescaled cap size for a variety of thickness ratios $\tau = \tilde{h}/h$. The pressure is rescaled by the classical buckling pressure p_0 of a sphere with the same properties as the remainder. In all cases, $\gamma = 10^4$, although the results when expressed with rescaled variables are largely insensitive to γ. Empty symbols signify a snap-through transition localized to the cap, whereas filled symbols signify catastrophic collapse of the entire shell. Some shells exhibit two distinct buckling events—snap-through of the cap at the lower pressure p_{c_1} and collapse of the rest of the shell at the higher pressure p_{c_2}. Other shells display only a single transition, which is always a catastrophic collapse of the whole shell, at the first buckling pressure p_{c_1}. The second buckling pressure p_{c_2} is not defined for these shells.

observe that when the soft spot is extremely thin compared to the rest of the shell ($\tau < 0.5$), pathway I is almost always observed: two distinct buckling events occur at pressures p_{c_1} and p_{c_2}, and there is a range of pressures $p_{c_1} < p < p_{c_2}$ over which the cap has experienced snap-through buckling but the shell is stable against further collapse. The exception is for extremely small spots ($\lambda \lesssim 1.5$) where buckling occurs *via* pathway III with a continuous deformation of the cap from its initial shape to a fully inverted shape, followed by a single catastrophic buckling event at a pressure p_{c_1}. For less drastic thickness changes ($\tau \geq 0.6$), pathway II is almost exclusively observed, *i.e.* a single catastrophic buckling event induces collapse of the entire shell, with no significant deviation from the spherical shape prior to buckling. For $\tau = 0.5$, pathway I is observed in a narrow range of spot sizes $1.5 < \lambda < 3.5$, and pathway II is observed outside this range. Note that, even when the cap size shrinks to zero ($\lambda \to 0$) the critical buckling pressure remains smaller than p_0, the buckling pressure of an ideal shell, due to inevitable small scale inhomogeneities introduced by the amorphous mesh that describes the shell (see Appendix E).

As expected, the snap-through buckling of the cap happens at higher pressures for thicker (*i.e.* stiffer) caps. However, for shells following pathway I ($0.2 \leq \tau \leq 0.5$), the pressure p_{c_2} at which the whole shell collapses has a very weak dependence on the thickness ratio τ. Except for some small deviations at small λ, the pressure of bulk collapse for these thickness ratios seems to follow a near-universal curve of p/p_0 as a function of λ. This trend is in contrast to shells following pathway II ($\tau > 0.5$), for which the pressure associated with large-scale collapse of the shell *does* depend strongly on τ. We also notice an interesting common structure in the p_{c_1}-vs.-λ curves for different thickness ratios, all of which have a distinctive concave-upwards shape with strong variations up to a spot size $\lambda \sim 3$–4 beyond which they level off to a roughly constant value that depends on τ.

To explain these features of the critical pressure function defined by $p = p_{c_1}(\lambda, \tau)$

and $p = p_{c_2}(\lambda, \tau)$, we analyze the various mechanisms that bring about the elastic buckling instability in the following sections.

4.3 Governing equations of shell theory

We begin by summarizing the equations governing the stresses and strains of elastic spherical shells. (A detailed derivation of the results summarized here is provided in Appendix F.) Initially, we consider completely uniform shells. For theoretical analysis, we use *shallow shell theory* [12], where we consider a section of the shell small enough so that slopes relative to a tangent plane at the basal point are small. Then, we set up a Cartesian coordinate system (x, y) in this tangent plane, and describe deformations of the shell in terms of tangential displacement fields $U(x, y), V(x, y)$ and the normal displacement $W(x, y)$. The nonlinear strain tensor is related to the displacements via

$$u_{xx} = U_{,x} + \frac{1}{2}W_{,x}^2 - \frac{W}{R}, \tag{4.6}$$

$$u_{yy} = V_{,y} + \frac{1}{2}W_{,y}^2 - \frac{W}{R}, \tag{4.7}$$

$$u_{xy} = \frac{1}{2}\left(U_{,y} + V_{,x} + W_{,x}W_{,y}\right), \tag{4.8}$$

where we use the notation $f_{,\alpha} \equiv \partial_\alpha f$ for spatial derivatives. The curvature tensor is approximately

$$k_{ij} = W_{,ij}. \tag{4.9}$$

Using these relations in the elastic energy, Eq. (4.5), and minimizing with respect to variations in U, V and W gives rise to three nonlinear equilibrium equations. These can however be reduced to one equilibrium equation and one compatibility condition by introducing a stress function χ, derivatives of which give the 2×2 stress tensor σ_{ij} at every point:

$$\sigma_{xx} = \chi_{,yy}; \quad \sigma_{yy} = \chi_{,xx}; \quad \sigma_{xy} = -\chi_{,xy}. \tag{4.10}$$

In terms of W and χ, the two equations of nonlinear shallow shell theory are

$$\kappa\nabla^4 W - \frac{1}{R}\nabla^2\chi - N_2(\chi, W) = p, \tag{4.11}$$

$$\frac{1}{Y}\nabla^4\chi + \frac{1}{R}\nabla^2 W + \frac{1}{2}N_2(W, W) = 0. \tag{4.12}$$

where

$$\nabla^2 f = f_{,xx} + f_{,yy}, \quad \nabla^4 f = \nabla^2(\nabla^2 f) = f_{,xxxx} + 2f_{,xxyy} + f_{,yyyy}, \tag{4.13}$$

and

$$N_2(f, g) = f_{,xx}g_{,yy} + f_{,yy}g_{,xx} - 2f_{,xy}g_{,xy} \tag{4.14}$$

defines a second-order nonlinear differential operator. Equations (4.11) and (4.12), together with appropriate boundary conditions, govern the deflections and stresses of a uniform shell. The presence of the nonlinear operator makes solving the shallow shell equations subtle and challenging, but they are amenable to analysis through scaling arguments and numerical methods.

4.3.1 Equations in polar coordinates

When dealing with shells with soft caps, it is advantageous to use polar coordinates r, θ rather than x, y, with the origin at the center of the soft region (so that $x = r\cos\theta, y = r\sin\theta$). In polar coordinates, the strain tensor reads

$$u_{rr} = U_{,r} - \frac{W}{R} + \frac{1}{2}W_{,r}^2, \tag{4.15}$$

$$u_{\theta\theta} = \frac{U}{r} + \frac{V_{,\theta}}{r} - \frac{W}{R} + \frac{1}{2}\left(\frac{W_{,\theta}}{r}\right)^2, \tag{4.16}$$

$$u_{r\theta} = \frac{1}{2}\left(\frac{U_{,\theta}}{r} + V_{,r} - \frac{V}{r} + \frac{W_{,r}W_{,\theta}}{r}\right), \tag{4.17}$$

the curvature tensor is

$$k_{rr} = W_{,rr}, \tag{4.18}$$

$$k_{\theta\theta} = \frac{W_{,r}}{r} + \frac{W_{,\theta\theta}}{r^2}, \tag{4.19}$$

$$k_{r\theta} = \frac{W_{,r\theta}}{r} - \frac{W_{,\theta}}{r^2}, \tag{4.20}$$

and stresses are given by

$$\sigma_{rr} = \frac{\chi_{,r}}{r} + \frac{\chi_{,\theta\theta}}{r^2}; \quad \sigma_{\theta\theta} = \chi_{,rr}; \quad \sigma_{r\theta} = \frac{\chi_{,\theta}}{r^2} - \frac{\chi_{,r\theta}}{r}. \tag{4.21}$$

The governing equations remain unchanged [Eqs. (4.11) and (4.12)] but with the differential operators

$$\nabla^2 f = f_{,rr} + \frac{f_{,r}}{r} + \frac{f_{,\theta\theta}}{r^2}, \quad \nabla^4 f = \nabla^2(\nabla^2 f), \tag{4.22}$$

$$N_2(f,g) = f_{,rr}\left(\frac{g_{,r}}{r} + \frac{g_{,\theta\theta}}{r^2}\right) + g_{,rr}\left(\frac{f_{,r}}{r} + \frac{f_{,\theta\theta}}{r^2}\right) - 2\left(\frac{f_{,r\theta}}{r} - \frac{f_{,\theta}}{r^2}\right)\left(\frac{g_{,r\theta}}{r} - \frac{g_{,\theta}}{r^2}\right). \tag{4.23}$$

4.4 Buckling of uniform spherical shells under pressure

In preparation for our analysis of nonuniform shells, we review here the buckling of *uniform* spherical shells under external pressure, following the approach in Ref. [39]. The classical buckling of spherical shells can be understood using a linearized analysis of the shell equations.

Prior to buckling, a consideration of the forces on a section of the shell shows that the shell contracts uniformly by an amount $W_0 = pR^2(1-\nu)/2Et$ and is in a uniform state of compressive stress $\sigma_{xx} = \sigma_{yy} = -pR/2$, corresponding to an Airy stress function $\chi_0 = -pR(x^2+y^2)/4$. The buckling mode can be obtained by linearizing the nonlinear shell equations around this pre-stressed state. Upon substituting $W = W_0 + W_1$ and $\chi = \chi_0 + \chi_1$ in Eq. (4.34) and keeping terms linear in the normal displacement W_1 and Airy

function χ_1, we find:

$$\kappa\nabla^4 W_1 - \frac{1}{R}\nabla^2\chi_1 + \frac{pR}{2}\nabla^2 W_1 = 0, \tag{4.24}$$

$$\nabla^4\chi_1 + \frac{Y}{R}\nabla^2 W_1 = 0. \tag{4.25}$$

The nonlinear coupling between the pre-stress and the normal deflection *via* the term $N_2(\chi_0, W_1)$ is responsible for the last term on the left-hand side of Eq. (4.24). We search for oscillatory solutions of the form $W_1 = Ae^{i\mathbf{q}\cdot\mathbf{x}}$, $\chi_1 = Be^{i\mathbf{q}\cdot\mathbf{x}}$ with some two-dimensional wavevector $\mathbf{q} = (q_x, q_y)$. Such a solution to Eqs. (4.24) and (4.25) can only exist provided

$$\kappa q^4 - \frac{pR}{2}q^2 + \frac{Y}{R^2} = 0, \tag{4.26}$$

with the requirement for oscillatory solutions being that the wavevector magnitude $q \equiv \sqrt{\mathbf{q}\cdot\mathbf{q}}$ is real and positive. The smallest value of p at which solutions with $q^2 > 0$ exist is $p = 4\sqrt{\kappa Y}/R^2 \equiv p_0$, and the corresponding wavevector magnitude of the solution that arises is $q = 1/\ell = \gamma^{1/4}/R$. This pressure is identified as the buckling pressure of the shell. Note that the instability would not exist without the coupling between χ_0 and W_1 mentioned above, and is a nonlinear effect even though it is captured by a linearized analysis.

The linearized buckling analysis shows that a uniform shell which contracts isotropically under low external pressures can release this compressive stress, at the cost of bending energy, by taking on an oscillatory transverse deflection. Such a deflection becomes energetically favorable at the pressure $p_0 = 4\sqrt{\kappa Y}/R^2$. In fact, there are many degenerate deflection modes that arise at this critical pressure, since all wavevectors $\mathbf{q}$ such that $q = |\mathbf{q}| = 1/\ell$ are allowed. The wavelength associated with these modes is $2\pi\ell = 2\pi R/\gamma^{1/4} \ll R$ since $\gamma \gg 1$ for thin shells. Thus, the buckling of spherical shells is triggered by one of many degenerate modes with wavelength much smaller than the shell

radius.

We have not established here that the oscillatory modes that arise at the buckling pressure are unstable toward further growth. This can be done by evaluating higher order terms in the elastic energy associated with the modes (see e.g. Ref. [12]). We do not reproduce that calculation here, but instead present a qualitative argument for the ultimate fate of the shell at the buckling pressure, from Ref. [5], which considers the energetics of inversions of sections of the shell. Thin spherical shells under pressure find it favorable to reduce their volume using nearly isometric inversions, which leave the metric within most of the inverted region unchanged and localize the elastic energy to the narrow rim of the inversion (which has a width of order ℓ). The energy associated with an inversion of depth d is characterized by a quantity we denote the Pogorelov energy [5, 31],

$$E_{\mathrm{el}} = c\kappa\gamma^{1/4}(d/R)^{3/2}, \tag{4.27}$$

where c is a dimensionless constant. (See Appendix A for the derivation of this scaling form.) If the shell is under external pressure p, the net energy including the work done by the pressure is $E = E_{\mathrm{el}} + p\Delta V$, where $\Delta V \sim -Rd^2$ is the volume change due to the inversion. We immediately see that at large values of inversion depth d, the second term dominates, and inversions can reduce their net energy by growing even deeper. The total energy $E(d)$ has a maximum when

$$\kappa\gamma^{1/4}\frac{d^{1/2}}{R^{3/2}} \sim pRd \Rightarrow \frac{d_{\max}}{R} \sim \left(\frac{\kappa}{pR^3}\right)^2\sqrt{\gamma}. \tag{4.28}$$

Therefore, for a particular pressure, inversions of depth $d > d_{\max}(p)$ grow uncontrollably, until some other constraint such as self-contact prevents further growth of the inversion. At the buckling pressure, $d_{\max}(p_0) \sim R/\sqrt{\gamma} \sim h$; thus, even an inversion of very small depth, comparable to the thickness h of the shell, is unstable to growth. Pogorelov's picture can be reconciled with the linear stability analysis sketched above as follows: the

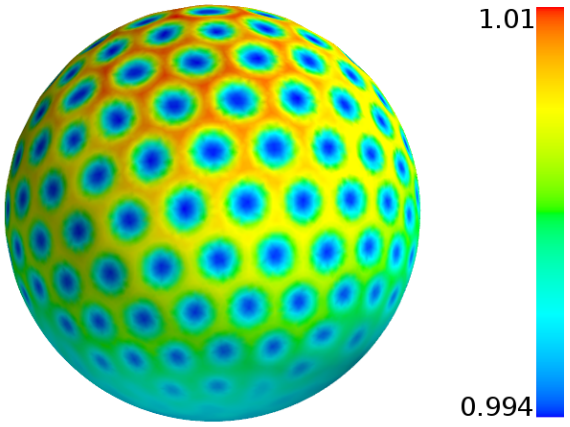

Figure 4.3: Simulation of a uniform shell with large Föppl-von Kármán number ($\gamma = 10^6$) under an external pressure above the buckling transition, and an inner ball of radius $R_{\text{inner}} = 0.99R$ that repels all mesh points with a steep repulsive potential. The repulsive potential prevents vertices from moving closer than a small amount to the center of the sphere, thus arresting the oscillatory buckling mode. The mesh is colored by the distance of each point from the center in units of R, to highlight small differences. Note the periodic array of indentations with amplitudes that vary slowly over the surface.

oscillatory buckling modes that arise at the buckling pressure can be thought of as many tiny inversions covering the entire sphere; any one of these inversions can grow uncontrollably, giving rise to the characteristic inverted shape of a buckled spherical shell. Thus the buckling mode is a transient, and the final buckled shape of the shell displays one or more large inversions that significantly reduce the enclosed volume of the shell, very similar to the final configuration in Fig. 4.1. These large inversions with depth comparable to the shell radius have additional features, such as the sharp points of stress focusing, that deviate from the Pogorelov isometric inversion, but the associated scaling of the elastic energy with depth is hardly changed [32, 30].

The transient buckling mode can only be observed in real shells by arresting its uncontrolled growth. This has been done for metallic thin shells by buckling a shell that

encloses a solid ball of slightly smaller radius: the deformed shell contacts the inner ball when the buckling mode arises, arresting it so it can be visualized [24]. We can replicate this remarkable experiment in our simulations by including a steep repulsive potential within the mesh and ramping up the external pressure until the shell buckles, at which point the internal repulsive potential prevents the unstable mode from growing uncontrollably. The result is shown in Fig. 4.3, showing the small-wavelength buckling pattern that extends over the shell.

4.5 Snap-through of soft caps

We now turn to the shells with soft spots, numerically investigated in Section 4.2. The radius of the soft spot, measured along a sphere geodesic, is $r_0 \equiv R\alpha$. We expect large changes in the buckling due to external pressure whenever $r_0 > \ell = R/\gamma^{1/4}$, the elastic length; *i.e.* $\lambda = (r_0/R)\gamma^{1/4} > 1$. Indeed, unless $\lambda \ll 1$, the soft spot will substantially influence the mechanics of the shell and, in particular, be the first region responding to the external pressure by either deforming continuously or by snap-through buckling when a threshold pressure is reached. The influence of the cap on the remainder is only expected to extend over a narrow region of width ℓ into the area occupied by the remainder. As a result, we expect the equations of shallow shell theory to also accurately describe the stresses in the remainder for small soft caps. We use polar coordinates, locating the origin at the center of the cap. We then have two sets of equations, one for the cap (with fields $\tilde{W}, \tilde{\chi}$ and elastic moduli $\tilde{Y}, \tilde{\kappa}$) when $r < R\alpha$ and one for the remainder (with fields W, χ and elastic moduli Y, κ) when $r > R\alpha$. The fields are related by matching displacements, stresses and moments at the boundary, $r = R\alpha$.

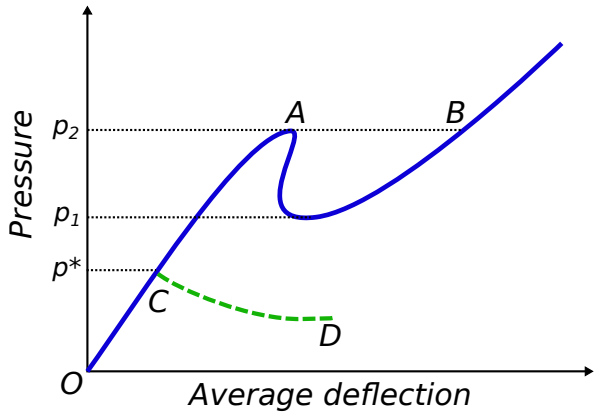

Figure 4.4: Representative pressure-deflection curve for a clamped shallow spherical cap (after Ref. [95]). The deflection is averaged over the area of the cap [see Eq. (4.29)]. Upon increasing the pressure, the average deflection jumps from A to B at the pressure p_2. The green dashed curve CD that branches off at p^* corresponds to a nonaxisymmetric deformation.

4.5.1 Mechanism for snap-through buckling

In the limit of an infinitely stiff remainder ($\tau = \tilde{h}/h \to 0$), all displacements along the cap boundary are restricted, and by continuity of slopes the slope of the cap shape at the boundary is fixed to be α. This limit corresponds to the problem of buckling of an elastic cap, clamped along the entire edge to restrict all deformations, under hydrostatic pressure. The buckling of clamped caps is a well-studied problem in shell theory, with a definitive numerical analysis conducted by Huang [95]. We expect that the snap-through buckling of caps embedded in thin shells with a stiff remainder follows a similar mechanism, which we summarize here.

At each value of pressure, one or more equilibrium solutions may exist for the fields within the cap. The signature of loss of stability under pressure is seen in the pressure-deflection curve associated with these solutions, qualitatively illustrated in Fig. 4.4 (after Ref. [95]). The curve OAB in Fig. 4.4 shows a representative pressure-deflection re-

lation for axisymmetric deflections. At low enough pressures, an analysis of the linearized equations shows that the cap deforms axisymmetrically and the deflection averaged over the cap,

$$\bar{\tilde{W}} = \frac{\int_0^{r_0} r\tilde{W}(r)\,dr}{\int_0^{r_0} r\,dr}, \tag{4.29}$$

grows with pressure ($r_0 = R\alpha$ is the radius of the soft spot boundary). At higher pressures, however, nonlinear effects become important, and the governing equations of the cap admit multiple solutions that satisfy the boundary conditions. In the range $p_1 < p < p_2$, for instance, three solutions exist at each pressure. When this happens, the pressure-deflection relation is no longer single-valued. With increasing pressure, at the maximum point A where two of the solutions merge, the cap deflection jumps directly to point B, signifying axisymmetric snap-though at pressure p_2. A subsequent slow decrease in pressure leads to a "snap-back" in the shape at the pressure p_1. We study this mechanism for caps embedded in spherical shells in Section 4.5.5.

However, for caps beyond a certain size, a *non*-axisymmetric deflection mode may appear at a lower pressure p^*, with as a pressure-deflection relation of the form of the dashed line in Fig. 4.4. Unlike the axisymmetric mode, the nonaxisymmetric deflection modes are highly degenerate. A stability analysis of such modes in shallow shells [12] shows that there is no stable shape in the vicinity of such a state; *i.e.* the slope of the curve CD is indeed negative at C. Therefore, the appearance of a nonaxisymmetric mode at $p^* < p_2$ triggers snap-through buckling of the cap to an inverted shape *via* the path OCD. In Fig. 4.4, we show $p^* < p_1$ for clarity, although this inequality need not hold in general. We consider the nonaxisymmetric buckling mode for our caps in Section 4.5.4. In our analysis, we assume that the appearance of a nonaxisymmetric deflection in the cap immediately triggers snap-through buckling of the cap, which is the case for clamped caps [95].

4.5.2 Non-dimensionalizing the equations

Since the snap-through of the cap is primarily determined by the deflections and stresses in the cap itself, we rescale all quantities with physical parameters that depend on the elastic properties of the cap. We define the nondimensional radial coordinate and pressure:

$$s = \frac{r}{\tilde{\ell}}, \tag{4.30}$$

$$\eta = \frac{p}{\tilde{p}_0} = \frac{pR^2}{4\sqrt{\tilde{\kappa}\tilde{Y}}}, \tag{4.31}$$

where $\tilde{\ell} = R/\tilde{\gamma}^{1/4}$ and $\tilde{p}_0 \equiv 4\sqrt{\tilde{\kappa}\tilde{Y}}/R^2$ is the classical buckling pressure associated with a uniform spherical shell with the elastic properties of the cap. We also define the rescaled fields in both the cap and the remainder

$$\tilde{w} = \frac{R}{\tilde{\ell}^2}\tilde{W}, \quad \tilde{\phi} = \frac{R^2}{\tilde{Y}\tilde{\ell}^4}\tilde{\chi}; \tag{4.32}$$

$$w = \frac{R}{\tilde{\ell}^2}W, \quad \phi = \frac{R^2}{\tilde{Y}\tilde{\ell}^4}\chi. \tag{4.33}$$

Upon substituting these quantities into the shell equations [Eqs. (4.11) and (4.12)], we obtain the following nondimensional equations for the cap:

$$\nabla^4\tilde{w} - \nabla^2\tilde{\phi} - N_2(\tilde{\phi}, \tilde{w}) = 4\eta, \tag{4.34}$$

$$\nabla^4\tilde{\phi} + \nabla^2\tilde{w} + \frac{1}{2}N_2(\tilde{w}, \tilde{w}) = 0, \tag{4.35}$$

and for the remainder:

$$\frac{1}{\tau^3}\nabla^4 w - \nabla^2\phi - N_2(\phi, w) = 4\eta, \tag{4.36}$$

$$\tau\nabla^4\phi + \nabla^2 w + \frac{1}{2}N_2(w, w) = 0, \tag{4.37}$$

where the differential operators are now defined using the variables (s, θ) rather than (r, θ).

From this analysis, we see that when cap size is rescaled by the elastic length scale $\tilde{\ell}$ and pressure by the classical buckling pressure $\tilde{p}_0$, the dependence on elastic moduli

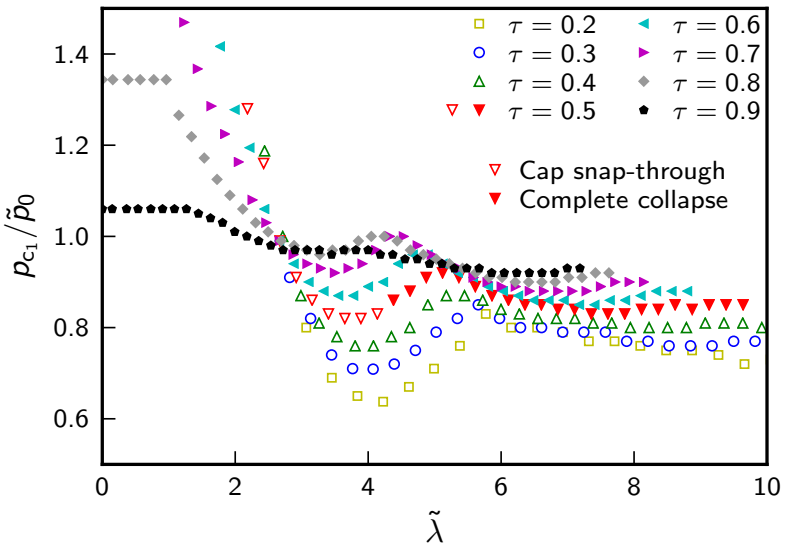

Figure 4.5: Reduced pressure $p_{c_1}/\tilde{p}_0$ of the first buckling event, whether a snap-through of the cap (for shells following buckling pathway I, empty symbols), or a catastrophic collapse of the whole shell (buckling pathways II and III, filled symbols), as a function of the dimensionless spot size $\tilde{\lambda} = \alpha\tilde{\gamma}^{1/4}$ in buckling simulations on shells with $\gamma = 10^4$. The data shown is the same as for the first buckling event in Fig. 4.2, but is rescaled using the cap parameters $\tilde{p}_0$ and $\tilde{\lambda}$ rather than the shell parametersp_0 and λ.

drops out, and caps of vastly different properties but the same thickness ratio τ relative to the remainder of the shell can be described by just two dimensionless quantities $\tilde{\lambda} = R\alpha/\tilde{\ell}$ and $\eta = p/\tilde{p}_0$ (as long as they are small enough that shallow shell theory applies).

Fig. 4.5 plots the pressure of the *first* buckling transition $\eta_{c_1} = p_{c_1}/\tilde{p}_0$ (whether it corresponds to a snap-through transition of the cap as for $\tau < 0.5$, or a collapse of the whole shell as for $\tau > 0.5$), as a function of the parameters τ and $\tilde{\lambda}$. When compared to Fig. 4.2, we see that the buckling pressures, when rescaled using $\tilde{p}_0$, vary over a much smaller range and display similar behavior as τ is changed. This observation suggests that the first buckling transition of the shell is always a snap-through transition of the cap, and that the mechanism of the snap-through does not vary significantly as τ is changed. Indeed, all of the η_{c_1}-vs.-$\tilde{\lambda}$ curves for the buckling pressure share similar characteristics

for the dependence of buckling pressure on cap size: there is an apparent kink in the range $5 < \tilde{\lambda} < 6$ that separates a convex dependence for smaller caps from a roughly constant dependence for larger caps. A similar feature is seen in the buckling pressure curve for *clamped* caps, *i.e.* shallow sections of spheres with clamped circular edges under pressure [95]. In that case, the kink separates values of $\tilde{\lambda}$ for which the buckling mode is *axisymmetric i.e.* with no circumferential angular dependence about the z axis, from $\tilde{\lambda}$ values for which the buckling is nonaxisymmetric and has some circumferential variation. Furthermore, no snap-through buckling is observed for clamped caps with $\tilde{\lambda} < 3.3$; below this size the cap deforms continuously as the pressure is increased. This is similar to the present case with shells that follow buckling pathway III, where no snap-through buckling of the cap is observed.

We first use our numerical results to test whether the structure of the η_{c_1}-vs.-$\tilde{\lambda}$ curves is linked to the buckling mode. We investigate the nature of the buckling mode that drives the snap-through of the cap by arresting its growth with an internal repulsive potential, as was done for the uniform sphere in Section 4.4. Fig. 4.6 illustrates the buckling mode that drives snap-through of the cap, as the cap size is varied for a shell with $\gamma = 10^4$ and $\tau = 0.4$. For small caps, the buckling mode is axisymmetric, whereas for large caps, it has a periodic structure in the circumferential direction, similar to the situation for clamped caps [95]. The nature of the buckling mode changes from axisymmetric to nonaxisymmetric around $\tilde{\lambda} = 5$, which corresponds to the kink in the η_{c_1}-vs.-$\tilde{\lambda}$ curve for $\tau = 0.4$ (see Fig. 4.5). The number of nodes in the circumferential direction then increases with cap size, although the wavelength of the buckling mode itself is hardly changed from an intrinsic size of order $\tilde{\ell}$. The dependence of the buckling pressure on cap size $\tilde{\lambda}$ in the nonaxisymmetric region is also weak.

This structure is retained for other values of τ, although the $\tilde{\lambda}$-value of the tran-

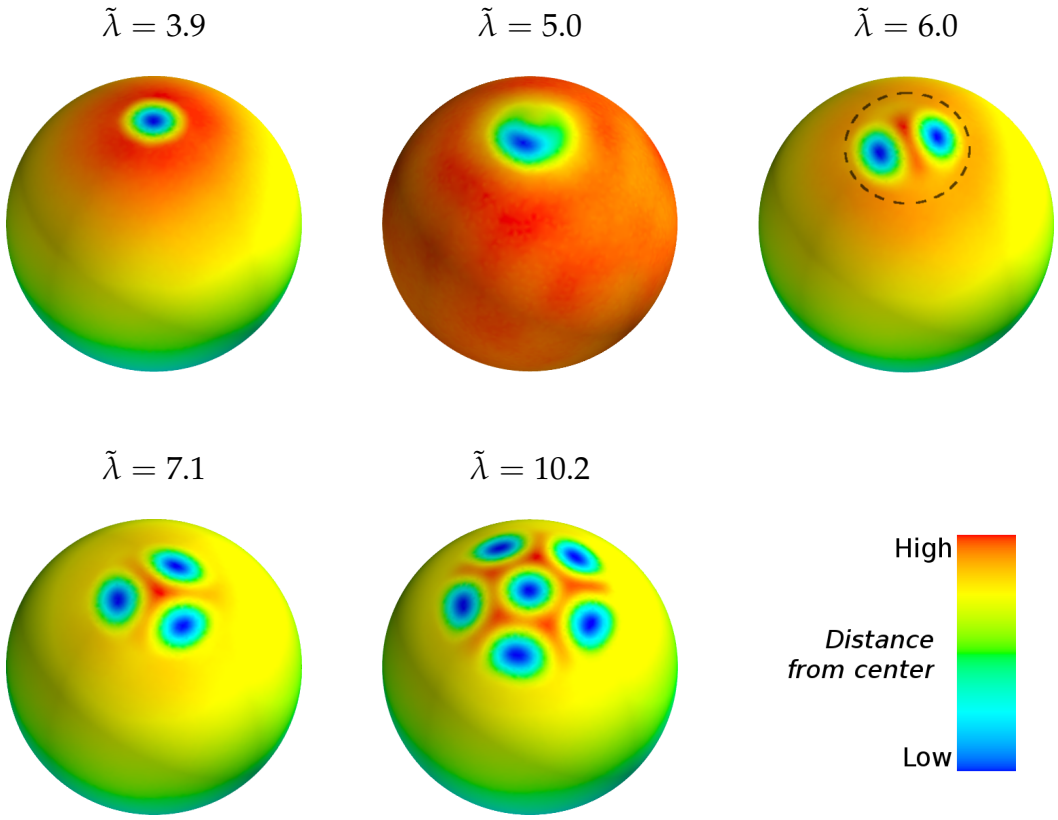

Figure 4.6: (a) Mode for snap-through buckling of a soft cap, for shells with $\gamma = 10^4$, $\tau = 0.4$, and various dimensionless cap sizes $\tilde{\lambda} = \alpha\tilde{\gamma}^{1/4}$. The buckling mode was arrested in numerical simulations by including an inner ball of radius $R_{\text{inner}} = 0.99R$ whose surface repels all mesh points with a steep repulsive potential. The mesh is colored by the distance of each point from the center of the sphere on a linear color scale, to highlight small differences. The soft region coincides with the region of large variations in deflection at the top of each shell—as an illustration, the dashed line shows the boundary of the soft region for the shell with $\tilde{\lambda} = 6.0$.

sition from axisymmetric to nonaxisymmetric buckling falls as τ approaches the uniform shell limit, $\tau = 1$. The roughly constant value of η_{c_1} for nonaxisymmetric buckling also approaches 1 as $\tau \to 1$, which is expected because buckling of a uniform shell with the thickness of the cap would happen at $\eta = 1$.

4.5.3 Analysis of linearized equations

The buckling of the cap is a nonlinear phenomenon, that arises due to the coupling terms in the shell equations [Eqs. (4.34)–(4.37)], which puts an exact analytical study out of reach. However, we can gain some insight about the behavior under pressure and the approach to buckling by linearizing the equations about some appropriate state of stress to get the so-called *Reissner* equations of shallow-shell theory [97, 98]. We saw in section 4.4 that a uniform shell contracts uniformly up to the point of buckling; we can expand deflections and stresses about this state of uniform pre-stress.

In the cap, the rescaled uniform radial deflection $\tilde{w}_0 = 2\eta(1-\nu)$ and Airy function $\tilde{\phi}_0 = -s^2\eta$ solve the shell equations exactly. Upon substituting $\tilde{w} = \tilde{w}_0 + \tilde{w}_1$ and $\tilde{\phi} = \tilde{\phi}_0 + \tilde{\phi}_1$ in Eqs. (4.34) and (4.35) and keeping terms linear in $\tilde{w}_1$ and $\tilde{\phi}_1$, we get the Reissner equations within the cap:

$$\nabla^4 \tilde{w}_1 + 2\eta \nabla^2 \tilde{w}_1 - \nabla^2 \tilde{\phi}_1 = 0, \tag{4.38}$$

$$\nabla^4 \tilde{\phi}_1 + \nabla^2 \tilde{w}_1 = 0, . \tag{4.39}$$

General axisymmetric solutions to the differential equations that satisfy the requirement of continuous and finite stresses at the origin are written in terms of real and imaginary

parts of J_0, the Bessel function of the first kind:

$$\tilde{w}_1(s) = c_1 \left[J_{\mathrm{R}}(s) + \frac{\eta}{\sqrt{1-\eta^2}} J_{\mathrm{I}}(s) \right] + c_2 \left[J_{\mathrm{I}}(s) - \frac{\eta}{\sqrt{1-\eta^2}} J_{\mathrm{R}}(s) \right] + c_3, \tag{4.40}$$

$$\tilde{\phi}_1(s) = \frac{1}{\sqrt{1-\eta^2}} \left[c_1 J_{\mathrm{I}}(s) - c_2 J_{\mathrm{R}}(s) \right], \tag{4.41}$$

where

$$J_{\mathrm{R}}(s) \equiv \mathrm{Re}[J_0(\tilde{\rho} s)]; \quad J_{\mathrm{I}}(s) \equiv \mathrm{Im}[J_0(\tilde{\rho} s)]; \quad \tilde{\rho} \equiv \left(\eta + i\sqrt{1-\eta^2} \right)^{1/2}. \tag{4.42}$$

Similarly, substituting $w = w_0 + w_1$ and $\phi = \phi_0 + \phi_1$, where $w_0 = 2\eta(1-\nu)\tau$ and $\phi_0 = -s^2\eta$, into the nonlinear equations for the remainder [Eqs. (4.36)–(4.37)], and keeping terms linear in w_1 and ϕ_1, gives the Reissner equations for the remainder:

$$\frac{1}{\tau^3} \nabla^4 w_1 + 2\eta \nabla^2 w_1 - \nabla^2 \phi_1 = 0, \tag{4.43}$$

$$\tau \nabla^4 \phi_1 + \nabla^2 w_1 = 0. \tag{4.44}$$

In the remainder, we look for solutions to the deflection and stress that decay to zero as $s \to 0$. These can can be written in terms of $H_0^{(1)}$, the Hankel function of the first kind:

$$w_1(s) = c_4 \left[H_{\mathrm{R}}(s) + \frac{\eta\tau^2}{\sqrt{1-\eta^2\tau^4}} H_{\mathrm{I}}(s) \right] + c_5 \left[H_{\mathrm{I}}(s) - \frac{\eta\tau^2}{\sqrt{1-\eta^2\tau^4}} H_{\mathrm{R}}(s) \right], \tag{4.45}$$

$$\phi_1(s) = \frac{1}{\tau^2\sqrt{1-\eta^2\tau^4}} [c_4 H_{\mathrm{I}}(s) - c_5 H_{\mathrm{R}}(s)], \tag{4.46}$$

where

$$H_{\mathrm{R}}(s) \equiv \mathrm{Re}[H_0^{(1)}(\rho s)]; \quad H_{\mathrm{I}}(s) \equiv \mathrm{Im}[H_0^{(1)}(\rho s)]; \quad \rho \equiv \left(\tau^3\eta + i\tau\sqrt{1-\eta^2\tau^4} \right)^{1/2}. \tag{4.47}$$

At the boundary we require continuity of the transverse deflection W and its first derivative $W_{,r}$, the radial displacement $U = r(u_{\theta\theta} + W/R)$ [or equivalently the strain component $u_{\theta\theta} = (\chi_{,rr} - \nu\chi_{,r}/r)/Y$], the radial stress $\sigma_{rr} = \chi_{,r}/r$, and the bending moment $M_{rr} = -\kappa(W_{,rr} + \nu W_{,r}/r)$. The resulting dimensionless equations, to be satisfied at the cap

edge $s = \tilde{\lambda}$, are:

$$\tilde{w} = w, \quad \tilde{w}_{,s} = w_{,s}, \quad \tilde{\phi}_{,s} = \phi_{,s}; \tag{4.48}$$

$$\tilde{\phi}_{,ss} - \nu\frac{\tilde{\phi}_{,s}}{\tilde{\lambda}} = \tau\left(\phi_{,ss} - \nu\frac{\phi_{,s}}{\tilde{\lambda}}\right); \tag{4.49}$$

$$\tau^3\left(\tilde{w}_{,ss} + \nu\frac{\tilde{w}_{,s}}{\tilde{\lambda}}\right) = \left(w_{,ss} + \nu\frac{w_{,s}}{\tilde{\lambda}}\right). \tag{4.50}$$

Note that the non-constant components $\tilde{w}_1, w_1, \tilde{\phi}_1, \phi_1$ must be nonzero for $\eta > 0$ since $\tilde{w}_0 \neq w_0$, $\tilde{\phi}_{0,s} \neq \phi_{0,s}$. For each pair of $\{\eta, \tilde{\lambda}\}$ values, the boundary conditions give rise to five linear equations which can be solved for the five constants $c_1 ... c_5$. We will call the result the *Reissner solution* for the deflection and stresses in the cap and the remainder.

Fig. 4.7 compares the solution of the Reissner equations to the transverse deflection from simulations for a few shells, with η values below the buckling threshold. The linearized solutions capture many features of the full solution, particularly in the vicinity of the boundary between the cap and the remainder and the period of the decaying oscillations in the cap.

4.5.4 Nonaxisymmetric buckling

The solution of the linearized equations is sufficient to obtain a qualitative understanding of the nonaxisymmetric buckling of large caps, which we have seen is largely independent of the cap size $\tilde{\lambda}$ for each value of τ. Fig. 4.8 shows the behavior of the axisymmetric Reissner solution for $\eta = 0.8$, close to the snap-through pressure, for caps of various sizes and thickness ratios relative to the remainder. This is expected to approximate the axisymmetric deflection of the shell before the nonaxisymmetric mode appears and causes the cap to snap through. From Fig. 4.8(a), we see that the solution develops a boundary layer which does not change significantly when $\tilde{\lambda} > 10$; the solutions for large cap size are related to each other by a simple shift along the r axis. (Clamped caps display a similar behav-

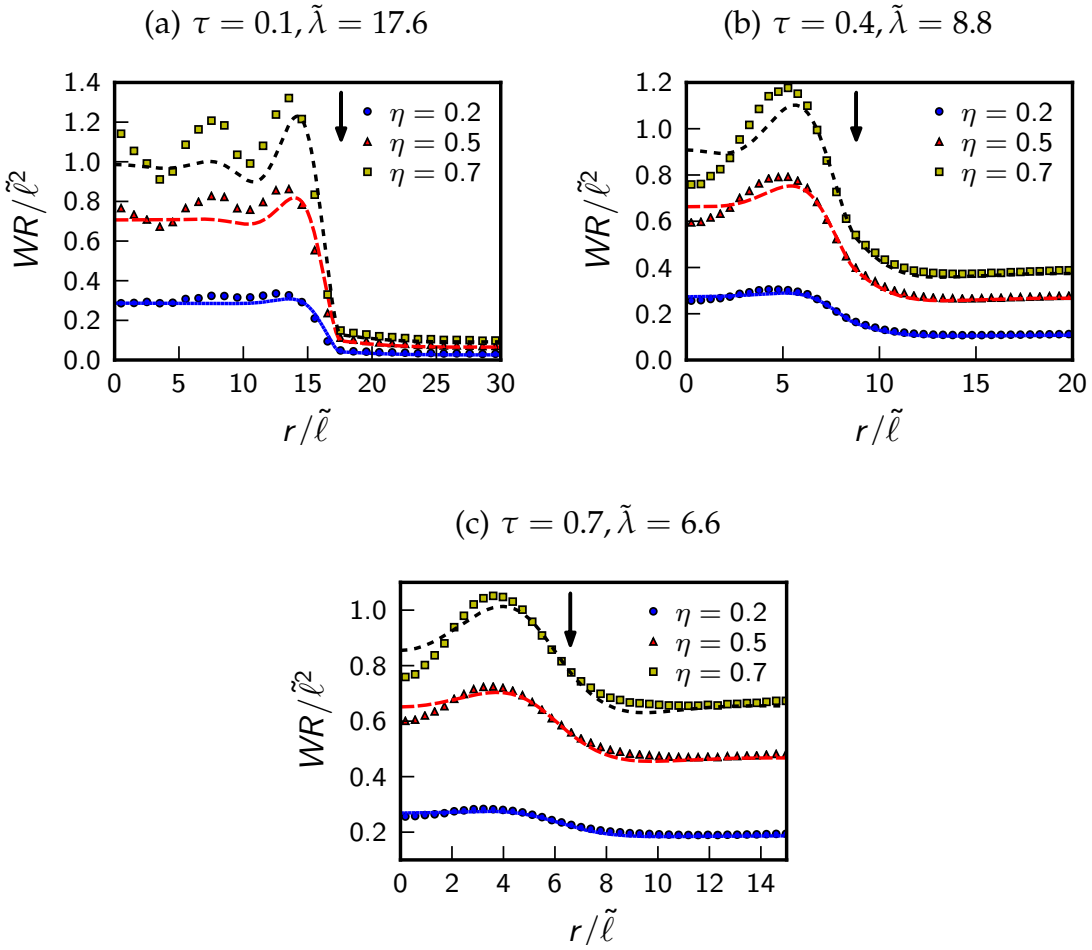

Figure 4.7: Comparison of the scaled normal deflection $WR/\tilde{\ell}^2$ as a function of radial position $r/\tilde{\ell}$ measured from simulations with an amorphous mesh (symbols), to the solution of the linearized shell equations (lines), for different values of the reduced pressure η. The values from simulations are obtained by averaging the positions of all mesh points sharing each r value (*i.e.* over all values of θ for each value of r). The three subfigures (a–c) correspond to three different shells, all with $\gamma = 10^4$ and cap angle $\alpha = \cos^{-1}(0.85)$, but with different cap-to-shell thickness ratios τ which changes the elastic length $\tilde{\ell}$ and therefore the dimensionless cap size $\tilde{\lambda} = R\alpha/\tilde{\ell}$. The vertical arrows indicate the r position of the boundary between the soft cap and the remainder. All three shells buckle around $\eta = 0.8$.

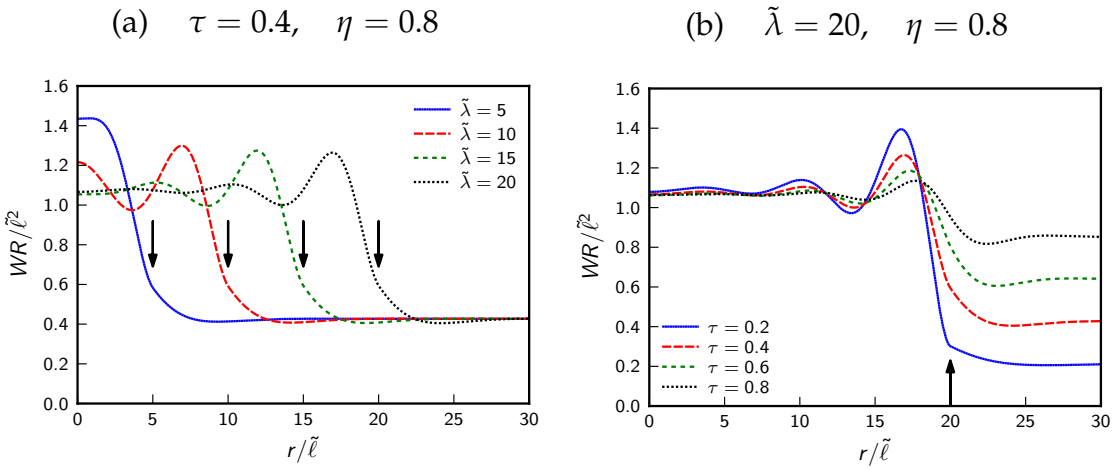

Figure 4.8: Reissner solution for the scaled normal deflection $WR/\tilde{\ell}^2$ for caps with (a) increasing cap size $\tilde{\lambda}$ at constant pressure η and thickness ratio τ, and (b) increasing thickness ratio at constant pressure and cap size. The vertical arrows indicate the r position of the boundary between the soft cap and the remainder.

ior [95].) Since the stresses are also largest in this region close to the cap-shell boundary, the behavior here dominates the buckling transition. It is likely that the relative insensitivity of the buckling pressure to the cap size for large caps is a consequence of boundary layer dominance.

To quantify this effect, we estimate the coupling between the excess stresses due to the boundary and any nonaxisymmetric mode that may arise. Recall that for uniform shells, the nontrivial buckling mode arose due to the coupling between gradients of the transverse displacement W_1 and the uniform pre-stress $\sigma_{xx} = \sigma_{yy} = -pR/2$ (section 4.4). Now we have an axisymmetric pre-stress $\{\tilde{w}_a, \tilde{\phi}_a\}$ that varies in the r direction, which couples to nonaxisymmetric fields $\{\tilde{w}_n, \tilde{\phi}_n\}$ which we shall assume small. We substitute $\tilde{w} = \tilde{w}_a + \tilde{w}_n$ and $\tilde{\phi} = \tilde{\phi}_a + \tilde{\phi}_n$ into the full nonlinear shell equations [Eqs. (4.34)–(4.35)] and keep terms linear in the nonaxisymmetric fields. For simplicity, we work in scaled Cartesian coordinates at a position on the x axis near the cap-shell boundary, so that $\tilde{w}_a(s) \approx \tilde{w}_a(x)$, and $x \approx \tilde{\lambda} \gg 1$ which means that the θ direction coincides approximately

with the y direction. Then the nonlinear coupling gives rise to terms of the form $\tilde{w}_{a,xx}\tilde{\phi}_{n,yy}$, $\tilde{\phi}_{a,xx}\tilde{w}_{a,yy}$ and $\tilde{w}_{a,xx}\tilde{w}_{n,yy}$. The equations for $\tilde{w}_n$ and $\tilde{\phi}_n$ now read

$$\nabla^4\tilde{w}_n - \nabla^2\tilde{\phi}_n - \tilde{w}_{a,xx}\tilde{\phi}_{n,yy} - \tilde{\phi}_{a,xx}\tilde{w}_{a,yy} = 0, \tag{4.51}$$

$$\nabla^4\tilde{\phi}_n + \nabla^2\tilde{w}_n + \tilde{w}_{a,xx}\tilde{w}_{n,yy} = 0. \tag{4.52}$$

For the uniform shell, only $\tilde{\phi}_{a,xx} = -2\eta$ was nonzero, but the presence of the cap-remainder boundary gives rise to a spatially varying $\tilde{w}_n$ and thus a nonzero $\tilde{w}_{a,xx}$ as well. In fact, $\tilde{\phi}_{a,xx} \approx -2\eta$ remains a good approximation to the pre-buckling Airy stress function in the cap, so the additional effects which bring down the buckling pressure below $\eta = 1$ are mainly due to the new coupling with $\tilde{w}_{a,xx}$. Let ξ denote a typical value of $\tilde{w}_{a,xx}$ in the boundary layer region. A rough estimate of its effect can be obtained from the equations

$$\nabla^4\tilde{w}_n - \nabla^2\tilde{\phi}_n - \xi\tilde{\phi}_{n,yy} + 2\eta\tilde{w}_{a,yy} = 0, \tag{4.53}$$

$$\nabla^4\tilde{\phi}_n + \nabla^2\tilde{w}_n + \xi\tilde{w}_{n,yy} = 0. \tag{4.54}$$

Similar in spirit to the stability calculation for uniform shallow shells, we look for solutions that oscillate in the y direction of the form $\tilde{w}_n, \tilde{\phi}_n \propto e^{iqy}$, which leads to the eigenvalue equation

$$q^4 - 2\eta q^2 + (1+\xi)^2 = 0. \tag{4.55}$$

Therefore, oscillatory solutions with $q^2 > 0$ exist only if

$$\eta > 1 + \xi. \tag{4.56}$$

According to this argument, regions of the axisymmetric deflection with negative curvature in the radial direction, $\xi \sim \tilde{w}_{a,ss} < 0$, cause nonaxisymmetric modes to appear at $\eta \approx 1 + \xi < 1$. The Reissner solution, as well as the full nonlinear solution, display these regions prominently in the boundary region near the cap-shell boundary (see Figs. 4.7 and

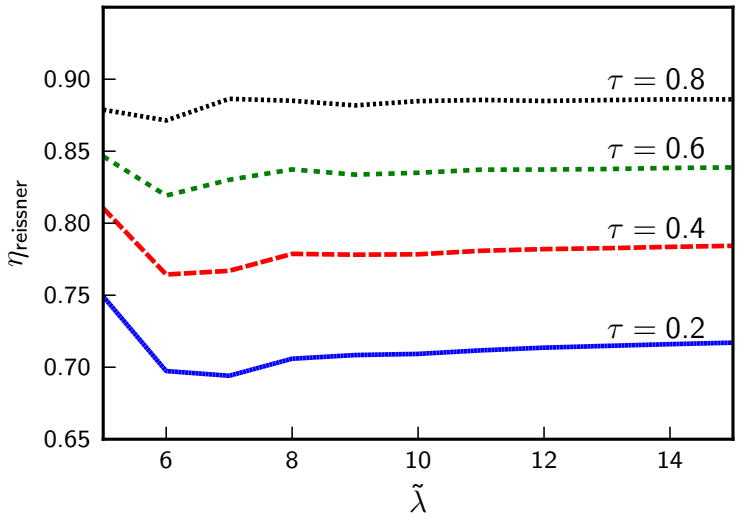

Figure 4.9: Estimate of the reduced pressure $\eta = p/\tilde{p}_0$ at which a nonaxisymmetric mode arises in the cap for various thickness ratios, using the criterion of Eq. (4.56) with the largest value of second derivative $\tilde{w}_{a,xx}$ of the Reissner solution for the cap as the estimate for $\tilde{\xi}$.

4.8). Therefore, the coupling of the nonaxisymmetric deformation with the pre-buckling axisymmetric solution can in fact give rise to a nonaxisymmetric solution at pressures *below* $\tilde{p}_0$, the buckling pressure of a complete shell with the same properties as the cap.

Figs. 4.7 and 4.8 show that the most negative value of the curvature in the axisymmetric deflection, $\tilde{w}_{a,xx}$, occurs at the sharp peak in $\tilde{w}_a$ in the boundary layer. The magnitude of the curvature depends on the pressure as well as the cap-shell thickness ratio. To estimate when a nonaxisymmetric mode may first arise, we take the value of $\tilde{w}_{a,xx}$ at this peak to be the scale $\tilde{\xi}$. We use the Reissner solution to find $\tilde{\xi}(\eta)$; the value η_{reissner} that solves the self-consistent equation $\eta = 1 + \tilde{\xi}(\eta)$ is a rough estimate of the buckling pressure. Fig 4.9 shows the result for large caps with different values of τ. Although our estimate ignores the s-dependence of $\tilde{w}_{a,xx}$ and the boundary conditions on $\tilde{w}_{a,xx}$ and $\tilde{w}_n$, it successfully reproduces the features associated with the nonaxisymmetric buckling pressure: η_{reissner} approaches an approximately constant value for $\tilde{\lambda} \gtrsim 6$, and this value gets

closer to 1 as $\tau \to 1$.

Our rough calculation also predicts the inverse wavelength of the circumferential buckling mode. The solution to Eq. (4.55) at the buckling pressure $\eta = 1 + \xi$ is $q = \sqrt{1+\xi} = \sqrt{\eta}$. Thus, the length scale of the circumferential oscillation is expected to be unchanged in the nonaxisymmetric buckling region, in agreement with Fig. 4.6.

4.5.5 Axisymmetric buckling

In the small $\tilde{\lambda}$ region, to the left of the kink in the buckling pressure curves (Fig. 4.5), we have seen that the snap-through is axisymmetric. The axisymmetric Reissner solution to the linearized equations, Eqs. (4.38), (4.39) ,(4.43), and (4.44), shows no discontinuity in the deflection as the pressure is increased; thus, the discontinuous snap-through of the cap happens only when the nonlinear terms are significant in the governing equations of the cap. To simplify our analysis, we assume that deflections in the remainder are small, so that the linearized approach introduced in Section 4.5.3 still applies in the remainder and the Reissner solution is sufficient to describe its response. This approximation is accurate for small thickness ratios τ, when the snap-through of the cap happens at small pressures compared to the buckling pressure of the remainder. (Fig. 4.2).

In the axisymmetric region, $\tilde{w}$ and $\tilde{\phi}$ are functions solely of s and the nonlinear governing equations of the cap [Eqs. (4.34)–(4.35)] simplify to

$$\nabla^4 \tilde{w} - \nabla^2 \tilde{\phi} - \frac{1}{s}\left(\tilde{\phi}_{,s}\tilde{w}_{,ss} + \tilde{w}_{,s}\tilde{\phi}_{,ss}\right) = 4\eta, \tag{4.57}$$

$$\nabla^4 \tilde{\phi} + \nabla^2 \tilde{w} + \frac{1}{s}\tilde{w}_{,s}\tilde{w}_{,ss} = 0, \tag{4.58}$$

expressions which can be integrated once to give equations for the derivative functions

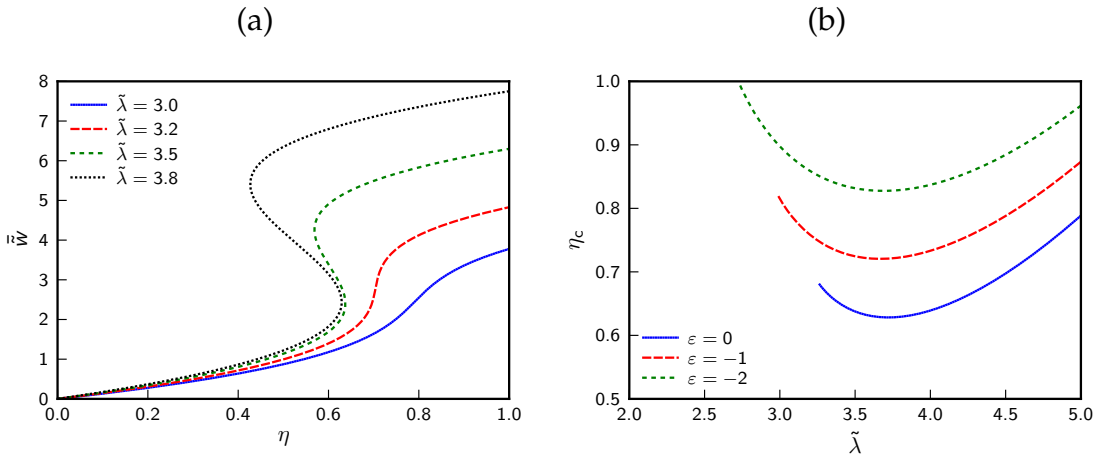

Figure 4.10: (a) Deflection $\tilde{w}$, averaged over the entire cap, as a function of the reduced pressure η, for the approximate solutions for the clamped cap obtained using the Galerkin method for different values of the cap size, $\tilde{\lambda}$. (b) Estimate of the buckling pressure using the Galerkin method, for different values of the circumferential strain ε at the boundary. The clamped cap corresponds to $\varepsilon = 0$.

$\Theta \equiv -\tilde{w}_{,s}$ and $\Phi \equiv \tilde{\phi}_{,s}$ [99, 95]:

$$s\Theta_{,ss} + \Theta_{,s} - \frac{\Theta}{s} + s\Phi - \Theta\Phi + 2\eta s^2 = 0, \tag{4.59}$$

$$s\Phi_{,ss} + \Phi_{,s} - \frac{\Phi}{s} - s\Theta + \frac{\Theta^2}{2} = 0. \tag{4.60}$$

In addition to these equations and the linearized equations [Eqs. (4.43) and (4.44)] in the remainder, the continuity equations [Eqs. (4.48)–(4.50)] must be satisfied at the boundary between cap and remainder.

Qualitative analysis

An approximate analytical solution to the nonlinear equations, computed using the Galerkin method [100], recovers many aspects of the snap-through buckling transition. We first consider the previously studied clamped cap limit [95], which corresponds to an infinitely stiff remainder, *i.e.* $\tau \to 0$. For a clamped cap, the tangent slope and all deformations at the boundary are fixed, whereas the shape and stresses at the origin must be continuous,

which leads to to the following boundary conditions for Θ and Φ:

$$\Theta(0) = \Phi(0) = 0, \tag{4.61}$$

$$\Theta(\tilde{\lambda}) = 0, \tag{4.62}$$

$$\tilde{\lambda}\Phi_{,s}(\tilde{\lambda}) - \nu\Phi(\tilde{\lambda}) = 0. \tag{4.63}$$

For small caps that exhibit axisymmetric buckling ($\tilde{\lambda} \lesssim 5$), the size of the cap is smaller than the length scale of oscillatory variations in $\tilde{w}$, which is set by $\tilde{\ell}$. As a result, the inward deflection $\tilde{w}$ has a maximum at the center of the cap and decays monotonically to zero at the cap boundary. Correspondingly, $\Theta(s)$ is zero at the origin and the cap boundary, and has a single extremal point in between. Many characteristics of the full solution to the nonlinear equations can be obtained by considering an approximate solution which reproduces these main features. We choose as our trial solution

$$\Theta(s) = As\left(1 - \frac{s}{\tilde{\lambda}}\right), \tag{4.64}$$

which automatically satisfies the boundary conditions. We obtain the value of A that best approximates the true solution using the Galerkin procedure: the trial solution, substituted into Eq. (4.60), provides a linear differential equation for Φ which can be solved with the corresponding boundary conditions to obtain a trial solution for $\Phi(s)$ that also depends on A. These solutions are substituted into the left hand side of Eq. (4.59), which is then multiplied by $\Theta(s)\,ds$ and integrated from $s = 0$ to $s = \lambda$ to get a third order algebraic equation for the deflection amplitude A:

$$\tilde{\lambda}^4(194A^3 - 1581A^2 + 2952A) + 151200A - 60480\tilde{\lambda}^2\eta = 0. \tag{4.65}$$

Roots of this equation provide the best estimate of the solution for the cap shape at any pressure. The buckling mechanism is evident from the nature of these roots. For small values of $\tilde{\lambda}$, Eq. (4.65) has a single real solution for all values of the pressure, and the average

deflection increases continuously as a function of η. This corresponds to buckling pathway III for small caps, in which the cap deforms smoothly to its inverted shape without snapping. However, for $\tilde{\lambda} > 3.25$, there is a range of pressures for which A, and consequently the cap-averaged deflection $\bar{\tilde{w}}$, can take on three real values. As a result, the pressure-deflection curves, shown in Fig. 4.10(a), take on the characteristic form of curve OAB in Fig. 4.4, and snap-through buckling occurs at the maximal value of η at which three real solutions exist (*i.e.*, at point A in Fig. 4.4). This snap-through pressure is obtained in the Galerkin solution by setting the discriminant of Eq. (4.65) to zero, and the solution is shown as the bottom curve in Fig. 4.10(b). The approximate solution reproduces many features of the buckling pressure of clamped caps in the axisymmetric region, such as the absence of a snap-through for caps below a certain size, and a non-monotonic dependence of buckling pressure on cap size.

Embedding the cap in a more flexible shell requires modifying the boundary conditions from the clamped limit. The full effect of the remainder on the cap at the boundary is complicated, and cannot be expressed succinctly. Requiring continuity of stresses and deformations across the boundary replaces Eqs. (4.62) and (4.63) with equations that relate the displacement and rotation angle at the boundary to the corresponding stresses and bending moments, themselves implicitly dependent on the solution to Θ and Φ. However, the qualitative effect of the remainder on the boundary conditions can be gauged from the Reissner solutions, which satisfy the same continuity conditions, albeit for linearized versions of the governing equations. The Reissner solutions suggest that as τ is changed from zero, $\Theta(\tilde{\lambda})$ will be positive but remains small, whereas $\Phi_{,s}(\tilde{\lambda}) - \nu\Phi(\tilde{\lambda})/\tilde{\lambda}$, which is proportional to the circumferential strain $u_{\theta\theta}$, will be negative because of the compression of the remainder under external pressure. As the thicknesses in the cap and the remainder become comparable, this circumferential strain becomes larger in magnitude. The qualitative

effect of this modified boundary condition on our approximate solution can be assessed by replacing the boundary condition on Φ, Eq. (4.63), with

$$\tilde{\lambda}\Phi_{,s}(\tilde{\lambda}) - \nu\Phi(\tilde{\lambda}) = \varepsilon, \tag{4.66}$$

where $\varepsilon < 0$ becomes increasingly negative as $\tau \to 1$, and recomputing the approximate Galerkin solution. The Reissner solutions show that $|\varepsilon|$ increases over a range $0 \lesssim |\varepsilon| \lesssim 2$ as τ is increased from 0 to 1, for pressures in the range of 0.7 – 0.8. The variation in the corresponding estimate for the snap-through pressure is shown in Fig. 4.10(b). As the circumferential strain at the boundary increases, the snap-through buckling pressure curve moves upward and the smallest value of $\tilde{\lambda}$ at which buckling is observed decreases, both in qualitative agreement with the trends in the snap-through pressure as τ is increased (see Fig. 4.5). Although our analysis is a highly simplified description of the true boundary conditions (which in reality depend subtly on $\tilde{\lambda}$, τ and η), it qualitatively captures the effect of the remainder on the snap-through transition.

Numerical analysis of governing equations

To make our analysis more quantitative, we use the Reissner solution in the shell remainder to establish the boundary conditions on Θ and Φ at the boundary, and then numerically solve the nonlinear governing equations in the cap. The continuity conditions, Eqs. (4.48)–(4.50), together with Eqs. (4.43) and (4.44) for the fields in the remainder, can be reduced to two equations that must be satisfied by Θ, Φ and its derivatives at $s = \tilde{\lambda}$. These equations depend on the dimensionless quantities $\tilde{\lambda}$, η and τ. Together with Eqs. (4.61), they provide a complete set of boundary conditions for the nonlinear differential equations of the cap, Eqs. (4.59) and (4.60), which are then solved numerically using the `bvp4c` differential equation solver in the MATLAB (Mathworks Inc.) scientific computing package.

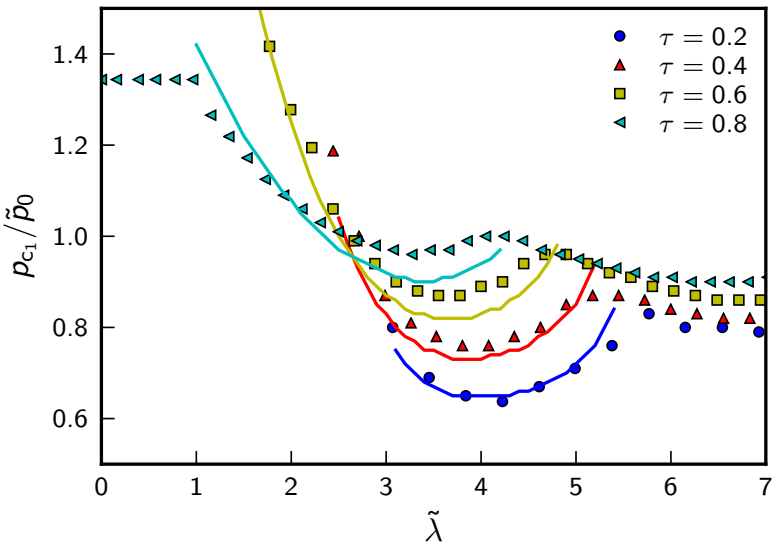

Figure 4.11: Snap-through pressure estimate from numerically solving the governing equations of the cap with boundary conditions set by the Reissner solution for the remainder (solid lines), compared to p_{c_1}, the first buckling pressure measured in simulations (symbols).

A discontinuity in the pressure-deflection curve for the computed solutions signals the snap-through buckling pressure, which we compare to the snap-through buckling pressure from simulations in Fig. 4.11. The results quantitatively replicate the observed behavior in simulations at low values of τ. Deviations from the results of simulations become larger as τ increases, because our assumption of linear behavior in the remainder becomes less accurate as $\tau \to 1$. However, these results confirm that snap-through buckling of the cap happens *via* an axisymmetric mode for small values of τ, which arises due to nonlinear couplings between deformations and stresses in the cap. The remainder influences the boundary conditions on these deformation and stress fields, which shifts the snap-through pressure closer to $\eta = 1$ as $\tau \to 1$.

Our results show that the dependence of the first buckling pressure p_{c_1} on the spot size and thickness can be explained by the loss of stability of a spherical cap of dimen-

sionless size $\tilde{\lambda}$, embedded in a remainder whose relative stiffness depends on the thickness ratio τ. Significantly, this "snap-through" loss of stability of the cap determines p_{c_1} for both buckling pathways I and II, even though the shapes of the shells at p_{c_1} differ dramatically between the two pathways (a snap-through localized to the cap for shells following pathway I, as opposed to a catastrophic collapse for shells following pathway II). From Fig. 4.2, we see that the transition from pathway I to pathway II occurs when this snap-through buckling pressure curve moves above the second buckling pressure p_{c_2} at which an inversion localized to the soft cap becomes unstable to catastrophic growth into the remainder of the shell. In contrast to p_{c_1}, which is determined primarily by the elastic properties of the cap, this second loss of stability is set mainly by the elastic properties of the remainder. We analyze this second loss of stability in the following section.

4.6 Collapse of the remainder

Whether through a continuous deformation or a snap-through buckling event, the soft cap attains an inverted shape, at a particular pressure determined largely by the thickness ratio τ (the dependence on the cap size itself is weak for large caps). The inversion is an example of a nearly isometric shape, that preserves the metric everywhere except for a narrow region at its rim (whose width is approximately the elastic length within the cap, $\tilde{\ell}$). When this inversion has formed, the fate of the remainder of the shell depends on the stability of the inversion against further growth into the remainder. A scaling argument shows why such an inversion is unstable for large enough pressures: suppose the inversion has grown so that the rim is entirely within the remainder. Then, as outlined in Section 4.4, there exists an inversion depth $d_{\max}(p) \sim (\kappa/pR^3)^2 R\sqrt{\gamma}$ that separates stable inversions from unstable ones. Inversions of depth $d > d_{\max}(p)$ can reduce their net energy by growing

deeper, leaving the shell unstable to complete collapse. Conversely, there is a pressure $p_{\mathrm{I}}(d) \sim (\kappa\gamma^{1/4}/R^3)\sqrt{R/d} \sim p_0\gamma^{-1/4}\sqrt{R/d}$ above which an inversion of depth d grows uncontrollably leading to collapse of the whole shell. But the inversion of the soft cap has the effect of 'seeding' an inversion with a depth $d_0/R \equiv 1-\cos\alpha \approx \alpha^2/2 \approx \lambda^2/2\sqrt{\gamma}$ within the remainder (here, d_0 is the cap height, an alternative way of measuring the cap size). If the snap-though of the cap happens at $p_{\mathrm{c}_1} < p_{\mathrm{I}}(d_0)$, the seeded inversion is stable over the range of pressures $p_{\mathrm{c}_1} < p < p_{\mathrm{I}}(d_0)$, and a second collapse of the whole shell occurs only when the pressure increases to $p_{\mathrm{c}_2} = p_{\mathrm{I}}(d_0)$. This corresponds to pathway I as described in Section 4.2. However, if the cap thickness is so high that snap-through happens at $p_{\mathrm{c}_1} > p_{\mathrm{I}}(d_0)$ (note that p_{c_1} is set by the cap elastic parameters while p_{I} is set by the remainder) then the inversion of the cap is immediately unstable to further growth into the remainder, and only a single collapse of the whole shell is observed at $p = p_{\mathrm{c}_1}$. This scenario corresponds to pathway II for collapse of the shell. Thus, a consideration of the stability of inversions at different pressures qualitatively explains the transition from pathway I to pathway II as the thickness of the cap increases relative to the shell (Fig. 4.2).

This approximate description does not take into account the precise evolution of the inversion energy as the rim of the inversion grows out of the cap into the remainder. This transition is crucial in determining the true value of $p_{\mathrm{I}}(h_0)$ and thus the pressure of collapse of the remainder. We study it in detail in the rest of this section.

4.6.1 Energetics of a nearly isometric inversion in a shell with a soft cap

To numerically investigate the energetics of inversions centered at the north pole for shells with soft caps, we artificially create inversions by indenting the mesh with hard spheres that are the same radius as the shell itself. (We use spherical indenters to avoid the polygonal inversions that are associated with inversions created by point indenters [101]. In

the present case, inversions are 'seeded' by the perfectly circular soft cap, and thus we are interested in inversions with perfectly circular rims.) To maintain equilibrium of forces, we prepare shells with two identical caps—one at the north pole and one at the south pole—and then squeeze the sphere between two indenters at each pole, although we report physical quantities (volume change and energy) for just one of the resulting inversions. The equilibrium configuration and corresponding elastic energy of the mesh are obtained by numerical minimization in the presence of the indenters. The depth of the inversion is varied by changing the distance between the indenting hard spheres. To prevent the shell from sliding out from between the indenters, we restrict a few mesh vertices in the vicinity of the poles to move only in the z direction.

Fig. 4.12 shows the elastic energy of inversions of depth d for shells with soft caps of various sizes [reported in terms of the cap height $d_0 = R(1 - \cos\alpha)$] at zero pressure, keeping the elastic properties of the shell and the cap unchanged. All energy curves can be divided into three distinct regions: $d \ll d_0$, when the inversion rim is localized within the soft cap; $d \gg d_0$, when the rim is localized in the remainder, and a transition region around $d \approx d_0$. This division is a direct consequence of the fact that the inversion rim is localized to a narrow region whose width is set by the elastic length scale which is small in both the cap and the remainder. As a result, the elastic energy approaches the Pogorelov scaling form [31] with the appropriate elastic constants in the small-d and large-d regions: $E_{\rm el} \to c\tilde{\kappa}\tilde{\gamma}^{1/4}(d/R)^{3/2} = c\tau^{5/2}\kappa\gamma^{1/4}(d/R)^{3/2}$ for $h \ll h_0$ and $E_{\rm el} \to c\kappa\gamma^{1/4}(d/R)^{3/2}$ for $d \gg d_0$. The best fit to the numerics is for $c = 19$, which is consistent with estimates from asymptotic analyses of the nonlinear shell equations governing the elastic energy of the inversion [31, 27] and was also independently checked *via* indentation simulations on uniform shells. The volume change associated with the inversion, meanwhile, is well-approximated by that of a perfectly isometric inversion and does not depend strongly on

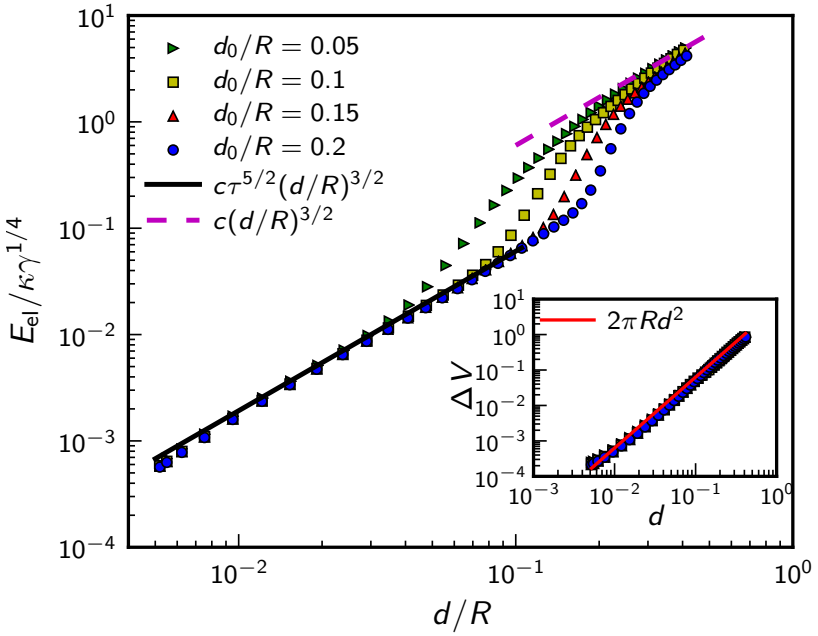

Figure 4.12: Elastic energy associated with an inversion of depth d, at zero pressure, for a shell with a soft cap of height d_0. In all cases, $\gamma = 8000$ and $\tau = 0.4$. The lines correspond to the Pogorelov form of the elastic energy for a nearly isometric inversion localized in the cap (solid line) and remainder (dotted line) respectively, with dimensionless prefactor $c = 19$. *Inset:* The volume reduction ΔV associated with the inversion matches the expectation for a purely isometric inversion, $\Delta V_{\text{iso}} = 2\pi d^2(3R - d)/3 \approx 2\pi R d^2$ for small caps.

the cap size (see inset to Fig. 4.12).

The stability of an inverted soft cap at finite pressure can now be studied by examining the behavior of the total energy $E_{\text{tot}}(d) = E_{\text{el}}(d) - p\Delta V(d)$ as the pressure is ramped up. Fig. 4.13(a) shows the total elastic energy for a pressurized shell with $\gamma = 8000$, $\tau = 0.4$ and cap size $d_0 = 0.2R$ (corresponding to $\lambda \approx 6$). For this shell, the cap snaps through to an inverted shape at $p_{c_1} = 0.13p_0$. The inversion localized to the cap is stable for pressures up to $0.22p_0$ because of the existence of a minimum in the energy curve at $d/R \approx 0.2$. However, at $p = 0.22p_0$, the energy minimum vanishes and the pressurized shell can reduce its energy indefinitely if the inversion grows into the remainder of the shell. Thus, the energetics of the inversion dictates that the remainder collapses completely at $p_{c_2} = 0.22p_0$, which matches the point of collapse observed in numerical collapse simulations (Fig. 4.2). The loss of stability of the remainder of the shell, triggered by the merging of two fixed points in the energy curve, is analogous to a limit of metastability at a first order phase transition, and is classified as a *saddle-node bifurcation* in dynamical systems theory [102].

To test this mechanism for loss of stability of the remainder, we analyzed the total energy $E_{\text{tot}}(d)$ from indentation simulations on shells with various cap sizes, to estimate the pressure at which the bifurcation occurs. This was compared to the pressure of collapse of the remainder as measured in pressure collapse simulations (Section 4.2). The results are reported in Fig. 4.13(b). The estimates from indentation simulations agree quantitatively with the pressure collapse simulations for cap sizes down to $\lambda \approx 1$. The discrepancy for smaller cap sizes is to be expected—when the cap size is small compared to the elastic length scale of the shell, there is no separation of scales that lets us consider the stability of an inverted cap in the remainder of the shell. In that case, the deformations of the cap and the remainder are closely coupled and jointly determine the pressure of collapse of the shell.

(a)

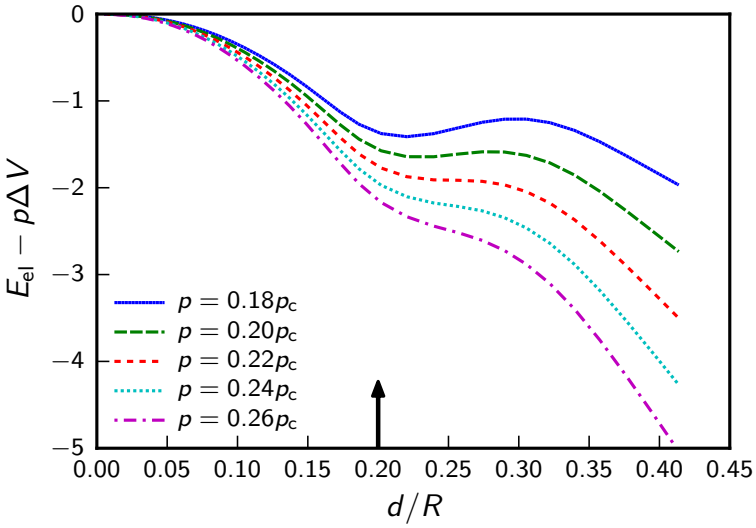

(b)

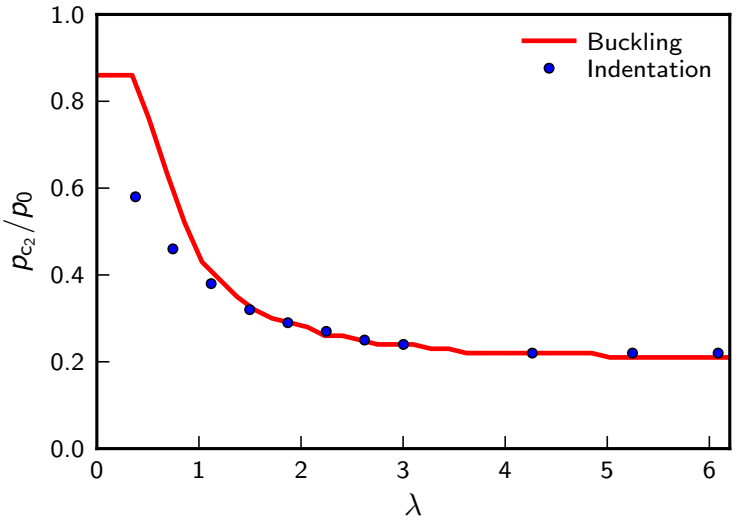

Figure 4.13: (a) Total energy of an inversion in a pressurized shell with $\gamma = 8000$, $\tau = 0.4$ and $\lambda = 6.09$ (corresponding to a cap height $d_0 = 0.2R$), showing that the shell with inversion confined to the cap becomes unstable for $p > 0.22p_0$. The arrow indicates the r coordinate of the border between the cap and the remainder. (b) Collapse pressure estimated using stability considerations from indentation simulations (symbols) compared to p_{c_2}, the pressure of catastrophic collapse of the remainder measured from pressure buckling simulations (line) for shells with $\gamma = 8000$, $\tau = 0.4$, as a function of the dimensionless cap size λ.

4.6.2 Dependence of collapse pressure on cap size and thickness

Having shown that stability considerations quantitatively determine p_{c_2} as a function of spot size for a particular value of the thickness ratio ($\tau = 0.4$), we now use scaling arguments to qualitatively understand how p_{c_2} changes with thickness ratio and cap size. Our previous estimate, $p_{c_2} = p_I(d_0) \sim p_0\gamma^{-1/4}\sqrt{R/d_0} \sim p_0/\lambda$ was inconsistent with the simulation results (Fig. 4.2) which show p_{c_2} approaching a constant value for large cap sizes rather than falling with cap size. (Recall that the cap height d_0 and the dimensionless cap size λ are related *via* $d_0 \approx R\lambda^2/2\sqrt{\gamma}$.) The previous estimate for p_{c_2} did not take into account the jump in the elastic energy $E_{el}(d)$ from $c\tau^{5/2}\kappa\gamma^{1/4}(d/R)^{3/2}$ to $c\kappa\gamma^{1/4}(d/R)^{3/2}$ when the inversion rim transitions from the cap into the remainder, which stabilizes the inversion of depth $d \approx d_0$ that arose due to the snap-through of the cap [see Fig. 4.12 and Fig. 4.13(a)]. This transition happens over some narrow depth range $d_0 \lesssim d \lesssim d_0 + \delta$, where δ is the depth change that causes the inversion rim radius $r \approx \sqrt{2dR}$ to increase from $r_0 = \sqrt{2d_0R}$ by an amount of order ℓ (*i.e.* the rim moved away from the cap boundary by an elastic length so that it no longer feels its influence). The required change in rim radius r corresponds to a depth change of order $\delta \sim \sqrt{d_0/R}\ell \sim \sqrt{d_0R}/\gamma^{1/4}$. The inversion of depth $d \approx d_0$ loses its stability when the jump in elastic energy is overcome by the pressure contribution, *i.e.* when $E_{tot}(d_0) \approx E_{tot}(d_0 + \delta)$. For $d_0 \gg \delta$, which corresponds to $\lambda \gg 1$ (the limit of large cap size), this criterion reduces to $c\kappa\gamma^{1/4}(d_0/R)^{3/2}(1-\tau^{5/2}) \approx 4\pi pRd_0\delta$. Therefore, we expect the second buckling pressure p_{c_2} to scale as

$$p_{c_2} \sim \frac{\kappa\gamma^{1/4}(d_0/R)^{3/2}(1-\tau^{5/2})}{Rd_0\delta} \sim \frac{\kappa\sqrt{\gamma}(d_0/R)^{3/2}(1-\tau^{5/2})}{(Rd_0)^{3/2}} \sim p_0(1-\tau^{5/2}), \qquad (4.67)$$

where we have used $p_0 = 4\sqrt{\kappa Y}/R^2 = 4\kappa\sqrt{\gamma}/R^3$ and $\delta \sim \sqrt{d_0R}/\gamma^{1/4}$. According to this estimate, the ratio p_{c_2}/p_0 is independent of cap size for large λ, consistent with the simulation results (Fig. 4.2). The predicted τ-dependence of the second buckling pressure

is also consistent with the simulation results: the limiting value of p_{c_2} for large λ falls from $p_{c_2} = 0.23p_0$ for $\tau = 0.2$ to $p_{c_2} = 0.21p_0$ for $\tau = 0.4$, consistent with $p_{c_2}/p_0 \propto (1 - \tau^{5/2})$.

By combining this result for the loss of stability of the remainder with the results of the previous sections, we can now fully explain the buckling pathways summarized in Fig. 4.2. The (p_{c_1}/p_0)-vs.-λ curves, set by the snap-through of the cap, move to higher values of p/p_0 as τ increases, whereas the (p_{c_2}/p_0)-vs.-λ curves, set by the stability of the inverted cap against further growth into the remainder, move to lower values as τ increases [Eq. (4.67)]. For $\tau \leq 0.4$, the former curve lies below the latter for all values of λ, and two distinct buckling transitions are observed at p_{c_1} and p_{c_2} (pathway I) over a wide range of cap sizes. For $\tau \geq 0.6$, the cap snap-through pressures lie *above* the stability curve of the remainder, and an inverted cap is immediately unstable to growing into the remainder, leading to collapse of the whole shell at p_{c_1} (pathway II) for all cap sizes. The separate buckling pressure curves cross at thickness ratio $\tau = 0.5$, and shells with this thickness ratio buckle *via* either pathway I or pathway II, depending on the size of the soft region.

4.7 Hysteresis

The buckling of uniform spherical shells is known to be *hysteretic* under cyclic changes in external pressure. A buckled shell with a large inversion re-inflates only when the pressure is brought down significantly below its buckling pressure p_0. This is illustrated in Fig. 4.14 for a numerical simulation on a uniform shell with $\gamma = 10^4$. The shell collapses close to p_0 (in practice, all simulated shells buckle slightly below the classical buckling pressure because of the finite mesh and the nonuniformity in the mesh, to which the buckling transition is very sensitive), but only reinflates when the pressure is brought down to about

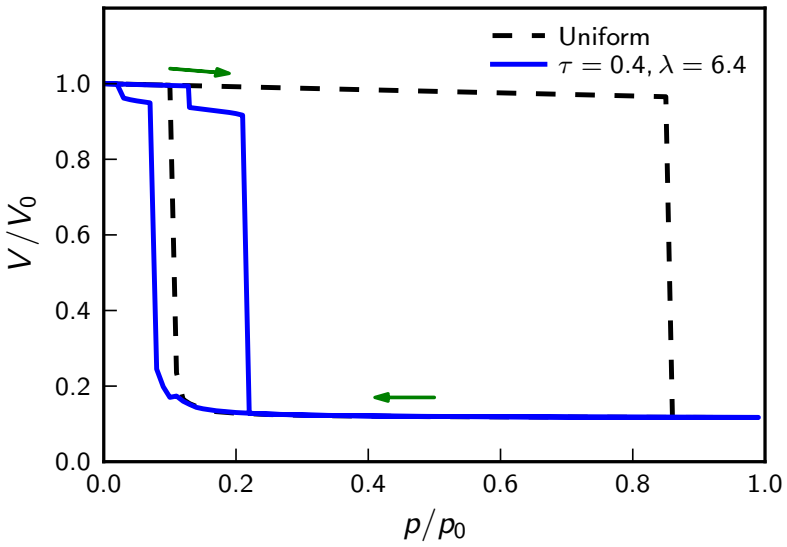

Figure 4.14: Hysteresis loops for cyclical pressure variation on a shell without (dashed) and with (solid) a soft spot with $\tau = 0.4$ and $\lambda = 6.4$. In both cases, $\gamma = 10^4$. The curves show the evolution of the enclosed volume V, normalized by the initial volume $V_0 = 4\pi R^3/3$, as the pressure is first ramped up to $p = p_0$ and then back down to zero in steps of $\Delta p = 0.01 p_0$.

10% of the buckling pressure.

This behavior can be understood from the Pogorelov scaling form [Eq. (4.27) and Appendix A] for the elastic energy of an inversion, which we have already seen leads to an inflation pressure $p_I(d) \sim \gamma^{-1/4}\sqrt{R/d}\,p_0$ to re-inflate an inversion of depth d. In collapsed shells, the inversion depth is comparable the shell radius, and as a result $p_I \sim \gamma^{-1/4} p_0$ is very small compared to the buckling pressure for thin shells with $\gamma \gg 1$. In practice, this makes spherical buckled capsules difficult to reinflate.

A large, thin soft region ($\tau < 0.5$, $\lambda \gtrsim 3$) mitigates hysteresis to some extent by bringing the buckling and reinflation pressures closer to each other. Fig. 4.14 shows the volume evolution of a shell with $\tau = 0.4$ and $\lambda = 6.4$ ($\tilde{\lambda} = \lambda/\sqrt{\tau} = 10.1$), corresponding to a cap of height of $d_0 = 0.2R$. The shell follows buckling pathway I (a snap-through

of the cap followed by buckling of the remainder at higher pressure, as in Fig. 4.1). The pressure of catastrophic collapse of the shell is brought down to $p_{c_2} = 0.22p_0$, and the shell reinflates when the pressure is about a third of this value. The soft region also exhibits some hysteresis of its own, snapping back to its initial configuration at a pressure of $0.03p_0$ which is lower than the snap-through pressure $p_{c_1} = 0.13p_0$. This cap hysteresis is characteristic of the bistable state with two equilibrium solutions that is responsible for snap-through buckling (Fig. 4.4).

These features may be exploited for applications that require shape changes of elastic capsules in response to changes in the pressure. First, the deflation and re-inflation pressures associated with large-scale collapse of the shell are brought much closer to each other for shells with soft spots (when $\tau < 0.4$), reducing the area of the hysteresis loop and making the shells more responsive to pressure cycling. Second, there is a wide range of parameters for which the soft spot can be inverted and re-inflated without collapsing the shell as a whole. This provides a mechanism for making capsules with a well-defined indentation (set by the cap size) that can be triggered or removed by changing the pressure. Such capsules could be used to make tunable "lock" colloids in a lock-and-key colloidal assembly system [37], which may be induced to associate with, or be indifferent to, smaller "key" colloids depending on whether the cap is inverted to form a receptacle for the keys.

4.8 Conclusion

Our analysis shows that a circular thin region in a spherical shell, although a simple inhomogeneity to describe, strongly influences the buckling properties in important and subtle ways. By varying the thickness and size of the soft region, we can induce the shell to follow three different buckling pathways, each of which can be understood by analyzing the

governing equations of the cap and the remainder. These pathways can be exploited to control the shell shapes swept out by varying the external pressure.

A wide range of inhomogeneities in thin shells remains to be explored. It is already evident that the shape of the soft region [38] and the number of soft spots [47] fundamentally changes the buckling behavior; a systematic study of soft spots with non-circular shapes and of multiple soft spots on the same shell could uncover additional ways to control and exploit the buckling transition. We could also consider sectors on a shell with a different 3D elastic modulus E compared to the remainder, allowing us to vary the ratio of 2D Young's moduli $\tilde{Y}/Y$ independently from the ratio of bending rigidities $\tilde{\kappa}/\kappa$. Localized variations in the shell curvature, already studied in the context of imperfect shells [41], may have interesting effects on the buckling properties as well. These and many more inhomogeneities in the shell properties can be explored using numerical simulations of the type used in this work.

Finally, we remark that a shell with a single soft region is likely to be less sensitive to imperfections in the shell shape than a uniform shell. The sensitivity of the buckling transition to even minute deviations in the shell shape (of the order of the shell thickness) from the perfect sphere has already been mentioned. This sensitivity occurs because the mode responsible for buckling of a uniform shell (pictured in Fig. 4.3) is highly degenerate [39]. Since many such modes exist, it is likely that one or more of the modes couples strongly with the spatial shape variation, and acquires a non-zero amplitude (thus triggering shell collapse) at a pressure lower than the classical buckling pressure p_0 for a perfect shell. Depending on the strength of the coupling, the instability is triggered at a pressure that may be anywhere from 20–80% of p_0 for real-world shells, even if the deviations from the perfect sphere are only of the order of the thickness of the shell [40]. As a result, the true pressure at which uniform shells lose stability can be unpredictable. In contrast, the

collapse of shells with thin soft spots ($\tau < 0.5$) is triggered by loss of stability of the snap-through state. As described in Section 4.6, this is governed by the energetics of nearly isometric inversions rather than the presence of highly degenerate modes. Since the scaling of the inversion energy with inversion depth is not sensitive to small imperfections, the buckling of the shell is expected to happen reliably at roughly $0.22p_0$ for large spots ($\lambda \gtrsim 4$), regardless of small deviations from the perfect shape. Even though the buckling pressure is greatly reduced by the soft spot, it can be known much more precisely. Paradoxically, introducing a known inhomogeneity in the shell thickness could make the buckling transition more reliable than for a uniform shell! This property could be exploited for applications, such as release of encapsulated materials under specific environmental conditions, that require precise control over the pressure at which buckling happens.

Chapter 5

Buckling of shells with a smoothly varying thickness profile

In this chapter, we study the buckling of spherical shells with a nonuniform thickness that varies continuously over the shell surface. We consider shells with a spatially varying shell thickness that gradually increases from one pole to the other, and is symmetric around the axis joining the the two poles. Such an inhomogeneity is completely different from the localized "soft spot" nonuniformity studied in Chapter 4. This work was motivated by buckling experiments on colloidal capsules with nonuniform thicknesses conducted by Sujit S. Datta, Shin-Hyun Kim and Alireza Abbaspourrad in the research group of Prof. David Weitz.

This chapter is organized as follows. We first summarize the fabrication and buckling of colloidal capsules that motivate the study. We then derive the buckling pressure and corresponding threshold volume change for inhomogeneous shells, as a function of the average shell thickness and the degree of inhomogeneity. We test our results against numerical simulations of pressurized inhomogeneous shells (details of which are presented in Appendix E), and show that they are consistent with experimental measurements of the buckling properties of polymer capsules. Finally, we numerically study how

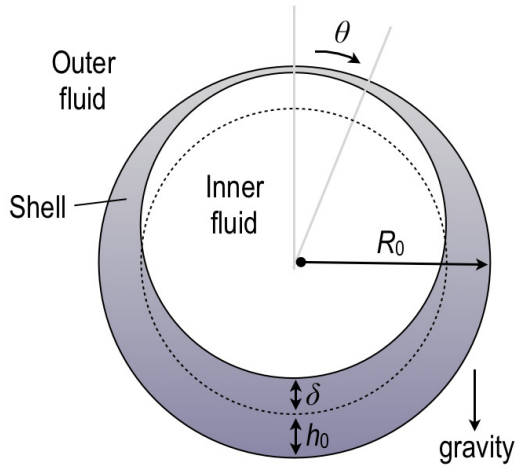

Figure 5.1: Schematic showing the capsule geometry investigated. The polymerized shell separates an inner droplet from the outer phase. When the double emulsions are fabricated, the inner droplet interface (dotted line) is concentric with the outer interface, but rises due to buoyant forces over time to produce a smoothly varying thickness. The degree of inhomogeneity δ is half the difference in thickness between the top and bottom poles, and the average thickness is h_0.

the hysteresis properties of the shells vary with the degree of inhomogeneity.

5.1 Experimental motivation

The contributions of Sujit S. Datta, Shin-Hyun Kim and Alireza Abbaspourrad (research group of Prof. David Weitz, Harvard University) to this section and to the experimental results in this chapter are gratefully acknowledged.

Monodisperse thin-shelled capsules were fabricated using water-oil-water droplets prepared by microfluidics [103]. The inner and outer phases of the droplets are a 10 wt % solution of polyvinyl alcohol (PVA), while the middle oil phase is a photo-polymerizable monomer solution. Since the PVA solution is less dense than the oil phase, the light inner water droplets gradually rise within the oil droplets. This causes the oil to gradually thin on one side of the droplet and thicken on the other; this effect is exploited to prepare cap-

sules with outer radius R_0 and spatially varying shell thickness

$$h(\theta) \approx h_0 - \delta \cos\theta, \tag{5.1}$$

where θ is the azimuthal angle measured from the top of the gravitationally-oriented shell, h_0 is the average shell thickness, and δ is the total distance moved by the inner droplet, as shown schematically in Fig. 5.1. The average radius of the mid-surface of the shell is $R \equiv R_0 - h_0/2$.

The oil used is polymerizable by exposure to ultraviolet (UV) light, and can be polymerized either as the capsules are produced *in situ*, or after different waiting times, t_w; varying the waiting times enables the fabrication of batches of capsules with different degrees of inhomogeneity. The shells are characterized by a Young's modulus $E \approx 600$ MPa. They are permeable to water but impermeable to Na^+ and Cl^- ions, which means that they experience an osmotic pressure in NaCl solution, and can reduce their internal volume in response to the pressure.

5.1.1 Measurement of buckling properties

The buckling process was quantified by performing ensemble measurements on batches of identically prepared capsules with known values of the shell geometry parameters h_0, δ and R. Three sets of capsules were tested with the following geometries: $\{h_0, R_0, \delta/h_0\} = \{1.2\mu\text{m}, 70\mu\text{m}, 0.20\}$, $\{1.3\mu\text{m}, 67\mu\text{m}, 0.23\}$, and $\{5.5\mu\text{m}, 55\mu\text{m}, 0.19\}$. Different osmotic pressures were applied to separate batches of capsules by mixing the suspensions in NaCl solution in the range 0.063–2.165 M, corresponding to pressure differences across the shell of $p = 0.025$–10.09 MPa. For each value of the osmotic pressure, roughly 75 identical capsules were monitored over time using optical microscopy. Buckling was signalled by the abrupt appearance of localized indentations in shells; the fraction of capsules that

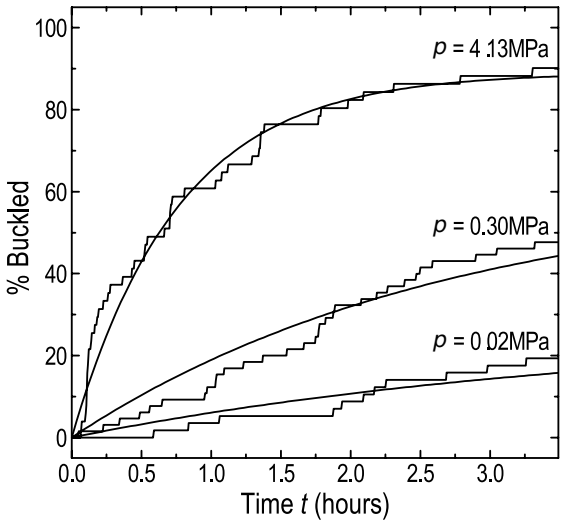

Figure 5.2: Fraction of capsules buckled over time for three different values of the osmotic pressure difference p. Capsules have mean shell thickness $h_0 = 1.2\mu$m, outer radius $R_0 = 70\mu$m, and thickness inhomogeneity $\delta/h_0 = 0.20$. Smooth lines show exponential fits.

buckled increased over time in a thickness- and pressure-dependent manner (Fig. 5.2). The behavior was quantified by fitting an empirical exponential relationship of buckling fraction with elapsed time (smooth curves in Fig. 5.2). The plateau value of the fit was used to estimate the total fraction of capsules that ultimately buckle at long times at the particular pressure, while the time constant of the fit yielded the characteristic time delay before the onset of buckling, t^* (explained in Section 5.3.1).

5.2 Buckling pressure of a shell with a smoothly varying thickness

The elastic energy of a shell with a varying thickness is the same as that used in Chapter 4 [Eq. (4.5)], but with position-dependent elastic moduli. We use shallow-shell theory [10, 12] to describe the displacements, restricting ourselves to a section of the shell of size $\sim L$, small enough so that slopes relative to a tangent plane at the basal point are small and

can be ignored at quadratic order, *i.e.* $(L/R)^2 \ll 1$ (see Appendix C.1). Upon setting up a Cartesian coordinate system (x, y) in the tangent plane with its origin at the basal point, the elastic energy in terms of the tangential displacement fields $U(x, y)$, $V(x, y)$ and the normal displacement $W(x, y)$ is [12]:

$$E_{\rm el} = \int dx\, dy \left[\frac{Eh(x,y)}{2(1-\nu^2)} \Big((u_{xx} + u_{yy})^2 - 2(1-\nu)(u_{xx}u_{yy} - u_{xy}^2) \Big) + \frac{Eh(x,y)^3}{24(1-\nu^2)} (W_{,xx} + W_{,yy})^2 - pW \right], \tag{5.2}$$

where E is the three-dimensional Young's modulus and ν the Poisson ratio of the shell material, and the strain tensor u_{ij} is related to the displacements *via* Eqs. (4.6)–(4.8). This expression ignores terms of order $(x/R)^2, (y/R)^2 \ll 1$.

For a uniform shell with $h(x, y) = h_0$, an analysis of the Euler-Lagrange equations associated with the elastic energy [Eq. (5.2)] predicts the buckling transition, as described in detail in Section 4.4. Here we summarize the key results of this analysis. Prior to buckling, the response of the shell to the uniform external pressure p is to compress uniformly by an amount

$$W_0 = \frac{pR^2(1-\nu)}{2Eh_0}, \tag{5.3}$$

building up uniform compressive shell stresses

$$\sigma_{xx}^0 = \sigma_{yy}^0 = -pR/2. \tag{5.4}$$

The elastic energy associated with this compressed state, which does not involve bending of the shell surface, is roughly $\sigma_{ij}^2/(Eh_0) \sim p^2R^2/(Eh_0)$ per unit area. When p gets large, it becomes energetically favorable for the shell to introduce some bending deformations to trade the elastic energy of pure compression for bending energy. The buckling transition is identified by the value of p for which a nonuniform deformation mode of the shell first arises which is energetically favorable compared to the uniform compression, which is (see

Section 4.4 for details)

$$p^*_{\delta=0} = \frac{2E}{\sqrt{3(1-\nu^2)}}\left(\frac{h_0}{R}\right)^2. \tag{5.5}$$

The associated displacement fields U, V and W vary sinusoidally in both x and y, with an associated wavelength

$$\lambda^*_{\delta=0} = \frac{2\pi}{[12(1-\nu^2)]^{1/4}}\sqrt{h_0 R} \ll R. \tag{5.6}$$

The wavelength associated with the buckling mode is very small for thin shells, which justifies the use of shallow-shell theory to calculate the buckling pressure—a shallow section of the shell with $L/R \ll 1$ can still accommodate many wavelengths of the buckling modes and provides a good description of the elastic energy of these modes [12].

We now consider an inhomogeneous shell with a continually varying shell thickness $h(\theta) = h_0 - \delta\cos\theta$ and radius R of the middle surface. By analogy with the buckling of homogeneous shells, we expect the buckling transition to be signalled by the existence of a nontrivial solution to the energy-minimizing displacement fields of the middle surface. Furthermore, we expect such a mode to first appear in the vicinity of the thinnest point of the sphere, $\theta = 0$. We consider a shallow section of the sphere, with Cartesian coordinates whose origin coincides with the thinnest point. As before, shallowness implies that the section is small enough that slopes are small compared to the base of the section. The elastic energy and the stress-strain relations are modified because the thickness of the shell is now position-dependent: $h(x,y) = h_0 - \delta\left(1 - Z(x,y)/R\right)$, where $Z(x,y) = \sqrt{R^2 - x^2 - y^2}$ is the shape of the undeformed middle surface of the shell. Expanding in powers of x/R and y/R, we have

$$h(x,y) = h_0 - \delta\left[1 + \frac{1}{2}\left(\frac{x^2+y^2}{R^2}\right) + ...\right] \tag{5.7}$$

However, the shallowness of the section implies that $(x/R)^2, (y/R)^2 \ll 1$, and the section is well-described by setting $h \approx h_0 - \delta$, a constant. The errors introduced by assuming a

constant shell thickness in the entire shallow section are of the same order as those introduced by the assumption of shallowness itself. Thus, the only modification to the shallow-shell theory calculation of the critical buckling pressure of the uniform shell is to set the shell thickness to $h = h_0 - \delta$, from which we readily obtain the buckling pressure

$$p^* = \frac{2E}{\sqrt{3(1-\nu^2)}} \left(\frac{h_0 - \delta}{R} \right)^2 . \tag{5.8}$$

The wavelength of the buckling modes that arise at this pressure is

$$\lambda^* = 2\pi \sqrt{(h_0 - \delta)R} / [12(1-\nu^2)]^{1/4}. \tag{5.9}$$

Again, $\lambda^* \ll R$ for thin shells with $h_0 \ll R$, justifying the assumptions made. Essentially, the spatial thickness variation of the capsules under study is so gentle that there is hardly any variation in the mechanical properties of the capsule at the scale of the small wavelength associated with the buckling modes. As a result, the buckling pressure is set by the thickness of the capsule in the vicinity of the thinnest spot, where it is approximately $h_0 - \delta$. (We could consider different sections of the capsule, with higher thicknesses, but the associated buckling mode would arise at a pressure higher than of Eq. (5.8).) Considering the magnitude of the terms excluded from the Euler-Lagrange equations by our approximation of constant thickness shows that the corrections to Eq. (5.8) from taking into account the spatial variation in thickness over the shallow shell would be smaller by a factor $O(\delta/R)$.

To test our theoretical arguments, we perform numerical simulations on shells with $0.01 \leq h_0/R \leq 0.04$ and $0 \leq \delta/h_0 \leq 0.9$ (see Appendix E for details of the simulation). The results are reported in Fig. 5.3(a), showing good agreement between the theoretical prediction and the simulation results. The slight discrepancy between theory and simulation likely reflects the sensitivity of the buckling transition to inevitable small scale inhomogeneities introduced by the amorphous mesh that describes the shell (see Ap-

(a)

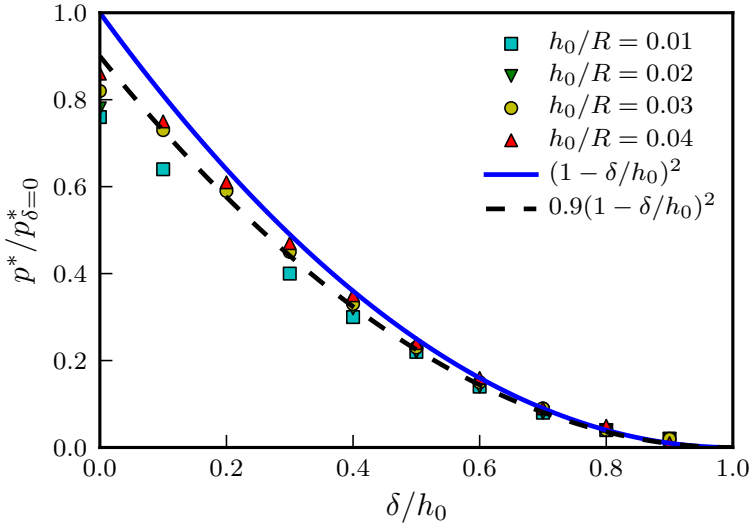

(b)

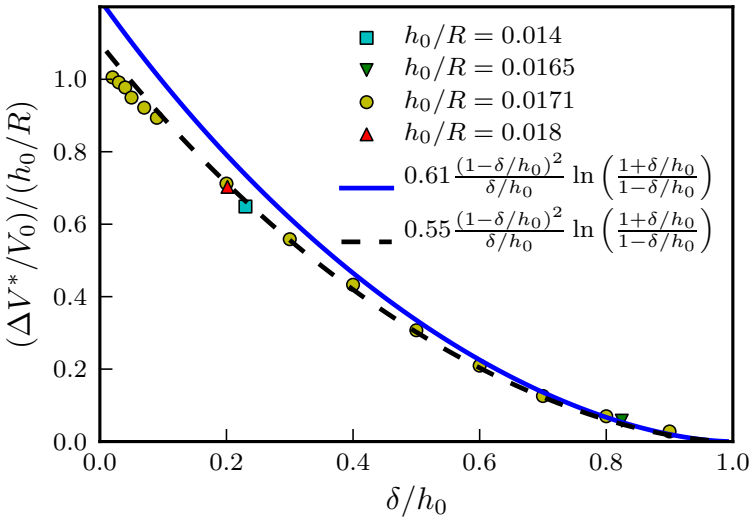

Figure 5.3: **(a)** Effect of inhomogeneity on the buckling pressure. The symbols show the buckling pressure from simulations for shells with various average thickness h_0 and inhomogeneity δ, normalized by the corresponding buckling pressure for uniform shells with the same average thickness, $p^*_{\delta=0} = 2E/\sqrt{3(1-\nu^2)} \times (h_0/R)^2$ [Eq. (5.5)]. The solid line shows the theoretical prediction, Eq. (5.8). **(b)** Threshold volume change at buckling, from simulations. The solid line shows the theoretical prediction [Eq. (5.12)], with $\nu = 1/3$. In both **(a)** and **(b)**, the dashed line shows 90% of the theoretical value. The systematic discrepancy of 10% or so between theory and simulation (higher for the extremely thin shells with $h_0/R = 0.01$) is likely a result of the sensitivity of the buckling transition to the small amount of disorder in the underlying simulation mesh.

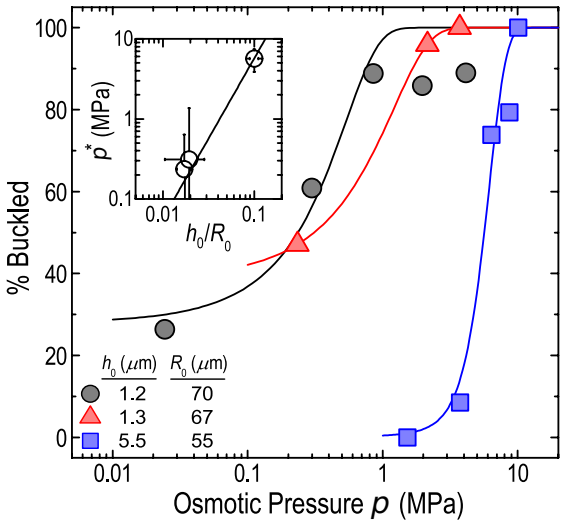

Figure 5.4: **Buckling pressure estimates from experiments.** Total fraction of capsules that have buckled at long times for varying p, for capsules with $\{h_0,\ R_0,\ \delta/h_0\} = \{1.2\mu\text{m},\ 70\mu\text{m},\ 0.20\}$ (circles), $\{1.3\mu\text{m},\ 67\mu\text{m},\ 0.23\}$ (triangles), and $\{5.5\mu\text{m},\ 55\mu\text{m},\ 0.19\}$ (squares). The curves are fits to the error function, the mean and standard deviation of which give the estimate of the buckling pressure p^* for each capsule geometry and the error associated with this estimate respectively. The inset shows this estimate, with the straight line showing $p^* \propto (h_0/R_0)^2$ scaling.

pendix E). This sensitivity is due to nonlinear couplings between the non-uniformities and the degenerate buckling modes that arise as the classically predicted buckling pressure is approached, which drive the transition to happen below the buckling pressure predicted by the linear stability analysis. We expect this sensitivity to be more pronounced for the uniform case, where the unstable modes extend over the entire shell, in contrast to the nonuniform case, where the unstable modes are localized in the shallow region near the thinnest part of the shell.

5.2.1 Comparison to experimental measurements

The form of the buckling pressure, Eq. (5.8), implies that shells with different thickness-to-radius ratios h_0/R but a constant value of the degree of inhomogeneity δ/h_0 exhibit a

buckling pressure that scales as $p^* \propto (h_0/R)^2$, similar to uniform shells. This is consistent with experimental estimates of the buckling pressure for three different capsule geometries with $\delta/h_0 \approx 0.2$, shown in Fig. 5.4. The dependence of the total fraction of buckled capsules on the external pressure, measured as described in Section 5.1.1, was fit to an error function (smooth curves in Fig. 5.4); the mean value of the distribution from this fit was used as an estimate of the buckling pressure p^* for each capsule geometry. A quadratic dependence of the buckling pressure of the buckling pressure on the mean thickness was observed: $p^* \approx (600 \pm 200)(h_0/R)^2$ MPa (inset to Fig. 5.4), which compares well to the theoretical estimate of $p^* \approx 470(h_0/R)^2$ MPa, obtained by substituting $E = 600$ MPa, $\nu = 0.33$ and $\delta/h_0 = 0.2$ in the shell theory expression, Eq. (5.8).

5.3 Volume change prior to buckling

Prior to buckling, the shell contracts in response to the external pressure, maintaining its spherical shape. The isotropic stresses in the shell as a result of this contraction are ultimately responsible for shell buckling, which occurs when it becomes energetically favorable for the shell to introduce nontrivial bending deformations and trade the elastic energy of this pure compression for bending energy. Buckling happens when the shell contraction, proportional to the applied pressure, crosses a threshold value at p^*. Therefore, there is a threshold internal volume reduction associated with this compression, which we call ΔV^*.

The experimental capsules differ from the idealized shells studied in Chapter 4 in having an inner fluid that takes time to permeate through the capsule. As a result, capsules exposed to an osmotic pressure at or higher than their buckling pressure do not buckle immediately, but take some time to eject the inner fluid and attain the threshold volume reduction ΔV^* before they buckle. The magnitude of this volume reduction thus

determines the dynamics of buckling for the colloidal capsules under study.

The volume change prior to buckling is determined by the initial prebuckling response of the shell to the external pressure. For a spherical shell, the only axisymmetric stress distribution in response to a uniform pressure p that is well-behaved at the poles is the uniform stress distribution, Eq. (5.4) [104]. In contrast to the uniform shell, however, the resulting transverse displacement varies with the shell thickness:

$$W_0(\theta) = \frac{pR^2(1-\nu)}{2Eh(\theta)} = \frac{pR^2(1-\nu)}{2E(h_0 - \delta cos\theta)}. \tag{5.10}$$

The volume change in response to pressures up to the buckling pressure is thus (to lowest order in the inward displacement)

$$\Delta V = 2\pi \int_0^\pi R^2 \sin\theta \, W_0(\theta) \, d\theta = \pi(1-\nu)\frac{pR^4}{Eh_0}\left[\frac{h_0}{\delta}\ln\left(\frac{1+\delta/h_0}{1-\delta/h_0}\right)\right]. \tag{5.11}$$

The threshold volume change immediately before buckling is obtained by substituting p^* [Eqn. (5.8)] for p in the above expression to get

$$\frac{\Delta V^*}{V_0} = \frac{1}{2}\frac{h_0}{R}\sqrt{\frac{3(1-\nu)}{1+\nu}}\left[\left(1-\frac{\delta}{h_0}\right)^2\frac{h_0}{\delta}\ln\left(\frac{1+\delta/h_0}{1-\delta/h_0}\right)\right], \tag{5.12}$$

where $V_0 = 4\pi R^3/3$ is the initial volume of the shell. We recover the result for uniform shells, $\Delta V^*/V_0 = \sqrt{3(1-\nu)/(1+\nu)} \times h_0/R$ (Ref. [29]) in the limit $\delta/h_0 \to 0$. Fig. 5.3(b) compares the analytical expression to numerical simulations on shells with various thicknesses and inhomogeneities, showing good agreement.

5.3.1 Time delay before buckling for experimental capsules

The prediction for the threshold volume change before buckling, Eq. (5.12), can be combined with the dynamics of fluid transport through the shell wall to predict the time delay between the application of osmotic pressures and the inception of buckling seen in the experiments. For a capsule to buckle, a volume ΔV^* of liquid must be ejected from its

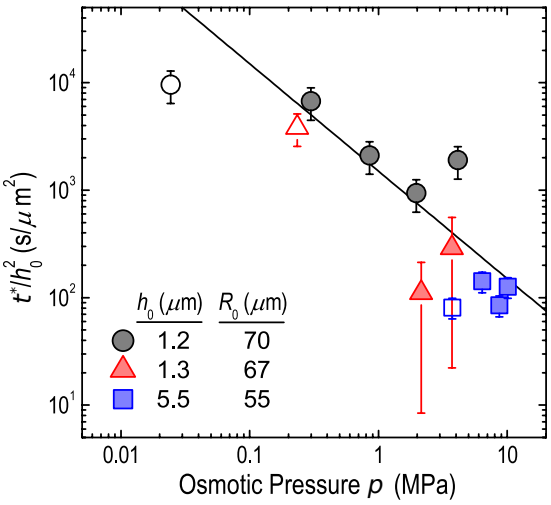

Figure 5.5: Time delay before the onset of buckling, t^*, normalized by h_0^2, for various external pressures p, for capsules with $\{h_0, R_0, \delta/h_0\} = \{1.2\mu\text{m}, 70\mu\text{m}, 0.20\}$ (circles); $\{1.3\mu\text{m}, 67\mu\text{m}, 0.23\}$ (triangles), and $\{5.5\mu\text{m}, 55\mu\text{m}, 0.19\}$ (squares). Filled symbols show $p > p^*$ while open symbols show $p < p^*$. Vertical error bars show uncertainty arising from estimated variation in h_0. Black line shows $\sim p^{-1}$ scaling.

interior. This is guaranteed to happen as long as the applied pressure difference p is above p^*. However, the time delay $t^* = \Delta V^*/Q$ before the onset of buckling depends on Q, the volumetric rate of fluid ejection, which is proportional to p. Therefore, capsules should buckle faster at higher pressures.

The fluid ejection rate Q can be calculated by integrating Darcy's law for the flow of a viscous fluid through a porous barrier over the entire capsule (see Appendix G.1); combining the result [Eq. (G.1)] with the derived expression for ΔV^* [Eq. (5.12)] gives

$$t^* \approx \frac{V_0}{Q_0}\sqrt{\frac{3(1-\nu)}{1+\nu}}\frac{h_0}{R_0}\left(1-\frac{\delta}{h_0}\right)^2, \tag{5.13}$$

where $Q_0 \equiv 4\pi R_0^2 pk/\mu h_0$ is the flow rate of a fluid of viscosity μ out of a *uniform* shell with thickness h_0 and permeability k. This expression is consistent with experimental observations that the time to onset of buckling decreases with applied pressure $p > p^*$, for shells with different geometries but identical degree of inhomogeneity $\delta/h_0 \approx 0.2$. For

these shells, we expect $t^*/h_0^2 \approx 0.8\mu/pk$ according to Eq. (5.13). Fig. 5.5 shows that the measurements of t^* at pressures above the critical buckling pressure (filled symbols) collapse when rescaled by h_0^2; by fitting these data (solid line), we obtain an estimate of the shell permeability, $k \approx 7 \times 10^{-24}\,\mathrm{m}^2$, which is consistent with an independent experimental measurement of shell permeability, $k \approx 2 \times 10^{-24}\,\mathrm{m}^2$, obtained by tracking the rate at which capsule volume decreases after the onset of buckling (described in Appendix G.2).

5.4 Postbuckling shapes

Because the growth of the inversion after buckling is determined by the slow dynamics of the inner fluid permeating through the capsules, the evolution of the inversion as it grows in depth can be observed in the experiments over time. The inhomogeneity is expected to affect the inversion, because the sharp rim of the inversion, where the stretching and bending energies are confined, moves through regions of varying thickness as the inversion grows. This large-deformation behavior cannot be captured in the linear analysis presented above; instead, we use numerical simulations to gain insight into the postbuckling behavior observed in experiments.

5.4.1 Experimental observations

Optical microscopy was used to monitor the evolution of the capsule morphologies after the onset of buckling, for shells with low ($\delta/h_0 \approx 0.2$) and high ($\delta/h_0 \approx 0.84$) inhomogeneity. Slightly inhomogeneous capsules typically buckled through the sudden formation of a single circular indentation. As this indentation grew over time, its perimeter eventually sharpened into straight ridges connected by 2-3 vertices [101, 32], as shown in Fig. 5.6(a). This sharpening reflects the unique physics of thin shells: because it is more difficult to

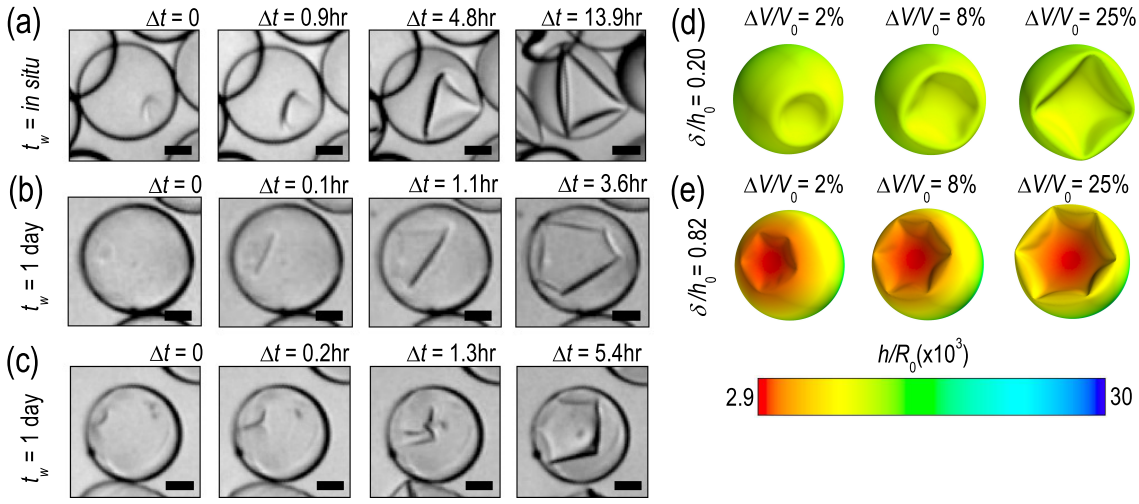

Figure 5.6: Folding pathways for different shell inhomogeneities. (a-c) Optical microscope images exemplifying buckling at $p = 0.86$ MPa of (a) slightly inhomogeneous capsules polymerized *in situ* ($t_w \approx 0$), with $\delta/h_0 \approx 0.2$, (b-c) very inhomogeneous capsules polymerized after a wait time $t_w = 1$ day, with $\delta/h_0 \approx 0.84$. Very inhomogeneous capsules buckle through the formation of either (b) one single indentation or (c) two indentations. Δt is time elapsed after buckling. Scale bars are 35μm. (d-e) Examples of simulated shells with similar geometries as the capsules shown in (a-c), for varying fractional volume reduction $\Delta V/V_0$. Color scale indicates the spatially-varying shell thickness.

compress the capsule shell than it is to bend it, localizing compressive deformations only along sharp lines and points on the capsule surface requires less energy than uniformly compressing the shell [13]. Interesting differences were observed for the very inhomogeneous capsules [Fig. 5.6(b)]. The initial folding pathway was similar; however, the perimeters of the indentations formed in these capsules sharpened into straight ridges connected by 4-5 vertices, more than in the slightly inhomogeneous case. Moreover, surprisingly, roughly 30% of the very inhomogeneous capsules buckled through the formation of one, then two, adjacent indentations, as exemplified in Fig. 5.6(c). The perimeters of these indentations grew over time, eventually meeting, coalescing, and sharpening into straight ridges connected by 4-5 vertices [Fig. 5.6(c)].

5.4.2 Numerical simulations

To investigate the influence of inhomogeneity on the shape of the inversion at large volume reductions, we simulate large volume reductions for two sets of geometric parameters: shells with $h_0/R = 0.018$ and $\delta/h_0 = 0.20$, similar to the more homogeneous capsules studied in experiments, and shells with $h_0/R = 0.0165$ and $\delta/h_0 = 0.82$, similar to the very inhomogeneous shells. We find the energy-minimizing configurations for a particular value of the enclosed volume V, which we reduce in steps of $0.0025V_0$ from $V_T = V_0$ to $V_T = 0.75V_0$ (further details of the numerical simulation are provided in Appendix E). For each set of geometric parameters, we investigate the robustness of the resulting shapes by performing eight different simulations, in each case varying the point on the underlying mesh that corresponds to the thinnest point of the shell. This effectively changes the random discretization of the shell in each instance.

In all instances, the shells buckle when the shell volume is reduced past ΔV^* (whose value is approximately $0.0115V_0$ for the more homogeneous shells and $0.0008V_0$ for the very inhomogeneous shells) to form a single circular indentation centered at the thinnest part of the shell. At larger volume changes, however, the shape of the inversion differs between the two shells and among different simulation instances for the same shell. In more homogeneous shells, the inversion remains circular up to a volume change of $\Delta V \approx 0.05V_0$, beyond which the perimeter sharpens into straight ridges connected by 4-5 vertices [Fig. 5.6(d)]. Three out of the eight simulation runs on the more homogeneous shells displayed inversions with 4 vertices, while the remaining five runs displayed inversions with 5 vertices. Remarkably, the two types of inversions do not differ significantly in their elastic energies, which explains why slight differences in the underlying mesh have a significant effect on the final shape.

The shape evolution of the inversions in very inhomogeneous shells is qualita-

tively different [Fig. 5.6(e)]. The inversion takes on a ridged appearance almost immediately after its formation, at a much smaller volume change ($\Delta V \approx 0.004 V_0$) compared to the more homogeneous shells. The number of vertices in the perimeter is also consistently higher for the very inhomogeneous shells: out of eight simulation runs, three displayed inversions with 5 vertices, four had inversions with 6 vertices, and one run displayed an inversion with 7 vertices. Again, there is no significant difference in the elastic energies of the competing shapes.

These results qualitatively agree with the experimental observations [Fig. 5.6(a-c)]. We note that while the exact number of vertices formed differs between the experiments and the numerical simulations, both show that the inversions in very inhomogeneous capsules develop more vertices than the more homogeneous case. However, in contrast to the experimental capsules [Fig. 3(c)], we do not systematically observe the formation of adjacent indentations in the simulations on very inhomogeneous shells. This is likely due to details of the inversion growth dynamics in the experiments, which are not captured in our quasi-equilibrium simulations.

5.5 Hysteresis properties

We saw in Chapter 4 that an inhomogeneity in the thickness can significantly change the hysteresis of the shell shape under cyclical changes in pressure. Shells with a smoothly varying thickness also display interesting hysteresis properties. As for uniform spherical shells, the shape after buckling has a large, nearly isometric inversion that significantly reduces the enclosed volume of the shell. However, the energetics of these inversions is modified by the inhomogeneity. Simulations of the postbuckling shape show that the inversion is centered around the thinnest region of the shell ($\theta = 0$). Since the rim remains

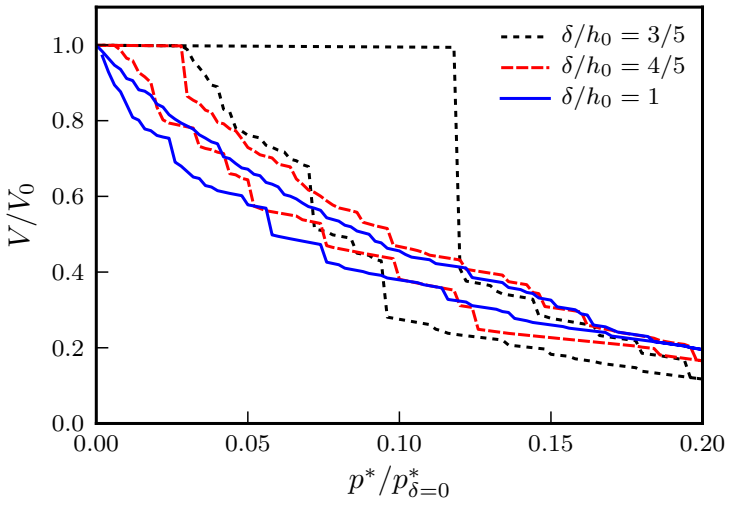

Figure 5.7: Hysteresis loops for cyclical pressure variation on simulated shells with $h_0/R = 0.03$ and various levels of inhomogeneity δ/h_0. The enclosed volume V is shown normalized by the initial volume $V_0 = 4\pi R^3/3$, as the pressure (normalized by the buckling pressure $p^*_{\delta=0}$ of a uniform shell with thickness h_0) is ramped up to $0.2p^*_{\delta=0}$ (upper section of each curve) and then back down to zero (lower section of each curve) in increments of $0.01p^*_{\delta=0}$. These curves may be compared to the hysteresis curve for a uniform shell from Fig. 4.14.

localized to a narrow region with width of order $\sqrt{hR}$, we may assume that the energy of the inversion still follows the Pogorelov scaling form,

$$E_{\text{el}} \propto Eh^{5/2}R^{1/2}(d/R)^{3/2}, \tag{5.14}$$

but the thickness experienced by the rim of the inversion now depends on the inversion depth. The angle θ subtended by the rim has a simple geometric relation with the depth d: $\theta = \cos^{-1}(1 - d/R)$. Upon substituting $h = h_0 - \delta\cos\theta = h_0 - \delta(1 - d/R)$ into Eq. (5.14), we see that the dominant scaling of the elastic energy is not $\sim d^{3/2}$ but $\sim d^2$ or higher powers of d at large depths, which is qualitatively different from the situation for uniform shells. Therefore, the total energy $E_{\text{tot}}(d) = E_{\text{el}}(d) - p\Delta V(d)$, where $\Delta V(d) \sim Rd^2$ is the volume reduction associated with the nearly isometric inversion, no longer falls without bound for large d, but instead reaches a stationary point for some value of d, which we call

d_{eq}. Therefore, inversions once formed do not grow uncontrollably but reach an equilibrium depth that may be smaller than R, and depends on the pressure.

The volume evolution of numerically simulated shells with different inhomogeneities under cyclical pressure changes, shown in Fig. 5.7, reflects this fact. The enclosed volume V/V_0 (where $V_0 = 4\pi R^3/3$ is the initial volume of the spherical shell) is measured in simulations on shells with various degrees of inhomogeneity but identical average thickness and radius, as the pressure is ramped up to $0.2p^*_{\delta=0}$ and then brought back down to zero in small increments. For shells with $\delta/h_0 < 1$, the buckling transition is apparent in an abrupt drop in the enclosed volume, at a pressure which is lower for the shell with higher inhomogeneity, consistent with Eq. (5.8). In striking contrast to uniform shells as well as shells with localized soft spots (Fig. 4.14), the volume change at the buckling transition is an inhomogeneity-dependent fraction of the total volume of the shell, and the volume continues to reduce further as the pressure increases. For instance, the shell with $\delta/h_0 = 3/5$ (dotted curve in Fig. 5.7) abruptly reduces its volume by roughly 60% at the buckling pressure (corresponding to an inversion of depth $d \approx 0.5R$), but the inversion continues to grow as the pressure is increased. The shell with $\delta/h_0 = 4/5$ (dashed curve in Fig. 5.7) experiences an even smaller reduction at the buckling threshold of about $0.15V_0$, and then smoothly reduces its volume upon further increase in the pressure. For both shells, the reinflation of the shell as the pressure is reduced is also much smoother than for uniform shells, and the area enclosed by the hysteresis loop is significantly reduced.

In the limit of a shell that is infinitesimally thin at its north pole, i.e $\delta \to h_0$, the hysteresis is almost completely eliminated. Such a shell does not exhibit a finite-pressure buckling transition [$p^*_{\delta\to h_0} = 0$ according to Eq. (5.8)]; instead, a tiny inversion forms at any nonzero pressure and grows smoothly as the pressure is increased (Fig. 5.7, solid curve). In this limit, the shell thickness experienced by the rim as the inversion depth d grows

is $h = h_0 d/R$, and the elastic energy associated with an inversion of depth d scales as $E_{\mathrm{el}} \sim E h_0^{5/2} R^{1/2} (d/R)^4$. The equilibrium inversion depth d_{eq} is set by $E_{\mathrm{el}} \sim p\Delta V \Rightarrow d_{\mathrm{eq}} \sim \sqrt{p}$. As a result, the volume reduction $\Delta V \sim d_{\mathrm{eq}}^2 \sim p$; *i.e.* the enclosed volume falls linearly as p increases, and the shell recovers along an almost identical path as the pressure is reduced back to zero. Highly inhomogeneous shells thus display a smooth, almost perfectly reversible volume change in response to continuous changes in pressure, in striking contrast to uniform spherical shells.

5.6 Conclusion

The combined experimental and theoretical analysis presented in this chapter shows that a smoothly varying inhomogeneity strongly influences the buckling properties of a spherical shell. As for shells with soft spots (studied in Chapter 4), the value of the buckling pressure is determined by the thinnest region, and the inhomogeneity also influences the shape evolution past buckling, although the nature of the buckling pathway and particularly the hysteresis behavior differ from both uniform shells and shells with localized soft spots. Shell theory, combined with Darcy's law, also explains the dynamics of the buckling process in experiments. Our results demonstrate that combining concepts of shell theory with novel fabrication techniques can open up new ways to control buckling in microstructures.

Appendix A

Elastic energy of nearly isometric inversions in spherical shells

In this Appendix, we present a scaling argument for the elastic energy of a nearly isometric inversion in a spherical shell. The treatment of large volume-reducing deformations in spherical shells as nearly isometric shape changes is originally due to Pogorelov [31], and a more recent nonlinear analysis of the shape can be found in Ref. [27]. Here, we reproduce an argument for the scaling of the elastic energy with the shell elastic moduli and the inversion depth, presented in Ref. [5].

In the limit of extremely thin spherical shells (with thickness h much smaller than the radius R), the energy density associated with changing the metric of the mid-surface scales as the Young's modulus $Y = Eh$, whereas the energy density associated with bending deformations scales as the bending rigidity $\kappa = Eh^3/12(1-\nu^2)$ (where ν is the Poisson ratio). Therefore, thin shells are nearly inextensible, and bending deformations are energetically preferred to stretching deformations. The shape of a nearly inextensible shell is close to an *isometric* transformation of the shell (although it cannot be identically isometric for finite Y, since every bending deformation of a shell must be accompanied by some finite stretching due to the curvature [5]). An isometric, volume-reducing transformation of

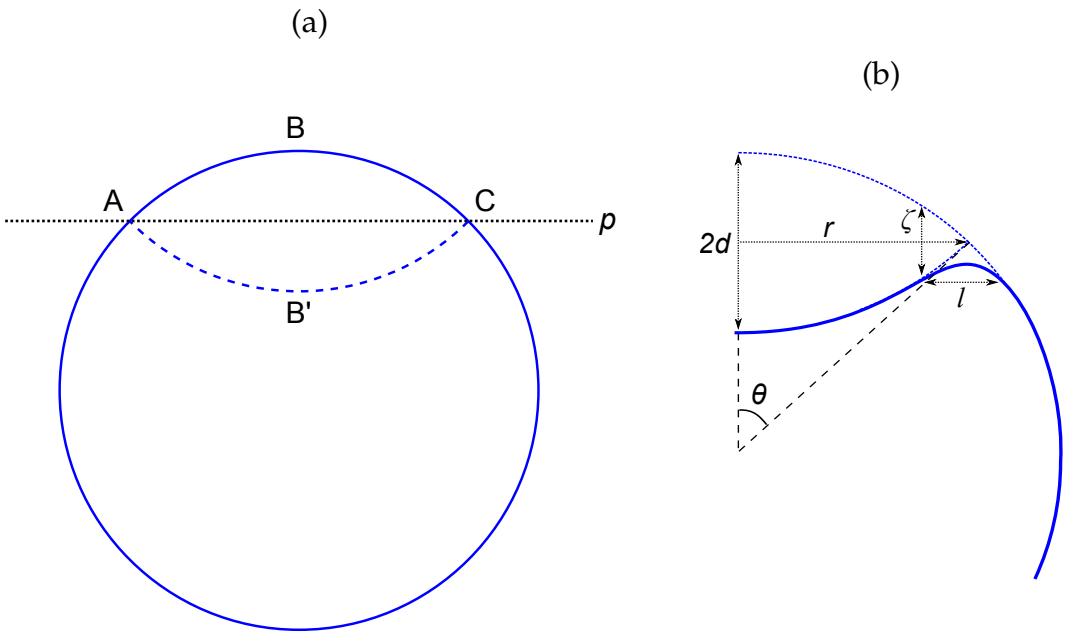

Figure A.1: **(a)** Isometric transformation on the sphere. The transformation is obtained by mirroring the section of the sphere containing the geodesic segment ABC in the plane p, so that $B \rightarrow B'$. **(b)** Parameters describing the nearly isometric inversion of the sphere, on which the singular rim of the isometric inversion, with radius r, is smoothed out due to some stretching in a region of width l. The angle θ subtended by the inversion rim at the center of the sphere relates r to the inversion depth d measured from the plane of reflection to the lowest point of the inversion, as well as the amplitude ζ of the deformation to its width l. The scaling analysis below shows that the width of the rim is indeed small compared to the radius for thin shells.

a spherical shell is obtained by a mirror reflection of a part of the shell in some plane that intersects it [Fig. A.1(a)]. Such a transformation preserves the metric of the mid-surface everywhere, and thus costs no stretching energy. However, the circular rim of the inversion is infinitely sharp, *i.e.* its curvature and correspondingly its bending energy diverge. The true deformation of the shell must deviate from the isometric shape close to the edge, paying a finite stretching energy cost to remove the singular behavior of the curvature. The net bending and stretching energies associated with this "smoothing out" of the singular edge determine the elastic energy associated with such an inversion. Its dependence on the elastic parameters and on the inversion size can be derived using scaling arguments.

We consider a nearly isometric inversion of depth d (measured from the reflecting plane) in a sphere of radius R. Suppose the deformations from the isometric transformation are confined to a circular strip of width l and radius r in the neighborhood of the singular rim of the associated isometric transformation of the shell [Fig. A.1(b)]. Relating the depth $d = R(1 - \cos\theta)$ and the rim radius $r = \sin\theta$ for small values of θ leads to

$$r \approx \sqrt{2dR}. \tag{A.1}$$

The amplitude of deformation ζ near the rim is also related to d by the requirement that the angle between the tangent at the rim and the mirror plane be θ. Hence, $\zeta/l \approx \tan\theta$, which gives

$$\zeta \approx \frac{lr}{R} \approx l\sqrt{\frac{2d}{R}}. \tag{A.2}$$

The elastic strain scales as ζ/R, and the stretching energy density is thus $Y \times (\text{strain})^2 \sim Y(\zeta/R)^2$. The curvature in the strip scales as ζ/l^2, giving rise to a bending energy density of $\kappa \times (\text{curvature})^2 \sim \kappa(\zeta/l^2)^2$. The total elastic energy is obtained by multiplying these energy densities with the area over which the strains are localized, which is $2\pi rl$. Minimizing the net elastic energy

$$E_{\text{el}} \sim c_1 Y(2\pi rl)(\zeta/R)^2 + c_2\kappa(2\pi rl)(\zeta/l^2)^2 \tag{A.3}$$

(where c_1 and c_2 are dimensionless constants) with respect to l gives

$$l \sim \left(\frac{\kappa R^2}{Y}\right)^{1/4} = \frac{\sqrt{hR}}{[12(1-\nu^2)]^{1/4}} \equiv \ell. \tag{A.4}$$

where ℓ is the elastic length associated with deformations in spherical shells [Eq. (1.5)]. For thin shells, $\ell \ll R$, justifying the assumption that the deformations are localized to a narrow region near the rim of the inversion. Substituting the relations (A.1), (A.2) and (A.4) in Eq. (A.3) gives the scaling form of the Pogorelov energy,

$$E_{\text{el}} \sim \kappa^{3/4} Y^{1/4} R^{1/2} \left(\frac{d}{R}\right)^{3/2} \sim Eh^{5/2} R^{1/2} \left(\frac{d}{R}\right)^{3/2}, \tag{A.5}$$

where we used the dependence of Y and κ on the shell thickness h for the second relation. In terms of the dimensionless Föppl-von Kármán number $\gamma \equiv YR^2/\kappa$, we have

$$E_{\rm el} \sim \kappa \gamma^{1/4} \left(\frac{d}{R}\right)^{3/2}. \tag{A.6}$$

In the above arguments, we ignored the background curvature of the shell in its undeformed state when we estimated the bending energy. (We assume that the shell is completely stress-free in its initial shape, and the preferred, or spontaneous, curvature of the mid-surface is $1/R$.) This is because the Pogorelov scaling form is relevant only for inversions beyond a particular size, set by the criterion that the inversion rim must be larger in radius than the elastic length scale which sets its width: $r \gg \ell \Rightarrow d \gg h$. For indentations with depth d of the order of the shell thickness h or smaller, the picture of a nearly isometric inversion with a well-defined narrow rim breaks down. (Instead, the entire indentation extends over a region whose size scales with ℓ, and the energy is quadratic in the indentation depth in that case.)

In the rim of the inversion, the curvature change we have kept in the approximation of the bending energy is $\Delta k = \zeta/\ell^2 \sim \sqrt{d/R}/\ell \sim \sqrt{d/h}/R$. For the Pogorelov scaling to be valid, $d \gg h \Rightarrow \Delta k \gg 1/R$, *i.e.* the curvature change is indeed large compared to the background curvature $1/R$ of the shell, which can be ignored when calculating the elastic energy in the narrow rim of the inversion.

The background curvature may also contribute in the interior of the inversion, away from the rim: although the metric has not changed in this region and there is no stretching energy cost, the curvature has changed sign from $1/R$ to $-1/R$, and there is an associated bending energy cost that scales as $\kappa \times (2/R)^2 \times \text{area} \sim \kappa(r/R)^2 \sim \kappa(d/R)$. This must be compared to the bending energy cost in the narrow rim, which scales as $\kappa(\Delta k)^2 \times (2\pi r\ell) \sim \kappa(d/R)\sqrt{d/h}$, which is again much larger than the bending contribution from

the background curvature provided $d \gg h$. Therefore, we are justified in ignoring the background curvature contribution to the bending energy.

Appendix B

Capillary clustering of microfibers: methods

In this Appendix, we provide details of the numerical and experimental methods used in Chapter 2.

B.1 Details of numerical simulation

The two-parameter cooperative sequential adsorption process was simulated in a program written in the C++ programming language. For each realization of the adsorption process for a particular set of (α, β) values, a two-dimensional binary state array (0 $\equiv$ "empty"; 1 $\equiv$ "occupied") of size equal to that of the lattice being simulated was initialized to zero (all positions vacant). Periodic boundary conditions were used to minimize finite-size effects. Initially all sites were assigned the same rate $k_0 = 1$ in arbitrary units. At each iteration of the sequential process, a site was chosen at random for an adsorption trial. The probability of a site being chosen was set to be proportional to the rate of adsorption assigned to it. If adsorption of a particle was allowed by the exclusion rules, the state of that site was changed to "occupied" and the adsorption rate of vacant sites at 3NN and 4NN positions was updated using the set values of α and β. The iterations continued until

no further adsorption was allowed by the exclusion rules. Since the evolution in time of the process was not of interest, the simulation was sped up by periodically eliminating sites at which adsorption was excluded from consideration as adsorption candidates so that the frequency of unsuccessful adsorption attempts remained low and the jammed state was attained quickly.

B.2 Experimental methods

The microfiber array was prepared in epoxy, using a polydimethylsiloxane (PDMS) mold fabricated from a silicon master. The fabrication of the mold is described in detail in Ref. [65]. The epoxy used was UVO-114 single component UV-initiated epoxy (Epoxy Technology, Inc.). Epoxy was poured into the PDMS mold using a pipette and allowed to cure under a B-100 UV lamp (UVP Blak-Ray) for 20 minutes, after which the mold was peeled off. The hardened epoxy sample was exposed to plasma in a FEMTO plasma system (Diener Electronic) for 20 seconds to improve its wettability. To induce clustering, the sample was placed on a flat surface and 10 μl of absolute anhydrous ethanol was dropped on it using a pipette. The ethanol was allowed to evaporate under ambient conditions.

Optical microscope images of the clustered microfiber sample used for pattern recognition were taken using a Leica DMRX microscope connected to a QImaging Evolution VF CCD camera. SEM images used for illustrations in Chapter 2 were recorded with a JEOL JSM-6390 scanning electron microscope.

Appendix C

Thermally fluctuating spherical shells: analytical calculations

In this Appendix, we provide detailed derivations of the theoretical results presented in Chapter 3.

C.1 Fields and strains in shallow shell theory

We describe the deformations of the sphere using *shallow shell theory* which we summarize here. We follow the presentation by Koiter and van der Heijden [12]. A shallow section of the sphere is isolated and Cartesian coordinates (x_1, x_2) are set up to define a plane that just touches the undeformed sphere at the origin and lies tangent to it; the z axis is thus normal to the sphere at the origin (Fig. C.1). We use the Monge representation to parametrize the undeformed shell by its height $z = Z(x_1, x_2)$ above the plane, where $Z(x_1, x_2)$ is the undeformed state corresponding to a sphere of radius R with its center located on the z-axis above the (x_1, x_2) plane;

$$Z(x_1, x_2) = R\left(1 - \sqrt{1 - \frac{x_1^2}{R^2} - \frac{x_2^2}{R^2}}\right) \tag{C.1}$$

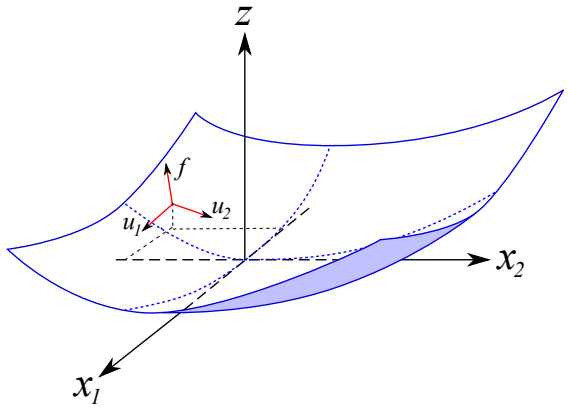

Figure C.1: The coordinate system in shallow shell theory. A section of the undeformed sphere is shown with the (x_1, x_2) plane tangential to it at the origin. The red arrows show the directions into which displacements $u_1(x_1, x_2)$, $u_2(x_1, x_2)$ and $f(x_1, x_2)$ are decomposed at a particular point in the coordinate plane.

The assumption in shallow shell theory is that the section of the shell under consideration is small enough that slopes $\partial_1 Z \sim x_1/R$ and $\partial_2 Z \sim x_2/R$ measured relative to the (x_1, x_2) plane are small. (Partial derivatives are denoted by $\partial/\partial x_i \equiv \partial_i$.) Then the undeformed state is approximately parabolic in x_1 and x_2,

$$Z(x_1, x_2) \approx \frac{x_1^2 + x_2^2}{2R}. \tag{C.2}$$

Deformations from this initial state are quantified *via* a local normal displacement $f(x_1, x_2)$ perpendicular to the undeformed surface and tangential displacements $u_1(x_1, x_2)$ and $u_2(x_1, x_2)$ within the shell along the projections of the x_1 and x_2 axes on the sphere respectively. In terms of these fields, a point $(x_1, x_2, Z(x_1, x_2))$ in the undeformed state moves to $(x_1 + u_1 - f\partial_1 Z, x_2 + u_2 - f\partial_2 Z, Z + f)$ to lowest order in the slopes $\partial_i Z = x_i/R$. The strain tensor is defined by the relation between the length ds' of a line element in the deformed state and the corresponding line element length ds in the undeformed state [5]:

$$(ds')^2 = ds^2 + 2u_{ij}dx_i dx_j. \tag{C.3}$$

With this definition and neglecting terms of order $(\partial_i Z)^2$ and their derivatives, we find the nonlinear strain tensor used in Chapter 3 [Eq. (3.2)],

$$u_{ij}(\mathbf{x}) = \frac{1}{2}\left(\partial_i u_j + \partial_j u_i + \partial_i f \partial_j f\right) - \delta_{ij}\frac{f}{R}. \tag{C.4}$$

The stretching energy is then given by [5]

$$G_s = \frac{1}{2}\int dS\, \left[2\mu u_{ij}^2 + \lambda u_{kk}^2\right], \tag{C.5}$$

where μ and λ are the Lamé coefficients and dS is an area element.

We also include a bending energy of the Helfrich form [105] that penalizes changes in local curvature:

$$G_b = \frac{\kappa}{2}\int dS\, (H - H_0)^2, \tag{C.6}$$

where κ is the bending rigidity, H the mean curvature and H_0 the spontaneous mean curvature (which we take to be equal everywhere to the curvature $2/R$ of the undeformed shell). For a shallow section of the shell, the local curvature can be written in terms of the height field $Z(x_1, x_2) + f(x_1, x_2)$ as

$$H = \nabla^2(Z + f) = \frac{2}{R} + \nabla^2 f, \tag{C.7}$$

where $\nabla^2 = \partial_{11} + \partial_{22}$ is the Laplacian in the tangential coordinate system. Finally the energy due to an external pressure p equals the work done,

$$W = -p\int dS\, f. \tag{C.8}$$

The area element is $dS = dx_1 dx_2/\sqrt{1 - (x_1^2 + x_2^2)/R^2} \approx dx_1 dx_2$ when terms of order $(x_i/R)^2$ and above are neglected. Summing the stretching, bending and pressure energies leads to the elastic energy expression $G = G_s + G_b + W$ used to study thermally fluctuating shells, Eq. (3.1).

Since we are restricted to a shallow section of the shell, the theory is strictly applicable only to deformations whose length scale is small compared to the radius R. The typical length scale ℓ of deformations can be obtained by balancing the bending and stretching energies G_b and G_s discussed above. Upon noting that the stretching free energy density in a region of size ℓ is $\mathcal{G}_s \sim Y(f/R)^2$, where Y is a typical elastic constant, and $\mathcal{G}_b \sim \kappa f^2/\ell^4$, we recover the Föppl-von Kármán length scale,

$$\ell^* = \frac{R}{\gamma^{1/4}}, \tag{C.9}$$

where the Föppl-von Kármán number is $\gamma = YR^2/\kappa$. More sophisticated calculations (sketched below) show that the relevant elastic constant is the 2D Young's modulus, $Y = 4\mu(\mu+\lambda)/(2\mu+\lambda)$.

For a shell made up of an elastic material of thickness h, taking Y and κ from the 3D Young's modulus of an isotropic solid within thin shell theory provides the estimate $\gamma \approx 10(R/h)^2$ [5]. For shallow shell theory to be valid, we need $\ell^* \ll R$. Hence shallow shell theory is valid when $\gamma \gg 1$ *i.e.* $R \gg h$, which is precisely the limit of large, thin curved shells which are most susceptible to thermal fluctuations. This agreement between shallow shell theory and more general shell theories that are applicable over entire spherical shells has been discussed by Koiter [106] in the context of the response of a shell to a point force at its poles. Shallow shell theory was also used to study the stability of pressurized shells by Hutchinson [39]. In both cases, shallow shell theory was shown to be valid for thin shells such that $h/R \ll 1$. Since thermal fluctuations are only relevant for shells with radii several orders of magnitude larger than their thickness, shallow shell theory is an excellent starting point for the extremely thin shells of interest to us here.

C.2 Elimination of in-plane phonon modes and uniform spherical contraction by Gaussian integration

A spherical shell under the action of a uniform external pressure that is lower than the critical buckling threshold responds by contracting uniformly by an amount f_0. The out-of-plane deformation field can then be written as a sum of its uniform and non-uniform parts,

$$f(\mathbf{x}) = f_0 + f'(\mathbf{x}) = f_0 + \sum_{\mathbf{q}\neq 0} f_{\mathbf{q}} e^{-i\mathbf{q}\cdot\mathbf{x}}, \tag{C.10}$$

where $f'(\mathbf{x})$ represents the contribution to the field from its $\mathbf{q} \neq 0$ Fourier components. (In this section, for ease of presentation we use the normalization $f_{\mathbf{q}} \equiv \frac{1}{A}\int d^2x\, f(\mathbf{x}) e^{i\mathbf{q}\cdot\mathbf{x}}$, where A is the area of integration in the (x_1, x_2) plane. The inverse transform is then $f(\mathbf{x}) = \sum_{\mathbf{q}} f_{\mathbf{q}} e^{-i\mathbf{q}\cdot\mathbf{x}}$.) With this decomposition, $\int d^2x\, f'(\mathbf{x}) = 0$ and thus only f_0 contributes to the pressure work W. On the other hand, only f' contributes to the nonlinear part of the strain tensor. Hence the elastic energy $G = G_b + G_s + W$ defined above is harmonic in the in-plane phonon fields $u_1(\mathbf{x})$ and $u_2(\mathbf{x})$ as well as the uniform contraction f_0. To analyze the effects of anharmonicity, it is useful to eliminate these fields and define an effective free energy [87],

$$G_{\text{eff}}[f'] = -k_{\text{B}}T \ln\left\{\int \mathcal{D}\vec{u}(x_1, x_2) \int df_0\, e^{-G[f', f_0, u_1, u_2]/k_{\text{B}}T}\right\}. \tag{C.11}$$

To carry out the functional integrals in Eq. (C.11) for a fixed out-of-plane displacement field $f'(\mathbf{x})$, the strain tensor u_{ij} must also be separated into its $\mathbf{q} = 0$ and $\mathbf{q} \neq 0$ components:

$$u_{ij} = \tilde{u}^0_{ij} + \sum_{\mathbf{q}\neq 0}\left[\frac{i}{2}\left(q_i u_j(\mathbf{q}) + q_j u_i(\mathbf{q})\right) + A_{ij}(\mathbf{q}) - \delta_{ij}\frac{f_{\mathbf{q}}}{R}\right] e^{-i\mathbf{q}\cdot\mathbf{x}} \tag{C.12}$$

where

$$A_{ij}(\mathbf{q}) = \frac{1}{2A}\int d^2x\, \partial_i f'\, \partial_j f'\, e^{i\mathbf{q}\cdot\mathbf{x}}. \tag{C.13}$$

The uniform part of the strain tensor has the following components:

$$\begin{aligned} \tilde{u}^0_{11} &= u^0_{11} + A_{11}(\mathbf{0}) - \frac{f_0}{R}, \\ \tilde{u}^0_{22} &= u^0_{22} + A_{22}(\mathbf{0}) - \frac{f_0}{R}, \\ \tilde{u}^0_{12} &= u^0_{12} + A_{12}(\mathbf{0}). \end{aligned} \tag{C.14}$$

Here, u^0_{ij} are the uniform in-plane strains that are *independent* of f_0. This restriction implies that $u^0_{11} + u^0_{22} = 0$ because a simultaneous uniform in-plane strain of the same sign in the x_1 and x_2 directions corresponds to a change in radius of the sphere and thus cannot be decoupled from f_0. Hence in addition to f_0 and u^0_{12}, there is only one more independent degree of freedom, $\Delta u^0 \equiv u^0_{11} - u^0_{22}$, that determines the uniform contribution to the strain tensor.

Finally we perform the functional integration in Eq. (C.11) over the phonon fields u_i as well as the three independent contributions to the uniform part of the strain tensor — f_0, $\tilde{u}^0_{12}$ and Δu^0. The resulting effective free energy is, upon suppressing an additive constant,

$$G_{\text{eff}} = \int d^2x \left[\frac{\kappa}{2} (\nabla^2 f')^2 + \frac{Y}{2} \left(\frac{1}{2} P^{\text{T}}_{ij} \partial_i f' \partial_j f' - \frac{f'}{R} \right)^2 \right] - A \frac{pR}{2} \left[A_{11}(\mathbf{0}) + A_{22}(\mathbf{0}) \right] \tag{C.15}$$

where $P^{\text{T}}_{ij} = \delta_{ij} - \partial_i \partial_j / \nabla^2$ is the transverse projection operator. Note that as a result of the integration the Lamé coefficients μ and λ enter only through the 2D Young's modulus $Y = 4\mu(\mu + \lambda)/(2\mu + \lambda)$. Finally, substituting

$$A_{11}(\mathbf{0}) + A_{22}(\mathbf{0}) = \frac{1}{2A} \int d^2x \, \left[(\partial_1 f')^2 + (\partial_2 f')^2 \right] = \frac{1}{2A} \int d^2x |\nabla f'|^2 \tag{C.16}$$

in Eq. (C.15) gives the effective free energy used in the analysis of thermal fluctuations in spherical shells, Eq. (3.3). In the following, we drop the prime on the out-of-plane displacement field since f_0 has now been eliminated. When only the harmonic contributions are considered, the equipartition result for the thermally generated Fourier components

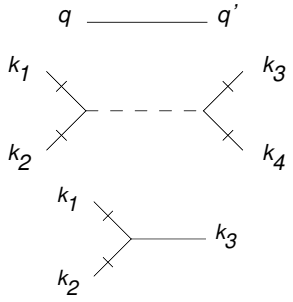

$$\frac{k_{\mathrm{B}}T}{\kappa q^4 - \frac{pR}{2}q^2 + \frac{Y}{R^2}}(2\pi)^2\delta^2(\mathbf{q}+\mathbf{q}')$$

$$\frac{Y}{8}[P^{\mathrm{T}}_{ij}(\mathbf{k}_1+\mathbf{k}_2)k_{1i}k_{2j}][P^{\mathrm{T}}_{lm}(\mathbf{k}_3+\mathbf{k}_4)k_{3l}k_{4m}](2\pi)^2\delta^2(\mathbf{k_1}+\mathbf{k_2}+\mathbf{k_3}+\mathbf{k_4})$$

$$\frac{Y}{2R}[P^{\mathrm{T}}_{ij}(\mathbf{k}_1+\mathbf{k}_2)k_{1i}k_{2j}](2\pi)^2\delta^2(\mathbf{k_1}+\mathbf{k_2}+\mathbf{k_3})$$

Figure C.2: The bare propagator for $f(\mathrm{q})$ and the vertices arising from the non-quadratic terms in G_{eff}. The slashes on specific legs denote spatial derivatives. $P^{\mathrm{T}}_{ij}(\mathbf{q}) = \delta_{ij} - q_i q_j/q^2$ is the transverse projection operator in momentum space. Note an unusual feature of this graphical perturbation theory: the system size, *i.e.* the sphere radius R, enters explicitly both in the propagator and as a coupling constant in the third order interaction vertex.

$f_{\mathbf{q}} = \int d^2x\, f(\mathbf{x}) \exp(i\mathbf{q}\cdot\mathbf{x})$ with two-dimensional wavevector $\mathbf{q}$ are

$$\langle f_{\mathbf{q}} f_{\mathbf{q}'}\rangle_0 = \frac{A k_{\mathrm{B}}T \delta_{\mathbf{q},-\mathbf{q}'}}{\kappa q^4 - \frac{pR}{2}q^2 + \frac{Y}{R^2}}. \tag{C.17}$$

where A is the area of integration in the (x_1, x_2) plane. This harmonic spectrum of fluctuating shells [Eq. (3.4)] takes on corrections due to the anharmonic terms that are calculated in the next section.

C.3 One-loop contributions to the self-energy

Here we describe the self-energy used to calculate the leading anharmonic corrections to the fluctuation spectrum of pressurized spherical shells. The Feynman rules obtained from the effective free energy $G_{\mathrm{eff}}[f]$ are summarized in Fig. C.2. Henceforth, Fourier components are defined as in Chapter 3: $f_{\mathbf{q}} = \int d^2x\, f(\mathbf{x}) \exp(i\mathbf{q}\cdot\mathbf{x})$ with two-dimensional wavevector $\mathbf{q}$. The inverse Fourier transformation of the out-of-plane deformation field is

$$f(\mathbf{x}) = \frac{1}{A}\sum_{\mathbf{q}\neq\mathbf{0}} f_{\mathbf{q}} e^{-i\mathbf{q}\cdot\mathbf{x}}, \tag{C.18}$$

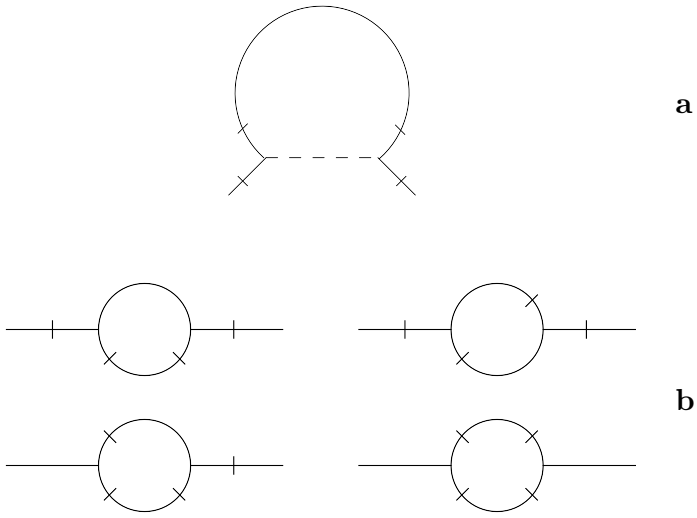

Figure C.3: One-loop corrections to the two-point height-height correlation function in momentum space. Note that in calculating the self-energy, the external propagators are not included; *i.e.* they are "amputated". The contribution in **a** resembles that for membranes with a flat ground state, except for the R-dependent pressure and mass terms in the propagator. The nonlinear corrections in **b**, however, arise from a cubic coupling constant proportional to $1/R$ and are unique to the spherical geometry.

where A is the area of integration in the (x_1, x_2) plane and the sum is over all allowed Fourier modes. The one-loop contribution to the self-energy $\Sigma(\mathbf{q})$ due to the anharmonic three-point vertex (cubic term in the energy) and the four-point vertex (quartic term) are summarized in Fig. C.3. Fig. C.3(a) is also present in the calculation for flat membranes [87], and provides a contribution

$$-Y \int \frac{d^2k}{(2\pi)^2} \frac{[P^{\mathrm{T}}_{ij}(\mathbf{k})q_i q_j]^2}{\kappa|\mathbf{q}+\mathbf{k}|^4 - \frac{pR}{2}|\mathbf{q}+\mathbf{k}|^2 + \frac{Y}{R^2}} \tag{C.19}$$

to the self-energy. Fig. C.3(b) involves two-vertex terms arising from the cubic coupling unique to shells with curvature (note that, despite "amputation" of the propagator legs, the diagrams are distinct because the slashes decide the momentum terms which survive

various index contractions in addition to determining the momentum of the transverse projection operator introduced at each vertex). The net contribution to the self-energy from the four diagrams in Fig. C.3(b) is

$$\frac{Y^2}{R^2}\int\frac{d^2k}{(2\pi)^2}\frac{1}{\left(\kappa|\mathbf{q}+\mathbf{k}|^4-\frac{pR}{2}|\mathbf{q}+\mathbf{k}|^2+\frac{Y}{R^2}\right)\left(\kappa k^4-\frac{pR}{2}q^2+\frac{Y}{R^2}\right)}\times$$
$$\left\{\frac{1}{2}[P^{\mathrm{T}}_{ij}(\mathbf{q})k_ik_j]^2+[P^{\mathrm{T}}_{ij}(\mathbf{k})q_iq_j]^2+[P^{\mathrm{T}}_{ij}(\mathbf{k})q_iq_j][P^{\mathrm{T}}_{lm}(\mathbf{k}+\mathbf{q})q_lq_m]+2[P^{\mathrm{T}}_{ij}(\mathbf{k})q_iq_j][P^{\mathrm{T}}_{lm}(\mathbf{q})k_lk_m]\right\} \tag{C.20}$$

While the inverse of the harmonic correlation function, Eq. (C.17), only contains terms of order q^0, q^2, q^4, the one-loop corrections to the spectrum [Eqs. (C.19–C.20)] generate terms with these powers of q as well as terms of order q^6 and above in the full inverse fluctuation spectrum. If we keep only terms of order q^4 and below in the calculation of the one-loop fluctuation spectrum, we can provide an approximate description of the low-q behavior of the shell in terms of effective elastic constants:

$$Ak_{\mathrm{B}}T\langle|f_{\mathbf{q}\to\mathbf{0}}|^2\rangle^{-1}\equiv\kappa_{\mathrm{R}}q^4-\frac{p_{\mathrm{R}}R}{2}q^2+\frac{Y_{\mathrm{R}}}{R^2}+O(q^6), \tag{C.21}$$

where Y_{R}, κ_{R} and p_{R} are the effective Young's modulus, bending rigidity and dimensionless pressure respectively. At long length scales, probes of the elastic properties of thermally fluctuating shells would provide information of these effective elastic constants rather than the "bare" constants Y, κ and p that describe the zero-temperature shell. Upon expanding the integrands in Eqs. (C.19–C.20) to O(q^4) the momentum integrals can be carried out analytically to obtain:

$$Y_{\mathrm{R}}=Y\left[1-\frac{3}{128\pi}\frac{k_{\mathrm{B}}T}{\kappa}\frac{\sqrt{\gamma}}{(1-\eta^2)^{3/2}}\left(\eta\sqrt{1-\eta^2}+\pi-\cos^{-1}\eta\right)\right], \tag{C.22}$$

$$\kappa_{\mathrm{R}}=\kappa\left[1+\frac{1}{30720\pi}\frac{k_{\mathrm{B}}T}{\kappa}\frac{\sqrt{\gamma}}{(1-\eta^2)^{7/2}}\left[\eta\sqrt{1-\eta^2}\left(-1699+3758\eta^2-2104\eta^4\right)\right.\right.$$
$$\left.\left.+15(61-288\eta^2+416\eta^4-192\eta^6)\left(\pi-\cos^{-1}\eta\right)\right]\right], \tag{C.23}$$

$$\eta_{\text{R}} = \eta + \frac{1}{1536\pi}\frac{k_B T}{\kappa}\frac{\sqrt{\gamma}}{\left(1-\eta^2\right)^{5/2}}\left[\sqrt{1-\eta^2}\left(64-67\eta^2\right)+3\left(21\eta-22\eta^3\right)\left(\pi-\cos^{-1}\eta\right)\right]. \tag{C.24}$$

where we have defined a dimensionless pressure $\eta \equiv p/p_{\text{c}}$ and $p_{\text{c}} = 4\sqrt{\kappa Y}/R^2$ is the classical buckling pressure of the shell. We see explicitly that the quantities diverge in the limit $\eta \to 1$. To lowest order in the external pressure, we have

$$Y_{\text{R}} \approx Y\left[1-\frac{3}{256}\frac{k_{\text{B}}T}{\kappa}\sqrt{\gamma}\left(1+\frac{4}{\pi}\frac{p}{p_{\text{c}}}\right)\right], \tag{C.25}$$

$$p_{\text{R}} \approx p+\frac{1}{24\pi}\frac{k_{\text{B}}T}{\kappa}p_{\text{c}}\sqrt{\gamma}\left(1+\frac{63\pi}{128}\frac{p}{p_{\text{c}}}\right), \tag{C.26}$$

and

$$\kappa_{\text{R}} \approx \kappa\left[1+\frac{61}{4096}\frac{k_{\text{B}}T}{\kappa}\sqrt{\gamma}\left(1-\frac{1568}{915\pi}\frac{p}{p_{\text{c}}}\right)\right]. \tag{C.27}$$

These are the approximate renormalized elastic quantities tabulated in Eqs. (3.7–3.9).

In evaluating the above expressions, the momentum integrals in Eqs. (C.19–C.20) must strictly speaking be carried out over the phase space of all allowed Fourier modes $f(\mathbf{k})$ of the system, which go from some low-k cutoff $k_{\text{min}} \sim 1/R$ to a high-k cutoff set by the microscopic lattice constant. However, since all integrals converge in the ultraviolet limit $k \to \infty$, the upper limit of the k-integrals can be extended to ∞. The integrals are well-behaved at low momenta due to the mass term $\sim Y/R^2$ in the propagator. Hence we carry out the momentum integrals over the entire two-dimensional plane of $\mathbf{k}$. The excess contribution to the self energy by including spurious Fourier modes with $0 < k < 1/R$, *i.e.* for wavevectors less than the natural infrared cutoff $k_{\text{min}} \sim 1/R$, gives rise to an error of roughly $1/\sqrt{\gamma}$ which is negligible for extremely thin shells. This correction is of similar magnitude to the errors introduced by using shallow shell theory (which is inaccurate for the longest-wavelength modes with wavevector $k \sim 1/R$) which are also negligible in the thin-shell limit.

C.4 Calculation of fluctuation spectrum with spherical harmonics

Whereas the perturbation theory calculations were carried out using a basis of Fourier modes in a shallow section of the shell to decompose the radial displacement field, the fluctuation spectrum is most efficiently measured in simulations using a spherical harmonics expansion. To compare the simulation results to the expected corrections from perturbation theory, we use the description of the shell in terms of the effective elastic constants Y_{R}, κ_{R} and p_{R}, Eqs. (3.7–3.9).

Consider a spherical shell of radius R with bending rigidity κ and Lamé coefficients λ and μ, experiencing a tangential displacement field $\mathbf{u} = (u_x, u_y)$ and a radial displacement field f. Like any smooth vector field, $\mathbf{u}$ can be decomposed into an irrotational (curl-free) part and a solenoidal (divergence-free) part: $\mathbf{u} \equiv \nabla\Psi + \mathbf{v}$, where the scalar function Ψ generates the irrotational component and $\mathbf{v}$ is the solenoidal component. Upon expanding $f \equiv \sum_{l,m} A_{lm} R Y_l^m$ and $\Psi \equiv \sum_{l,m} B_{lm} R^2 Y_l^m$ in terms of spherical harmonics $Y_l^m(\theta, \phi)$, the elastic energy of the deformation to quadratic order in the fields is given by [89]

$$\begin{aligned} G = R^2 \sum_{l,m} \Bigg\{ \left[\frac{\kappa}{2} \frac{(l+2)^2 (l-1)^2}{R^2} + 2K \right] A_{lm}^2 - 2Kl(l+1) A_{lm} B_{lm} \\ + \frac{1}{2} l(l+1) \left[(K+\mu) l(l+1) - 2\mu \right] B_{lm}^2 \Bigg\} + G_{\mathrm{sol}}(\mathbf{v}), \end{aligned} \tag{C.28}$$

where $K = \lambda + \mu$ is the bulk modulus. The solenoidal component $\mathbf{v}$ does not couple to the radial displacement field and provides an independent contribution G_{sol} which is purely quadratic in the field $\mathbf{v}$.

To this elastic energy, we also add the surface energy-like contribution $G_{\mathrm{S}} = -(pR/2)\Delta A$ due to the "negative surface tension" $-pR/2$ present in the shell when it is uniformly compressed in response to an external pressure p. Here ΔA is the excess area due to deformations about the average radius. In terms of spherical harmonic coefficients,

this area change can be written [107]

$$\Delta A \approx R^2 \sum_{l>1,m} A_{lm}^2 \left[1 + \frac{l(l+1)}{2}\right]. \tag{C.29}$$

As we did for the elastic energy in shallow shell theory, we can now integrate out the quadratic fluctuating quantities B_{lm} and the solenoidal field $\mathbf{v}$ to obtain an effective free energy in terms of the radial displacements alone:

$$G_{\text{eff}} = \frac{R^2}{2} \sum_{l>1,m} \left\{ \frac{\kappa(l+2)^2(l-1)^2}{R^2} - pR\left[1 + \frac{l(l+1)}{2}\right] + \frac{4\mu(\mu+\lambda)(l^2+l-2)}{(2\mu+\lambda)(l^2+l)-2\mu} \right\} A_{lm}^2. \tag{C.30}$$

The fluctuation amplitude is obtained *via* the equipartition theorem:

$$\begin{aligned} k_B T \langle |A_{lm}|^2 \rangle_0^{-1} &= \kappa(l+2)^2(l-1)^2 - pR^3\left[1 + \frac{l(l+1)}{2}\right] + \frac{4\mu(\mu+\lambda)(l^2+l+2)}{(2\mu+\lambda)(l^2+l)-2\mu} R^2 \\ &= \kappa(l+2)^2(l-1)^2 - pR^3\left[1 + \frac{l(l+1)}{2}\right] + \frac{Y}{1 + \frac{Y}{2\mu(l^2+l-2)}} R^2. \end{aligned} \tag{C.31}$$

where $Y = 4\mu(\mu+\lambda)/(2\mu+\lambda)$ is the 2D Young's modulus introduced earlier. The effect of anharmonic contributions to the fluctuation spectrum can now be calculated by using the effective temperature-dependent quantities Y_{R}, κ_{R} and p_{R} in place of the bare elastic constants in the above expression. However, the last term in Eq. (C.31) also requires knowledge of the thermal corrections to the Lamé coefficient μ which was eliminated in the shallow shell calculation when the tangential displacement fields were integrated out. For the discretized stretching energy used in the simulations, we have $\mu = 3Y/8$. If we assume that this relationship is not significantly changed by the anharmonic corrections to one-loop order, then $\mu_{\text{R}} \approx 3Y_{\text{R}}/8$. Upon substituting this approximation together with the other effective elastic parameters in Eq. (C.31), we find

$$k_B T \langle |A_{lm}|^2 \rangle^{-1} \approx \kappa_{\text{R}}(l+2)^2(l-1)^2 - p_{\text{R}} R^3\left[1 + \frac{l(l+1)}{2}\right] + Y_{\text{R}} R^2 \left[\frac{3(l^2+l-2)}{3(l^2+l)-2}\right] \tag{C.32}$$

which is the same as Eq. (3.10).[1]

C.5 Linear response of the shell to point forces

We calculate the response of the shallow shell to a point force at the origin, corresponding to a force field $h(\mathbf{x}) = F\delta^2(\mathbf{x})$. The Fourier decomposition of this force field is

$$h_{\mathbf{q}} = F, \text{ for all } \mathbf{q}. \tag{C.33}$$

The linear response of the deformation field f to this force is related to its fluctuation amplitudes in the *absence* of the force, $\langle |f_{\mathbf{q}}|^2 \rangle_{h=0}$, by the fluctuation-response theorem:

$$\langle f_{\mathbf{q}} \rangle = \frac{\langle |f_{\mathbf{q}}|^2 \rangle_{h=0}}{Ak_{\mathrm{B}}T} h_{\mathbf{q}} = \frac{\langle |f_{\mathbf{q}}|^2 \rangle_{h=0}}{Ak_{\mathrm{B}}T} F. \tag{C.34}$$

The inward deflection at the origin is then

$$\langle f(\mathbf{x}=0) \rangle = \frac{1}{A} \sum_{\mathbf{q}} \langle f_{\mathbf{q}} \rangle = \frac{F}{A^2 k_B T} \sum_{\mathbf{q}} \langle |f_{\mathbf{q}}|^2 \rangle_{h=0}. \tag{C.35}$$

This can be related to $\langle f^2 \rangle$, the mean square fluctuations of the deformation field in real space which is a position-independent quantity in the absence of nonuniform external forces:

$$\begin{aligned} \langle f^2 \rangle \equiv \langle [f(\mathbf{x})]^2 \rangle_{h=0} &= \frac{1}{A^2} \sum_{\mathbf{q}} \sum_{\mathbf{q}'} \langle f_{\mathbf{q}} f_{\mathbf{q}'} \rangle e^{-i(\mathbf{q}+\mathbf{q}')\cdot\mathbf{x}} \\ &= \frac{1}{A^2} \sum_{\mathbf{q}} \langle |f_{\mathbf{q}}|^2 \rangle_{h=0}. \end{aligned} \tag{C.36}$$

From Eqs. (C.35) and (C.36), we obtain

$$\langle f(\mathbf{x}=0) \rangle = \frac{F}{k_B T} \langle f^2 \rangle. \tag{C.37}$$

[1] If, as is more likely, the thermal corrections to μ and Y do differ to $O(k_B T)$, we can nevertheless estimate that the resulting error term introduced by the assumption $\mu_{\mathrm{R}} \approx 3Y_{\mathrm{R}}/8$ is suppressed by a factor $4/[3(l^2 + l - 2) + 4]$ relative to the anharmonic corrections and is thus at least an order of magnitude smaller than the anharmonic contribution itself when $l > 1$.

This equation relates the depth of the indentation due to a force F at the origin to the mean square fluctuations of the deformation field f in the absence of such a force.

When only harmonic contributions are considered, Eq. (C.17) gives us the mean square amplitude $\langle |f_{\mathbf{q}}|^2 \rangle_0 = Ak_BT/(\kappa q^4 - pRq^2/2 + Y/R^2)$ in terms of the elastic constants and external pressure. Upon taking the continuum limit of the sum over wavevectors $\sum_{\mathbf{q}} \to A \int d^2q/(2\pi)^2$, we can calculate the fluctuation amplitudes exactly:

$$\langle f^2 \rangle = \int \frac{d^2q}{(2\pi)^2} \frac{k_BT}{\kappa q^4 - \frac{pR}{2}q^2 + \frac{Y}{R^2}} = \frac{Rk_BT}{8\sqrt{\kappa Y}} \frac{1 + \frac{2}{\pi}\sin^{-1}\eta}{\sqrt{1-\eta^2}}, \tag{C.38}$$

where $\eta = p/p_c = pR^2/(4\sqrt{\kappa Y})$ is the dimensionless pressure, and $\eta < 1$, *i.e.* we restrict ourselves to pressures below the classical buckling pressure. From Eqs. (C.37) and (C.38), we get the linear relation between the indentation force and the depth of the resulting deformation:

$$F = \frac{8\sqrt{\kappa Y}}{R} \frac{\sqrt{1-\eta^2}}{1 + \frac{2}{\pi}\sin^{-1}\eta} \langle f(\mathbf{x} = 0) \rangle. \tag{C.39}$$

The temperature drops out and we obtain a result valid for $T = 0$ shells as well. The expression reproduces the well-known Reissner solution [97] for the linear response of a spherical shell to a point force when $\eta = 0$, and also reproduces the recent result from Vella et al [108] for indentations on spherical shells with an *internal* pressure when $\eta < 1$. At finite temperatures, however, anharmonic effects contribute terms of order $(k_BT)^2$ and higher to $\langle f^2 \rangle$, making the response temperature-dependent.

In the simulations, the shells contract by a small amount due to thermal fluctuations, even in the absence of external forces. Thus, indentations are measured relative to the thermally averaged pole-to-pole distance of the shell at finite temperature, $\langle z_0 \rangle < 2R$. Equal and opposite inward forces are applied to the north and south poles of the shell to maintain a force balance (see details in Appendix D.3) and the resulting average pole-to-pole distance, $\langle z \rangle$, is measured. This corresponds to an average indentation depth of

$(\langle z_0 \rangle - \langle z \rangle)/2$ at each pole, with associated force [from Eq. (C.37)]

$$F = \frac{k_B T}{\langle f^2 \rangle} \frac{(\langle z_0 \rangle - \langle z \rangle)}{2} \equiv k_{\rm s}(\langle z_0 \rangle - \langle z \rangle), \tag{C.40}$$

i.e. the shell as a whole acts as a spring with spring constant

$$k_{\rm s} = \frac{k_B T}{2\langle f^2 \rangle}. \tag{C.41}$$

At $T = 0$, we have

$$k_{\rm s} = \frac{4\sqrt{\kappa Y}}{R} \frac{\sqrt{1-\eta^2}}{1 + \frac{2}{\pi} \sin^{-1} \eta}; \tag{C.42}$$

in particular, $k_{\rm s} = 4\sqrt{\kappa Y}/R$ in the absence of external pressure. Anharmonic contributions change the fluctuation amplitude $\langle f^2 \rangle$ and hence the linear response. To lowest order in temperature, the effects of anharmonic contributions can be obtained by using the renormalized elastic constants calculated using perturbation theory [Eqs. (C.25)–(C.27)] in Eq. (C.42) and keeping terms to $O(T)$. In particular, even if the bare pressure $p = 0$, the renormalized dimensionless pressure $p_{\rm R}$ is nonzero and affects the spring constant, as do the temperature-dependent effective elastic moduli. The result in this case is

$$k_{\rm s}(T > 0) \approx \frac{4\sqrt{\kappa Y}}{R} \left[1 - 0.0069 \frac{k_B T}{\kappa} \sqrt{\gamma} \right]. \tag{C.43}$$

This completes the derivation of Eq. (3.13).

Appendix D

Simulations of thermally fluctuating shells

In this Appendix, we present details of the numerical simulations used to probe the mechanics of thermally fluctuating shells. We gratefully acknowledge the contributions of Gerrit Vliegenthart (Forschungszentrum Jülich, Germany) to this work.

D.1 Monte Carlo Simulations of randomly triangulated shells

A random triangulation of radius R_0 is constructed by distributing N nodes on the surface of a sphere with the required radius. The first two of these nodes are fixed at the north and the south pole of the sphere whereas the positions of the remaining $N-2$ nodes are randomized and equilibrated in a Monte Carlo simulation. During this equilibration process the nodes interact *via* a steeply repulsive potential (the repulsive part of a Lennard Jones potential). After equilibration, when the energy has reached a constant value on average, the simulation is stopped and the final configuration is 'frozen'. The neighbors of all nodes are determined using a Delaunay triangulation [109]. The spherical configurations as well as the connection lists are used in further simulations.

In subsequent simulations nearest neighbors are permanently linked by a har-

monic potential giving rise to a total stretching energy [110],

$$E_{\mathrm{s}} = \frac{k}{2}\sum_{i,j}(|r_{ij} - r_{ij}^0|^2), \tag{D.1}$$

where the sum runs over all pairs of nearest neighbors, r_{ij} is the distance between two neighbors and r_{ij}^0 the equilibrium length of a spring. The equilibrium length r_{ij}^0 is determined at the start of the simulation, when the shell is still perfectly spherical and thus the stretching energy vanishes for the spherical shape. The spring constant k is related to the two-dimensional Lamé coefficients $\lambda = \mu = \sqrt{3}k/4$ and the two-dimensional Young modulus $Y = 2k/\sqrt{3}$ [110].

The mean curvature (more precisely, twice the mean curvature) at node i is discretized using [91, 111, 112]

$$H_i = \frac{1}{\sigma_i}\mathbf{n}_i \cdot \sum_{j(i)} \frac{\sigma_{ij}}{l_{ij}}(\mathbf{r}_i - \mathbf{r}_j) \tag{D.2}$$

where $\mathbf{n}_i$ is the surface (unit) normal at node i (the average normal of the faces surrounding node i), $\sigma_i = \sum_{j(i)} \sigma_{ij} l_{ij}$ is the area of the dual cell of node i, $\sigma_{ij} = l_{ij}[\cot\theta_1 + \cot\theta_2]/2$ is the length of a bond in the dual lattice and $l_{ij} = |\mathbf{r}_i - \mathbf{r}_j|$ is the distance between the nodes i and j. The total curvature energy is,

$$E_{\mathrm{b}} = \frac{\kappa}{2}\sum_i \sigma_i (H_i - H_0)^2 \tag{D.3}$$

with κ the bending rigidity and H_0 the spontaneous curvature at node i. In all simulations $H_0 = 2/R_0$ (since H_i is twice the mean curvature). In the cases of elastic shells under pressure a term PV is added to the Hamiltonian where P is the external pressure and V the volume of the shell.

Similar elastic networks with stretching and bending potentials have been studied in relation to the stability of membranes, icosahedral and spherical shells that contain defects [77, 83, 28, 110, 113, 114] or defect scars [112, 115, 116, 117] as well as for the deformation of icosahedral viruses [80, 81, 82] and the crumpling of elastic sheets [90].

Simulations are performed for shells of 5530 ($R_0 = 20\ r_0$), 22117 ($R_0 = 40\ r_0$) and 41816 ($R = 55\ r_0$) nodes. The Hookean spring constant and the bending rigidity are taken such that the shells have Föppl-von-Kármán numbers in the range $650 < \gamma < 35000$ and that the dimensionless temperature is in the range $2 \times 10^{-6} < k_\mathrm{B}T/\kappa < 0.5$. Monte Carlo production runs consist typically of 1.25×10^8 Monte Carlo steps where in a single Monte Carlo step an attempt is made to update the positions of all nodes once on average. Configurations were stored for analysis typically every $N_\mathrm{samp} = 2000$ Monte Carlo steps. For the largest system (41816 nodes), such a run took about 700 days of net CPU time spread over several simultaneous runs in a Linux cluster of Intel XEON X5355 CPUs. For the smaller shells, the computational time scaled down roughly linearly with system size.

D.2 The fluctuation spectrum from computer simulations

For a particular configuration of a simulated shell, the coefficients A_{lm} of the expansion of the radial displacements in spherical harmonics [Eq. (3.10)] are determined by a least squares fit of the node positions to a finite number l_M of (real) spherical harmonics. In practice we have used $l_M = 26$ as the upper wavenumber cutoff for all simulations. At each temperature and pressure, this procedure is repeated for about 10000 independent configurations and the results averaged to obtain the curves presented in Fig. 3.2.

D.3 Simulations of shells indented by point-like forces

To perform indentation simulations, two harmonic springs are attached to the north and south pole of the shell. This leads to an additional term in the Hamiltonian,

$$V_\mathrm{s} = \frac{1}{2}k_\mathrm{i}\left(z_\mathrm{i}^\mathrm{N} - z^\mathrm{N}\right)^2 + \frac{1}{2}k_\mathrm{i}\left(z_\mathrm{i}^\mathrm{S} - z^\mathrm{S}\right)^2/2,$$

where $k_\mathrm{i} = \kappa/r_0^2$ is the spring constant of the indenter. Here, one end of the springs, at positions z^N and z^S, is attached to the vertices at the north and south pole, respectively. The positions of the other end of the springs, at z_i^N and z_i^S, are fixed externally and determine the indentation force and depth, as indicated in Fig. D.1.

By changing z_i^N and z_i^S, the depth of the indentation can be varied. After the springs are fixed a certain distance apart, the thermally average pole-to-pole distance $\langle z \rangle$ is measured and compared to its value in the absence of a force, $\langle z_0 \rangle$. The instantaneous force at the poles is calculated from the instantaneous extension of the harmonic springs after each N_samp Monte Carlo steps; thermal averaging then determines the average corresponding to $\langle z \rangle$. This provides the force-indentation curves in Fig. 3.3(a–b).

D.4 Measuring the effective spring constant from fluctuations

It is very difficult to unambiguously identify the linear regime in the force-indentation curves to measure the temperature-dependent spring constants. Extracting the effective spring constant of shell deformation k_s from a linear fit in the small indentation region is subject to inaccuracies and sensitivity to the number of points included in fitting. Instead, we extract the spring constants of thermally fluctuating shells by using the relation Eq. (C.41) between k_s and the fluctuations in z_0 (see Appendix C.5 for derivation):

$$k_\mathrm{s} \approx \frac{k_\mathrm{B}T}{\langle z_0^2 \rangle - \langle z_0 \rangle^2}. \tag{D.4}$$

It is straightforward to measure the average pole-to-pole distance of the fluctuating shell in the *absence* of external forces, $\langle z_0 \rangle = \langle R - f_\mathrm{N} - f_\mathrm{S} \rangle$, where f_N and f_S are the inward displacements at the north and south poles respectively. Since the displacements at the poles are expected to be independent of each other, the mean squared fluctuations

in z_0 are closely related to the mean square fluctuations in f:

$$\langle z_0^2 \rangle - \langle z_0 \rangle^2 \approx 2\langle f^2 \rangle. \tag{D.5}$$

The spring constant can thus be measured indirectly from the fluctuations in the pole-to-pole distance using Eq. (C.41):

$$k_s = \frac{k_B T}{2\langle f^2 \rangle} \approx \frac{k_B T}{\langle z_0^2 \rangle - \langle z_0 \rangle^2}. \tag{D.6}$$

This procedure was used to measure the temperature-dependent spring constants reported in Fig. 3.3(c).

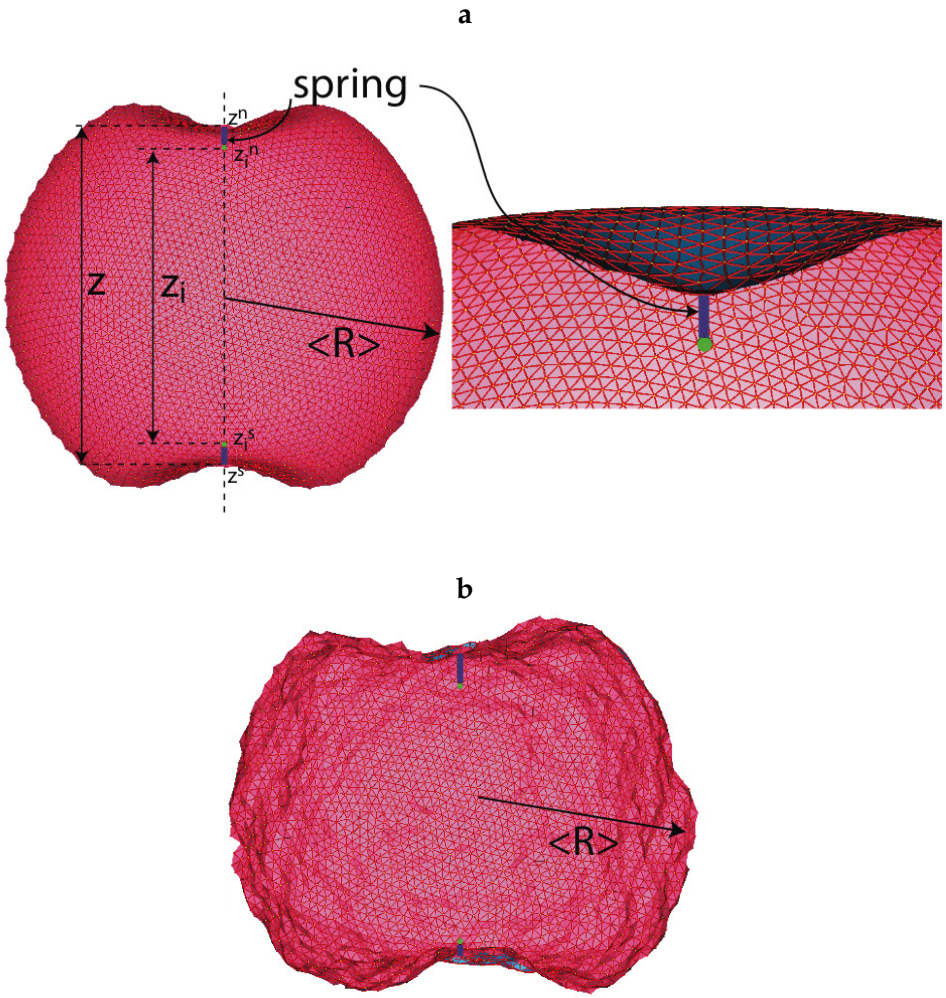

Figure D.1: Illustration of the indentation simulation of a randomly triangulated shell. Shown here are vertical cuts through a shell of radius $R_0 = 20\ r_0$ at low (**a**) and high (**b**) temperatures. (**a**) A shell at low dimensionless temperature $k_BT/\kappa\sqrt{\gamma} = 10^{-5}$, at which anharmonic effects are negligible, is indented by two harmonic springs (dark blue lines) attached to the north (z^{N}) and south (z^{S}) pole of the shell. Fixing the springs at a separation $z_i = z_{\mathrm{i}}^{\mathrm{N}} - z_{\mathrm{i}}^{\mathrm{S}}$ leads to a pole separation z. The green points indicate the positions $z_{\mathrm{i}}^{\mathrm{N}}$ and $z_{\mathrm{i}}^{\mathrm{S}}$ of the fixed end points of the springs. A close-up of the north pole of the shell is shown on the right. The mesh contains a minority of 5 and 7-fold coordinated vertices in addition to 6-fold coordinated ones. (**b**) Illustration of a fluctuating indented shell at $R_0 = 20\ r_0$ and $k_BT/\kappa\sqrt{\gamma} = 15$.

Appendix E

Numerical simulations of zero-temperature shells

In this Appendix, we present the detailed procedure used to simulate the buckling of thin spherical shells when thermal fluctuations are unimportant. These simulations were used in Chapters 4 and 5. In our simulations, the shells are composed of "amorphous" randomly-positioned points connected by springs. Similar models have been used to study the deformations of uniform spherical shells [28], viruses [77, 80, 81, 82, 83] and pollen grains [38]. The computer programs used to conduct these numerical simulations are based on code generously provided by Eleni Katifori.

For our simulations, we discretize the elastic energies on a floating mesh of 20,000 points. The initial mesh (a section of which is shown in Fig. E.1) is disordered, with a distribution of nearest neighbor distances, to eliminate the effect of the 12 regularly spaced five-fold disclinations that inevitably arise when tiling a spherical surface with equilateral triangles [77]. The disordered mesh is created by confining 20,000 points on the surface of a sphere, introducing a steep repulsive potential between nearest neighbor pairs (the repulsive part of a Lennard-Jones potential) and letting the points equilibrate at finite temperature *via* a Monte Carlo simulation. Once the system has equilibrated, the point posi-

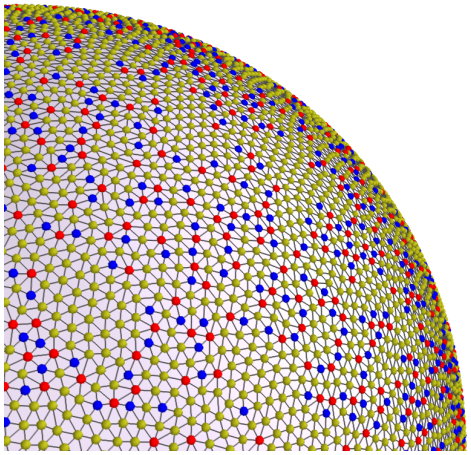

Figure E.1: Disordered mesh used in simulations. For clarity, only one octant of the mesh is shown. Mesh points are colored according to the number of nearest neighbors: blue (five neighbors), yellow (six neighbors) or red (seven neighbors); and nearest-neighbor pairs are connected by lines.

tions are "frozen" and the nearest neighbors calculated as the edges of the convex hull of the set of points. This set of points and bonds is computed once and used as the initial configuration for all the simulations.

The elastic stretching energy of deformations from the initial unstrained configuration is approximated by a harmonic spring energy associated with bonds connecting nearest-neighbor pairs [110]:

$$E_s = \sum_{\langle ij \rangle} \frac{\sqrt{3}}{4} Y (r_{ij} - r_{ij}^0)^2 \tag{E.1}$$

where r_{ij} and r_{ij}^0 are the lengths in the deformed and initial states of the bond connecting nearest-neighbor mesh points i and j. This form reproduces the stretching energy component of the elastic energy [Eq. (4.5)] in the continuum limit, with $\nu = 1/3$ [110].

Previously used discretizations of the bending energy in terms of the angles between surface normals of adjacent facets in the mesh [110, 38] are not suitable for disordered meshes [91]. Instead, we reconstruct the change in curvature k_{ij} from the mean

curvature H_i and Gaussian curvature K_i estimated at each point i. This requires the discretized surface area A and enclosed volume V of the shell, obtained by treating the mesh as a polyhedron with planar triangular facets whose edges are the nearest-neighbor bonds. Each facet j contributes an area $A_j = |(\mathbf{r}_{j_2} - \mathbf{r}_{j_1}) \times (\mathbf{r}_{j_3} - \mathbf{r}_{j_1})|/2$, where $\mathbf{r}_{j_i}$ ($i \in \{1,2,3\}$) are the position vectors of the three mesh points j_i that define the facet. The tetrahedron defined by the origin and the three vertices of each facet j contributes a signed volume $V_j = [\mathbf{r}_{j_1} \cdot (\mathbf{r}_{j_2} \times \mathbf{r}_{j_3})]/6$ to the total volume of the polyhedron. The contribution correctly calculates the enclosed volume of the mesh, provided the facet vertices j_1, j_2 and j_3 are ordered so that the vector $(\mathbf{r}_{j_2} - \mathbf{r}_{j_1}) \times (\mathbf{r}_{j_3} - \mathbf{r}_{j_1})$ points towards the outside of the shell. An estimate of the signed mean curvature at mesh point i is [118]

$$H_i = \frac{1}{2} \frac{\mathbf{F}_i \cdot \mathbf{N}_i}{\mathbf{N}_i \cdot \mathbf{N}_i} \tag{E.2}$$

where $\mathbf{F}_i = \nabla_{\mathbf{r}_i} A$ is the gradient of the discretized surface area $A = \sum_j A_j$ with respect to $\mathbf{r}_i$, and $\mathbf{N}_i = \nabla_{\mathbf{r}_i} V$ is the gradient of the discretized volume $V = \sum_j V_j$. The Gaussian curvature at each point is estimated using the Gauss-Bonnet theorem:

$$K_i = \frac{1}{\sigma_i} \left(2\pi - \sum_{j(i)} \alpha_j \right) \tag{E.3}$$

where α_j is the angle subtended by facet j at point i, and the sum is over all triangular facets sharing point i. $\sigma_i = \sum_{j(i)} A_j/3$ is the area associated with each vertex, computed as one-third of the sum of areas A_j of the facets $j(i)$ sharing point i. The discretized bending energy is [94]

$$E_b = \sum_i \frac{\kappa \sigma_i}{2} \left[4 \left(H_i - \frac{1}{R} \right)^2 - 2(1-\nu) \left(K_i - \frac{2H_i}{R} + \frac{1}{R^2} \right) \right]. \tag{E.4}$$

The pressure is implemented by adding a term pV to the total energy, where the enclosed volume V of the shell is approximated by the polyhedral volume enclosed by the mesh. This net discretized energy $E_s + E_b + pV$ of the $3 \times 20,000$ mesh points is then

minimized using the BFGS quasi-Newton optimization algorithm, which finds local minima accessible smoothly from the initial state. We use the freely available GNU Scientific Library [119] to perform the minimization. The final configuration is checked for stability to a small random perturbation of all the point positions.

Buckling of spherical shells under pressure is simulated by setting the pressure initially to zero, then ramping it up in discrete small steps, finding the local energy minimum at each incremental value of the pressure. A buckling event is identified by a sudden large volume change between small changes in pressure. To prevent well-separated parts of the mesh from intersecting each other when the shell collapses, we constrain the internal volume of the mesh from falling below 10% of the original volume, by adding a term $E_{\text{cons}} = \mu/(V - 0.1V_0)^6$ to the total energy, where$V_0 = 4\pi R^3/3$ is the enclosed volume of the undeformed shell, and μ is kept small so that the constraint term only becomes relevant when V gets very close to V_0.

In Chapter 4, we investigate the nature of the unstable buckling mode by arresting its growth as soon as it appears. To do this, we simulate a solid inner ball centered at the origin (taken to be the center of the undeformed spherical shell) with a slightly smaller radius than the shell. We include a repulsive energy $E_{\text{rep}} = \sum_i \epsilon/(r_i - R_{\text{inner}})^{12}$, where r_i is the distance of point i from the origin, and $R_{\text{inner}} = 0.99R$ is the radius of the simulated inner ball. The strength $\epsilon \sim 10^{-25} Y R^2$ is kept very small so that points in the mesh only feel the influence of this repulsion when they are very close to the inner ball surface, which happens only when buckling has occurred.

To find energy-minimizing configurations at a particular target volume V_T in Chapter 5, we use the penalty method [120, 38]. We add a penalizing term $E_{\text{vol}} = \Lambda(V - V_T)^2$ to the energy, where V is the volume enclosed by all the facets of the mesh, with Λ initially chosen to be very small. We increment Λ systematically between successive mini-

mizations of the total energy, until the difference between the actual and target volumes is negligible.

Appendix F

Derivation of the nonlinear equations of shallow shell theory

In this Appendix, we outline the derivation of the nonlinear differential equations of shallow shell theory for a spherical shell, Eqs. (4.11) and (4.12), starting with the elastic energy of deformations for a Hookean shell [Eq. (4.5)]. Shallow shell theory considers a section of the shell small enough so that slopes relative to a tangent plane at the basal point are small. Then, we set up a Cartesian coordinate system (x, y) in this tangent plane, and describe deformations of the shell in terms of tangential displacement fields $U(x, y)$, $V(x, y)$ and the normal displacement $W(x, y)$ (see Appendix C.1). In this shallow shell coordinate system, the strain tensor u_{ij} and bending tensor k_{ij} are expressed in terms of the displacement fields as [12]

$$u_{xx} = U_{,x} + \frac{1}{2}W_{,x}^2 - \frac{W}{R}, \tag{F.1}$$

$$u_{yy} = V_{,y} + \frac{1}{2}W_{,y}^2 - \frac{W}{R}, \tag{F.2}$$

$$u_{xy} = u_{yx} = \frac{1}{2}\left(U_{,y} + V_{,x} + W_{,x}W_{,y}\right), \tag{F.3}$$

and

$$k_{ij} = W_{,ij}. \tag{F.4}$$

where we use the notation $f_{,\alpha} \equiv \partial_\alpha f$ for spatial derivatives. The total energy, including the elastic contribution [Eq. (4.5)] as well as the contribution due to a finite external pressure p, reduces to

$$\begin{aligned} E_{\text{tot}} = \int dx\, dy \Bigg[& \frac{Y}{2(1-\nu^2)} \Big((u_{xx}+u_{yy})^2 - 2(1-\nu)(u_{xx}u_{yy} - u_{xy}^2) \Big) \\ & + \frac{\kappa}{2} \Big((W_{,xx}+W_{,yy})^2 - 2(1-\nu)(W_{,xx}W_{,yy} - W_{,xy}^2) \Big) - pW \Bigg], \end{aligned} \tag{F.5}$$

up to corrections of order $(L/R)^2$.

Upon minimizing E_{tot} with respect to variations in U, V and W, we obtain the equations,

$$\kappa \nabla^4 W - \frac{1}{R}(\sigma_{xx} + \sigma_{yy}) - (\sigma_{xx}W_{,x} + \sigma_{xy}W_{,y})_{,x} - (\sigma_{xy}W_{,x} + \sigma_{yy}W_{,y})_{,y} = p, \tag{F.6}$$

$$\sigma_{xx,x} + \sigma_{xy,y} = 0, \tag{F.7}$$

$$\sigma_{xy,x} + \sigma_{yy,y} = 0, \tag{F.8}$$

where $\nabla^2 f = f_{,xx} + f_{,yy}$, $\nabla^4 f = \nabla^2(\nabla^2 f)$, and σ_{ij} is the 2D stress tensor, with components

$$\sigma_{xx} = \frac{Y}{1-\nu^2}(u_{xx} + \nu u_{yy}), \tag{F.9}$$

$$\sigma_{yy} = \frac{Y}{1-\nu^2}(u_{yy} + \nu u_{xx}), \tag{F.10}$$

$$\sigma_{xy} = \sigma_{yx} = \frac{Y}{1+\nu} u_{xy}. \tag{F.11}$$

Eqs. (F.7) and (F.8) are automatically satisfied by introducing the Airy stress function χ, derivatives of which give the stress tensor [5]:

$$\sigma_{xx} = \chi_{,yy}; \quad \sigma_{yy} = \chi_{,xx}; \quad \sigma_{xy} = -\chi_{,xy}. \tag{F.12}$$

When σ_{ij} is written in terms of the Airy function, Eq. (F.6) becomes

$$\kappa \nabla^4 W - \frac{1}{R}\nabla^2 \chi - N_2(\chi, W) = p, \tag{F.13}$$

where

$$N_2(f,g) = f_{,xx}g_{,yy} + f_{,yy}g_{,xx} - 2f_{,xy}g_{,xy} \tag{F.14}$$

is a second-order nonlinear differential operator. Although any choice of the function $\chi(x,y)$ automatically satisfies Eqs. (F.7) and (F.8), χ must also be related to real displacement fields U, V and W *via* Eqs. (F.9)–(F.11). Eliminating the fields U and V from these three equations reduces them to a single compatibility condition for χ:

$$\frac{1}{Y}\nabla^4\chi + \frac{1}{R}\nabla^2 W + \frac{1}{2}N_2(W,W) = 0. \tag{F.15}$$

Equations (F.13) and (F.15) are the two nonlinear equations of shallow spherical shells, used for the analysis in Chapter 4. They are a specific case of the *Donnell-Mushtari-Vlasov* equations for shallow shells of general curvature [10].

Appendix G

Fluid flow through an inhomogeneous spherical capsule

In this Appendix, we provide details of the fluid ejection out of spherical inhomogeneous capsules prepared by microfluidics and studied in Chapter 5. The contribution of Sujit S. Datta (Harvard University) to this Appendix is gratefully acknowledged.

G.1 Flow rate out of an inhomogeneous capsule

The buckling of a capsule is driven by the fluid ejection from the capsule interior, due to the imposed osmotic pressure difference across the capsule shell, p. This is resisted by the mechanical pressure required to compress the shell, p_m, at most $p_m \approx 2E(1-\nu)^{-1}h_0(1/R^* - 1/R_0) \approx 3E(h_0/R_0)[(1-\Delta V^*/V_0)^{-1/3} - 1]$, where R^* is the radius of the shell at buckling. For the shells studied in this work, $p_m < p^*$; we thus expect the buckling dynamics to be dominated by the imposed osmotic pressure for $p \gg p^*$, and we neglect p_m in the simple model presented here.

We now estimate the flow rate out of an inhomogeneous capsule due to p; the capsule has shell thickness $h(\theta) = h_0 - \delta\cos\theta$, as shown in Fig. 5.1. We use spherical coordinates (r, θ, ϕ) centered on the capsule center. For an arbitrary area element $\mathrm{d}A$ on

the shell surface at (R_0, θ, ϕ), the local volumetric ejection rate is given by Darcy's law, $\mathrm{d}A \cdot k/\mu h(\theta)$, where k is the shell permeability and μ is the fluid viscosity. Integrating this over the entire shell surface yields the total ejection rate through the shell:

$$Q = R_0^2 \int_0^{2\pi} \mathrm{d}\phi \int_0^{\pi} \sin\theta \frac{pk}{\mu(h_0 - \delta\cos\theta)} \mathrm{d}\theta = \frac{4\pi R_0^2 pk}{\mu h_0} \cdot \frac{1}{2\delta/h_0} \ln\left(\frac{1+\delta/h_0}{1-\delta/h_0}\right). \tag{G.1}$$

G.2 Estimate of capsule permeability

We estimate the capsule permeability k by measuring the change in the radius of a circular indentation r over time, immediately after it is formed in the shell, as shown in Fig. G.1. We assume the volume of the indentation ΔV_{cap} is given by that of a spherical cap having radius $r(t)$. The permeability is then given by $k \approx \frac{\mu h_0 d(\Delta V_{cap})/d(\Delta t)}{p \cdot 4\pi R_0^2}$. In reality, the edges of the indentation are rounded, with radius of curvature $\sim \sqrt{h_0 R_0} \sim 15\mu$m [5]; we thus expect our estimated ΔV_{cap} to over-predict the actual ΔV, and consequently, we expect to under-predict the shell permeability by a factor ~ 2.

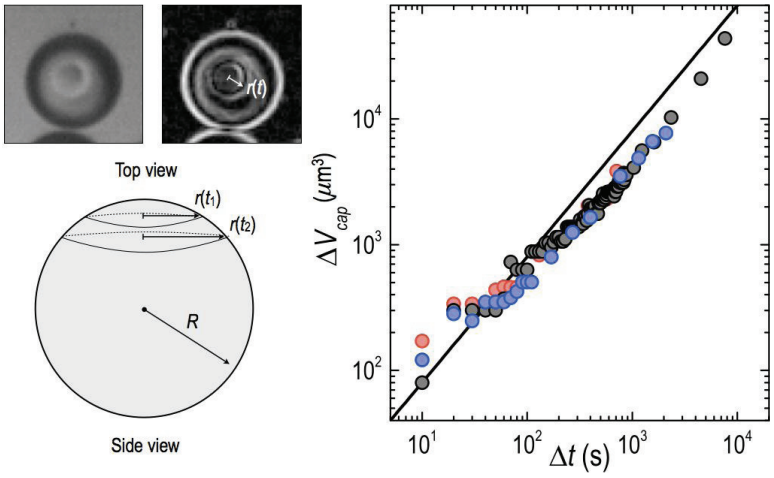

Figure G.1: Change in the volume of a circular indentation formed in a capsule, ΔV_{cap}, over time Δt. The indentation forms at $\Delta t = 0$. Top left panel shows the top view of the indentation formation, measured using optical microscopy; we use image processing to detect the edge of the indentation, shown in the panel to the right, and track the radius of the indentation over time, $r(t)$. We assume a spherical cap geometry, schematically shown in the side view, to calculate ΔV_{cap}; the data are shown for three different capsules (different colors). We fit the small-time dynamics ($\Delta t < 10^2$s) to measure the permeability. The capsules have $h_0/R_0 = 0.1$ and $\delta/h_0 \approx 0.2$, and are buckled at $p = 10$ MPa.

Bibliography

[1] Whitesides, G. M. & Grzybowski, B. Self-assembly at all scales. *Science* **295**, 2418–2421 (2002).

[2] Bico, J., Roman, B., Moulin, L. & Boudaoud, A. Adhesion: Elastocapillary coalescence in wet hair. *Nature* **432**, 690–690 (2004).

[3] Kralchevsky, P. A. & Nagayama, K. Capillary forces between colloidal particles. *Langmuir* **10**, 23–36 (1994).

[4] De Gennes, P.-G., Brochard-Wyart, F. & Quéré, D. *Capillarity and wetting phenomena: drops, bubbles, pearls, waves* (Springer, 2003).

[5] Landau, L. & Lifshitz, E. *Theory of Elasticity, Third Edition* (Butterworth-Heinemann, 1986).

[6] Fan, J.-G., Dyer, D., Zhang, G. & Zhao, Y.-P. Nanocarpet effect: Pattern formation during the wetting of vertically aligned nanorod arrays. *Nano Letters* **4**, 2133–2138 (2004).

[7] Pokroy, B., Kang, S. H., Mahadevan, L. & Aizenberg, J. Self-organization of a mesoscale bristle into ordered, hierarchical helical assemblies. *Science* **323**, 237–240 (2009).

[8] Evans, J. W. Random and cooperative sequential adsorption. *Reviews of Modern Physics* **65**, 1281 (1993).

[9] Talbot, J., Tarjus, G., Van Tassel, P. & Viot, P. From car parking to protein adsorption: an overview of sequential adsorption processes. *Colloids and Surfaces A: Physicochemical and Engineering Aspects* **165**, 287–324 (2000).

[10] Niordson, F. *Shell Theory* (North-Holland, Amsterdam, 1986).

[11] Nelson, D. R., Piran, T. & Weinberg, S. (eds.) *Statistical mechanics of membranes and surfaces, 2nd edition* (World Scientific Singapore, 2004).

[12] van der Heijden, A. M. A. *W. T. Koiter's Elastic Stability of Solids and Structures* (Lecture notes compiled by the author, Cambridge University Press, 2009).

[13] Witten, T. A. Stress focusing in elastic sheets. *Reviews of Modern Physics* **79**, 643 (2007).

[14] De Gennes, P.-G. *Scaling concepts in polymer physics* (Cornell University Press, 1979).

[15] Bowick, M. & Travesset, A. The statistical mechanics of membranes. *Physics Reports* **344**, 255–308 (2001).

[16] Nelson, D. R. & Peliti, L. Fluctuations in membranes with crystalline and hexatic order. *J. Physique* **48**, 1085–1092 (1987).

[17] Aronovitz, J. A. & Lubensky, T. C. Fluctuations of solid membranes. *Physical Review Letters* **60**, 2634 (1988).

[18] Le Doussal, P. & Radzihovsky, L. Self-consistent theory of polymerized membranes. *Physical Review Letters* **69**, 1209 (1992).

[19] Elsner, N. *et al.* Mechanical properties of freestanding polyelectrolyte capsules: a quantitative approach based on shell theory. In *Characterization of Polymer Surfaces and Thin Films*, 117–123 (Springer, 2006).

[20] Hermanson, K., Huemmerich, D., Scheibel, T. & Bausch, A. Engineered microcapsules fabricated from reconstituted spider silk. *Advanced Materials* **19**, 1810–1815 (2007).

[21] Park, Y. *et al.* Measurement of red blood cell mechanics during morphological changes. *Proceedings of the National Academy of Sciences* **107**, 6731–6736 (2010).

[22] Katifori, E., Alben, S. & Nelson, D. R. Collapse and folding of pressurized rings in two dimensions. *Physical Review E* **79**, 056604 (2009).

[23] Fery, A., Dubreuil, F. & Möhwald, H. Mechanics of artificial microcapsules. *New Journal of Physics* **6**, 18–18 (2004).

[24] Carlson, R., Sendelbeck, R. & Hoff, N. Experimental studies of the buckling of complete spherical shells. *Experimental Mechanics* **7**, 281–288 (1967).

[25] Berke, L. & Carlson, R. Experimental studies of the postbuckling behavior of complete spherical shells. *Experimental Mechanics* **8**, 548–553 (1968).

[26] Zoelly, R. *Über ein Knickungsproblem an der Kugelschale*. Ph.D. thesis, Eidgenössischen Technischen Hochschule, Zurich (1915).

[27] Audoly, B. & Pomeau, Y. *Elasticity and geometry: from hair curls to the non-linear response of shells* (Oxford University Press, 2010).

[28] Vliegenthart, G. A. & Gompper, G. Compression, crumpling and collapse of spherical shells and capsules. *New Journal of Physics* **13**, 045020 (2011).

[29] Knoche, S. & Kierfeld, J. Buckling of spherical capsules. *Physical Review E* **84**, 046608 (2011).

[30] Quilliet, C. Numerical deflation of beach balls with various poisson's ratios: From sphere to bowl's shape. *The European Physical Journal E: Soft Matter and Biological Physics* **35**, 1–9 (2012).

[31] Pogorelov, A. V. *Bendings of surfaces and stability of shells* (American Mathematical Society, Providence, RI, 1988).

[32] Pauchard, L. & Rica, S. Contact and compression of elastic spherical shells: The physics of a 'ping-pong' ball. *Philosophical Magazine Part B* **78**, 225–233 (1998).

[33] Gordon, V. D. *et al.* Self-assembled polymer membrane capsules inflated by osmotic pressure. *Journal of the American Chemical Society* **126**, 14117–14122 (2004).

[34] Shum, H. C., Kim, J.-W. & Weitz, D. A. Microfluidic fabrication of monodisperse biocompatible and biodegradable polymersomes with controlled permeability. *Journal of the American Chemical Society* **130**, 9543–9549 (2008).

[35] Datta, S. S., Shum, H. C. & Weitz, D. A. Controlled buckling and crumpling of nanoparticle-coated droplets. *Langmuir* **26**, 18612–18616 (2010).

[36] Quilliet, C., Zoldesi, C., Riera, C., van Blaaderen, A. & Imhof, A. Anisotropic colloids through non-trivial buckling. *The European Physical Journal E: Soft Matter and Biological Physics* **27**, 13–20 (2008).

[37] Sacanna, S., Irvine, W. T. M., Chaikin, P. M. & Pine, D. J. Lock and key colloids. *Nature* **464**, 575–578 (2010).

[38] Katifori, E., Alben, S., Cerda, E., Nelson, D. R. & Dumais, J. Foldable structures and the natural design of pollen grains. *Proceedings of the National Academy of Sciences* **107**, 7635 –7639 (2010).

[39] Hutchinson, J. Imperfection sensitivity of externally pressurized spherical shells. *J. Appl. Mech* **34**, 49–55 (1967).

[40] Wunderlich, W. & Albertin, U. Buckling behaviour of imperfect spherical shells. *International Journal of Non-Linear Mechanics* **37**, 589–604 (2002).

[41] Koga, T. & Hoff, N. J. The axisymmetric buckling of initially imperfect complete spherical shells. *International Journal of Solids and Structures* **5**, 679–697 (1969).

[42] Drmota, M., Scheidl, R., Troger, H. & Weinmüller, E. On the imperfection sensitivity of complete spherical shells. *Computational Mechanics* **2** (1987).

[43] Papadopoulos, V. & Papadrakakis, M. The effect of material and thickness variability on the buckling load of shells with random initial imperfections. *Computer Methods in Applied Mechanics and Engineering* **194**, 1405–1426 (2005).

[44] Baumgart, T., Hess, S. T. & Webb, W. W. Imaging coexisting fluid domains in biomembrane models coupling curvature and line tension. *Nature* **425**, 821–824 (2003).

[45] Veatch, S. L. & Keller, S. L. Separation of liquid phases in giant vesicles of ternary mixtures of phospholipids and cholesterol. *Biophysical Journal* **85**, 3074–3083 (2003).

[46] Lazarus, A., Florijn, H. C. B. & Reis, P. M. Geometry-induced rigidity in nonspherical pressurized elastic shells. *Physical Review Letters* **109**, 144301 (2012).

[47] Shim, J., Perdigou, C., Chen, E. R., Bertoldi, K. & Reis, P. M. Buckling-induced encapsulation of structured elastic shells under pressure. *Proceedings of the National Academy of Sciences* (2012).

[48] Xia, Y., Gates, B. & Li, Z. Y. Self-assembly approaches to three-dimensional photonic crystals. *Advanced Materials* **13**, 409–413 (2001).

[49] Rothemund, P. W. Using lateral capillary forces to compute by self-assembly. *Proceedings of the National Academy of Sciences* **97**, 984–989 (2000).

[50] Cohen, A. E. & Mahadevan, L. Kinks, rings, and rackets in filamentous structures. *Proceedings of the National Academy of Sciences* **100**, 12141–12146 (2003).

[51] Py, C., Bastien, R., Bico, J., Roman, B. & Boudaoud, A. 3d aggregation of wet fibers. *Europhysics Letters* **77**, 44005 (2007).

[52] Zhao, Y. P. & Fan, J. G. Clusters of bundled nanorods in nanocarpet effect. *Applied Physics Letters* **88**, 103123 (2006).

[53] Fan, J.-G. & Zhao, Y.-P. Characterization of watermarks formed in nano-carpet effect. *Langmuir* **22**, 3662–3671 (2006).

[54] Chandra, D., Yang, S., Soshinsky, A. A. & Gambogi, R. J. Biomimetic ultrathin whitening by capillary-force-induced random clustering of hydrogel micropillar arrays. *ACS Applied Materials & Interfaces* **1**, 1698–1704 (2009).

[55] Segawa, H. *et al.* Top-gathering pillar array of hybrid organic-inorganic material by means of self-organization. *Applied Physics A: Materials Science & Processing* **83**, 447–451 (2006).

[56] Chandra, D., Taylor, J. A. & Yang, S. Replica molding of high-aspect-ratio (sub-) micron hydrogel pillar arrays and their stability in air and solvents. *Soft Matter* **4**, 979–984 (2008).

[57] Wu, D. *et al.* Self-organization of polymer nanoneedles into large-area ordered flowerlike arrays. *Applied Physics Letters* **95**, 091902–091902 (2009).

[58] Sidorenko, A., Krupenkin, T., Taylor, A., Fratzl, P. & Aizenberg, J. Reversible switching of hydrogel-actuated nanostructures into complex micropatterns. *Science* **315**, 487–490 (2007).

[59] Chandra, D. & Yang, S. Capillary-force-induced clustering of micropillar arrays: is it caused by isolated capillary bridges or by the lateral capillary meniscus interaction force? *Langmuir* **25**, 10430–10434 (2009).

[60] Wu, F. Dimers on two-dimensional lattices. *International Journal of Modern Physics B* **20**, 5357–5371 (2006).

[61] Sanders, D. E. & Evans, J. W. Correlated percolation in island-forming processes: Analysis of cooperative filling on a square lattice. *Physical Review A* **38**, 4186 (1988).

[62] Evans, J. W., Bartz, J. A. & Sanders, D. E. Multicluster growth via irreversible cooperative filling on lattices. *Physical Review A* **34**, 1434 (1986).

[63] Evans, J., Nord, R. & Rabaey, J. Nonequilibrium c (2×2) island formation during chemisorption: Scaling of spatial correlations and diffracted intensity. *Physical Review B* **37**, 8598 (1988).

[64] Evans, J. & Nord, R. Structure and diffracted intensity in a model for irreversible island-forming chemisorption with domain boundaries. *Journal of Vacuum Science & Technology A: Vacuum, Surfaces, and Films* **5**, 1040–1044 (1987).

[65] Pokroy, B., Epstein, A. K., Persson-Gulda, M. & Aizenberg, J. Fabrication of bioinspired actuated nanostructures with arbitrary geometry and stiffness. *Advanced Materials* **21**, 463–469 (2009).

[66] Kralchevsky, P. A. & Nagayama, K. Capillary interactions between particles bound to interfaces, liquid films and biomembranes. *Advances in Colloid and Interface Science* **85**, 145–192 (2000).

[67] Gibaud, F. & Aizenberg, J. high-speed video of cluster formation. unpublished.

[68] Evans, J. W., Burgess, D. R. & Hoffman, D. K. Irreversible random and cooperative processes on lattices: Spatial correlations. *Journal of Mathematical Physics* **25**, 3051–3063 (1984).

[69] Rabani, E., Reichman, D. R., Geissler, P. L. & Brus, L. E. Drying-mediated self-assembly of nanoparticles. *Nature* **426**, 271–274 (2003).

[70] Bernardes, A. T. Computer simulations of spontaneous vesicle formation. *Langmuir* **12**, 5763–5767 (1996).

[71] Ivanovska, I. L. *et al.* Bacteriophage capsids: Tough nanoshells with complex elastic properties. *Proceedings of the National Academy of Sciences* **101**, 7600 –7605 (2004).

[72] Michel, J. P. *et al.* Nanoindentation studies of full and empty viral capsids and the effects of capsid protein mutations on elasticity and strength. *Proceedings of the National Academy of Sciences* **103**, 6184 –6189 (2006).

[73] Klug, W. S. *et al.* Failure of viral shells. *Physical Review Letters* **97**, 228101 (2006).

[74] Gao, C., Donath, E., Moya, S., Dudnik, V. & Möhwald, H. Elasticity of hollow polyelectrolyte capsules prepared by the layer-by-layer technique. *The European Physical Journal E: Soft Matter and Biological Physics* **5**, 21–27 (2001).

[75] Lulevich, V. V., Andrienko, D. & Vinogradova, O. I. Elasticity of polyelectrolyte multilayer microcapsules. *The Journal of Chemical Physics* **120**, 3822 (2004).

[76] Zoldesi, C. I., Ivanovska, I. L., Quilliet, C., Wuite, G. J. L. & Imhof, A. Elastic properties of hollow colloidal particles. *Physical Review E* **78**, 051401 (2008).

[77] Lidmar, J., Mirny, L. & Nelson, D. R. Virus shapes and buckling transitions in spherical shells. *Physical Review E* **68**, 051910 (2003).

[78] Nguyen, T. T., Bruinsma, R. F. & Gelbart, W. M. Elasticity theory and shape transitions of viral shells. *Physical Review E* **72**, 051923 (2005).

[79] Nguyen, T. T., Bruinsma, R. F. & Gelbart, W. M. Continuum theory of retroviral capsids. *Physical Review Letters* **96**, 078102–4 (2006).

[80] Vliegenthart, G. A. & Gompper, G. Mechanical deformation of spherical viruses with icosahedral symmetry. *Biophysical Journal* **91**, 834–841 (2006).

[81] Buenemann, M. & Lenz, P. Mechanical limits of viral capsids. *Proceedings of the National Academy of Sciences* **104**, 9925 –9930 (2007).

[82] Buenemann, M. & Lenz, P. Elastic properties and mechanical stability of chiral and filled viral capsids. *Physical Review E* **78**, 051924 (2008).

[83] Siber, A. & Podgornik, R. Stability of elastic icosadeltahedral shells under uniform external pressure: Application to viruses under osmotic pressure. *Physical Review E (Statistical, Nonlinear, and Soft Matter Physics)* **79**, 011919–5 (2009).

[84] Pomeau, Y. & Résibois, P. Time dependent correlation functions and mode-mode coupling theories. *Physics Reports* **19**, 63–139 (1975).

[85] Forster, D., Nelson, D. R. & Stephen, M. J. Large-distance and long-time properties of a randomly stirred fluid. *Physical Review A* **16**, 732 (1977).

[86] Lee, P. A. & Ramakrishnan, T. V. Disordered electronic systems. *Reviews of Modern Physics* **57**, 287 (1985).

[87] Nelson, D. R. Theory of the crumpling transition. In *Statistical mechanics of membranes and surfaces, 2nd edition*, chap. 5, 131–148 (World Scientific Singapore, 2004).

[88] Aronovitz, J., Golubovic, L. & Lubensky, T. C. Fluctuations and lower critical dimensions of crystalline membranes. *Journal de Physique* **50**, 609–631 (1989).

[89] Zhang, Z., Davis, H. T. & Kroll, D. M. Scaling behavior of self-avoiding tethered vesicles. *Physical Review E* **48**, R651 (1993).

[90] Vliegenthart, G. A. & Gompper, G. Forced crumpling of self-avoiding elastic sheets. *Nature Materials* **5**, 216–221 (2006).

[91] Gompper, G. & Kroll, D. Random surface discretizations and the renormalization of the bending rigidity. *Journal de Physique I* **6**, 16 (1996).

[92] Waugh, R. & Evans, E. Thermoelasticity of red blood cell membrane. *Biophysical Journal* **26**, 115–131 (1979).

[93] Evans, E. A. Bending elastic modulus of red blood cell membrane derived from buckling instability in micropipet aspiration tests. *Biophysical Journal* **43**, 27–30 (1983).

[94] Datta, S. S. *et al.* Delayed buckling and guided folding of inhomogeneous capsules. *Physical Review Letters* **109**, 134302 (2012).

[95] Huang, N.-C. Unsymmetrical buckling of thin shallow spherical shells. *Journal of Applied Mechanics* **31**, 447–457 (1964).

[96] Shilkrut, D. *Stability of Nonlinear Shells: On the Example of Spherical Shells* (Elsevier, Amsterdam, 2002).

[97] Reissner, E. Stresses and small displacements of shallow spherical shells. I. *Journal of Mathematics and Physics (Massachusetts Institute of Technology)* **25**, 80–85 (1946).

[98] Reissner, E. Stresses and small displacements of shallow spherical shells. II. *Journal of Mathematics and Physics (Massachusetts Institute of Technology)* **25**, 279–300 (1946).

[99] Budiansky, B. *Proceedings of the Symposium on the Theory of Thin Elastic Shells*, 64 (North Holland Publishing Co., Amsterdam, 1969).

[100] Dubin, D. *Numerical and analytical methods for scientists and engineers using Mathematica* (Wiley-Interscience, 2003).

[101] Vaziri, A. & Mahadevan, L. Localized and extended deformations of elastic shells. *Proceedings of the National Academy of Sciences* **105**, 7913 –7918 (2008).

[102] Strogatz, S. *Nonlinear dynamics and chaos* (Perseus Books Group, 2001).

[103] Kim, S.-H., Kim, J. W., Cho, J.-C. & Weitz, D. A. Double-emulsion drops with ultra-thin shells for capsule templates. *Lab on a Chip* **11**, 3162–3166 (2011).

[104] Novozhilov, V. *The theory of thin elastic shells* (P. Noordhoff Ltd., Groningen, 1964).

[105] Helfrich, W. Elastic properties of lipid bilayers: theory and possible experiments. *Zeitschrift für Naturforschung. Teil C: Biochemie, Biophysik, Biologie, Virologie* **28**, 693 (1973).

[106] Koiter, W. *Progress in Applied Mechanics, The Prager Anniversary Volume*, vol. 155, 169 (The Macmillan Co., New York, 1963).

[107] Milner, S. T. & Safran, S. A. Dynamical fluctuations of droplet microemulsions and vesicles. *Physical Review A* **36**, 4371 (1987).

[108] Vella, D., Ajdari, A., Vaziri, A. & Boudaoud, A. The indentation of pressurized elastic shells: from polymeric capsules to yeast cells. *Journal of The Royal Society Interface* (2011).

[109] Renka, R. J. Algorithm 772: STRIPACK: delaunay triangulation and voronoi diagram on the surface of a sphere. *ACM Transactions on Mathematical Software* **23**, 416–434 (1997).

[110] Seung, H. S. & Nelson, D. R. Defects in flexible membranes with crystalline order. *Physical Review A* **38**, 1005 (1988).

[111] Itzykson, C. *Proceedings of the GIFT Seminar, Jaca 85, J. Abad* et al *Eds.*, 130–188 (World Scientific, Singapore, 1986).

[112] Kohyama, T., Kroll, D. M. & Gompper, G. Budding of crystalline domains in fluid membranes. *Physical Review E* **68**, 061905 (2003).

[113] Gompper, G. & Kroll, D. M. Triangulated-Surface Models of Fluctuating Membranes. In *Statistical mechanics of membranes and surfaces, 2nd edition*, chap. 12, 359–426 (World Scientific Singapore, 2004).

[114] Widom, M., Lidmar, J. & Nelson, D. R. Soft modes near the buckling transition of icosahedral shells. *Physical Review E (Statistical, Nonlinear, and Soft Matter Physics)* **76**, 031911–11 (2007).

[115] Bowick, M. J., Nelson, D. R. & Travesset, A. Interacting topological defects on frozen topographies. *Physical Review B* **62**, 8738 (2000).

[116] Bausch, A. R. *et al.* Grain boundary scars and spherical crystallography. *Science* **299**, 1716–1718 (2003).

[117] Kohyama, T. & Gompper, G. Defect scars on flexible surfaces with crystalline order. *Physical Review Letters* **98**, 198101 (2007).

[118] Brakke, K. A. The surface evolver. *Experimental Mathematics* **1**, 141–165 (1992).

[119] Galassi, M. *et al. The GNU Scientific Library Reference Manual, Third Edition* (2009). URL `http://www.gnu.org/software/gsl`.

[120] Siber, A. Buckling transition in icosahedral shells subjected to volume conservation constraint and pressure: Relations to virus maturation. *Physical Review E (Statistical, Nonlinear, and Soft Matter Physics)* **73**, 061915–10 (2006).